

Numerical and Experimental Study on Ship Motion Control Systems in Shallow Water

Changyuan Chen

Doctoral dissertation submitted to obtain the academic degree of
Doctor of Maritime Engineering

Supervisors

Prof. Evert Lataire, PhD - Prof. Guillaume Delefortrie, PhD

Department of Civil Engineering
Faculty of Engineering and Architecture, Ghent University

June 2021



Numerical and Experimental Study on Ship Motion Control Systems in Shallow Water

Changyuan Chen

Doctoral dissertation submitted to obtain the academic degree of
Doctor of Maritime Engineering

Supervisors

Prof. Evert Lataire, PhD - Prof. Guillaume Delefortrie, PhD

Department of Civil Engineering
Faculty of Engineering and Architecture, Ghent University

June 2021



ISBN 978-94-6355-496-1

NUR 969, 974

Wettelijk depot: D/2021/10.500/44

Members of the Examination Board

Chair

Prof. Patrick De Baets, PhD, Ghent University

Other members entitled to vote

Prof. Guillaume Crevecoeur, PhD, Ghent University

Katrien Eloot, PhD, Flanders Hydraulics Research

Prof. Sanghyun Kim, PhD, Inha University, South Korea

Prof. Em. Marc Vantorre, PhD, Ghent University

Prof. Lu Zou, PhD, Shanghai Jiao Tong University, China

Supervisors

Prof. Evert Lataire, PhD, Ghent University

Prof. Guillaume Delefortrie, PhD, Ghent University



Flanders
Hydraulics Research



Flanders
State of the Art

『天行健，君子以自强不息，
地势坤，君子以厚德载物』 -- 《易经》

As heaven maintains vigor through movements, a gentleman should constantly strive for self-perfection.

As earth's condition is receptive devotion, a gentleman should hold the outer world with broad mind.

-- Book of Changes

Preface

“It is good to have an end to journey toward; but it is the journey that matters, in the end.”

-- Ursula K. Le Guin, The Left Hand of Darkness

The last four years have been a crucial journey of growth for me, both as an individual and as a researcher. A journey that manifested itself with several opportunities and challenges, the one that provided me with invaluable experiences and visions. It has not come to an end though; I am now approaching just a milestone. At this point of time, I would like to express my sincere gratitude to all those who inspired, encouraged, guided, and supported me during this journey.

My deepest gratitude is foremost to my two supervisors, Professor Evert Lataire (Ghent University) and Professor Guillaume Delefortrie (Flanders Hydraulics Research and Ghent University). Dear Evert, thank you for welcoming me to embark onboard of the UGent-FHR ship and giving me the opportunity to pursue my PhD at Maritime Technology Division. Your insight into my research plan and progress are the source of power for me to keep everything on the right track. I am very grateful for your patient instruction, constructive suggestions and meticulous remarks. Dear Guillaume, I really appreciate your tremendous help in generating new ideas, to implement the algorithms in the test facilities, set and coordinate the experimental and simulation programs, for providing quick feedback and detailed comments on research results and manuscripts. Your scrupulous attitude, profound knowledge and “doorkeeper” theory are extremely important factors to ensure the quality of research. Thank you for guiding me how to conduct scientific research and become an independent researcher. I have counted myself lucky many times to conduct my PhD study under all your close supervision.

I would like to express my great gratitude to the jury members. Thank you for being part of my committee, for having reviewed my thesis, for your valuable comments, for your time to take part in my defence.

A special word of gratitude goes to emeritus Professor Marc Vantorre. Thank you for opening the door to this wonderful team, leading me to this very interesting research topic and for numerous valuable comments and suggestions in the first two years of my PhD study. Thank you for being so actively available and being the driving force, even after your retirement. I also would like to extend my gratitude to Katrien for sharing knowledge and organizing seminars for me, for helping me to gain insight into this project, for the fruitful collaboration.

This research project would not have been possible to complete without the aid of my UGent (ex-)colleagues. To all my colleagues-turned-friends: In barely 4 years, we've experienced so many happy and memorable moments together: Briscola, Karting, Billiards, Hallows' Eve party, Christmas market, PhD café... I really enjoyed the office work and life in MTD with every of you. Manasés, I am very grateful for your encouragement and support. You always took time to help me, answering questions, solving problems and cheering me up when I was stressed. Marc Mansuy, you have been really kind and were always available for help. I learned a lot from you about fast time simulations. Thanks for being such a nice friend. Ellen, I genuinely thank you for all your good administrative arrangement and assistance. Maxim Candries, my officemate, I have enjoyed sharing the office with you. Apart from our daily conversations, you have tried to give me more insight into the life, society and culture in Belgium. Thank you for your great help and interesting discussions. Thibaut, you have always been a good friend to me. I have very much enjoyed our discussions, both scientific and non-scientific ones. I am grateful for all the moments and the time we shared together, and also for your continued assistance. Luca, it has been such a valuable experience to work with you in testing experimental control algorithms. Travelling to Canada and Germany for meetings together has been very interesting and meaningful. Thanks for being such a great colleague and friend. Ajie and Asif, we have many similar cultural backgrounds, it was a wonderful experience working with you, I really enjoyed having you guys around. I also thank Tianlong, Marco, Maxime, Gael, Rajita, Djahida, Alec, Bernhard, Bart, Ivandito, Danie for your pleasant conversations.

My appreciation is extended to the operational staffs of the FHR towing tank, especially to Luc for ensuring the smooth running of experiments and taking fantastic photos of test facilities. I am also grateful to Jeroen for collaborating with me on the simulation project, for generously sharing research data and results. Special appreciation to Kristien, Stefan, Wim, Pepe for your contributions to the development of the fast time simulator.

My family has undoubtedly been the greatest energy source for me in the pursuit of the doctoral degree. I wish to thank my parents, elder sisters, and lovely nephews for your support, encouragement and deepest love. Without your warm care, I would have never been where I am today. I would like to thank my beloved girlfriend, Jinluan Chen. Your unending support motivated me to climb to the top of the ideal. The journey between Ghent and Rotterdam has been a voyage to success and happiness. These two cities have witnessed our wonderful life and days of endeavour together.

感谢所有在我博士期间给予我帮助和支持的亲人和朋友！我将不乱于心、不困于行、不畏将来、不念过去，为了最初的梦想坚持不懈的走下去！

Finally, I would like to thank YOU, reader, for the interest you have in this study, I wish you pleasant journey throughout the book.

Changyuan Chen
Ghent, March 2021

Summary

Motivation

An autopilot is a control algorithm that can steer a ship on a predetermined course or path without human intervention. The rapid development of maritime autonomous surface ships (MASS) will increase the demand for advanced autopilots. In literature, numerous control algorithms have been developed for ship autopilots, but most studies focus on the complex theoretical approaches, which are usually accompanied by a large number of formula calculations, hence resulting in “explosion of complexity” and “curse of dimensionality” problems. These problems heavily hinder the practical application of controllers, on the contrary, a concise, robust, and adaptive control algorithm is needed in practical engineering.

To evaluate the performance of the developed theoretical algorithms, controllers are usually tested in a virtual, simulated environment. There are still some gaps between simulation and actual application, it is necessary to assess the application of autopilots in real scenarios and validate the simulation results. Nevertheless, only a limited number of studies have been conducted to investigate the performance of controllers via experiments. Most experimental studies concentrate on small-sized ships in deep water. There is a paucity of data on large-sized ships in shallow water, which in fact demands more control actions. In deep water, the ship does not need high manoeuvring capability and has consistent manoeuvring behaviour. The manoeuvring capability is challenged in shallow water and the local under keel clearance heavily affects this challenge. Consequently, the investigation of autopilots for large-sized ships in shallow water is very essential.

Goals and Approach

The main goal of the present research is to design novel and practical ship’s autopilots taking into account the effects of finite water depth. The autopilot algorithms should be suitable for implementation in the control system of the Towing Tank for Manoeuvres in Confined Water and the fast time ship manoeuvring simulator at Flanders Hydraulics Research (FHR). New developments can also be expected in the frame of unmanned shipping and maritime autonomous surface ships.

To achieve this objective, an extensive literature study has been performed to list the state-of-the-art with respect to the ship autopilots. The existing research in literature on control algorithms for automated ship operations up to control of

unmanned vessels was collected and summarised, and knowledge gaps in these studies were identified. As a control algorithm has to be implemented in a mathematical model for manoeuvring simulation, knowledge about various ship manoeuvring mathematical models has been gathered.

On top of that, new control algorithms from simple course control to complex path following control have been designed. The effectiveness of the developed control methods was firstly tested in a Matlab environment. To evaluate the performance of the designed autopilots in real scenarios and investigate their application capabilities, free-running model tests with several autopilot algorithms have been conducted using a scale model of a Liquefied Natural Gas (LNG) carrier in the Towing Tank for Manoeuvres in Confined Water at Flanders Hydraulics Research (co-operation with Ghent University). The selected control algorithms were tested at six different forward speeds and four water depths focusing on the autopilots' performance in shallow water. Based on the experimental results, the application potentials of the autopilots for controlling a surface ship in shallow water were discussed.

From experimental results, effects of water depth and speed on ship's manoeuvrability, steering model and motion control were investigated to extend the knowledge on ship manoeuvring and predict ship's behaviour accurately in shallow water. The influence of under keel clearance and speed on the acceleration tests and zigzag manoeuvres were analysed. The shallow water effect on the ship steering model was discussed via theoretical analysis and experimental validation. The investigation of the effects of speed and water depth on the ship motion controller's parameters and performance was executed.

The designed control algorithms were implemented in a ship manoeuvring simulator to conduct numerical simulation studies. The performance of controllers was analysed by controlling a 6 DOF shallow water manoeuvring model following the prescribed paths at various speeds and water depths. Numerical results were also compared against experimental results to validate the simulation performance. The applicability of controllers was investigated by the simulation of the ship transiting a canal, and the influence of bank effects and speed controller on controllers' performance was also presented.

Main findings

Results obtained from model tests indicate that the designed autopilots could successfully follow the desired trajectories and avoid obstacles with satisfactory control effects in shallow water, but their performance varied in different scenarios. Research results imply the tested controllers can be applied in the towing tank, but for optimum selection of autopilot algorithms, multiple factors including controller parameters, trajectory, and test condition, etc. should be taken into consideration.

Both speed and water depth have a considerable influence on the ship's manoeuvrability and controllability. Especially, water depth restrictions changed the hydrodynamic forces, reduced the propulsion efficiency and manoeuvrability,

the ship became more difficult to manoeuvre and control in shallow water. These impacts on ship manoeuvring, modelling and motion control cannot be neglected.

Numerical results matched well with the experimental results despite slight discrepancies and the effectiveness of simulation results were validated. The applicability of the controllers in real scenarios was verified by the simulation of the ship passing through a canal. The results indicate that the designed controllers could be applied in the fast time simulator.

Main contributions

An intelligent machine learning method was proposed in order to accurately identify the parameters of ship mathematical models and solve the problems of difficult estimating nonlinear terms by traditional approaches. A novel path planning algorithm was proposed to automatically generate a smooth and optimal path in a complex environment.

The application potential of the designed controllers was investigated using a scale model (experimental study) instead of the complex theoretical analysis. The experimental results will provide an overview of the application capabilities of various controllers in real scenarios for future reference among the maritime scientific community.

A large number of model tests (5000) were carried out at different water depths and speeds. Particular attention has been given to the controllers' performance in shallow water. Effects of water depth on the parameters and performance of controllers were discussed, while the approach of optimizing the controllers' tracking capacity in shallow water was introduced. To solve the speed and water-depth dependency problems of the PID controller's coefficients, a new adaptive controller was proposed. To comprehensively evaluate the performance of autopilots, an innovative method combining the model evaluation mechanism and the grey relational decision-making theory was proposed.

Numerical simulations were conducted in a ship manoeuvring simulator using a 6 DOF shallow water model, which could better describe the dynamics and kinematics of the ship, thereby improving the accuracy of the simulation. The results will provide a reference for the development of autopilots in ship manoeuvring simulators. Simulation results have been validated by model tests. This will fill the gap in the current research, where most research only applies the controllers in simulations but have limited information on their performance in real cases (no validation), especially in shallow water. The application ability of the designed controllers was investigated in the real scenarios, meanwhile the influence of bank effects and speed controller was studied in practical engineering.

Samenvatting

Motivatie

Een stuurautomaat is een controlealgoritme dat een schip zonder menselijke tussenkomst op een vooraf bepaalde koers of pad kan sturen. De snelle ontwikkeling van maritieme autonome oppervlakteschepen (MASS) zal de vraag naar geavanceerde autopiloten doen toenemen. In de literatuur zijn talrijke sturingsalgoritmen ontwikkeld voor stuurautomaten voor schepen, maar de meeste studies richten zich op de complexe theoretische benaderingen, die gewoonlijk gepaard gaan met een groot aantal formuleberekeningen, hetgeen resulteert in “explosie van complexiteit” en “vloek van de dimensionaliteit” problemen. Deze problemen vormen een ernstige belemmering voor de praktische toepassing van regelaars, integendeel, een beknopt, robuust en adaptief regelalgoritme is nodig in de praktische techniek.

Om de prestaties van de ontwikkelde theoretische algoritmen te evalueren, worden controllers gewoonlijk getest in een virtuele, gesimuleerde omgeving. Tussen simulatie en werkelijke toepassing gaapt nog een zekere kloof; het is noodzakelijk de toepassing van automatische piloten in reële scenario's te beoordelen en de simulatieresultaten te valideren. Niettemin is slechts een beperkt aantal studies uitgevoerd om de prestaties van besturingen via experimenten te onderzoeken. De meeste experimentele studies zijn toegespitst op schepen van kleine afmetingen in diep water. Er is een tekort aan gegevens over grote schepen in ondiep water, dat in feite meer regelacties vereist. In diep water heeft het schip geen groot manoeuvreervermogen nodig en vertoont het een consistent manoeuvreergedrag. In ondiep water wordt het manoeuvreervermogen op de proef gesteld en heeft de plaatselijke kielspeling een grote invloed op deze uitdaging. Bijgevolg is het onderzoek van stuurautomaten voor grote schepen in ondiep water zeer essentieel.

Doelstellingen en aanpak

Het hoofddoel van het huidige onderzoek is het ontwerpen van nieuwe en praktische scheepsstuurautomaten die rekening houden met de effecten van eindige waterdiepte. De stuurautomaatalgoritmen moeten geschikt zijn voor implementatie in het controlesysteem van de Sleptank voor Manoeuvres in Besloten Water en de snelle tijdssimulator voor scheepsmanoeuvres bij Flanders Hydraulics Research (FHR). Nieuwe ontwikkelingen kunnen ook worden verwacht in het kader van onbemande scheepvaart en maritieme autonome oppervlakteschepen.

Om dit doel te bereiken is een uitgebreide literatuurstudie verricht om de stand van de techniek met betrekking tot de stuurautomaten voor schepen in kaart te brengen. Het bestaande onderzoek in de literatuur naar besturingsalgoritmen voor geautomatiseerde scheepsoperaties tot en met de besturing van onbemande vaartuigen is verzameld en samengevat, en hiaten in de kennis in deze studies zijn geïdentificeerd. Aangezien een besturingsalgoritme moet worden geïmplementeerd in een wiskundig model voor manoeuvreersimulatie, is kennis verzameld over verschillende wiskundige modellen voor scheepsmanoeuvres.

Bovendien werden nieuwe controle-algoritmen ontworpen, gaande van eenvoudige koerscontrole tot complexe trajectvolgende controle. De doeltreffendheid van de ontwikkelde controlemethodes werd eerst getest in een Matlab-omgeving. Om de prestaties van de ontworpen stuurautomaten in reële scenario's te evalueren en hun toepassingsmogelijkheden te onderzoeken, werden vrijlopende modeltests met verschillende stuurautomaatalgoritmen uitgevoerd met een schaalmodel van een Liquefied Natural Gas (LNG) carrier in de Sleep tank voor Manoeuvres in Besloten Water van Flanders Hydraulics Research (in samenwerking met de Universiteit Gent). De geselecteerde besturingsalgoritmen werden getest bij zes verschillende voorwaartse snelheden en vier waterdieptes, waarbij de nadruk lag op de prestaties van de stuurautomaat in ondiep water. Op basis van de experimentele resultaten werden de toepassingsmogelijkheden van de stuurautomaten voor het besturen van een oppervlakteschip in ondiep water besproken.

Aan de hand van experimentele resultaten werden de effecten van waterdiepte en snelheid op de manoeuvreerbaarheid van het schip, het stuurmodel en de bewegingscontrole onderzocht om de kennis over scheepsmanoeuvres uit te breiden en het gedrag van schepen in ondiep water nauwkeurig te voorspellen. De invloed van de kielvrijheid en de snelheid op de acceleratietests en zigzagmanoeuvres werden geanalyseerd. Het effect van ondiep water op het scheepsstuurmodel werd besproken via theoretische analyse en experimentele validatie. De effecten van snelheid en waterdiepte op de parameters en prestaties van de bewegingsregelaar van het schip werden onderzocht.

De ontworpen regelalgoritmen werden geïmplementeerd in een simulator voor het manoeuvreren van schepen om numerieke simulatiestudies in snelle tijd uit te voeren. De prestaties van de regelaars werden geanalyseerd door een 6 DOF ondiep water manoeuvreermodel te besturen volgens de voorgeschreven paden bij verschillende snelheden en waterdieptes. Numerieke resultaten werden ook vergeleken met experimentele resultaten om de simulatieprestaties te valideren. De toepasbaarheid van de regelaars werd onderzocht door simulatie van het schip dat door een kanaal vaart, en de invloed van oevereffecten en snelheidsregelaar op de prestaties van de regelaars werd ook gepresenteerd.

Belangrijkste bevindingen

De resultaten van modelproeven geven aan dat de ontworpen stuurautomaten met succes de gewenste trajecten konden volgen en obstakels konden ontwijken met bevredigende controle-effecten in ondiep water, maar hun prestaties varieerden in

verschillende scenario's. De onderzoeksresultaten impliceren dat de geteste regelaars kunnen worden toegepast in de sleeptank, maar voor een optimale selectie van stuurautomaalgoritmen moet rekening worden gehouden met meerdere factoren, waaronder de parameters van de regelaar, het traject, en de testconditie, enz.

Zowel de snelheid als de waterdiepte hebben een aanzienlijke invloed op de manoeuvreerbaarheid en bestuurbaarheid van het schip. Met name waterdieptebeperkingen veranderden de hydrodynamische krachten, verminderden de voortstuwings efficiëntie en de manoeuvreerbaarheid, het schip werd moeilijker te manoeuvreren en te controleren in ondiep water. Deze effecten op het manoeuvreren van het schip, de modellering en de bewegingscontrole kunnen niet worden verwaarloosd.

De numerieke resultaten kwamen goed overeen met de experimentele resultaten, ondanks kleine verschillen, en de effectiviteit van de simulatieresultaten werd gevalideerd. De toepasbaarheid van de regelaars in reële scenario's werd geverifieerd door de simulatie van een schip dat door een kanaal vaart. De resultaten geven aan dat de ontworpen regelaars kunnen worden toegepast in de snelle tijdsimulator.

Belangrijkste bijdragen

Er werd een intelligente methode van machinaal leren voorgesteld om de parameters van wiskundige scheepsmodellen nauwkeurig te identificeren en de problemen op te lossen van het moeilijk schatten van niet-lineaire termen door traditionele benaderingen. Een nieuw algoritme voor padplanning werd voorgesteld om automatisch een vloeiend en optimaal pad te genereren in een complexe omgeving.

Het toepassingspotentieel van de ontworpen regelaars werd onderzocht met behulp van een echt schip (experimentele studie) in plaats van de complexe theoretische analyse. De experimentele resultaten zullen een overzicht geven van de toepassingsmogelijkheden van de verschillende regelaars in reële scenario's voor toekomstige referentie binnen de maritieme wetenschappelijke gemeenschap.

Een groot aantal modelproeven (5000) werd uitgevoerd bij verschillende waterdiepten en snelheden. Bijzondere aandacht werd geschonken aan de prestaties van de regelaars in ondiep water. De effecten van de waterdiepte op de parameters en de prestaties van de regelaars werden besproken, terwijl de benadering van het optimaliseren van het volgvormen van de regelaars in ondiep water werd geïntroduceerd. Om de problemen met de snelheid en de afhankelijkheid van de waterdiepte van de coëfficiënten van de PID-regelaar op te lossen, werd een nieuwe adaptieve regelaar voorgesteld. Om de prestaties van stuurautomaten uitgebreid te evalueren, werd een innovatieve methode voorgesteld die het model-evaluatiemechanisme en de grijze-relatieve besluitvormingstheorie combineert.

Numerieke simulaties werden uitgevoerd in een scheepsmanoeuvresimulator met gebruikmaking van een 6 DOF ondiep water model, dat de dynamica en kinematica van het schip beter kon beschrijven, waardoor de nauwkeurigheid van de simulatie werd verbeterd. De resultaten zullen als referentie dienen voor de ontwikkeling van stuurautomaten in scheepsmanoeuvresimulators. De simulatieresultaten zijn gevalideerd door modelproeven. Dit vult de leemte in het huidige onderzoek, waar de meeste onderzoeken de regelaars alleen in simulaties toepassen, maar beperkte informatie hebben over hun prestaties in echte gevallen (geen validatie), vooral in ondiep water. De toepasbaarheid van de ontworpen regelaars werd onderzocht in reële scenario's, terwijl de invloed van oevereffecten en snelheidsregelaars werd bestudeerd in de praktische engineering.

Table of Contents

<i>Preface</i>	<i>i</i>
<i>Summary</i>	<i>iii</i>
<i>Samenvatting</i>	<i>vii</i>
<i>Table of Contents</i>	<i>xi</i>
<i>Nomenclature</i>	<i>xv</i>
1 Introduction	3
1.1 Research background	3
1.1.1 Fast time simulator	3
1.1.2 Maritime autonomous surface ships	5
1.2 Problems and opportunities	7
1.2.1 Control algorithms.....	7
1.2.2 Control performance in shallow water.....	7
1.2.3 Modelling of marine surface ships.....	8
1.2.4 Underactuated characteristics	9
1.2.5 Path following control	9
1.3 Research objectives and methods	11
1.3.1 Research objectives	11
1.3.2 Research methods.....	11
1.4 Outline of thesis	13
1.5 Reference	15
2 State of the art	17
2.1 Development of ship mathematical models	17
2.1.1 Ship mathematical models.....	17
2.1.2 Ship mathematical model parameters	20
2.2 Development of ship motion control	23
2.2.1 Historical remarks.....	23
2.2.2 Classification of controllers.....	24
2.3 Development of path following control	29
2.3.1 Overview	29
2.3.2 Path planning system	29
2.3.3 Guidance system.....	32
2.3.4 Control system.....	34
2.4 Reference	37
3 Ship motion mathematical models	59
3.1 Coordinate systems	59
3.1.1 Overview	59
3.1.2 Earth and ship bound coordinate systems.....	60

3.2	Ship mathematical models	62
3.2.1	1 DOF Manoeuvring model.....	62
3.2.2	3 DOF Manoeuvring model.....	63
3.2.3	6 DOF Manoeuvring model.....	66
3.3	Parameter identification methods	72
3.3.1	Overview	72
3.3.2	Nonlinear Least Squares method.....	72
3.3.3	Fitting Least Squares method	73
3.3.4	Nonlinear Least Squares Support Vector Machine.....	74
3.3.5	Optimised NLSSVM by BAS method.....	76
3.4	Application of identification methods	80
3.4.1	Application on roll motion model	80
3.4.2	Application on ship response model.....	92
3.5	Reference	100
4	<i>Path plan, guidance, navigation, and control</i>	103
4.1	General discussion	103
4.2	Path planning system	105
4.2.1	Overview	105
4.2.2	Manually planning method.....	105
4.2.3	Automatically planning method	105
4.3	Guidance system	117
4.3.1	Overview	117
4.3.2	Determination of LOS angle.....	117
4.3.3	Selection of current waypoint.....	118
4.3.4	Sign of cross track error	120
4.4	Navigation system	121
4.5	Reference	123
5	<i>Motion control systems</i>	125
5.1	General discussion	125
5.2	PID controller	127
5.2.1	Controller structure.....	127
5.2.2	Determination of time constant T and gain K	128
5.2.3	Determination of PID parameters.....	130
5.3	Internal model controller	131
5.3.1	Controller structure.....	131
5.3.2	Controller design	132
5.4	Adaptive PID controller	134
5.4.1	Controller structure.....	134
5.4.2	Controller design	135
5.5	Fuzzy controller	136
5.5.1	Controller structure.....	136
5.5.2	Controller design	136
5.6	Fuzzy PID controller	140
5.6.1	Controller structure.....	140
5.6.2	Controller design	140
5.7	Backstepping controller	144
5.7.1	Controller structure.....	144

5.7.2	Controller design	144
5.8	Nonlinear feedback and nonlinear decoration filters	148
5.8.1	Nonlinear feedback filter	148
5.8.2	Nonlinear decoration filter.....	149
5.9	Speed controller	151
5.9.1	Controller structure.....	151
5.9.2	Determination of K_{pu} and K_{iu}	151
5.9.3	Tolerance interval and propeller rate limiter	151
5.10	Controller performance evaluation.....	153
5.10.1	Evaluation procedure	153
5.10.2	Evaluation mechanism.....	153
5.10.3	Model selection mechanism	154
5.11	Reference	156
6	Experimental program	159
6.1	General discussion	159
6.2	Experimental setup.....	160
6.2.1	Towing tank.....	160
6.2.2	Ship model.....	162
6.3	Beam and coordinate systems.....	164
6.3.1	Captive and free running model tests	164
6.3.2	Coordinate systems in towing tank.....	166
6.4	Test conditions	168
6.4.1	Water depths	168
6.4.2	Forward speeds.....	170
6.5	Post processing.....	172
6.5.1	Postprocessing theory	172
6.5.2	Postprocessing by softwares	173
6.6	Experimental results	176
6.6.1	Self-propulsion tests	176
6.6.2	Zigzag tests.....	178
6.6.3	Course tests.....	182
6.6.4	Path following tests	186
6.7	Shallow water and speed effects	202
6.7.1	Effects on manoeuvring indices K and T	202
6.7.2	Effects on controller parameters.....	207
6.7.3	Effects on controller performance	211
6.7.4	Improvement of controllers' performance.....	217
6.8	Reference.....	223
7	Numerical simulation studies.....	225
7.1	General discussion	225
7.2	Track controller in fast-time simulator	228
7.2.1	Prescience model based track controller.....	228
7.2.2	Proposed track controller.....	229
7.3	Ship model validation.....	231
7.4	Numerical simulation results.....	233
7.4.1	Overview	233
7.4.2	Folding line path following simulation.....	233

7.4.3	Curved path following and obstacle avoidance simulation	235
7.5	Comparison with experimental results	236
7.5.1	Folding line path following	236
7.5.2	Curved path and obstacle avoidance.....	238
7.6	Application of the track controller on the Panama Canal	243
7.6.1	Performance of controllers	243
7.6.2	Bank effect on controllers' performance	246
7.6.3	Influence of speed controller	254
7.7	Application of the track controller on the Western Scheldt	258
7.7.1	Overview	258
7.7.2	Track Controller Input	259
7.7.3	Results and discussions	262
7.8	Reference.....	271
8	Conclusions and recommendations	273
8.1	Conclusions	273
8.1.1	General discussion.....	273
8.1.2	System identification for obtaining ship mathematical models.....	274
8.1.3	New path following control system.....	274
8.1.4	Build experiment and simulation platforms.....	275
8.1.5	Experimental studies	276
8.1.6	Numerical simulation studies	277
8.2	Recommendations	279
8.2.1	Theoretical studies.....	279
8.2.2	Experimental studies	280
8.2.3	Simulation studies	280
9	Publications and Grants.....	283
9.1	List of publications	283
9.2	List of Grants.....	284
10	Appendices.....	287
10.1	General discussion	287
10.2	Configuration of the simulator	287
10.2.1	Input and output to the simulator.....	287
10.2.2	Configuration of autopilot file.....	288
10.2.3	Controller parameters	291
10.2.4	Configuration of speed controller.....	297
10.3	Reference.....	300
	List of Figures	301
	List of Tables	311

Nomenclature

These lists give a non-exhaustive overview of the symbols and abbreviations used throughout the thesis.

Latin symbols

a	Nonlinear constant of Nomoto model	(s ² /rad ²)
A_R	Rudder area	(m ²)
B	Breadth	(m)
c	tuning factor	(-)
C_B	Block coefficient	(-)
D_p	Propeller diameter	(m)
Fr	Froude number	(-)
Fr_h	Depth-related Froude number	(-)
GM	Metacentric height	(m)
h	Water depth	(m)
H_R	Height of rudder	(m)
I_{xx}, I_{yy}, I_{zz}	Moment of inertia about x, y, z axes	(kgm ²)
K	Gain of Nomoto model	(1/s)
K	Roll moment	(Nm)
K_d	Derivative coefficient	(s)
K_{dn}	Adaptive derivative coefficient	(-)
K_i	Integral coefficient	(1/s)
K_{in}	Adaptive integral coefficient	(-)
KM	Transverse metacentre above keel	(m)
K_p	Proportional coefficient	(-)
K_{pn}	Adaptive proportional coefficient	(-)
L_{PP}	Length between perpendiculars	(m)
L_{OA}	Length over all	(m)
m	Mass of ship	(kg)
n	Propeller rate	(rps)
M	Pitch moment	(Nm)
N	Yaw moment	(Nm)
$Oxyz$	Body-bound coordinate system	(-)
$O_0x_0y_0z_0$	Earth-bound coordinate system	(-)
P	Propeller pitch	(m)
P_{los}	Position of line-of-sight algorithm	(m)
p	Roll angular velocity	(rad/s)
q	Pitch angular velocity	(rad/s)

r	Yaw angular velocity	(rad/s)
T	Time constant of 1 st order Nomoto model	(s)
T_1, T_2, T_3	Time constants of 2 nd order Nomoto model	(s)
T_e	Cross track error	(m)
T_M	Draft at midship	(m)
u	Surge velocity	(m/s)
v	Sway velocity	(m/s)
w	Heave velocity	(m/s)
x_G	Longitudinal position of center of gravity	(m)
x	Longitudinal coordinate	(m)
X	Surge force	(N)
y	Transverse coordinate	(m)
y_G	Lateral position of center of gravity	(m)
Y	Sway force	(N)
z	Vertical coordinate	(m)
z_G	Vertical position of center of gravity	(m)
Z	Heave force	(N)

Greek symbols

β	Drift angle	(deg)
β_c	Internal model control coefficient	(-)
γ	Penalty factor	(-)
γ_i	Grey relational degree	(-)
δ	Rudder angle	(deg or rad)
ζ	Relative damping ratio	(-)
θ	Pitch angle	(deg)
ξ	Grey relational coefficient	(-)
ρ	Water density	(kg/m ³)
σ	Kernel parameter	(-)
ϕ	Roll angle	(deg)
ψ, Ψ	Heading angle	(deg)
ψ_d, Ψ_d	Desired heading angle	(deg)
ψ_e, Ψ_e	Heading angle error	(deg)
ψ_{los}, Ψ_{los}	Heading angle of line-of-sight algorithm	(deg)
ω_b	Bandwidth frequency	(1/s)
ω_n	Natural frequency	(1/s)
∇	Displacement volume	(m ³)

Subscripts

o	Earth
b	Body
hyd	Hydrostatic
H	Hull

<i>inv</i>	Inverse
<i>i,j,k,m,n</i>	Positive integers
<i>IC</i>	Inertia and Centrifugal
<i>l</i>	Left
<i>P</i>	Propeller
<i>r</i>	Right
<i>ret</i>	Retardation
<i>R</i>	Rudder

Superscripts

'	Nondimensional
---	----------------

Accents

·	Time derivative
^	Estimated value
→	Vector
	Absolute value

Abbreviations

2D	Two-dimensional
3D	Three-dimensional
ACO	Ant Colony Optimization
ALOS	Adaptive Line Of Sight
ANFIS	Adaptive Neuro Fuzzy Inference System
APF	Artificial Potential Field
ATFMS	Angle-guidance Tuned Fast Marching Square
BAS	Beetle Antennae Search
BP	Backstepping
CC	Course Control
CFD	Computational Fluid Dynamics
CMT	Circular Motion Tests
CPM	Control Plant Models
CPU	Central Processing Unit
CV	Cross Validation
DGPS	Differential Global Positioning System
DOF	Degrees Of Freedom
DP	Dynamic Positioning
DVS	Dynamic Virtual Ship
EAs	Evolutionary Algorithms
EKF	Extended Kalman filter
Exp.	Experiment
FHR	Flanders Hydraulics Research

FLS	Fitting Least Squares
FMM	Fast Marching Method
FMS	Fast Marching Square
FTS	Fast Time Simulator
FuzzyTC	Fuzzy based Track Controller
GA	Genetic Algorithm
GNC	Guidance Navigation Control
GPS	Global Positioning System
GVF	Gradient Vector Field
GWO	Grey Wolf Optimizer
H_∞	H-infinity
ILOS	Integral Line Of Sight
IMC	Internal Model Control
IMO	International Maritime Organization
ITTC	International Towing Tank Conference
JTTC	Japanese Towing Tank Conference
KCS	KRISO Container Ship
kn	Knots (Unit of speed)
LNG	Liquefied Natural Gas
LOS	Line Of Sight
LQG	Linear Quadratic Gaussian
LQR	Linear Quadratic Regulator
LS	Least Squares
MAE	Mean Absolute Error
MASS	Maritime Autonomous Surface Ships
mHEI	mean Heading Error Integral
MIMO	Multiple Input Multiple Output
ML	Maximum Likelihood
MMG	Manoeuvring Modelling Group
MPC	Model Predictive Control
mRI	mean Rudder Integral
mRTV	mean Rudder Total Variation
mTEI	mean Track Error Integral
MTE	Maximum Track Error
NLS	Nonlinear Least Squares
NLSSVM	Nonlinear Least Squares Support Vector Machine
NN	Neural Network
ORCA	Optimal Reciprocal Collision Avoidance
PD	Proportional Derivative
PF	Path Following
PIANC	The World Association for Waterborne Transport Infrastructure
PID	Proportional Integral Derivative
PLOS	Predictor-based Line Of Sight
PM	Positioning Mooring
PMTC	Prescience Model based Track Controller
PPM	Process Plant Models
PSO	Particle Swarm Optimization
RANS	Reynolds-Averaged Navier-Stokes

RBF	Radial Basis Function
Ref.	Reference
R.E.	Relative Error
RMSE	Root Mean Square Error
Sim.	Simulation
SI	System Identification
SMC	Sliding Mode control
SVM	Support Vector Machine
SRK	Scheldt Radar Chain
TFMS	Tuned Fast Marching Square
TT	Trajectory Tracking
UAV	Unmanned Aerial Vehicle
UGent	Ghent University
ULCS	Ultra Large Container Ship
UKC	Under Keel Clearance
USVs	Unmanned surface vehicles
VF	Vector Field
WP	Way Point

Ship motion control systems

1	Introduction.....	3
1.1	Research background.....	3
1.1.1	Fast time simulator	3
1.1.2	Maritime autonomous surface ships	5
1.2	Problems and opportunities.....	7
1.2.1	Control algorithms.....	7
1.2.2	Control performance in shallow water	7
1.2.3	Modelling of marine surface ships	8
1.2.4	Underactuated characteristics	9
1.2.5	Path following control	9
1.3	Research objectives and methods.....	11
1.3.1	Research objectives	11
1.3.2	Research methods.....	11
1.4	Outline of thesis	13
1.5	Reference.....	15

*Ability is what you're capable of doing. Motivation determines what you do.
Attitude determines how well you do it.*

-- Lou Holtz

1

Introduction

1.1 Research background

1.1.1 Fast time simulator

A ship manoeuvring simulator is one of the common techniques for checking new navigation areas, assessing channel safety, and analysing confined and shallow water effects on the ship, etc. The simulation offers a cost-effective and efficient approach for identifying potential risks when designing a fairway. Two types of simulators are used at Flanders Hydraulics Research (FHR) and Ghent University (UGent), i.e. the real time simulator and the fast time simulator (Figure 1.1).

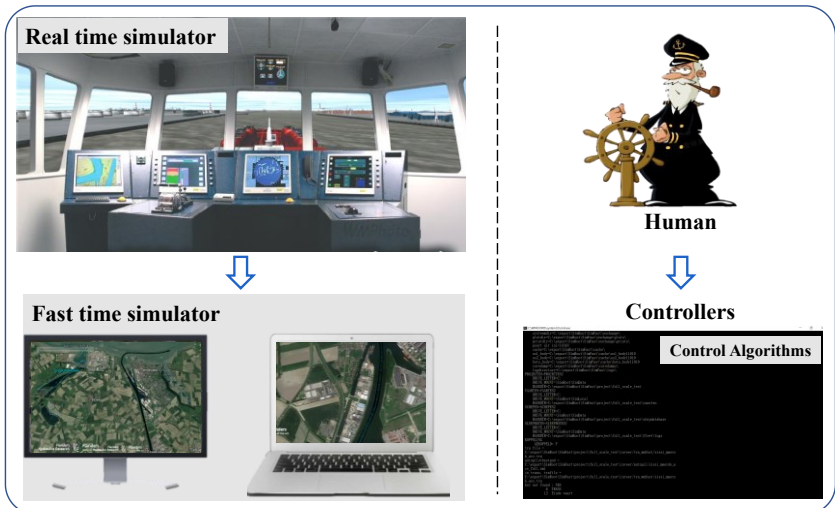


Figure 1.1 Real time simulator and fast time simulator.

During real time simulator studies, experienced captains or pilots take command of the virtual ship, which allows him/her to get acquainted with the future situation, while his/her experience can be incorporated in the study. During fast time simulation runs, on the other hand, the human element is eliminated and replaced by a control algorithm (Figure 1.1). The computer algorithm in the fast time simulator is referred to as “autopilot”, which is initially developed for track-keeping control in a confined channel. In order to avoid confusion with on-board autopilots, the term “track controller” will be used instead during simulation studies. This algorithm does not only provide new control actions (rudder deflection) at discrete time intervals with the help of a prediction model, which can deal with complex, highly non-linear ship behaviour, but also controls the engine speed thus setting the propeller rate.

Figure 1.2 presents an example of the track controller performance in fast time simulator, where a bulk carrier ($L_{PP} \times B \times T_M : 229.5 \times 36.9 \times 12.5 \text{ m}^3$) sailed southbound on the Canal Ghent-Terneuzen. The positions of the bulk carrier from the full-scale measurement (green trajectory) are plotted together with the positions generated by the track controller in the fast time simulations (blue trajectory). One can observe that there are small deviations between two trajectories due to the selected controller parameters, such as the weight coefficients and anticipation time, etc.



Figure 1.2 Example of the track controller performance on the Canal Ghent-Terneuzen in fast time simulator.

Even though the present track controller is rather advanced, a number of shortcomings have been detected during recent applications. In particular, the control settings often have to be adapted to the specific environmental conditions, bathymetries (e.g. irregular banks) and planned interactions with other shipping traffic (meeting and overtaking manoeuvres). Moreover, the track controller cannot be used for simulating manoeuvres (berthing, unberthing, swinging, backing) which require the use of propeller orders astern, use of bow and stern

thrusters, tug assistance. In order to optimize the present model, intelligent and advanced control strategies need to be taken into account. Apart from the classic PID control theory, fast time simulation track controllers can be based on fuzzy logic control, neural network control, and other more advanced or sophisticated control algorithms.

1.1.2 Maritime autonomous surface ships

In recent years, maritime autonomous surface ships (MASS) are becoming increasingly interesting for academia, governments, and industry, because of their low cost and high automation compared with fully manned marine vehicles, also because of their broad application potentials, such as unmanned shipping (inland shipping), environmental monitoring, ocean resource exploration, scientific research, military and hydrographic surveys, etc. Figure 1.3 shows the application scenarios of MASS.



Figure 1.3 Application scenarios of maritime autonomous surface ships (MASS) (Tran et al., 2014).

The concept of maritime autonomous surface ships has been introduced by the International Maritime Organization (IMO) on the basis of various names such as “unmanned surface vessels, USVs (Figure 1.4)” and “unmanned cargo ships (Figure 1.5)”, etc., where the USVs focus on small scale vessels and the unmanned cargo ships concentrate on large scale ones (IMO, 2017; Wang et al., 2019). In terms of the MASS, four levels of autonomy were specified by the IMO (IMO, 2018): (1) ships with automated processes and decision support; (2) remotely controlled ships with seafarers not on board; (3) remotely controlled ships without seafarers on board; (4) fully autonomous ships. As can be seen, the

human operation is expected to be reduced and replaced by automatic control systems. In this context, an accurate and reliable autopilot system is needed to achieve full automation of ships.



(a) Mariner USV



(b) Oceanalpha M40 USV

Figure 1.4 Unmanned surface vessels (USVs): (a) Mariner USV (photo retrieved from <https://www.maritimrobotics.com/mariner>); (b) Oceanalpha M40 USV (photo retrieved from <https://www.oceanalpha.com/product-item/m40/>).



Figure 1.5 Rolls-Royce unmanned cargo ships (photo retrieved from <https://www.rolls-royce.com/marine>).

1.2 Problems and opportunities

1.2.1 Control algorithms

The research on ship motion control algorithm has recently received more attention in order to develop a state-of-the-art autopilot. In literature, most studies focus on the development of theoretical algorithms. These theoretical methods are usually accompanied by a large number of formula calculations, which result in problems with respect to “explosion of complexity”, “curse of dimensionality”, and “large calculation consumption”, etc. These complex control algorithms will hinder their practical implementation. On the contrary, a concise, accurate, robust and adaptive control algorithm is needed in practical engineering.

1.2.2 Control performance in shallow water

To study the performance of the developed control algorithms, in literature they are usually tested in a numerical simulation environment. However, there are still some differences between numerical simulation and actual application. Thus, it is necessary to evaluate the application of autopilots in real scenarios. It is important to point out that in literature, only a limited number of experimental studies have been performed to validate these theoretical algorithms, the related works have been briefly summarized in Chapter 2, where most experimental studies focused on small-sized ships (e.g. USVs) in deep water. There is a paucity of data on large-sized ships (e.g. unmanned cargo ships) in shallow water, which in fact demands more control actions. Any ship will sooner or later manoeuvre in a port area, which by definition is a confined area. For instance, the Port of Antwerp Bruges (Belgium) has an LNG terminal in shallow water (see Figure 1.6). In deep water, the ship does not need high manoeuvring capabilities and has consistent manoeuvring behaviour. Nevertheless, the manoeuvring capability is challenged in shallow water and the local under keel clearance heavily affects this challenge. Because limited water depth reduces the under keel clearance (UKC), hence changes the ship hydrodynamics and increases the control difficulty (Chen et al., 2020). Consequently, the investigation of autopilots for large-sized ships in shallow water is necessary for practical application.



Figure 1.6 LNG terminal in port of Antwerp Bruges (photo retrieved from <https://www.fluxys.com/en/products-services/activities/lng>).

1.2.3 Modelling of marine surface ships

In order to develop an advanced control system, ship mathematical models are essential. Applying accurate mathematical models combined with effective simulation tools such as the fast time simulator can improve the accuracy of simulation and reduce the impact of uncertainty on controller performance. Mathematical models may be formulated in different levels of complexity, which can be distinguished between process plant models (PPM) and control plant models (CPM) (Sørensen, 2013). The process plant model is a detailed modelling of the actual physical process. The main aim of this model is to simulate the real plant dynamics, including control inputs, external disturbances, and various forces, etc. The control plant model is simplified from the process plant model including only the most important physical properties. The latter may be a part of the model-based controller or be applied in stability analysis of the control system.

No matter what kind of ship models, they all contain several linear and nonlinear coefficients to describe the ship's behaviours. In order to obtain accurate model parameters, except for extensive experiments, system identification combined with full scale measurement or model test data is regarded as one of the most efficient techniques. However, the estimation of some parameters is still difficult, due to the nonlinear and coupled characteristics of ship models, the effect of parameter drift, and uncertainty increases with the order of the model, etc. (Luo and Li, 2017). An efficient approach to determine model parameters accurately is still absent, especially for the online parameter identification method.

1.2.4 Underactuated characteristics

Most surface ships are a type of typical underactuated systems. This is because the underactuated systems can simplify the controller design, reduce cost, and consume less energy (Mykland, 2017). A marine craft is underactuated if it has less control inputs than generalized coordinates (Fossen, 2011).

For the design of a traditional autopilot for a 3 DOF surface ship model, only one actuator in yaw is needed to control ship heading. To solve the path following problem, an additional actuator in the surge is required. The main challenge for the underactuated ship is that there is no actuator for sway dynamics, which are very responsive to environmental disturbances. That may generate the non-holonomic nature of ship kinematics and dynamics equations, which would increase the difficulty of controller design. To improve the ability to complete complex missions, the fully-actuated control systems should be further investigated so as to develop advanced automatic facilities (Zhang et al., 2017).

1.2.5 Path following control

The use of marine surface vessels for various missions is increasing, in which path following is one of the most widely used missions. The goal is to control a ship following a waypoint-based path without any time constraints. Normally, a path following control system is constructed as three independent subsystems, refer to the guidance, navigation, and control (GNC) systems (Fossen, 2011). Before using the path following control system, waypoints should be generated by a path planning module. Figure 1.7 presents the signal flow of the GNC system.

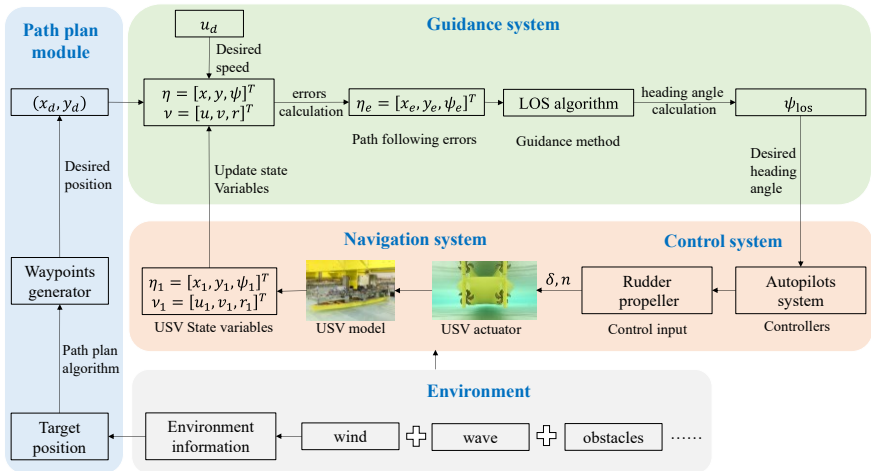


Figure 1.7 Signal and data transmission between the guidance, navigation, and control systems.

In addition to the design of advanced control algorithm, the development of path planning, guidance, and navigation subsystems also play very important roles in

the path following control system. In order to improve the autonomy of marine surface vessels, autonomous path planning is an extremely important research area. It includes offline (global) path planning and online (local) path planning. For traditional offline path planning algorithms, the computations take a lot of time and usually result in some unwanted waypoints. Challenges for online path planning are the real-time computability and the integration with the obstacle detection and collision avoidance system. These challenges open the possibility to develop intelligent path planning algorithms so as to plan a safe, smooth, and short path.

Furthermore, the guidance system is used to continuously compute the desired position, velocity, and acceleration of a ship to be used by the motion control system. Line of sight (LOS) guidance is one of the most common methods, which minimizes the cross track error by controlling the heading angle (Fossen et al., 2002). The LOS guidance law is simple and easy to apply. However, the conventional LOS guidance law is susceptible to environmental disturbances due to the wind, waves, and currents, etc. In order to improve the LOS guidance method, the adaptive look-ahead distance and waypoint selection should be considered. Moreover, the development of guidance algorithms needs to consider actual engineering requirements and test them in practice.

1.3 Research objectives and methods

1.3.1 Research objectives

The main objective of the present research is to develop a practical ship motion control system taking into account the effects of shallow and confined waters. The research of the control system contains path planning, guidance, navigation, and control subsystems. The developed control system is able to cope with a variety of complex conditions applicable to channel and canal. Furthermore, the control system can be implemented into the towing tank and ship manoeuvring simulators to create an accurate and reliable control performance for conducting experiments and simulations in complex situations. The development of a new control system can also be expected to be applied in the frame of unmanned shipping, autonomous ships, and automatic berthing, etc.

Software tools will be developed to reduce fast time simulation runs of vessel transits for waterway capacity studies accounting for detailed manoeuvring performance of the ships involved.

One or more practical cases will be studied for evaluating the developed control systems and tools in a practical environment. The case studies will focus on conditions that are more typical for the situation access channels, waterways, and ports.

1.3.2 Research methods

1.3.2.1 Literature study

First, an extensive literature study will be performed to know the state-of-the-art with respect to ship motion control systems. The literature is related to control systems for automated ship operations up to control of unmanned vessels. As the control algorithms have to be implemented in a mathematical model for manoeuvring simulation, it is required to have more knowledge on this topic, and more specifically on the development of manoeuvring models and the determination of their parameters.

1.3.2.2 Development of control systems

Starting from the control system in use at Ghent University and FHR, and based on the literature study, and improved, revised or even alternative control systems will be developed, which includes the following features:

- The control parameters should be as few as possible but meet the accuracy of practical engineering applications. The control settings should possibly be varied over a given desired trajectory.
- A more flexible speed control along the trajectory should be possible, and the possibility of controlling the rate of turn (yaw rate) in bends should be foreseen.
- The development of such a control system should take into account the

effects of confinement (by parameters such as bank distance and under keel clearance).

- The control system should be able to cope with obstacles.

1.3.2.3 Implementation, validation and application

In the next step, the developed control systems will be implemented, validated, and applied in the towing tank and fast time simulators at Flanders Hydraulics Research (FHR).

- Model tests in the Towing Tank for Manoeuvres in Confined Water will be conducted in order to investigate the performance of the developed control systems and select the preferred control algorithms.
- Simulations studies will be executed in the fast time simulators in order to evaluate whether the controllers studied in the towing tank exhibit satisfactory performance in simulation settings and whether their application in simulation of complex situations can be improved.
- The developed control systems and processing tools will be applied to selected cases to study their application potentials in practical engineering.

1.4 Outline of thesis

Figure 1.8 shows the outline of thesis that will be elaborated chapter by chapter.

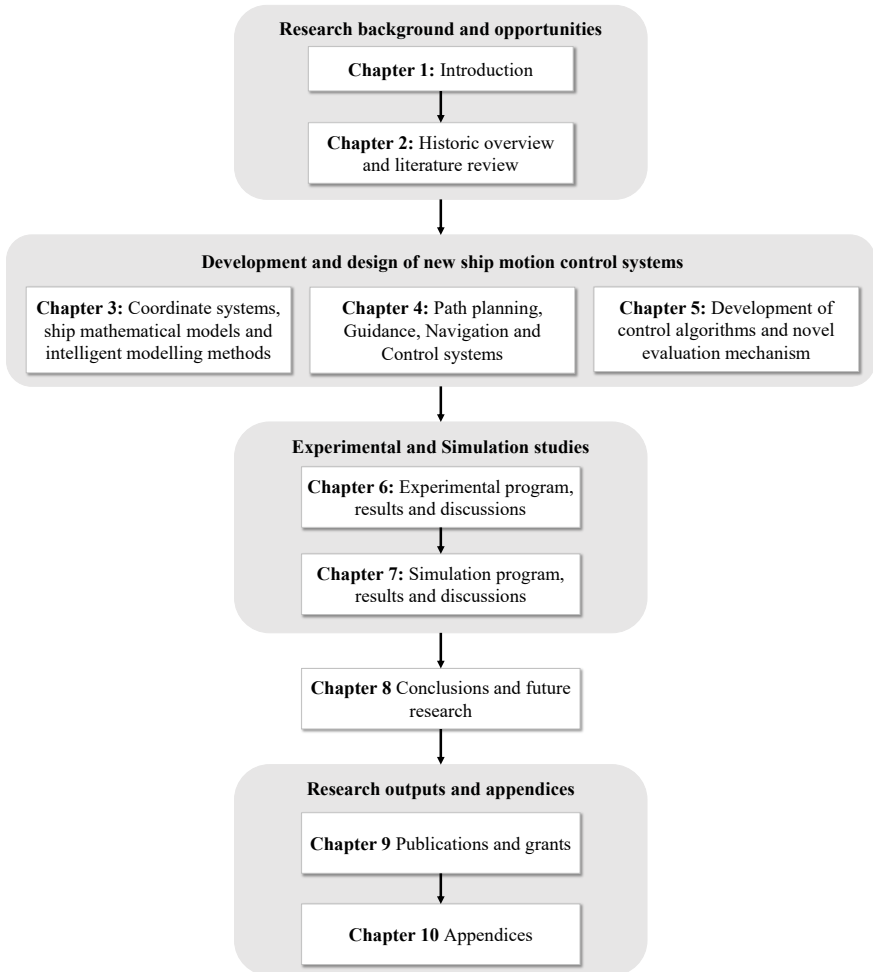


Figure 1.8 Outline of thesis.

Chapter 2 presents a historical overview of relevant research based on an extensive literature study. The state-of-the-art research with respect to ship mathematical models, ship motion control system, and path following control are comprehensively discussed.

Chapter 3 introduces the coordinate systems and different types of ship mathematical models involved in this research. Various model parameter identification methods are extensively discussed, an intelligent system identification method is proposed and applied to determine the parameters of ship motion mathematical models.

Chapter 4 provides a detailed description of the guidance, navigation, and control systems. A new path planning algorithm is proposed and employed to automatically plan a desired path with virtual obstacles in the towing tank environment.

Chapter 5 discusses extensively the structure and principle of relevant motion controllers and how to determine their parameters. An innovative evaluation mechanism is introduced to assess the controllers' performance.

Chapter 6 elaborates the experimental program conducted in FHR towing tank. The experimental results obtained from self-propulsion, zigzag, course, and path following tests are analysed. In addition, the shallow water effects on standard manoeuvres, controllers' parameters and performance are also discussed in this chapter.

Chapter 7 explains the numerical simulation program in the fast time simulator and discusses the simulation results, which are compared with experimental results to validate the control algorithms. Finally, the developed autopilots are evaluated in the simulation of the ship sailing in a canal.

Chapter 8 gives the overall conclusions and recommendations for future research.

Chapter 9 provides the lists of publications and grants.

Chapter 10 elucidates how to configure the fast time simulator.

1.5 Reference

- Chen, C. Y., Delefortrie, G., and Lataire, E.,** 2020. *Experimental investigation of practical autopilots for maritime autonomous surface ships in shallow water*. Ocean Engineering, 218, 108246.
- Fossen, T. I.,** 2011. *Handbook of marine craft hydrodynamics and motion control*. John Wiley & Sons Ltd. United Kingdom.
- Fossen, T. I., Breivik, M., and Skjetne, R.,** 2002. *Light of sight path following of underactuated marine craft*. Science And Technology, 1–6.
- IMO.,** 2017. *Report of the maritime safety committee on its 98th session*. London,UK.
- IMO.,** 2018. *Report of the maritime safety committee on its 100th session*. London,UK.
- Luo, W. L., and Li, X. Y.,** 2017. *Measures to diminish the parameter drift in the modeling of ship manoeuvring using system identification*. Applied Ocean Research, 67, 9–20.
- Mykland, A.,** 2017. *Low-cost observer and path-following adaptive autopilot for ships*. Norwegian University of Science and Technology, Norway (thesis).
- Sørensen, A. J.,** 2013. *Marine control systems: propulsion and motion control of ships and ocean structures*. Retrieved from <http://folk.ntnu.no/assor/publications/marcyb.pdf>⁰<http://citeseerx.ist.ps.u.edu/viewdoc/download?doi=10.1.1.714.8372&rep=rep1&type=pdf>
- Tran, N. H., Choi, H. S., Baek, S. H., and Shin, H. Y.,** 2014. *Tracking control of an unmanned surface vehicle*. *Recent Advances in Electrical Engineering and Related Sciences. Lecture Notes in Electrical Engineering*. Springer, Berlin, Heidelberg.
- Wang, L., Wu, Q., Liu, J., Li, S., et al.,** 2019. *State-of-the-art research on motion control of maritime autonomous surface ships*. Journal of Marine Science and Engineering, 7, 1–32.
- Zhang, G. Q., Deng, Y. J., and Zhang, W. D.,** 2017. *Robust neural path-following control for underactuated ships with the DVS obstacles avoidance guidance*. Ocean Engineering, 143, 198–208.

Ship motion control systems

2	<i>State of the art</i>	17
2.1	Development of ship mathematical models	17
2.1.1	Ship mathematical models.....	17
2.1.2	Ship mathematical model parameters.....	20
2.2	Development of ship motion control	23
2.2.1	Historical remarks	23
2.2.2	Classification of controllers.....	24
2.3	Development of path following control	29
2.3.1	Overview	29
2.3.2	Path planning system.....	29
2.3.3	Guidance system.....	32
2.3.4	Control system.....	34
2.4	Reference	37

The farther backward you can look, the farther forward you can see.

--Winston Churchill

2

State of the art

2.1 Development of ship mathematical models

2.1.1 Ship mathematical models

2.1.1.1 Types based upon model formulation

Mathematical models play a very important role in describing the ship's motions, predicting the ship's manoeuvrability and designing the ship's controllers, etc. The historical development of ship mathematical models can be traced back to 1946, Davidson and Schiff (1946) used the knowledge of rigid-body dynamics and fluid mechanics to propose a ship motion mathematical model for the first time. After continuous exploration and development, at present, the ship mathematical models applied to ship motion control systems can be classified into the hydrodynamic models, the response models, and other types of models, etc. The classification of ship mathematical models according to model formulation is shown in Table 2.1.

Table 2.1 Classification of ship mathematical models based upon model formulation.

Model types	Specific types	Formula (e.g.)
Hydrodynamic models	Whole-ship model	$\begin{cases} m(\dot{u} - vr - x_G r^2) = X(\dot{u}, \dot{v}, \dot{r}, u, v, r, \delta) \\ m(\dot{v} - ur - x_G r^2) = Y(\dot{u}, \dot{v}, \dot{r}, u, v, r, \delta) \\ I_{zz} \dot{r} + mx_G(\dot{v} + ur) = N(\dot{u}, \dot{v}, \dot{r}, u, v, r, \delta) \end{cases}$
	Modular model	$\begin{cases} m(\dot{u} - vr - x_G r^2) = X_H + X_R + X_P \\ m(\dot{v} - ur - x_G r^2) = Y_H + Y_R + Y_P \\ I_{zz} \dot{r} + mx_G(\dot{v} + ur) = N_H + N_R + N_P \end{cases}$
Response models	Nomoto model	$T\dot{r} + a_1 r + a_3 r^3 = K\delta$

		$T_1 T_2 \ddot{r} + (T_1 + T_2) \dot{r} + K H_B(r) = K \delta + K T_3 \dot{\delta}$
Other models	Fossen model	$M \dot{v} + C(v)v + D(v)v = \tau + b$

The hydrodynamic models are of two types and recognized as the whole-ship model and the modular model. The whole-ship model is also called the polynomial model. One of the most famous whole-ship models is the Abkowitz model, which was named after Prof. Abkowitz in 1964 (Abkowitz, 1964). The Abkowitz model is based on the Taylor series expansion of hydrodynamic forces and moments about suitable initial conditions, where the hydrodynamic forces and moments acting on the hull, propeller, and rudder are treated as a whole. Based on Abkowitz's research, Norrbin (1971) combined theoretical analysis and experiments to incorporate empirical models for the hydrodynamic effects, which also belongs to the whole-ship model.

Another type of model is the modular model, also called the physical model. An example of the modular model is the MMG model (Ogawa et al., 1977), which was proposed by a research group called Manoeuvring Modelling Group (MMG) in the Japanese Towing Tank Conference (JTTC). According to the concept of the MMG model, afterwards, the expression of hydrodynamic forces acting on ships was presented by Ogawa and Kasai (1978) and Inoue, et al. (1981), etc. In the MMG model, each of the ship's individual elements (such as the hull, rudder, and propeller) is considered as a separate module and contributes to the total hydrodynamic forces acting on the ship. Yasukawa and Yoshimura (2015) summarized the MMG standard methods for ship manoeuvring predictions, including manoeuvring simulation model, procedure, analysis method and prediction method, etc.

Except for the hydrodynamic models, the response model or the so-called Nomoto model (Nomoto et al., 1957) is preferred in practical applications because of its simple structure, which can reflect the relationship between the motion responses of the ship and the rudder deflection. The response model is commonly used to study course control problems.

In addition, there are some other mathematical models widely used in the field of ship motion control, such as Fossen's ocean vehicle models, which have become a standard for marine ship motion control systems (Fossen, 2011). On top of that, a guidance, navigation, and control (GNC) Matlab toolbox was developed by the research team of T.I. Fossen (Fossen, 2011; Perez et al., 2006). The toolbox provides the necessary resources for the rapid implementation of mathematical models of marine systems with a focus on control system design. Using the GNC toolbox, researchers can quickly construct ship motion control simulation systems based on different types of ship models, such as Mariner class vessel, Esso Osaka tanker, and Container ship, etc. Furthermore, a comprehensive overview of mathematical manoeuvring models can be found in Eloot (2006).

2.1.1.2 Types based upon degrees of freedom

When designing control systems for marine surface ships, except for the 6 DOF model, the reduced-order mathematical models are often adopted, because most ships are underactuated (not actuated in all six degrees of freedom). For instance, 3 DOF underactuated surface ships are normally equipped with propellers and rudders for only surge and yaw motions (Sun et al., 2017), there is no actuator for controlling the sway motion. Thus, according to the degrees of freedom, ship mathematical models can be usually classified into (Fossen, 2011):

1 DOF (one degree of freedom) model can be used to design forward speed controller (surge), heading autopilot (yaw), and roll damping system, etc.

3 DOF (three degrees of freedom) model is usually a horizontal plane model for surface ships, including surge, sway, and yaw motions. The 3 DOF model can be used to design the path following control systems and trajectory tracking systems.

4 DOF (four degrees of freedom) model is formed by adding the roll motion to the 3 DOF model, which includes the surge, sway, yaw, and roll motions. The 4 DOF model is usually used in manoeuvring simulations where it is important to include the roll motion for ship's with low stability lever or for the purpose of reducing roll by active control of fins, or rudders.

6 DOF (six degrees of freedom) model includes surge, sway, heave, roll, pitch, and yaw motions, which is used to simulate and predict motions of ships in all six degrees of freedom.

Table 2.2 lists the related examples about the applications of different DOFs mathematical models for the development of ship motion controllers.

Table 2.2 Examples about the applications of different DOFs mathematical models for the development of ship motion controllers.

Degree of models	Application (e.g.)
1 DOF	Azzeri et al. (2015), Chen et al. (2019a), Das (2015), Liu (2017), Luo and Cong (2016), Witkowska et al. (2007), Yu et al. (2008), Zhang et al.(2016), Zhu et al. (2018), Zwierzewicz (2013)
3 DOF	Fu et al. (2017), Fossen et al. (2002, 2015), Liu et al. (2015), Mizuno et al. (2012), Mooney and Johnson (2009), Mu et al. (2018), Park et al. (2017), Pettersen and Nijmeijer (2001), Serrano et al. (2014), Skjetne et al. (2004), Wang and Er (2016), Yang et al. (2011), Yang and Zhang (2015), Zhang et al. (2014, 2015)
4 DOF	Brasel (2013), Faramin et al. (2019), Kolyubin and Shiriaev (2014), Li et al. (2009b), Tristan Perez and Blanke (2002), Wang et al. (2019, 2020)
6 DOF	Delefortrie et al. (2016), Krishnamurthy et al. (2005), Sandurawan et al. (2010), Teng (2020), Zhang (2017)

2.1.2 Ship mathematical model parameters

Ship mathematical models are fundamental for the study of controller designs and numerical simulations, while ship mathematical model parameters or hydrodynamic coefficients determine the accuracy of its performance. To obtain desired performance, a math model based on a correct formulation of the physical reality, provided with parameter values with sufficient accuracy is deemed necessary.

In order to determine the parameters (hydrodynamic coefficients) in the ship mathematical models, several methods can be adopted, including the use of a database or empirical formulas, captive model tests, CFD-based computations, or system identification methods combined with full-scale trials or free running model tests (ITTC, 2005; Luo, 2016; Patalong, 2012). See Figure 2.1 for better understanding.

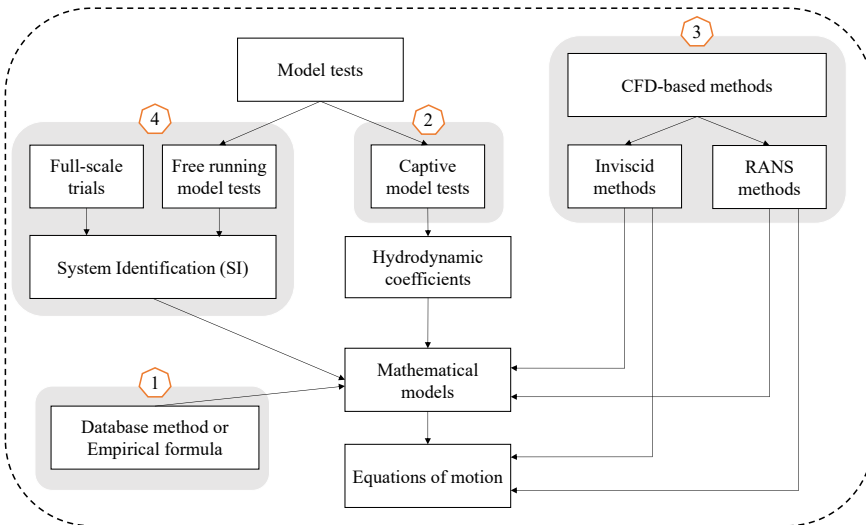


Figure 2.1 Methods for determining the hydrodynamic coefficients of the ship manoeuvring mathematical models.

Database method establishes regression equations or empirical formulas based on the existing database of manoeuvring parameters obtained from extensive full-scale trials or model tests (Abkowitz, 1964; Lee et al., 2003). Oltmann (2003) reviewed the database methods during the period of 1970 to 1993, and suggested a regression method for the formulation of damping coefficients which focuses on the aft hull form of a ship. Wagner Smitt (1970) regressed data of PMM tests with 35 various models, the trends were developed of the influence of some ship dimensions on the course stability. Norrbin (1971) investigated a similar database. Based on the results of model tests with different kinds of ships, Inoue (1981) studied semi-empirically the hydrodynamic derivatives in manoeuvring mathematical models for fitting the measured results to describe the hydrodynamic forces. Clarke et al. (1983) presented the empirical formulas for the main added

mass coefficients. Katsuro Kijima (1993) revised the formula of Inoue (1981) by including additional terms to enhance estimation accuracy. Yoshimura and Ma (2003) proposed the empirical formula of linear hydrodynamic derivatives for fish vessels based on the obtained database. The empirical methods are simple and quick to use, but the prediction accuracy and reliability can be limited when the ship dimensions are outside the database (extrapolation problem). It is also clear that due to computational power available today, better options are available and such methods are less used.

Captive model test methods are applied to directly determine hydrodynamic coefficients based on captive model tests, which mainly include rotating arm tests (RAT), circular motion tests (CMT), and planar motion mechanism (PMM) tests, etc. For instance, pure sway mode is used to determine the sway dependent derivatives, pure yaw is used to obtain the yaw dependent derivatives and the combined sway and yaw mode is used to obtain coupled sway and yaw dependent derivatives (Shenoi et al., 2013). Chislett and Strom Tejsen (1965) determined the hydrodynamic derivatives of the Abkowitz for the Mariner ship through PMM tests. Norrbin (1971) obtained hydrodynamic derivatives of a large tanker by using the PMM results. In Yoshimura and Ma (2003), the hydrodynamic derivatives and interference coefficients of the MMG model for 5 fish vessels were obtained via the circular motion tests (CMT). Eloot and Vantorre (1998) introduced alternative captive manoeuvring tests for the determination of a reliable mathematical model, and discussed their possibilities and limitations. Kim et al. (2003) conducted captive model tests with a 4 DOF PMM system for large container ships in order to obtain their hydrodynamic derivatives. More recent works are presented by Eloot and Vantorre (2003), Kim et al. (2003), Delefortrie et al. (2016), Jeon et al. (2016), etc. Although the captive model test method is considered to be one of the most effective methods, it still has some limitations, such as model scale problems, time consuming, and expensive, etc.

Since the 1990s, computational fluid dynamics (CFD) methods are gradually applied for the estimation of manoeuvrability and the determination of hydrodynamic derivatives, etc. The CFD-based approaches include the inviscid methods and Reynolds-averaged Navier–Stokes (RANS) methods. In Toxopeus (2006), a mathematical model for the bare hull forces and moments based on the viscous-flow calculation was given. Ishiguro and Ohmori (2003) used NICE CFD code to determine hydrodynamic derivatives, and tried to use CFD for the evaluation of manoeuvrability. Yamasaki and Masuda (2001) calculated the linear hydrodynamic coefficients of tankers by using CFD, the simulation results were validated by the CMT tests. Rajita Shenoi et al. (2013) applied a RANSE based CFD solver STARCCM+ to determine the linear, nonlinear and coupled hydrodynamic derivatives of a container ship (S175). In spite of great progress in computational fluid dynamics (CFD) and its successful applications to manoeuvrability, practical simulation-oriented mathematical models still are often devised on the basis of experimental data (Sutulo and Guedes Soares, 2014). Compared with other approaches, CFD-based methods are both very time consuming and computationally expensive, meanwhile its calculation accuracy largely depends on the experience and knowledge of the analyst.

In recent years, the majority of efforts are devoted to developing advanced system identification techniques, so to obtain desired parameters in the mathematical model of ship manoeuvring motion (Chen et al., 2019b). In literature one can find that traditional methods including the extended Kalman filter method (EKF) (Perera et al., 2015), the maximum likelihood method (ML) (Cao et al., 2015), and the least squares method (Liu et al., 2013), have been successfully applied to identify ship model parameters. Abkowitz (1980) applied the extended Kalman filter method (EKF) and full-scale measurement data to identify the hydrodynamic coefficients of the Abkowitz model. Åström and Källström (1976) combined sea trials data and the maximum likelihood method (ML) to perform system identification studies for obtaining hydrodynamic derivatives. Koyama et al. (1973) adopted the least squares method to identify the time constant T and gain K of the ship response model. However, these traditional methods presented some pitfalls, such as ill-conditioned solutions, dependency on initial state and parameter drift, among others (Luo and Li, 2017). Moreover, the nonlinear terms of ship model parameters are difficult to be obtained by conventional approaches, and also uncertainty increases with the order of the model. To overcome these issues, intelligent parameter identification strategies such as the Neural Network (NN) have been developed and are considered to provide better results (Rajesh et al., 2010; Velagic, 2007; Xing and McCue, 2010). The NN-based algorithms are able to achieve satisfactory performance for the identification of the simple Nomoto model and more complex MMG or Abkowitz models, but the major problem is that such methods need to be trained with large sample data and are prone to falling into local minima. Since 2009, Prof. Zou Zao-jian from Shanghai Jiao Tong University applied a support vector machine (SVM) method to identify the ship model parameters. Compared with other intelligent approaches, using large samples of simulation or experimental data to estimate unknown parameters, the SVM-based methods only depend on limited support vectors based on small samples. Besides, the structure risk minimization theory instead of empirical risk minimization is adopted by the method to solve optimisation problems. A global optimisation result is obtained, and local optimisation issues are avoided. Many valuable research results have been achieved via SVM-based methods, for instance: Luo (2009), Luo and Zou (2009), Xu et al. (2013), Zhang and Zou (2011, 2013), more recently Luo et al. (2016), Hou et al. (2018), Wang et al. (2020). On the top of the above research, this work introduced a novel NLSSVM (Nonlinear Least Squares Support Vector Machine) algorithm for the identification of the ship's model, which is a new generation of machine learning method and can accurately obtain model parameters (Chen et al., 2019b, 2019c). A detailed description of the NLSSVM method will be presented in section 3.3.

2.2 Development of ship motion control

2.2.1 Historical remarks

With the development of advanced control theory, state-of-the-art control approaches are continually being designed to improve autopilots' performance. The proposed control methods vary from simple to advanced and intelligent. Figure 2.2 presents the historical development from the early autopilot to modern ship control systems.

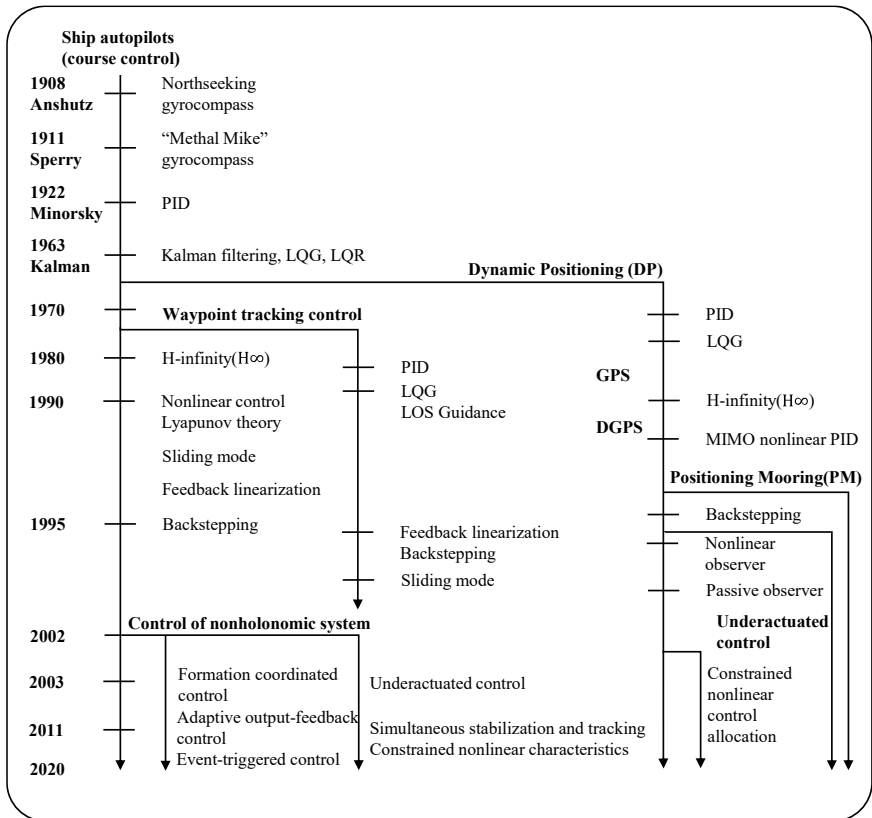


Figure 2.2 Historical development from the early autopilot to modern ship control systems.

The history of ship's autopilots started with the invention of northseeking gyrocompass by Anschütz (1908). Three years later, the gyrocompass was extended to ship steering and closed-loop control by Elmer Sperry (1911), who developed the first ship steering mechanism, so-called "Metal Mike". The invention of the gyrocompass provided the possibility for the development of ship's course autopilots. In the early 1920s, Minorsky (1922) presented a detailed analysis of the feedback control system, and formulated a three-term control law, which is known as the proportional integral derivative (PID) controller. The PID

has been one of the most commonly used controllers in the design of ship's autopilot system. The success of PID controller is on basis of its capacity to efficiently and robustly control ship's dynamic system, while having an extremely simple structure and intuitive tuning procedures. Many works using the PID controller followed by, to mention some relevant examples: Polkinghorne et al. (1993), Moradi and Katebi (2001), AlfaroCid et al. (2006), Moreira et al. (2007), Nguyen et al. (2004), and more recent works were presented by Breivik and Loberg (2011), Švec et al. (2014), Liu et al. (2017), Yang et al. (2019).

Modern autopilots using the Linear-Quadratic-Gaussian (LQG) and H-infinity (H_∞) control design methods have been published in the literature by a large number of authors, for instance: Katebi et al. (1985), Desanj et al. (1995), Holzhuter (1997), Donha et al. (1998), Hu et al. (2003), Elkaim (2006), Liu and Fang (2007), Annamalai and Motwani (2013). Hereafter, efforts have been made to develop more advanced control algorithms. For instance, the sliding mode control (Ashrafiuon et al., 2008; Das, 2014; Lv et al., 2017; Papoulias and Healey, 1992), the backstepping control (Witkowska et al., 2007; Xia et al., 2014; Zakartchouk and Morishita, 2009), the fuzzy control (Kumar et al., 2011; Van Amerongen et al., 1977; Xiang et al., 2018), and the neural network controller (Bums, 1995; Lacki, 2018), etc. Yet, in practice, using a single control approach may not yield a satisfactory control effect as using a combination of several control techniques. Examples of the latter approach are the fuzzy PID control (Kumar et al., 2011), the PID control based on neural network (Li et al., 2012), the fuzzy sliding mode control (Cui et al., 2016), the adaptive Neuro-Fuzzy inference system (ANFIS) (Zhang et al., 2006), the sliding backstepping control (Liu et al., 2011), etc. Despite great effort has been devoted to the development of more advanced control approaches, the PID controller is still one of the most popular controllers in practice.

2.2.2 Classification of controllers

2.2.2.1 Overview

The controllers in literature can be divided into different categories according to different classification standards. In present work, three classification standards are considered (Figure 2.3):

- 1) According to the control missions or objectives;
- 2) According to whether the control algorithms depend on the ship mathematical model;
- 3) According to mechanical structure or the number of actuators. More detailed descriptions will be presented in the following subsections.

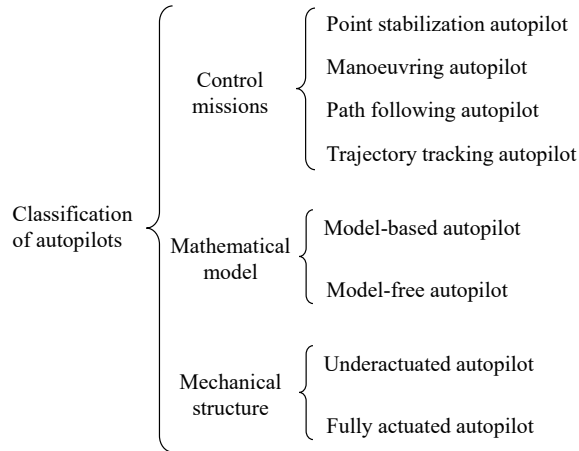


Figure 2.3 Classification of ship motion controllers.

2.2.2.2 Based upon control missions

Different control laws found in literature can be mainly divided into four groups according to their control missions (Fossen, 2011; Liu et al., 2016; Xiang et al., 2018), and the related studies are briefly summarized in Table 2.3.

The **point stabilization autopilot** is the most basic control mechanism, which stabilizes the ship in a desired position and orientation. But this control strategy is difficult to achieve a continuous control for the ship. The point stabilization controllers are mainly used for dynamic positioning (DP) and automatic berthing control systems, etc. Compared with the DP control system, the automatic berthing control is relatively complex, due to all six degrees of freedom of system configuration need to be stabilized. At present, the ship's berthing is still carried out with the assistance of tugboats, but in the near future, automatic berthing will become a possibility with the development of control technology and having a ship equipped with the necessary actuators.

The **1-DOF manoeuvring autopilot** (Figure 2.4) can also be called the course controller, which mainly consists of two types: course keeping controller and course changing controller. Course keeping for ships is the core of automatic navigation, which maintains a certain course (straight-line) sailing at a certain speed, which is ship course stability. In contrast, a course changing controller is used to steer a ship to change its course when the ship needs to avoid obstacles or other ships. From the point of ship manoeuvring, zig-zag manoeuvring and turning circle motion are performed by using a course changing autopilot.

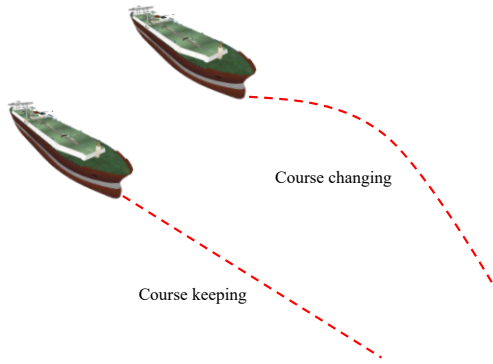


Figure 2.4 Illustration of 1-DOF manoeuvring: course keeping and changing.

The **path following autopilot** (Figure 2.5): path following steering behaviour allows the ship to follow a predefined path made of points and lines. The ship is only required to follow a pre-planned path with spatial convergence alone, without any time constraint.

The **trajectory tracking autopilot** (Figure 2.5): in trajectory tracking mission, the ship is required to track a time dependent trajectory, i.e. the ship must arrive at a certain point at a certain time. Therefore, the space and time constraints are mixed into a trajectory tracking control assignment.

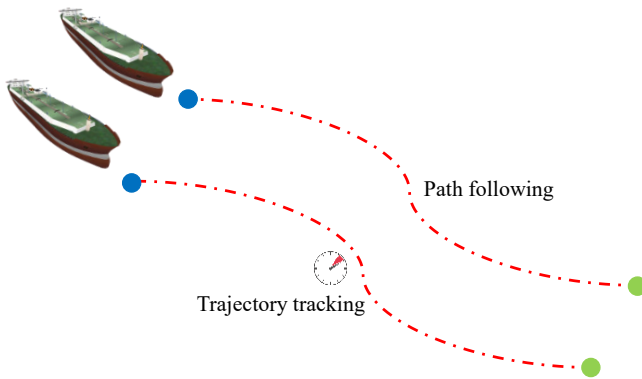


Figure 2.5 Illustration of path following and trajectory tracking control.

Table 2.3 Classification of controllers according to the control missions.

Classification	Reference
Point stabilization	Du et al. (2013), Im and Nguyen (2017), Li et al. (2008), Li et al. (2017), Lindegaard (2003), Mizuno et al. (2012), Nguyen et al. (2007), Pettersen and Fossen (2000), Piao et al. (2019), Rindarocoy and Johansen (2013), Sørensen (2011), Ye

	et al. (2017), Zakartchouk and Morishita (2009), Zhang et al. (2017)
1-DOF manoeuvring	Azzeri et al. (2015), Chen et al. (2019a), Lacki (2018), Liu et al. (2011), Lopez et al. (1998), Luo and Cong (2016), Yu et al. (2008), Zhang et al. (2016, 2018), Zhu et al. (2018), Zwierzewicz (2013)
Path following	Fossen et al. (2002), Fossen et al. (2015), Liu et al. (2014), Moreira et al. (2007), Mu et al. (2018), Oh and Sun (2010), Wang et al. (2009), Wang et al. (2010), Woo et al. (2019), Xu and Guedes Soares (2016), Yang and Zhang (2015), Zhang et al. (2015),
Trajectory tracking	Duan and Zhu (2012), Elmokadem et al. (2017), Guerreiro et al. (2013), Li et al. (2016), Liu et al. (2015), Lv et al. (2017), Pathan et al. (2012), Shen and Wang (2018), Wang et al. (2018), Zheng et al. (2017)

2.2.2.3 Based upon mathematical model

To fulfil the previous mentioned control tasks, the controller can be further subdivided into two categories according to whether the control algorithms rely on a ship mathematical model (the model-based method) or not (the model-free method) (Chen et al., 2020; Lee et al., 2010). The model-based controller needs an accurate mathematical model describing the control plant, in other words, the controller coefficients are obtained based on the ship's mathematical model parameters. For instance, the PID controller's proportional, integral and derivative coefficients (K_p , K_i , K_d) are derived from the ship mathematical model's manoeuvring indices (the time constant T and the gain K). In addition to classical PID control, other model-based techniques have been used to design ship autopilot systems, such as the robust control (Donha et al., 1998), the LQG control (Holzhuter, 1997; Katebi et al., 1985), IMC control (Lee et al., 2010; Saari and Djemai, 2012), and slide mode control (Ejaz and Chen, 2017). Examples of free-model control laws are the fuzzy controller (Bhattacharyya et al., 2011; Fraga and Liu, 2011; Van Amerongen et al., 1977; Zadeh, 1965) and neural network controller (Bavarian, 1988; Lacki, 2018; Unar, 1999), among others. These methods do not rely on the control plant parameters, but on expert experience or learning based on historical data.

2.2.2.4 Based upon control mechanical structure

According to mechanical structure or the number of actuators, the controllers can be classified into two types:

- 1) Control the fully actuated ships;
- 2) Control underactuated ships.

When designing the ship's motion control system, it is important to distinguish both. The difference between the fully actuated and underactuated ship is whether the degree of freedom of the ship is equal to the control input dimension. For

instance: a marine surface ship can move freely in the 3D space and has a maximum of 6 DOF. A fully actuated ship operating in 6 DOF must be configured by the actuators that can generate independent forces and moments in all directions (Fossen, 2011). In most cases, this is not practical. For instance, a ship is equipped with one (two) rudder (s) and one (two) propeller (s), which cannot satisfy a 6 DOF motion control objective, even 3DOF cannot be fully achieved. This type of ship is so-called the underactuated ship.

In literature, except for a small amount of research focused on the development of controllers for the fully actuated ships, to mention some relevant examples: Almeida et al. (2007), Breivik et al. (2006), Khaled and Chalhoub (2011), Tee and Ge (2006), Wang et al. (2018), Zheng et al. (2017), etc. Most studies concentrated on designing controllers for underactuated ships (Do, 2010; Do and Pan, 2006; Mu et al., 2018; Oh and Sun, 2010; Pereira et al., 2008; Sun et al., 2017; Zhang et al., 2017), because most marine surface ships are usually equipped with rudders and propellers for surge and yaw motions only, while being without any actuators for direct control of sway motion (Zhang et al., 2015).

2.3 Development of path following control

2.3.1 Overview

Ship path following control is one of the most important research branches among the ship motion control community. Figure 2.6 displays the structure of the ship path following control system. It generally consists of four subsystems: a path planning system, a guidance system, a control system, and a navigation system. To solve the practical application problems of ship path following control, literature review will be presented from the control-related three aspects: path planning, guidance, and motion control.

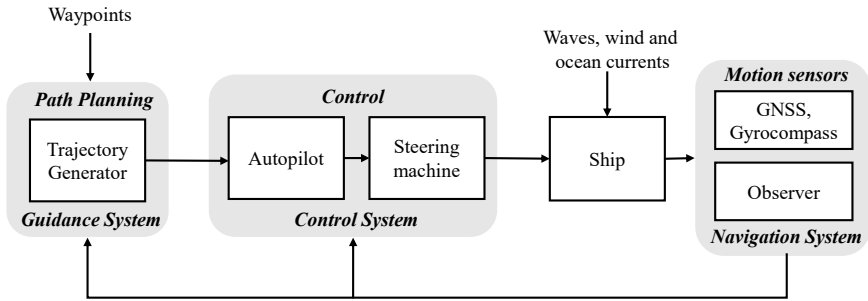


Figure 2.6 Structure of the ship path following control system.

2.3.2 Path planning system

Path planning is a very crucial aspect for marine surface ships that sail in open sea, harbour waters and inland waters, etc. Seafarers need to plan a safe and optimal path based on a waypoint generator in order to avoid static and dynamic obstacles. The path planning approaches can be clarified into global, local, and hybrid path planning algorithms, etc. (Liu et al., 2016; Yu et al., 2019).

2.3.2.1 Global path planning

Global path planning is also called route planning, which is used to plan a path in a large scale area, for instance, the planned path from a port of Norway to a port of Belgium (Figure 2.7). The global approaches are suitable for situations where all the environmental information is available and there are only static obstacles without considering moving vehicles. The global path can be planned offline by using optimization theory such as genetic algorithm (GA) or common path finding heuristic algorithms such as A* algorithm (Campbell et al., 2012; Larson et al., 2006).

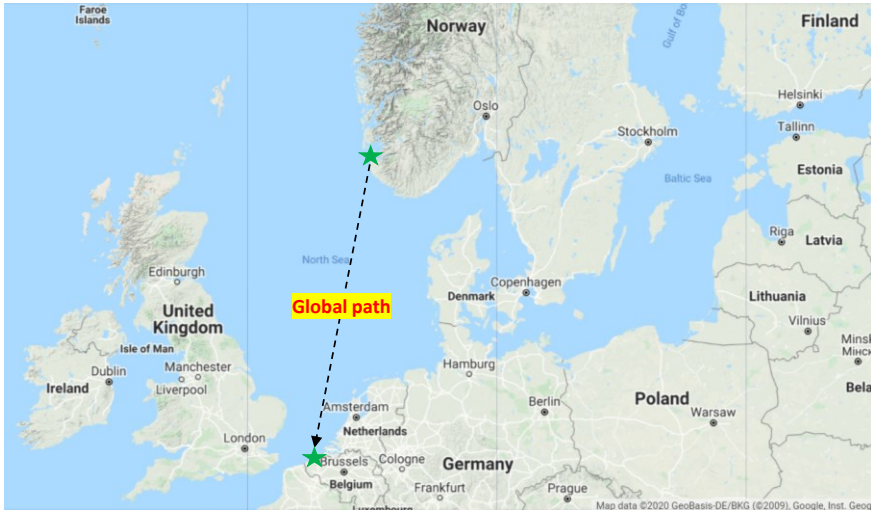


Figure 2.7 Global path planning from a port of Norway to a port of Belgium.

Evolutionary algorithms (EAs) as a class of artificial intelligence methods are increasingly used for global path planning (Kanakakis and Tsourveloudis, 2007). EAs are usually characterized into multiple-objective optimization problems, where the cost (fitness) function is optimized with specified constraints. Genetic algorithm (GA) is considered as one of the most common used methods for generating waypoints (Campbell et al., 2012; Fan et al., 2016; Liu et al., 2016; Qu et al., 2005). Other optimization methods include particle swarm optimization (PSO) (Wang et al., 2016), Ant colony optimization (ACO) (Lazarowska, 2015; Wu et al., 2017), Grey wolf optimizer (GWO) (Wang et al., 2019), etc. Due to the optimization process requires a lot of computing time, such methods are difficult to achieve real-time planning, thus they are generally restricted to offline implementation.

Except for the Evolutionary algorithms, the heuristic search algorithms are also applied in path planning. The A* algorithm is one of the most widely-used heuristic search methods, which can quickly find the optimal path with a small number of waypoints (Larson et al., 2006; Naus and Wąż, 2013; Yu et al., 2019). However, the conventional A* algorithms cost large computational memory and easily cause unwanted sharp turns. These disadvantages result in the difficulty of real-time path planning.

2.3.2.2 Local path planning

Local path planning methods are also named dynamic path planning or online planning. It is used to update the path or waypoint database in case of time-varying situations such as moving ships (collision avoidance) and weather (weather routing), etc. The relevant information is available only in local areas, and the desired path can be only obtained in a real-time environment. Figure 2.8 shows an example for local path planning from a port of Norway to a port of Belgium.

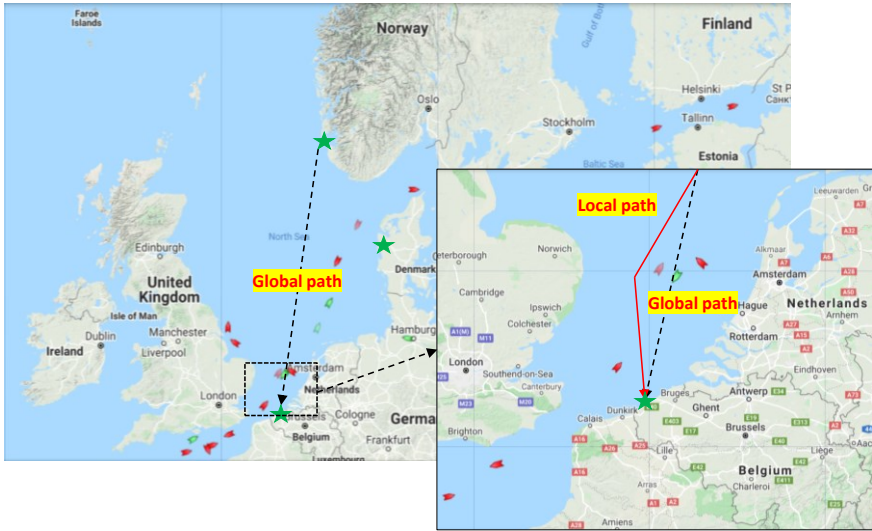


Figure 2.8 Local path planning from a port of Norway to a port of Belgium.

Numerous studies focused on local path planning to meet the demands of real-time path planning or avoiding dynamic vehicles. The algorithms include Artificial potential field (APF) (Lyu and Yin, 2018, 2019; Wu et al., 2017; Xie et al., 2016), Optimal reciprocal collision avoidance (ORCA) algorithm (Zhao et al., 2016), Rolling windows method (Wang et al., 2016), Velocity obstacle (Kuwata et al., 2014; Zhuang et al., 2016), Voronoi diagram (Candeloro et al., 2017), etc.

2.3.2.3 Hybrid path planning

In order to ensure the safety, effectiveness and application of path planning in a dynamic environment, great efforts have been devoted to the development of hybrid path planning algorithms. Hybrid path planning methods usually combine the global planning approaches with local ones together to obtain the optimal path. The first step is to plan a global path based on static environmental information using the global planning method. The second step is to adjust the path in local areas in case of changing environment or moving vehicles.

Xie et al. (2016) combined the Dijkstra's algorithm and artificial potential field (APF) algorithm to achieve global and local path planning, and the combination can effectively improve the path planning ability in a complex environment. In Yu et al. (2019), the global path was firstly planned by the A* algorithm, and then the artificial potential field (APF) was employed for local path planning. In addition, some research tried to further improve the path planning algorithm, to mention some relevant examples: Campbell et al. (2014), and Liu et al. (2017), etc. Among the above research, the FMM-based (fast marching method) algorithm is considered as one of the most reliable path planning approaches (Chen et al., 2020; Garrido et al., 2020; Yan et al., 2020). Because the FMM-based algorithms can quickly generate the optimal and smooth paths in a complex environment, which

enables it to be used in a static and dynamic environment. Thus, in this research, a novel FMM-based path planning method was proposed and used, which was named as angle-guidance tuned fast marching square (ATFMS). The development of the ATFMS method will be presented in section 4.2.

2.3.3 Guidance system

2.3.3.1 General discussion

Guidance system is used to automatically guide the ship navigation based on the waypoints generated by the path planning algorithms and the ship's motion state including position, speed, acceleration, etc. Guidance algorithms are commonly used for ship's path following control, which mainly include the line-of-sight (LOS) guidance method, vector field (VF) guidance method, dynamic virtual ship (DVS) guidance method, etc.

2.3.3.2 Line-of-sight (LOS) guidance method

Line-of-sight (LOS) or improved LOS is frequently used for ship path following control system (Fossen, 2011; Moreira et al., 2007). The basic principle of the LOS algorithm is that if a ship converges to a constant heading angle (Ψ_{los}) between the ship and target, then the ship can eventually converge to the target position (P_{los}). See Figure 2.9 for better understanding. Breivik and Fossen (2004, 2005) presented the principle of the LOS algorithm in detail.

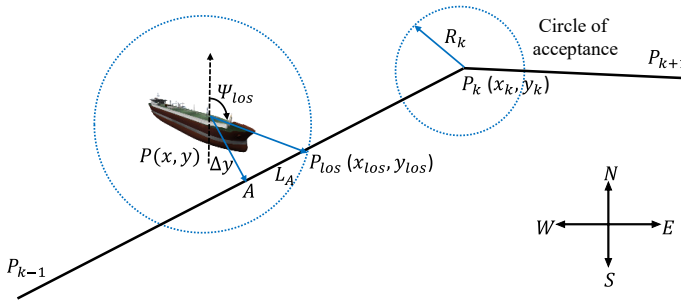


Figure 2.9 Illustration of line-of-sight (LOS) guidance system.

The LOS guidance algorithm has been widely applied by numerous studies. Lekkas and Fossen (2013) presented an overview of the LOS guidance laws for marine surface ships. In Fossen (2011), the principle and application of the LOS algorithm were elaborated. Further studies can be found in Annamalai and Motwani, (2013), Breivik et al. (2008), Caccia et al. (2008), Desa et al. (2007), Fredriksen and Pettersen (2006), Naem et al. (2012), Peng et al. (2013), Piao et al. (2019), Sharma and Sutton (2013).

In order to improve the performance of the conventional LOS guidance algorithm, some modified version of LOS algorithms have been proposed, examples as such: a new method was proposed to improve the convergence of the LOS algorithm via

dynamic circle (Lúcia Moreira et al., 2005). An improved LOS guidance algorithm was proposed, which can adjust adaptively based on the path following error (Liu et al., 2017). A new predictor-based LOS (PLOS) guidance algorithm was presented in Liu et al. (2016), where the predictor was used for the estimation of the ship's sideslip due to environmental disturbances. Caharija (2016) introduced an integral line-of-sight guidance algorithm (ILOS) in order to compensate for the drift effect of environmental disturbance. Mu et al. (2018) proposed an adaptive line-of-sight guidance method (ALOS), where the traditional LOS algorithm was optimized by the fuzzy algorithm. The LOS algorithm was coupled with a manual biasing scheme to improve its performance (Naeem et al., 2012).

2.3.3.3 Vector field (VF) guidance method

The definition of the vector field (VF) is similar to that of potential fields, which have been widely used as a tool for the guidance of unmanned aerial vehicle (UAV) (Nelson et al., 2006). Figure 2.10 shows two examples of the vector field guidance for straight-line and circular path following. Sujit et al. (2014) presented a detailed analysis for the vector field path following. Nelson et al. (2007) developed a vector field guidance method for accurate path following control of miniature air vehicles. The performance of the proposed guidance law for straight-line and circular arcs paths was presented. In Wilhelm and Clem (2019), a gradient vector field (GVF) algorithm was proposed to guide UAV following specified paths and avoid obstacles. Although the VF guidance method is commonly used in the guidance of unmanned aerial vehicle (UAV), few studies have used this method in the field of path following guidance for marine surface ships. Xu and Guedes Soares (2016) designed a waypoint guidance algorithm for surface marine vessels using a vector field, and the stability of the vector field was analysed by the Lyapunov function. Although this guidance approach is characterized by its low computational consumption and effective implementation, there are some drawbacks that hinder its applications. The defects include that it is easy to fall into the local minimum problem or obtain an unreachable target (Campbell et al., 2012).

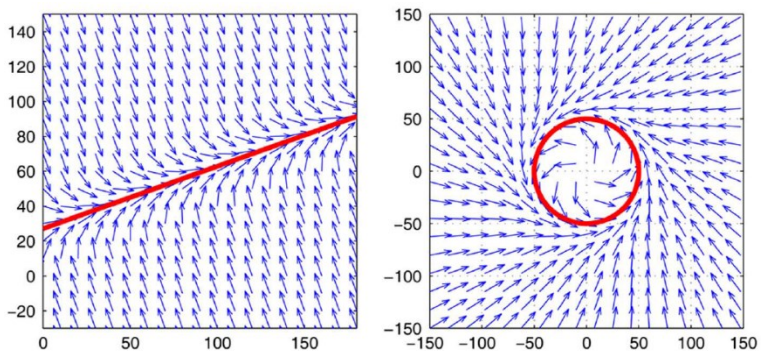


Figure 2.10 Illustration of the vector field guidance for straight-line and circular path following (Nelson et al., 2007).

2.3.3.4 Dynamic virtual ship (DVS) guidance method

A novel Dynamic virtual ship (DVS) guidance method was designed for waypoint-based path following control for marine surface ships. Figure 2.11 demonstrates the general framework of the DVS guidance principle. The approach assumes that the reference path is generated via a virtual ship, thus it is called Dynamic Virtual Ship (DVS) algorithm. The aim of the DVS guidance is to provide a virtual ship as the reference for the controller design, and the virtual ship sails automatically following the reference path with the desired speed. (Zhang and Zhang, 2015) presented the detailed development process of the DVS algorithm. Further studies are available in Zhang and Zhang (2017), Zhang et al. (2017, 2018, 2019), and Deng et al. (2019), etc.

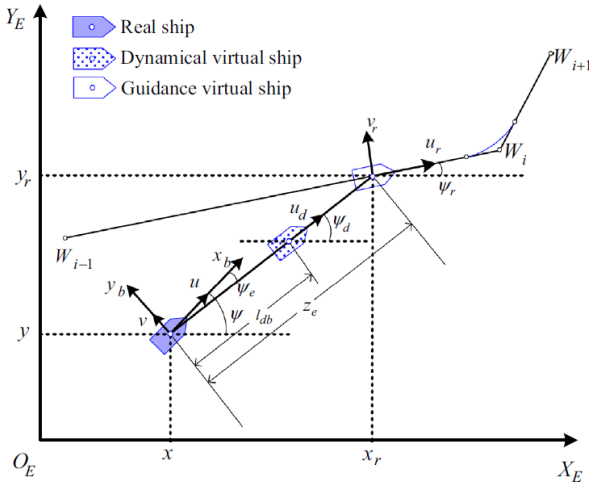


Figure 2.11 General framework of dynamic virtual ship (DVS) guidance principle (Zhang and Zhang, 2015).

To summarize, despite great efforts have been given to the development of advanced guidance algorithms such as the vector filed (VF) and dynamic virtual ship (DVS), the LOS-based algorithm is still one of the most popular guidance methods in practice. Thus, the LOS-based guidance method will be used in this research.

2.3.4 Control system

The path following control system is used to control the ship following a waypoint-based path with the help of a guidance algorithm. The controller plays a core role in the path following system, and numerous control algorithms have been developed for path following control missions. For instance: the PID controller (Caccia et al., 2008, 2005; Desa et al., 2007; Lyu and Yin, 2019; Lúcia Moreira et al., 2005), the LQG controller (Annamalai and Motwani, 2013), the model predictive controller (Annamalai and Motwani, 2013; Oh and Sun, 2010), the backstepping controller (Breivik and Fossen, 2004; Fredriksen and Pettersen,

2006), the genetic algorithm (Sharma and Sutton, 2013), the neural networks controller (Peng et al., 2013), the fuzzy LQG controller (Naeem et al., 2012), etc. The related work has been summarized in Table 2.3.

However, most research mentioned above was conducted via theoretical approaches. These algorithms are often complex and thus difficult to be directly applied in practical engineering. Therefore, it is necessary to evaluate the application of autopilots in real case scenarios. Full scale measurement and model test are two reliable means to investigate the application potential for various controllers, the related works are briefly summarized in Table 2.4. Compared with the model experiments, full scale results can reflect the actual behaviour of controllers free of scale effects and any model assumptions. However, it can be quite expensive and time-consuming, and some controllers cannot guarantee safety thus is infeasible in the design stage. Hence, the model test is the predominant approach. A special advantage of the model test is that it is especially suitable for applications in shallow water condition, where the water depth can be arbitrarily selected and accurately adjusted.

Table 2.4 Summary of the control approaches with experimental investigation.

Controller	Tasks	Reference
Adaptive	TT	Mooney and Johnson (2011)
Antidisturbance controller	PF	Gu et al. (2019)
Backstepping	PF, TT	(Do and Pan, 2006), Gadre et al. (2012), Li et al., (2009a), Pettersen and Nijmeijer (2001), Skjetne et al. (2004, 2005), Sonnenburg and Woolsey (2012) , Zakartchouk and Morishita (2009)
Fuzzy	PF	Naeem et al. (2012), Paroka et al. (2017), Vaneck (1997)
Fuzzy PID	PF, TT	Breivik et al. (2008), Lee et al. (2014)
H_∞	TT, CC	Morawski and Pomirski (1998), Yu et al. (2008)
IMC	PF	Lee et al. (2010) Design and experiment of a small boat track-keeping autopilot Saari and Djemai (2012) Ship motion control using multi-controller structure
LQG	PF, CC	Annamalai and Motwani (2013), Elkaim (2006) , Naeem et al. (2008), Sharma et al. (2012)
MPC	CC, TT	Annamalai et al. (2014, 2015), Guerreiro et al. (2013)
Output Feedback	PF	Kyrkjebø et al. (2007), Lindegaard and Fossen (2003), Wondergem et al. (2011)
PID	CC,PF,TT	Beck et al. (2009), Bibuli et al. (2012), Breivik and Loberg (2011), Caccia et al. (2005, 2008), Desa et al. (2007), Liu et al.

		(2017), Mooney and Johnson (2009), Moreira et al. (2007), Mu et al. (2018), Pereira et al. (2008), Naeem et al. (2012), Piao et al. (2019), Švec et al. (2014), Hinostroza et al. (2018), Yang et al. (2019)
SMC	PF	AlfaroCid et al. (2005), Ashrafiuon et al., (2008)
Neural network	TT	Wang et al. (2019, 2020)

Note: CC: Course Control, PF: Path Following, TT: Trajectory Tracking.

2.4 Reference

- Abkowitz, M. A.**, 1964. *Lectures on ship hydrodynamics-steering and manoeuvrability*. Lyngby, Denmark.
- Abkowitz, M. A.**, 1980. *Measurement of hydrodynamic characteristics from ship maneuvering trials by system identification*. Transactions - Society of Naval Architects and Marine Engineers, 88, 283–318.
- AlfaroCid, E., McGookin, E. W., and MurraySmith, D. J.**, 2006. *GA-optimised PID and pole placement real and simulated performance when controlling the dynamics of a supply ship*. IEE Proceedings - Control Theory and Applications, 153(2), 228–236.
- AlfaroCid, E., McGookin, E. W., MurraySmith, D. J., and Fossen, T. I.**, 2005. *Genetic algorithms optimisation of decoupled sliding mode controllers: simulated and real results*. Control Engineering Practice, 13(6), 739–748.
- Almeida, J., Silvestre, C., and Pascoal, A.**, 2007. *Path-following control of fully-actuated surface vessels in the presence of ocean currents*. IFAC Proceedings Volumes, 40(17), 26–31.
- Annamalai, A. S. K., and Motwani, A.**, 2013. *A comparison between LQG and MPC autopilots for inclusion in a navigation, guidance and control system*. Plymouth University.
- Annamalai, A. S. K., Sutton, R., Yang, C., Culverhouse, P., et al.**, 2014. *Innovative adaptive autopilot design for uninhabited surface vehicles*. In *25th IET Irish Signals & Systems Conference 2014 and 2014 China-Ireland International Conference on Information and Communications Technologies (ISSC 2014/CICT 2014)*. Limerick, Ireland.
- Annamalai, A. S. K., Sutton, R., Yang, C., Culverhouse, P., et al.**, 2015. *Robust adaptive control of an uninhabited surface vehicle*. Journal of Intelligent and Robotic Systems: Theory and Applications, 78(2), 319–338.
- Anschütz, R.**, 1908. *A pioneer in navigation technology*. Retrieved from <https://www.raytheon-anschuetz.com/company/history/>
- Ashrafiuon, H., Muske, K. R., McNinch, L. C., and Soltan, R. A.**, 2008. *Sliding-mode tracking control of surface vessels*. IEEE Transactions on Industrial Electronics, 55(11), 4004–4012.
- Åström, K. J., and Källström, C.**, 1976. *Identification on ship steering dynamics*. Automatica, 12, 9–12.
- Azzeri, M. N., Adnan, F. A., and Zain, M. Z. M.**, 2015. *Review of course keeping control system for unmanned surface vehicle*. Jurnal Teknologi, 74(5), 11–20.

- Bavarian, B.**, 1988. *Introduction to neural networks for intelligent control*. IEEE Control Systems Magazine, 8(2), 3–7.
- Beck, E., Kirkwood, W., Caress, D., Berk, T., et al.**, 2009. *A small waterplane area twin hull autonomous platform for shallow water mapping*. In *2008 IEEE/OES Autonomous Underwater Vehicles*. Woods Hole, MA, USA.
- Bhattacharyya, S. K., Rajesh, G., and Gupta, D. K.**, 2011. *Fuzzy autopilot for ship maneuvering*. International Shipbuilding Process., 58, 191–218.
- Bibuli, M., Caccia, M., Lapierre, L., and Bruzzone, G.**, 2012. *Guidance of unmanned surface vehicles: experiments in vehicle following*. IEEE Robotics and Automation Magazine, 19(3), 92–102.
- Brasel, M.**, 2013. *Adaptive LQR control system for the nonlinear 4-DoF model of a container vessel*. In *2013 18th International Conference on Methods & Models in Automation & Robotics (MMAR)*. Miedzyzdroje, Poland.
- Breivik, M., and Fossen, T. I.**, 2004. *Path following of straight lines and circles for marine surface vessels*. IFAC Proceedings Volumes, 37(10), 65–70.
- Breivik, M., and Fossen, T. I.**, 2005. *Principles of guidance-based path following in 2D and 3D*. In *Proceedings of the 44th IEEE Conference on Decision and Control, and the European Control Conference, CDC-ECC '05*. Seville, Spain.
- Breivik, M., Hovstein, V. E., and Fossen, T. I.**, 2008. *Straight-line target tracking for unmanned surface vehicles*. Modeling, Identification and Control, 29(4), 131–149.
- Breivik, M., and Loberg, J. E.**, 2011. *A virtual target-based underway docking procedure for unmanned surface vehicles*. IFAC Proceedings Volumes, 44(1), 13630–13635.
- Breivik, M., Strand, J. P., and Fossen, T. I.**, 2006. *Guided dynamic positioning for fully actuated marine surface vessels*. In *7th IFAC Conference on Manoeuvring and Control of Marine Craft*.
- Bums, R. S.**, 1995. *The use of artificial neural networks for the intelligent optimal control of surface ships*. IEEE Journal of Oceanic Engineering, 20(1), 65–72.
- Caccia, M., Bibuli, M., Bono, R., and Bruzzone, G.**, 2008. *Basic navigation, guidance and control of an Unmanned Surface Vehicle*. Autonomous Robots, 25(4), 349–365.
- Caccia, M., Bono, R., and Bruzzone, G.**, 2005. *An autonomous craft for the study of sea-air interactions*. IEEE Robotics and Automation Magazine, 12(3), 95–105.

- Caharija, W.**, 2016. *Integral line-of-sight guidance and control of underactuated marine vehicles: theory, simulations, and experiments*. Norwegian University of Science and Technology.
- Campbell, S., Naeem, W., and Irwin, G. W.**, 2012. *A review on improving the autonomy of unmanned surface vehicles through intelligent collision avoidance manoeuvres*. *Annual Reviews in Control*, 36(2), 267–283.
- Campbell, Sable, AbuTair, M., and Naeem, W.**, 2014. *An automatic COLREGs-compliant obstacle avoidance system for an unmanned surface vehicle*. *Proceedings of the Institution of Mechanical Engineers Part M: Journal of Engineering for the Maritime Environment*, 228(2), 108–121.
- Candeloro, M., Lekkas, A. M., and Sørensen, A. J.**, 2017. *A Voronoi-diagram-based dynamic path-planning system for underactuated marine vessels*. *Control Engineering Practice*, 61, 41–54.
- Cao, J., Zhuang, J. Y., Xu, F., Yin, J. C., et al.**, 2015. *Parametric estimation of ship maneuvering motion with integral sample structure for identification*. *Applied Ocean Research*, 52, 212–221.
- Chen, C. Y., Delefortrie, G., and Lataire, E.**, 2020. *Experimental investigation of practical autopilots for maritime autonomous surface ships in shallow water*. *Ocean Engineering*, 218, 108246.
- Chen, C. Y., Tello Ruiz, M., Delefortrie, G., and Lataire, E.**, 2019a. *An energy-efficient adaptive course control system for ocean surface ships*. In *11th International Workshop on Ship and Marine Hydrodynamics*. Hamburg, Germany.
- Chen, C. Y., Tello Ruiz, M., Delefortrie, G., Mei, T. L., et al.**, 2019b. *Parameter estimation for a ship's roll response model in shallow water using an intelligent machine learning method*. *Ocean Engineering*, 191, 1–10.
- Chen, C. Y., Tello Ruiz, M., Lataire, E., Delefortrie, G., et al.**, 2019c. *Ship manoeuvring model parameter identification using intelligent machine learning method and the beetle antennae search algorithm*. In *Proceedings of the ASME 2019 38th International Conference on Ocean, Offshore and Arctic Engineering*. Glasgow, Scotland.
- Chen, P. F., Huang, Y. M., Papadimitriou, E., Mou, J. M., et al.**, 2020. *Global path planning for autonomous ship: a hybrid approach of fast marching square and velocity obstacles methods*. *Ocean Engineering*, 214, 107793.
- Chislett, M. S., and Strom Tejsen, J.**, 1965. *Planar motion mechanism tests and full-scale steering and manoeuvring predictions for a Mariner class vessel*. *International Shipbuilding Progress*, 12(129), 201–224.
- Clarke, D., Gelding, P., and Hine, G.**, 1983. *The application of manoeuvring criteria in hull design using linear theory*. In *Transactions of the Royal*

Institution of Naval Architects, RINA. London, UK.

- Cui, R. X., Zhang, X., and Cui, D.,** 2016. *Adaptive sliding-mode attitude control for autonomous underwater vehicles with input nonlinearities.* Ocean Engineering, 123, 45–54.
- Das, S.,** 2014. *Applicability of sliding mode control in autopilot design for ship motion control.* In *IEEE International Conference on Recent Advances and Innovations in Engineering (ICRAIE-2014).* Jaipur, India.
- Das, S.,** 2015. *Ships steering autopilot design by Nomoto model.* International Journal on Mechanical Engineering and Robotics (IJMER), 3(3), 37–41.
- Davidson, K. S. M., and Schiff, L. I.,** 1946. *Turning and course-keeping qualities.* Transactions—Society of Naval Architects Marine Engineers, 54, 152–200.
- Delefortrie, G., Eloot, K., Lataire, E., Van Hoydonck, W., et al.,** 2016. *Captive model tests based on 6 DOF shallow water manoeuvring model.* In *International conference on ship manoeuvring in shallow and confined water with special focus on ship bottom interaction (4th MASHCON).* Hamburg, Germany.
- Deng, Y. J., Zhang, X. K., Im, N., Zhang, G. Q., et al.,** 2019. *Event-triggered robust fuzzy path following control for underactuated ships with input saturation.* Ocean Engineering, 186, 106122.
- Desa, E., Maurya, P. K., Pereira, A., Pascoal, A. M., et al.,** 2007. *A small autonomous surface vehicle for ocean color remote sensing.* IEEE Journal of Oceanic Engineering, 32(2), 353–364.
- Desanj, D. S., Katebi, M. R., and Grumble, M. J.,** 1995. *H_∞ robust autopilot design.* IFAC Proceedings Volumes, 28(2), 115–122.
- Do, K. D.,** 2010. *Practical control of underactuated ships.* Ocean Engineering, 37(13), 1111–1119.
- Do, K. D., and Pan, J.,** 2006. *Robust path-following of underactuated ships: Theory and experiments on a model ship.* Ocean Engineering, 33(10), 1354–1372.
- Donha, D. C., Desanj, D. S., Katebi, M. R., and Grumble, M. J.,** 1998. *H_∞ adaptive controller for autopilot applications.* International Journal of Adaptive Control and Signal Processing, 12, 623–648.
- Du, J. L., Yang, Y., Wang, D. H., and Guo, C.,** 2013. *A robust adaptive neural networks controller for maritime dynamic positioning system.* Neurocomputing, 110, 128–136.
- Duan, H. Q., and Zhu, Q. D.,** 2012. *Trajectory tracking control of ships based*

- on an adaptive backstepping neural network. CAAI Transactions on Intelligent Systems, 7(3), 259–264.
- Ejaz, M., and Chen, M.,** 2017. *Sliding mode control design of a ship steering autopilot with input saturation*. International Journal of Advanced Robotic Systems, 14(3), 1–13.
- Elkaim, G. H.,** 2006. *The atlantis project: a GPS-guided wing-sailed autonomous catamaran*. Navigation, Journal of the Institute of Navigation, 53(4), 237–247.
- Elmer Sperry.,** 1911. *History of sperry marine*. Retrieved from <https://www.sperrymarine.com/corporate-history/sperry-marine>
- Elmokadem, T., Zribi, M., and Kamal, Y. T.,** 2017. *Trajectory tracking sliding mode control of underactuated AUVs*. Nonlinear Dynamics, 84, 1079–1091.
- Eloot, K.,** 2006. *Selection, experimental determination and evaluation of a mathematical model for ship manoeuvring in shallow water*. Ghent University, Belgium (PhD thesis).
- Eloot, K., and Vantorre, M.,** 2003. *Development of a tabular manoeuvring model for hull forces applied to full and slender ships in shallow water*. In *International conference on marine simulation and ship maneuverability (Marsim '03)*. Kanazawa, Japan.
- Eloot, Katrien, and Vantorre, M.,** 1998. *Alternative captive manoeuvring tests: possibilities and limitations*. In *Symposium on forces acting on a manoeuvring vessel (MAN98)*. Val de Reuil, France.
- Fan, Y., Sun, X., Wang, G., and Zhao, Y.,** 2016. *On evolutionary genetic algorithm in path planning for a USV collision avoidance*. ICIC Express Letters, 10, 1691–1696.
- Faramin, M., Goudarzi, R. H., and Maleki, A.,** 2019. *Track-keeping observer-based robust adaptive control of an unmanned surface vessel by applying a 4-DOF maneuvering model*. Ocean Engineering, 183, 11–23.
- Fossen, T. I.,** 2011. *Handbook of marine craft hydrodynamics and motion control*. John Wiley & Sons Ltd. United Kingdom.
- Fossen, T. I., Breivik, M., and Skjetne, R.,** 2002. *Light of sight path following of underactuated marine craft*. Science And Technology, 1–6.
- Fossen, T. I., Pettersen, K. Y., and Galeazzi, R.,** 2015. *Line-of-sight path following for dubins paths with adaptive sideslip compensation of drift forces*. IEEE Transactions on Control Systems Technology, 23(2), 820–827.
- Fraga, R., and Liu, S.,** 2011. *Double fuzzy logic control for the ship path following*. In *The 2th International Conference on Intelligent Control and*

Information Processing. Harbin, China.

- Fredriksen, E., and Pettersen, K. Y.,** 2006. *Global κ -exponential way-point maneuvering of ships: Theory and experiments*. *Automatica*, 42(4), 677–687.
- Fu, M. Y., Li, M. Y., and Xie, W. B.,** 2017. *Finite-time trajectory tracking fault-tolerant control for surface vessel based on time-varying sliding mode*. *IEEE Access*, 6, 2425–2433.
- Gadre, A. S., Sonnenburg, C., Du, S., Stilwell, D. J., et al.,** 2012. *Guidance and control of an unmanned surface vehicle exhibiting sternward motion*. In *2012 Oceans*. Virginia, USA.
- Garrido, S., Alvarez, D., and Moreno, L. E.,** 2020. *Marine applications of the fast marching method*. *Frontiers in Robotics and AI*, 7(2), 1–12.
- Gu, N., Peng, Z. H., Wang, D., Shi, Y., et al.,** 2019. *Antidisturbance coordinated path following control of robotic autonomous surface vehicles: theory and experiment*. *IEEE/ASME Transactions on Mechatronics*, 24(5), 2386–2396.
- Guerreiro, B. J., Silvestre, C., Cunha, R., and Pascoal, A.,** 2013. *Trajectory tracking nonlinear model predictive control for autonomous surface craft*. In *2013 European Control Conference, ECC*. Zürich, Switzerland.
- Hinostroza, M. A., Soares, C. G., and Xu, H.,** 2018. *Motion planning, guidance and control system for autonomous surface vessel*. In *Proceedings of the International Conference on Offshore Mechanics and Arctic Engineering - OMAE*. Madrid, Spain.
- Holzhtuter, T.,** 1997. *LQG approach for the high-precision track control of ships*. *IEE Proceedings: Control Theory and Applications*, 144(2), 121–127.
- Hou, X. R., Zou, Z. J., and Liu, C.,** 2018. *Nonparametric identification of nonlinear ship roll motion by using the motion response in irregular waves*. *Applied Ocean Research*, 73, 88–99.
- Hu, S., Yang, P., Juang, J. Y., and Chang, B. C.,** 2003. *Robust nonlinear ship course-keeping control by H_∞ I/O linearization and μ -synthesis*. *International Journal of Robust and Nonlinear Control.*, 13, 55–70.
- Im, N., and Nguyen, V.,** 2017. *Artificial neural network controller for automatic ship berthing using head-up coordinate system*. *International Journal of Naval Architecture and Ocean Engineering*, 10(3), 1–15.
- Inoue, S., Hirano, M., and Kijima, K.,** 1981. *Hydrodynamic derivatives on ship manoeuvring*. *International Shipbuilding Progress*, 28(321), 112–125.
- Inoue, S., Hirano, M., Kijima, K., and Takashina, J.,** 1981. *A practical calculation method of ship maneuvering motion*. *International Shipbuilding*

- Progress, 28(325), 207–222.
- Ishiguro, T., and Ohmori, T.,** 2003. *Optimized hull form design at initial design stage considering manoeuvrability, propulsive performance and sea-keeping performance*. In *International conference on marine simulation and ship maneuverability (Marsim ' 03)*. Kanazawa, Japan.
- ITTC.,** 2005. *Final Report and Recommendations to the 24th ITTC*. Edinburgh, UK.
- Jeon, M. J., Lee, D. H., Lee, D. M., Nguyen, V. M., et al.,** 2016. *Estimation of static hydrodynamic coefficient in waves using static drift test*. In *AETA 2015: Recent Advances in Electrical Engineering and Related Sciences*. Ho Chi Minh, Vietnam.
- Kanakakis, V., and Tsurveloudis, N.,** 2007. *Evolutionary path planning and navigation of autonomous underwater vehicles*. In *Proceedings of 15th Mediterranean Conference on Control & Automation*. Athens, Greece.
- Katebi, M. R., Grimble, M. J., and Byrne, J.,** 1985. *LQG adaptive autopilot design*. IFAC Proceedings Volumes, 18(5), 1293–1298.
- Katsuro Kijima, S. T.,** 1993. *On a prediction method of ship manoeuvring characteristics*. In *International Conference on Marine Simulation and Ship Maneuverability (MARSIM' 93)*. Newfoundland, Canada.
- Khaled, N., and Chalhoub, N. G.,** 2011. *A dynamic model and a robust controller for a fully-actuated marine surface vessel*. *Journal of Vibration and Control*, 17(6), 801–812.
- Kim, S. Y., Kim, Y. G., Son, N. S., Lee, S. W., et al.,** 2003. *Manoeuvring characteristics of a large container ship*. In *International conference on marine simulation and ship maneuverability (Marsim' 03)*. Kanazawa, Japan.
- Kolyubin, S. A., and Shiriaev, A. S.,** 2014. *Dynamics-consistent motion planning for underactuated ships using virtual holonomic constraints*. In *2014 Oceans*. St. John's, NL, Canada.
- Koyama, T., Watanabe, T., and Watanabe, I.,** 1973. *An application of the least square method to the ship maneuverability identification*. *Journal of the Society of Naval Architects of Japan*, 134, 173–181.
- Krishnamurthy, P., Khorrami, F., and Fujikawa, S.,** 2005. *A modeling framework for six degree-of-freedom control of unmanned sea surface vehicles*. In *Proceedings of the 44th IEEE Conference on Decision and Control*. Seville, Spain.
- Kumar, V., Nakra, B. C., and Mittal, A. P.,** 2011. *A review on classical and fuzzy pid controllers*. *International Journal of Intelligent Control Systems*,

16(3), 170–181.

Kuwata, Y., Wolf, M. T., Zarzhitsky, D., and Huntsberger, T. L., 2014. *Safe maritime autonomous navigation with COLREGS, using velocity obstacles*. IEEE Journal of Oceanic Engineering, 39(1), 110–119.

Kyrkjebø, E., Pettersen, K. Y., Wondergem, M., and Nijmeijer, H., 2007. *Output synchronization control of ship replenishment operations: Theory and experiments*. Control Engineering Practice, 15(6), 741–755.

Lacki, M., 2018. *Ship course-keeping with neuroevolutionary algorithms*. Scientific Journals of the Maritime University of Szczecin., 54(126), 70–74.

Larson, J., Bruch, M., and Ebken, J., 2006. *Autonomous navigation and obstacle avoidance for unmanned surface vehicles*. In *Proceedings of SPIE - The International Society for Optical Engineering*. San Diego, United States.

Lazarowska, A., 2015. *Ship's trajectory planning for collision avoidance at sea based on Ant Colony Optimisation*. Journal of Navigation, 68, 291–307.

Lee, S. D., Tzeng, C. Y., and Chen, B. J., 2014. *Design and experiment of a fuzzy PID track-keeping ship autopilot*. In *Oceans 2014 - Taipei*. Taipei.

Lee, S. D., Yu, C. H., Hsiu, K. Y., Hsieh, Y. F., et al., 2010. *Design and experiment of a small boat track-keeping autopilot*. Ocean Engineering, 37, 208–217.

Lee, T. I., Ahn, K. S., Lee, H. S., and Yum, D. J., 2003. *On an empirical prediction of hydrodynamic coefficients for modern ship hulls*. In *International conference on marine simulation and ship maneuverability*. Kanazawa, Japan.

Lekkas, A., and Fossen, T. I., 2013. *Line-of-sight guidance for path following of marine vehicles*. Advanced in Marine Robotics, 63–92.

Li, G. Y., Li, W., Hildre, H. P., and Zhang, H. X., 2016. *Online learning control of surface vessels for fine trajectory tracking*. Journal of Marine Science and Technology, 21(2), 251–260.

Li, J. H., Lee, P. M., Jun, B. H., and Lim, Y. K., 2008. *Point-to-point navigation of underactuated ships*. Automatica, 44(12), 3201–3205.

Li, W., Sun, Y., Chen, H., and Wang, G., 2017. *Model predictive controller design for ship dynamic positioning system based on state-space equations*. Journal of Marine Science and Technology, 22(3), 426–431.

Li, Z. ., Hu, J. Q., and Huo, X. X., 2012. *PID control based on RBF neural network for ship steering*. In *2012 World Congress on Information and Communication Technologies*. Trivandrum, India.

- Li, Z., Sun, J., and Oh, S.,** 2009,a. *Design, analysis and experimental validation of a robust nonlinear path following controller for marine surface vessels.* Automatica, 45, 1649–1658.
- Li, Z., Sun, J., and Oh, S.,** 2009,b. *Path following for marine surface vessels with rudder and roll constraints: an MPC approach.* In *Proceedings of the American Control Conference.* St. Louis, MO, USA.
- Lindegaard, K., and Fossen, T. I.,** 2003. *Fuel-efficient rudder and propeller control allocation for marine craft: experiments with a model ship.* IEEE Transactions on Control Systems Technology, 11(6), 850–862.
- Lindegaard, K. P.,** 2003. *Acceleration Feedback in Dynamic Positioning.* Norwegian University of Science and Technology.
- Liu, C. G., Chu, X. M., Wang, L., Xie, S., et al.,** 2015. *Trajectory tracking controller for underactuated surface vessels based on model predictive control.* Journal of Shanghai Jiaotong University, 49(12), 1842–1854.
- Liu, C., Zou, Z. J., and Yin, J. C.,** 2014. *Path following and stabilization of underactuated surface ships based on hierarchical sliding mode.* International Journal of Innovative Computing, Information & Control, 10(3), 909–918.
- Liu, C., Zou, Z. J., and Yin, J. C.,** 2015. *Trajectory tracking of underactuated surface vessels based on neural network and hierarchical sliding mode.* Journal of Marine Science and Technology (Japan), 20(2), 322–330.
- Liu, G. Y., Hou, Y. B., Luo, Y., and Li, D.,** 2017. *Genetic algorithm's application for optimization of PID parameters in dynamic positioning vessel.* In *2017 3rd International Conference on Mechanical, Electronic and Information Technology Engineering (ICMITE 2017).* Chengdu China.
- Liu, L., Wang, D., Peng, Z. H., and Wang, H.,** 2016. *Predictor-based LOS guidance law for path following of underactuated marine surface vehicles with sideslip compensation.* Ocean Engineering, 124, 340–348.
- Liu, S., and Fang, L.,** 2007. *Application of H_∞ control in rudder/flap vector robust control of a ship's course.* Journal of Marine Science and Application, 6(3), 62–67.
- Liu, T., Dong, Z. P., Du, H. W., Song, L. F., et al.,** 2017. *Path following control of the underactuated USV based on the improved line-of-sight guidance algorithm.* Polish Maritime Research, 24(1), 3–11.
- Liu, T. W., Wang, H. B., Dang, Y., and Yang, S. R.,** 2013. *A ships parameter identification arithmetic based on improved ant colony algorithm.* Applied Mechanics and Materials, 347–350(1662), 3450–3455.
- Liu, W. J., Sui, Q. M., Xiao, H. R., and Zhou, F. Y.,** 2011. *Sliding backstepping*

control for ship course with nonlinear disturbance observer. Journal of Information & Computational Science, 8(16), 3809–3817.

- Liu, Y. C., Bucknall, R., and Zhang, X. Y.,** 2017. *The fast marching method based intelligent navigation of an unmanned surface vehicle.* Ocean Engineering, 142, 363–376.
- Liu, Z. Q.,** 2017. *Ship adaptive course keeping control with nonlinear disturbance observer.* IEEE Access., 5, 17567–17575.
- Liu, Z. X., Zhang, Y. M., Yu, X., and Yuan, C.,** 2016. *Unmanned surface vehicles: an overview of developments and challenges.* Annual Reviews in Control, 41, 71–93.
- Lopez, M. J., Terron, J., Consegliere, A., and Mascarenas, C.,** 1998. *Course-keeping and course-changing H-infinity controller for a Ferry.* In *IFAC Workshop on Intelligent Components for Vehicles.* Seville, Spain.
- Luo, W. L.,** 2009. *On the modeling of ship manoeuvring motion by using support vector machines.* Shanghai Jiao Tong University (PhD thesis).
- Luo, W. L.,** 2016. *Parameter identifiability of ship manoeuvring modeling using system identification.* Mathematical Problems in Engineering, 2016, 1–10.
- Luo, W. L., and Cong, H. C.,** 2016. *Control for ship course-keeping using optimized support vector machines.* Algorithms, 9(3), 1–15.
- Luo, W. L., Guedes Soares, C., and Zou, Z. J.,** 2016. *Parameter identification of ship maneuvering model based on support vector machines and particle swarm optimization.* Journal of Offshore Mechanics and Arctic Engineering, 138(3), 1–8.
- Luo, W. L., and Li, X. Y.,** 2017. *Measures to diminish the parameter drift in the modeling of ship manoeuvring using system identification.* Applied Ocean Research, 67, 9–20.
- Luo, W. L., and Zou, Z. J.,** 2009. *Models identification parametric of ship maneuvering models by using support vector machines.* Journal of Ship Research, 53(1), 19–30.
- Lv, S. L., Wang, N., Wang, Y., Yin, J. C., et al.,** 2017. *Nonsingular terminal sliding mode based trajectory tracking control of an autonomous surface vehicle with finite-time convergence.* In *Advances in Neural Networks - ISNN 2017.* Sapporo, Hakodate, and Muroran, Hokkaido, Japan.
- Lyu, H. G., and Yin, Y.,** 2018. *Ship's trajectory planning for collision avoidance at sea based on modified artificial potential field.* In *2017 2nd International Conference on Robotics and Automation Engineering, ICRAE 2017.* Shanghai, China.

- Lyu, H. G., and Yin, Y.,** 2019. *COLREGS-constrained real-time path planning for autonomous ships using modified artificial potential fields*. Journal of Navigation, 72(3), 588–608.
- Minorsky, N.,** 1922. *Directional stability of automatically steered bodies*. Journal of the American Society for Naval Engineers, 34(2), 280–309.
- Mizuno, N., Kakami, H., and Okazaki, T.,** 2012. *Parallel simulation based predictive control scheme with application to approaching control for automatic berthing*. In *9th IFAC Conference on Manoeuvring and Control of Marine Craft*. Arenzano, Italy.
- Mooney, J. G., and Johnson, E. N.,** 2009. *Path-following algorithms and experiments for an unmanned surface vehicle*. Journal of Field Robotics, 26(8), 669–688.
- Mooney, J. G., and Johnson, E. N.,** 2011. *Comprehensive framework for tracking control and thrust allocation for a highly overactuated autonomous surface vessel*. Journal of Field Robotics, 28(1), 80–100.
- Moradi, M. H., and Katebi, M. R.,** 2001. *Predictive PID control for ship autopilot design*. IFAC Proceedings Volumes, 34(7), 375–380.
- Morawski, L., and Pomirski, J.,** 1998. *Ship track-keeping: Experiments with a physical tanker model*. Control Engineering Practice, 6(6), 763–769.
- Moreira, L., Fossen, T. I., and Guedes Soares, C.,** 2007. *Path following control system for a tanker ship model*. Ocean Engineering, 34, 2074–2085.
- Moreira, Lúcia, Fossen, T. I., and Soares, C. G.,** 2005. *Modeling, guidance and control of “Esso Osaka” model*. IFAC Proceedings Volumes, 16, 85–90.
- Mu, D. D., Wang, G. F., Fan, Y. S., Bai, Y. M., et al.,** 2018,a. *Fuzzy-based optimal adaptive line-of-sight path following for underactuated unmanned surface vehicle with uncertainties and time-varying disturbances*. Mathematical Problems in Engineering, 2018, 1–12.
- Mu, D. D., Wang, G. F., Fan, Y. S., Bai, Y. M., et al.,** 2018,b. *Path following for podded propulsion unmanned surface vehicle: theory, simulation and experiment*. IEEE Transactions on Electrical and Electronic Engineering, 13(6), 911–923.
- Naeem, W., Sutton, R., and Xu, T.,** 2012. *An integrated multi-sensor data fusion algorithm and autopilot implementation in an uninhabited surface craft*. Ocean Engineering, 39, 43–52.
- Naeem, W., Xu, T., Sutton, R., and Tian, A.,** 2008. *The design of a navigation, guidance, and control system for an unmanned surface vehicle for environmental monitoring*. Proceedings of the Institution of Mechanical Engineers Part M: Journal of Engineering for the Maritime Environment,

222(2), 67–79.

- Naeem, Wasif, Irwin, G., and Yang, A.,** 2012. *COLREGs-based collision avoidance strategies for unmanned surface vehicles*. *Mechatronics*, 22(6), 669–678.
- Naus, K., and Wąż, M.,** 2013. *The idea of using the A* algorithm for route planning an unmanned vehicle “Edredon.”* *Scientific Journals Maritime University of Szczecin*, 36(108), 143--147.
- Nelson, D. R., Barber, D. B., McLain, T. W., and Beard, R. W.,** 2006. *Vector field path following for small unmanned air vehicles*. In *Proceedings of the American Control Conference*. Minnesota, USA.
- Nelson, D. R., Barber, D. B., McLain, T. W., and Beard, R. W.,** 2007. *Vector field path following for miniature air vehicles*. *IEEE Transactions on Robotics*, 23(3), 519–529.
- Nguyen, T., Sørensen, A. J., and Tong Quek, S.,** 2007. *Design of hybrid controller for dynamic positioning from calm to extreme sea conditions*. *Automatica*, 43, 768–785.
- Nguyen, V., Le, T., Do, T., Nguyen, T., et al.,** 2004. *Study on an effective adaptive ship autopilot*. In *The 8th IEEE International Workshop on Advanced Motion Control, 2004. AMC '04*. Kawasaki, Japan.
- Nomoto, K., Taguchi, T., Honda, K., and Hirano, S.,** 1957. *On steering qualities of ships*. Technical Report. International Shipbuilding Progress, 4(35), 57–66.
- Norrbin, N. H.,** 1971. *Theory and observations on the use of a mathematical model for ship manoeuvring in deep and confined waters*. In *Publication No.68 of the Swedish State Shipbuilding Experimental Tank*. Göteborg, Sweden.
- Ogawa, A., and Kasai, H.,** 1978. *On the mathematical method of manoeuvring motion of ships*. International Shipbuilding Progress, 25(292), 306–319.
- Ogawa, A., Koyama, T., and Kijima, K.,** 1977. *MMG report-I, on the mathematical model of ship manoeuvring (in Japanese)*. Bull Soc Naval Archit Jpn, 575, 22–28.
- Oltmann, P.,** 2003. *Identification of hydrodynamic damping derivatives-a pragmatic approach*. In *International conference on marine simulation and ship maneuverability (Marsim '03)*. Kanazawa, Japan.
- Oh, S. R., and Sun, J.,** 2010. *Path following of underactuated marine surface vessels using line-of-sight based model predictive control*. *Ocean Engineering*, 37, 289–295.

- Papoulias, F. A., and Healey, A. J.,** 1992. *Path control of surface ships using sliding modes*. Journal of Ship Research, 36(2), 141–153.
- Park, B. S., Kwon, J. W., and Kim, H.,** 2017. *Neural network-based output feedback control for reference tracking of underactuated surface vessels*. Automatica, 77, 353–359.
- Paroka, D., Kamil, M. F., and Muhammad, A. H.,** 2017. *Experimental study on automatic control for collision avoidance of ships*. Makara Journal of Technology, 21(3), 137–144.
- Patalong, K.,** 2012. *Standard manoeuvres simulation of a fishing vessel*. “Dunărea de Jos” University of Galați.
- Pathan, D. M., Unar, M. A., and Memon, Z. A.,** 2012. *Fuzzy logic trajectory tracking controller for a tanker*. Mehran University Research Journal of Engineering and Technology, 31(2), 315–324.
- Peng, Z., Wang, D., Chen, Z., Hu, X., et al.,** 2013. *Adaptive dynamic surface control for formations of autonomous surface vehicles with uncertain dynamics*. IEEE Transactions on Control Systems Technology, 21(2), 513–519.
- Pereira, A., Das, J., and Sukhatme, G. S.,** 2008. *An experimental study of station keeping on an underactuated ASV*. In *2008 IEEE/RSJ International Conference on Intelligent Robots and Systems*. Nice, France.
- Perera, L. P., Oliveira, P., and Guedes Soares, C.,** 2015. *System identification of nonlinear vessel steering*. Journal of Offshore Mechanics and Arctic Engineering, 137(3), 1–7.
- Perez, T., Smogelif, N., Fossen, T. I., and Sørensen, A. J.,** 2006. *An overview of the marine systems simulator (MSS): a simulink toolbox for marine control systems*. Modeling, Identification and Control, 27(4), 259–275.
- Perez, Tristan, and Blanke, M.,** 2002. *Mathematical ship modeling for control*.
- Pettersen, K. Y., and Fossen, T. I.,** 2000. *Underactuated dynamic positioning of a ship - experimental results*. IEEE Transactions on Control Systems Technology, 8(5), 856–863.
- Pettersen, K. Y., and Nijmeijer, H.,** 2001. *Underactuated ship tracking control: Theory and experiments*. International Journal of Control, 74(14), 1435–1446.
- Piao, Z. J., Guo, C., and Sun, S.,** 2019. *Research into the automatic berthing of underactuated unmanned ships under wind loads based on experiment and numerical analysis*. Journal of Marine Science and Engineering, 7, 1–22.
- Polkinghorne, M. N., Roberts, G. N., and Burns, R. S.,** 1993. *Small marine*

vessel application of a fuzzy PID autopilot. IFAC Proceedings Volumes, 26(2), 1013–1016.

- Qu, Y. H., Pan, Q., and Yan, J. G.,** 2005. *Flight path planning of UAV based on heuristically search and genetic algorithms*. In *31st Annual Conference of IEEE Industrial Electronics Society, 2005. IECON 2005*. Raleigh, NC, USA.
- Rajesh, G., Rajasekhar, G. G., and Bhattacharyya, S. K.,** 2010. *System identification for nonlinear maneuvering of ships using neural network*. Journal of Ship Research, 54(1), 1–14.
- Rindarocoy, M., and Johansen, T. A.,** 2013. *Fuel optimal thrust allocation in dynamic positioning*. In *9th IFAC Conference on Control Applications in Marine Systems*. Osaka, Japan.
- Saari, H., and Djemai, M.,** 2012. *Ship motion control using multi-controller structure*. Ocean Engineering, 55, 184–190.
- Sandurawan, D., Kodikara, N., Keppitiyagama, C., and Rosa, R.,** 2010. *A six degrees of freedom ship simulation system for maritime education*. International Journal on Advances in ICT for Emerging Regions, 3(2), 34–47.
- Serrano, M. E., Scaglia, G. J. E., Godoy, S. A., Mut, V., et al.,** 2014. *Trajectory tracking of underactuated surface vessels: A linear algebra approach*. IEEE Transactions on Control Systems Technology, 22(3), 1103–1111.
- Sharma, S. K., Naeem, W., and Sutton, R.,** 2012. *An autopilot based on a local control network design for an unmanned surface vehicle*. Journal of Navigation, 65(2), 281–301.
- Sharma, S. K., and Sutton, R.,** 2013. *A genetic algorithm based nonlinear guidance and control system for an uninhabited surface vehicle*. Journal of Marine Engineering and Technology, 12(2), 29–40.
- Shen, Z. P., and Wang, R.,** 2018. *Adaptive sliding mode trajectory tracking control of underactuated ship based on DSC-MLP*. Systems Engineering and Electronics, 40(3), 643–651.
- Shenoi, R., Krishnankutty, P., Selvam, P., and Kulshrestha, A.,** 2013. *Prediction of manoeuvring coefficients of a container ship by numerically simulating HPMM using RANSE based solver*. In *Third international conference on ship manoeuvring in shallow and confined water*. Ghent, Belgium.
- Skjetne, R., Fossen, T. I., and Kokotović, P. V.,** 2005. *Adaptive maneuvering, with experiments, for a model ship in a marine control laboratory*. Automatica, 41, 289–298.

- Skjetne, R., Smogeli, Ø. N., and Fossen, T. I.,** 2004. *A nonlinear ship manoeuvring model: identification and adaptive control with experiments for a model ship*. *Modeling, Identification and Control*, 25(1), 3–27.
- Sonnenburg, C., and Woolsey, C. A.,** 2012. *An experimental comparison of two USV trajectory tracking control laws*. In *2012 Oceans*. Hampton Roads, VA, USA.
- Sørensen, A. J.,** 2011. *A survey of dynamic positioning control systems*. *Annual Reviews in Control*, 35, 123–136.
- Sujit, P. B., Saripalli, S., and Sousa, J. B.,** 2014. *Unmanned aerial vehicle path following: a survey and analysis of algorithms for fixed-wing unmanned aerial vehicles*. *IEEE Control Systems Magazine*, 34(1), 42–59.
- Sun, Z. J., Zhang, G. Q., Yi, B. W., and Zhang, W. D.,** 2017. *Practical proportional integral sliding mode control for underactuated surface ships in the fields of marine practice*. *Ocean Engineering*, 142, 217–223.
- Sutulo, S., and Guedes Soares, C.,** 2014. *An algorithm for offline identification of ship manoeuvring mathematical models from free-running tests*. *Ocean Engineering*, 79, 10–25.
- Švec, P., Thakur, A., Raboin, E., Shah, B. C., et al.,** 2014. *Target following with motion prediction for unmanned surface vehicle operating in cluttered environments*. *Autonomous Robots.*, 36(4), 383–405.
- Tee, K. P., and Ge, S. S.,** 2006. *Control of fully actuated ocean surface vessels using a class of feedforward approximators*. *IEEE Transactions on Control Systems Technology*, 14(4), 750–756.
- Teng, Y. X.,** 2020. *Research on mathematical model and dynamic positioning control algorithm of six degrees of freedom maneuvering in marine ships*. *Journal of Intelligent & Fuzzy Systems*, 38, 1299–1309.
- Toxopeus, S.,** 2006. *Calculation of hydrodynamic manoeuvring coefficients using viscous-flow calculations*. In *7th ICHD International Conference on Hydrodynamics*. Ischia, Italia.
- Unar, M. A.,** 1999. *Ship steering control using feedforward neural networks*. University of Glasgow, United Kingdom (PhD thesis).
- Van Amerongen, J., Van Nauta Lemke, H. R., and Van Der Veen, J. C. T.,** 1977. *An autopilot for ships designed by fuzzy sets*. In *Proceedings 5th IFAC/IFIP Conference on Digital Computer Applications to Process, Control*. Hague, Netherlands.
- Vaneck, T. W.,** 1997. *Fuzzy guidance controller for an autonomous boat*. *IEEE Control Systems Magazine*, 17(2), 43–51.

- Velagic, J.**, 2007. *Design of ship controller and ship model based on neural network identification structures*. In *2006 World Automation Congress*. Budapest, Hungary.
- Wagner Smitt, L.**, 1970. *Steering and manoeuvring of ships-full scale and model tests*. *European Shipbuilding*, 6, 86–96.
- Wang, C., Mao, Y. S., Du, K. J., Hu, B. Q., et al.**, 2016. *Simulation on local obstacle avoidance algorithm for unmanned surface vehicle*. *International Journal of Simulation Modelling*, 15(3), 460–472.
- Wang, J., Liu, J. Y., Yi, H., and Wu, N. L.**, 2018. *Adaptive non-strict trajectory tracking control scheme for a fully actuated unmanned surface vehicle*. *Applied Sciences*, 8(4), 1–18.
- Wang, N., and Er, M. J.**, 2016. *Direct adaptive fuzzy tracking control of marine vehicles with fully unknown parametric dynamics and uncertainties*. *IEEE Transactions on Control Systems Technology*, 24(5), 1845–1852.
- Wang, X. F., Zou, Z. J., Li, T. S., and Luo, W. L.**, 2009. *Discrete and analytic model predictive control for path following of underactuated ships*. In *Proceedings of the ASME 2009 28th International Conference on Ocean, Offshore and Arctic Engineering (OMAE 2009)*. Hawaii, USA.
- Wang, X. F., Zou, Z. J., Wang, Y., and Li, T. S.**, 2010. *Path following control of underactuated ships based on unscented Kalman filter*. *Journal of Shanghai Jiaotong University (Science)*, 15(1), 108–113.
- Wang, Y. Y., Chai, S. H., and Nguyen, H. D.**, 2019. *Unscented Kalman Filter trained neural network control design for ship autopilot with experimental and numerical approaches*. *Applied Ocean Research*, 85, 162–172.
- Wang, Y. Y., Chai, S. H., and Nguyen, H. D.**, 2020. *Experimental and numerical study of autopilot using Extended Kalman Filter trained neural networks for surface vessels*. *International Journal of Naval Architecture and Ocean Engineering*, 12, 314–324.
- Wang, Y. Y., Yao, P., and Dou, Y. M.**, 2019. *Monitoring trajectory optimization for unmanned surface vessel in sailboat race*. *Optik*, 176, 394–400.
- Wang, Z. H., Guedes Soares, C., and Zou, Z. J.**, 2020. *Optimal design of excitation signal for identification of nonlinear ship manoeuvring model*. *Ocean Engineering*, 196, 106778.
- Wilhelm, J. P., and Clem, G.**, 2019. *Vector field UAV guidance for path following and obstacle avoidance with minimal deviation*. *Journal of Guidance, Control, and Dynamics*, 42(8), 1848–1856.
- Witkowska, A., Tomera, M., and Śmierczalski, R.**, 2007. *A backstepping approach to ship course control*. *International Journal of Applied*

- Mathematics and Computer Science, 17(1), 73–85.
- Wondergem, M., Lefeber, E., Pettersen, K. Y., and Nijmeijer, H.,** 2011. *Output feedback tracking of ships*. IEEE Transactions on Control Systems Technology, 19(2), 442–448.
- Woo, J., Yu, C., and Kim, N.,** 2019. *Deep reinforcement learning-based controller for path following of an unmanned surface vehicle*. Ocean Engineering, 183, 155–166.
- Wu, P., Xie, S. R., Liu, H. L., Li, M., et al.,** 2017. *Autonomous obstacle avoidance of an unmanned surface vehicle based on cooperative manoeuvring*. Industrial Robot, 44(1), 64–74.
- Xia, G. Q., Wu, H. Y., and Shao, X. C.,** 2014. *Adaptive filtering backstepping for ships steering control without velocity measurements and with input constraints*. Mathematical Problems in Engineering, 2014(3), 1–9.
- Xiang, X., Yu, C., Lapierre, L., Zhang, J., et al.,** 2018. *Survey on fuzzy-logic-based guidance and control of marine surface vehicles and underwater vehicles*. International Journal of Fuzzy Systems, 20(2), 572–586.
- Xie, S. R., Wu, P., Liu, H. L., Yan, P., et al.,** 2016. *A novel method of unmanned surface vehicle autonomous cruise*. Industrial Robot.
- Xing, Z. L., and McCue, L.,** 2010. *Modeling ship equations of roll motion using neural networks*. Naval Engineers Journal, 122(3), 49–60.
- Xu, F., Zou, Z. J., and Yin, J. C.,** 2013. *On-line modeling of ship maneuvering motion based on support vector machines*. Journal of Beijing University of Aeronautics and Astronautics November, 39(11), 1153–1557.
- Xu, H. T., and Guedes Soares, C.,** 2016. *Vector field path following for surface marine vessel and parameter identification based on LS-SVM*. Ocean Engineering, 113, 151–161.
- Yamasaki, K., and Masuda, S.,** 2001. *Application of CFD to the Study of Ship Manoeuvrability on Initial Stage of Hull Design*. Journal of the Society of Naval Architects of Japan, 2001(189), 55–62.
- Yan, X. P., Wang, S. W., Ma, F., Liu, Y. C., et al.,** 2020. *A novel path planning approach for smart cargo ships based on anisotropic fast marching*. Expert Systems with Applications, 159, 113558.
- Yang, L., and Zhang, J. P.,** 2015. *Path following of underactuated surface vessels based on neural sliding mode*. In *2015 IEEE International Conference on Mechatronics and Automation, ICMA 2015*. Beijing, China.
- Yang, T. T., Guo, Y. J., Zhou, Y., and Wei, S. W.,** 2019. *Joint communication and control for small underactuated USV based on mobile computing*

technology. IEEE Access, 7, 160610–160622.

Yang, Y., Du, J. L., Guo, C., and Li, G. Q., 2011. *Trajectory tracking control of nonlinear full actuated ship with disturbances*. In *2011 International Conference of Soft Computing and Pattern Recognition (SoCPaR)* (pp. 318–323).

Yasukawa, H., and Yoshimura, Y., 2015. *Introduction of MMG standard method for ship maneuvering predictions*. *Journal of Marine Science and Technology*, 20(1), 37–52.

Yoshimura, Y., and Ma, N., 2003. *Manoeuvring prediction of fish vessels*. In *International Conference on Marine Simulation and Ship Maneuverability (MARSIM' 03)*. Kanazawa, Japan.

Yu, J. B., Deng, W., Zhao, Z. Y., Wang, X. Y., et al., 2019. *A hybrid path planning method for an unmanned cruise ship in water quality sampling*. IEEE Access, 7, 87127–87140.

Yu, Z. Y., Bao, X. P., and Nonami, K., 2008. *Course keeping control of an autonomous boat using low cost sensors*. *Journal of System Design and Dynamics*, 2(1), 389–400.

Zadeh, L. A., 1965. *Fuzzy sets*. *Information and Control*, 8(3), 338–353.

Zakartchouk, A., and Morishita, H. M., 2009. *A backstepping controller for dynamic positioning of ships: numerical and experimental results for a shuttle tanker model*.

Zhang, G. Q., Deng, Y. J., and Zhang, W. D., 2017. *Robust neural path-following control for underactuated ships with the DVS obstacles avoidance guidance*. *Ocean Engineering*, 143, 198–208.

Zhang, G. Q., Deng, Y. J., Zhang, W. D., and Huang, C. F., 2018. *Novel DVS guidance and path-following control for underactuated ships in presence of multiple static and moving obstacles*. *Ocean Engineering*, 170, 100–110.

Zhang, G. Q., Zhang, C. L., Zhang, X. K., and Deng, Y. J., 2019. *ESO-based path following control for underactuated vehicles with the safety prediction obstacle avoidance mechanism*. *Ocean Engineering*, 188, 106259.

Zhang, G. Q., and Zhang, X. K., 2015. *A novel DVS guidance principle and robust adaptive path-following control for underactuated ships using low frequency gain-learning*. *ISA Transactions*, 56, 75–85.

Zhang, G. Q., and Zhang, X. K., 2017. *Practical robust neural path following control for underactuated marine vessels with actuators uncertainties*. *Asian Journal of Control*, 19(1), 173–187.

Zhang, G. Q., Zhang, X. K., and Guan, W., 2014. *Concise robust adaptive path-*

- following control of underactuated ships using DSC and MLP. *Journal of Harbin Engineering University*, 3(9), 1053–1059.
- Zhang, G. Q., Zhang, X. K., and Zheng, Y. F.**, 2015. *Adaptive neural path-following control for underactuated ships in fields of marine practice*. *Ocean Engineering*, 104, 558–567.
- Zhang, Q., Zhang, X. K., and Im, N. K.**, 2017. *Ship nonlinear-feedback course keeping algorithm based on MMG model driven by bipolar sigmoid function for berthing*. *International Journal of Naval Architecture and Ocean Engineering*, 9(5), 525–536.
- Zhang, R.**, 2017. *The study of 6-DOF motion simulation platform for passenger ship*. In *5th International Conference on Mechatronics, Materials, Chemistry and Computer Engineering (ICMMCCE 2017)*. Chongqing, China.
- Zhang, X. G., and Zou, Z. J.**, 2011. *Identification of Abkowitz model for ship manoeuvring motion using ε -support vector regression*. *Journal of Hydrodynamics*, 23(3), 353–360.
- Zhang, X. G., and Zou, Z. J.**, 2013. *Estimation of the hydrodynamic coefficients from captive model test results by using support vector machines*. *Ocean Engineering*, 73, 25–31.
- Zhang, X. K., Jin, Y. C., and Guo, G.**, 2006. *ANFIS applied to a ship autopilot design*. In *Proceedings of the 2006 International Conference on Machine Learning and Cybernetics*. Dalian, China.
- Zhang, X. K., Zhang, G. Q., and Chen, X. J.**, 2016. *A novel nonlinear feedback control and its application to course-keeping autopilot*. *Journal of Marine Science and Technology (Taiwan)*, 24(2), 192–198.
- Zhang, X. K., Zhang, Q., Ren, H. X., and Yang, G. P.**, 2018. *Linear reduction of backstepping algorithm based on nonlinear decoration for ship course-keeping control system*. *Ocean Engineering*, 147, 1–8.
- Zhao, Y. X., Li, W., and Shi, P.**, 2016. *A real-time collision avoidance learning system for Unmanned Surface Vessels*. *Neurocomputing*, 182, 255–266.
- Zheng, Z. W., Huang, Y. T., Xie, L. H., and Zhu, B.**, 2017. *Adaptive trajectory tracking control of a fully actuated surface vessel with asymmetrically constrained input and output*. *IEEE Transactions on Control Systems Technology*, 26(5), 1851–1859.
- Zheng, Z. W., Jin, C., Zhu, M., and Sun, K. W.**, 2017. *Trajectory tracking control for a marine surface vessel with asymmetric saturation actuators*. *Robotics and Autonomous Systems*, 97, 83–91.
- Zhu, M., Hahn, A., and Wen, Y. Q.**, 2018. *Identification-based controller design*

using cloud model for course-keeping of ships in waves. Engineering Applications of Artificial Intelligence, 75, 22–35.

Zhuang, J. Y., Zhang, L., Zhao, S. Q., Cao, J., et al., 2016. *Radar-based collision avoidance for unmanned surface vehicles. China Ocean Engineering, 30(6), 867–883.*

Zwierzewicz, Z., 2013. *On the ship course-keeping control system design by using robust feedback linearization. Polish Maritime Research, 20(77), 70–76.*

Ship motion control systems

3	Ship motion mathematical models.....	59
3.1	Coordinate systems.....	59
3.1.1	Overview	59
3.1.2	Earth and ship bound coordinate systems.....	60
3.2	Ship mathematical models	62
3.2.1	1 DOF Manoeuvring model.....	62
3.2.2	3 DOF Manoeuvring model.....	63
3.2.3	6 DOF Manoeuvring model.....	66
3.3	Parameter identification methods.....	72
3.3.1	Overview	72
3.3.2	Nonlinear Least Squares method.....	72
3.3.3	Fitting Least Squares method	73
3.3.4	Nonlinear Least Squares Support Vector Machine.....	74
3.3.5	Optimised NLSSVM by BAS method.....	76
3.4	Application of identification methods.....	80
3.4.1	Application on roll motion model	80
3.4.2	Application on ship response model.....	92
3.5	Reference.....	100

He who loves practice without theory is like the sailor who boards ship without a rudder and compass and never knows where he may cast.

-- Leonardo da Vinci

3

Ship motion mathematical models

3.1 Coordinate systems

3.1.1 Overview

The mathematical model of a ship is the basis for the study of ship motion control and the execution of numerical simulations. In manoeuvring, the motion of a marine surface ship is in six degrees of freedom (6 DOF). Table 3.1 and Figure 3.1 depict all six degrees of freedom in a motion of a ship, where three are related to the translational motions: surge, sway, and heave, the other three are associated with the rotational motions: roll, pitch, and yaw.

- **Surge:** longitudinal motion (x direction), usually superimposed on the steady propulsive motion.
- **Sway:** sideways motion (y direction).
- **Heave:** vertical motion (z direction).
- **Roll:** rotation about the longitudinal axis (x axis).
- **Pitch:** rotation about the transverse axis (y axis).
- **Yaw:** rotation about the vertical axis (z axis).

Table 3.1 Notation and sign conventions for ship motion.

DOF	Motions and Rotation Components	Forces and Moments	Positions and Euler angles	Linear and Angular velocities
1	Surge	X	x	u
2	Sway	Y	y	v
3	Heave	Z	z	w
4	Roll	K	φ	p
5	Pitch	M	θ	q
6	Yaw	N	ψ	r

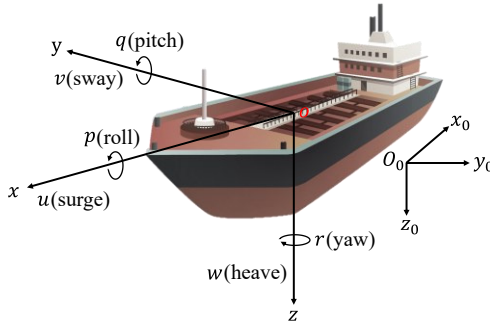


Figure 3.1 Notation and sign conventions for ship motion description.

3.1.2 Earth and ship bound coordinate systems

In order to construct a mathematical model to describe the ship's motions in all 6 degrees of freedom (DOF), two coordinate systems are required, the earth-bound coordinate system $O_0x_0y_0z_0$ and the ship-bound coordinate system $Oxyz$. All axes systems are right handed. The coordinate systems are shown in Figure 3.2.

The earth-bound coordinate system $O_0x_0y_0z_0$ (E-frame) is fixed to earth surface with its axes O_0x_0 , O_0y_0 and O_0z_0 pointing north, east and down of the earth's tangent plane, respectively. The $O_0x_0y_0$ plane coincides with the mean water level. The body-bound coordinate system (b-frame) is $Oxyz$, with its origin on amidships, the x -axis positive to the bow, the y -axis positive starboard, the z -axis positive downwards.

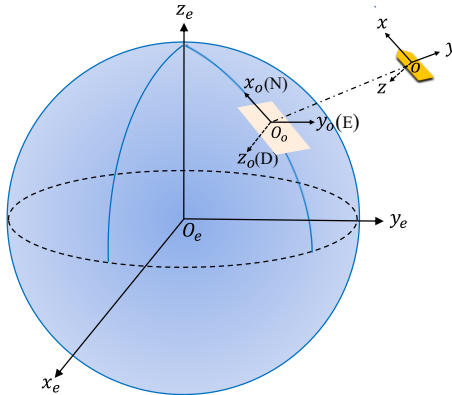


Figure 3.2 Coordinate systems: earth-centered inertial (ECI) coordinate system $O_e x_e y_e z_e$; earth-bound coordinate system $O_0 x_0 y_0 z_0$; body-bound coordinate system $O x y z$.

Figure 3.3 shows the ship-bound and earth-bound coordinate systems in 6 DOF: projections on the x_0y_0 -plane, y_0z_0 -plane and x_0z_0 -plane, where x is the longitudinal coordinate, y is the transverse coordinate, z is the vertical coordinate,

Ψ is the heading angle, φ is the roll angle, θ is the trim angle, u is the surge velocity, v is the sway velocity, w is the heave velocity, p is the roll angular velocity, q is the pitch angular velocity, r is the yaw angular velocity, X is the surge force, Y is the sway force, Z is the heave force, K is the roll moment, M is the pitch moment, N is the yaw moment, n is the propeller rate, δ is the rudder angle, β is the drift angle, CG is the centre of gravity.

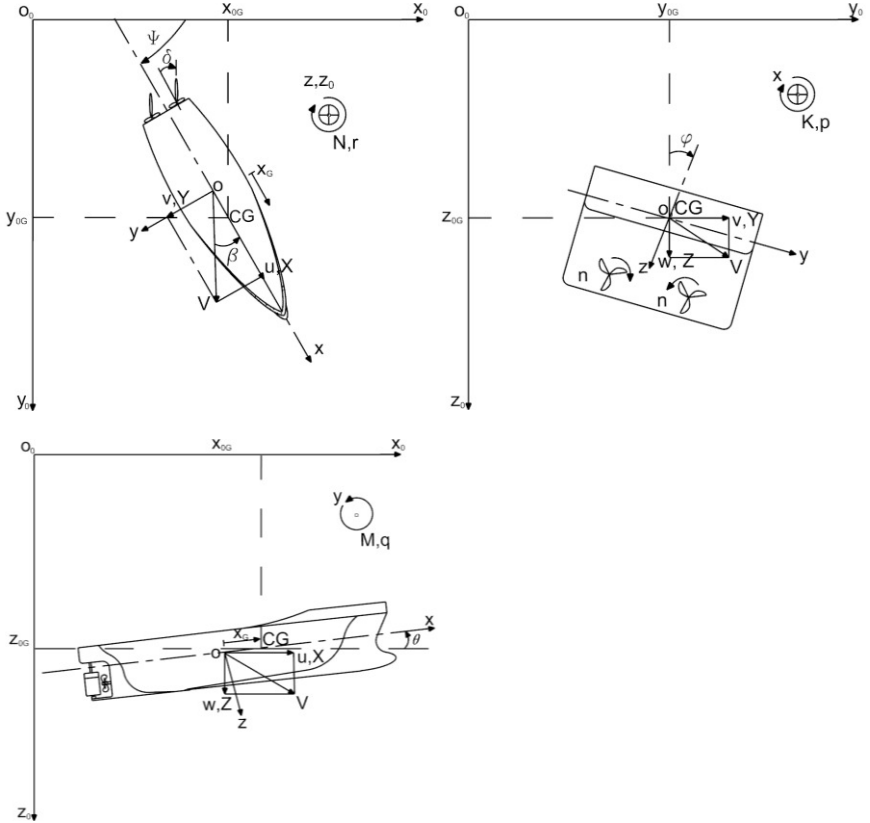


Figure 3.3 Ship bound and earth bound coordinate systems in 6 DOF: projections on the x_0y_0 -plane, y_0z_0 -plane and x_0z_0 -plane.

3.2 Ship mathematical models

3.2.1 1 DOF Manoeuvring model

To design heading autopilots, a simplified ship manoeuvring mathematical model is generally used. The forward speed u is assumed as a constant, and only sway motion v and yaw motion r are considered. The manoeuvring model is written as:

$$M\dot{v} + N(u_0)v = B\delta \quad (3.1)$$

where

$$M = \begin{bmatrix} m - Y_{\dot{v}} & mx_G - Y_{\dot{r}} \\ mx_G - N_{\dot{v}} & I_{zz} - N_{\dot{r}} \end{bmatrix} \quad (3.2)$$

$$v = [v, r]^T \quad (3.3)$$

$$N(u_0) = \begin{bmatrix} -Y_v & mu_0 - Y_r \\ -N_v & mx_G u_0 - N_r \end{bmatrix} \quad (3.4)$$

$$B = \begin{bmatrix} Y_{\delta} \\ N_{\delta} \end{bmatrix} \quad (3.5)$$

where m is the mass of ship; $Y_{\dot{v}}, \dots, N_{\dot{v}}$ refer to the hydrodynamic derivatives; u_0 is the constant forward speed; v is the sway speed; r is the yaw rate; δ is the rudder angle; x_G is the coordinate of the centre of gravity.

A linear model for the ship steering equation is obtained by eliminating the sway velocity from Eq. (3.1), well-known as the 2nd order Nomoto model (Nomoto et al., 1957):

$$T_1 T_2 \ddot{r} + (T_1 + T_2) \dot{r} + r = K\delta + K T_3 \dot{\delta} \quad (3.6)$$

where T_1, T_2 and T_3 are the time constants; K represents the gain.

Application of the Laplace transformation to Eq. (3.6) yields:

$$\frac{r(s)}{\delta(s)} = \frac{K(1 + T_3 s)}{(1 + T_1 s)(1 + T_2 s)} \quad (3.7)$$

where s represents the Laplace operator.

Assume the time constant $T = T_1 + T_2 - T_3$, then the 1st order Nomoto model is obtained as:

$$\frac{r(s)}{\delta(s)} = \frac{K}{(1 + Ts)} \quad (3.8)$$

Eq. (3.8) can be expressed in the form to illustrate the relationship between rudder angle and heading angle, by virtue of $r(s) = s\Psi(s)$:

$$\frac{\Psi(s)}{\delta(s)} = \frac{K}{s(1 + Ts)} \quad (3.9)$$

where Ψ is the heading angle.

The time-domain expression of Eq. (3.9) is written as:

$$T\ddot{\Psi} + \dot{\Psi} = K\delta \quad (3.10)$$

The linear Nomoto model (Eq. (3.10)) is widely applied to design ship course autopilot because the Nomoto model is simple and can reflect the ship's manoeuvring characteristics.

3.2.2 3 DOF Manoeuvring model

3.2.2.1 Overview

For a rigid-body, the dynamic equations of motion are normally split into two parts: 1) *kinematics* is the study of motion without considering the forces that cause motions; 2) *dynamics* relates the action of forces on bodies to their resulting motions (Skjetne et al., 2004).

3.2.2.2 Kinematic equations

The motion of a ship in 3 DOF can be described by the following vectors:

$$\eta = [x, y, \psi]^T \quad (3.11)$$

$$\nu = [u, v, r]^T \quad (3.12)$$

where η represents the position and orientation vectors in the earth-bound coordinate system; ν is the linear and angular velocity vectors in the body-bound coordinate system; x and y are the longitudinal and lateral displacements, respectively; u and v are the velocities of surge and sway, respectively; r is the angular velocity of yaw; ψ is the angle of yaw.

Because the horizontal motion of a ship is described by the surge, sway and yaw motion components, the dynamics related to the motion in heave (w), roll (p) and pitch (q) are neglected, i.e. $w = p = q = 0$. Thus, the rotation matrix used in 3 DOF horizontal plane is:

$$R(\psi) = R_z(\psi)^T = \begin{bmatrix} \cos(\psi) & -\sin(\psi) & 0 \\ \sin(\psi) & \cos(\psi) & 0 \\ 0 & 0 & 1 \end{bmatrix} \quad (3.13)$$

where $R(\cdot)$ and $R_z(\cdot)$ represent the rotation matrices.

The kinematic equations of motion in 3 DOF yields:

$$\dot{\eta} = R(\psi)v \quad (3.14)$$

$$\begin{bmatrix} \dot{x} \\ \dot{y} \\ \dot{\psi} \end{bmatrix} = \begin{bmatrix} \cos(\psi) & -\sin(\psi) & 0 \\ \sin(\psi) & \cos(\psi) & 0 \\ 0 & 0 & 1 \end{bmatrix} \begin{bmatrix} u \\ v \\ r \end{bmatrix} \quad (3.15)$$

The Eq. (3.15) can be rewritten as:

$$\dot{x} = u \cos(\psi) - v \sin(\psi) \quad (3.16)$$

$$\dot{y} = u \sin(\psi) + v \cos(\psi) \quad (3.17)$$

$$\dot{\psi} = r \quad (3.18)$$

3.2.2.3 Equations of motion

The equations of motion for a 3 DOF ship model, used for designing controllers, can be expressed as (Do and Pan, 2009; Fossen, 2011):

$$(M_{RB} + M_A)\dot{v} + (C_{RB}(v) + C_A(v))v + D(v)v = \tau + b \quad (3.19)$$

where M_{RB} is the rigid-body inertia matrix; M_A is the added mass matrix; $C_{RB}(v)$ is the rigid-body Coriolis and centripetal matrix; $C_A(v)$ is the added (hydrodynamic) Coriolis and centripetal matrix; $D(v)$ is the damping matrix; τ represents the control input, forces and moments generated by the propulsion system and the rudder deflection; b refers to the unknown environmental disturbances (e.g. waves, wind and ocean currents, etc).

Assume that the ship is port-starboard symmetric and has homogeneous mass distribution, the centre of gravity of the ship is located at a distance x_G along the x -axis in the b-frame, and $y_G = 0$. Based on the above assumption, the rigid-body inertia matrix M_{RB} can be expressed as:

$$M_{RB} = \begin{bmatrix} m & 0 & 0 \\ 0 & m & mx_G \\ 0 & mx_G & I_{zz} \end{bmatrix} \quad (3.20)$$

where m is the ship mass and I_{zz} is the moment of inertia about the z -axis in the b-frame.

The rigid-body Coriolis and centripetal matrix $C_{RB}(v)$ can be written as:

$$C_{RB}(v) = \begin{bmatrix} 0 & 0 & -m(x_G r + v) \\ 0 & 0 & mu \\ m(x_G r + v) & -mu & 0 \end{bmatrix} \quad (3.21)$$

In an ideal fluid, there are various hydrodynamic effects on the ship, e.g. the added mass, the restoring forces, and the damping (Ejaz and Chen, 2017). In the simplified 3 DOF model, only the major hydrodynamic effects are considered, and the minor effects are neglected. Thus, we can obtain:

$$M_A = \begin{bmatrix} -X_{\dot{u}} & 0 & 0 \\ 0 & -Y_{\dot{v}} & -Y_{\dot{r}} \\ 0 & -N_{\dot{v}} & -N_{\dot{r}} \end{bmatrix} \quad (3.22)$$

$$C_A = \begin{bmatrix} 0 & 0 & Y_{\dot{v}}v + \frac{1}{2}(Y_{\dot{r}} + N_{\dot{v}})r \\ 0 & 0 & -X_{\dot{u}}u \\ -Y_{\dot{v}}v - \frac{1}{2}(Y_{\dot{r}} + N_{\dot{v}})r & X_{\dot{u}}u & 0 \end{bmatrix} \quad (3.23)$$

$$D(v) = \begin{bmatrix} -X_{\dot{u}} - X_{|u|}|u| & 0 & 0 \\ 0 & -Y_v - Y_{|v|}|v| - Y_{|r|}|r| & -Y_r - Y_{|v|}|v| - Y_{|r|}|r| \\ 0 & -N_v - N_{|v|}|v| - N_{|r|}|r| & -N_r - N_{|v|}|v| - N_{|r|}|r| \end{bmatrix} \quad (3.24)$$

where $X_{(\cdot)}$, $Y_{(\cdot)}$ and $N_{(\cdot)}$ refer to the hydrodynamic coefficients.

The control input τ consists of three components: the surge force τ_u , the sway force τ_v and the yaw moment τ_r .

$$\tau = [\tau_u, \tau_v, \tau_r]^T \quad (3.25)$$

The input τ of generalized control forces and moments are associated with the propeller revolutions $n = (n_1, n_2, n_3)$ and rudder angles $\delta = (\delta_1, \delta_2)$ through a nonlinear mapping (Skjetne et al., 2005):

$$\tau = B f_c(v, n, \delta) \quad (3.26)$$

where $B \in R^{3 \times 5}$ is an actuator configuration matrix; $f_c(\cdot)$ represents a function that for each velocity v relates the actuator set-points (n, δ) to a vector of forces. Obtaining the optimal actuator set-points (n, δ) for each commanded force τ is so-called control allocation (Johansen et al., 2005).

Alternatively, Eq. (3.19) can be reformulated as:

$$M\dot{v} + C(v)v + D(v)v = \tau + b \quad (3.27)$$

where M indicates the total mass matrix including rigid-body inertia and hydrodynamic added inertia terms; $C(v)$ is the total Coriolis and centripetal matrix.

$$M = M_{RB} + M_A = \begin{bmatrix} m - X_{\dot{u}} & 0 & 0 \\ 0 & m - Y_{\dot{v}} & mx_G - Y_{\dot{r}} \\ 0 & mx_G - N_{\dot{v}} & I_{zz} - N_{\dot{r}} \end{bmatrix} \quad (3.28)$$

$$C(v) = C_{RB}(v) + C_A = \begin{bmatrix} 0 & 0 & -m(x_C r + v) + Y_{\dot{v}} v + \frac{1}{2}(Y_{\dot{r}}) \\ 0 & 0 & mu - X_{\dot{u}} u \\ m(x_C r + v) - Y_{\dot{v}} v - \frac{1}{2}(Y_{\dot{r}} + N_{\dot{v}}) r & -mu + X_{\dot{u}} u & 0 \end{bmatrix} \quad (3.29)$$

It is worth mentioning that the simplified 3 DOF ship model is widely used to develop the controllers for path following and trajectory tracking.

3.2.3 6 DOF Manoeuvring model

3.2.3.1 Overview

In general, 3 DOF (surge, sway and yaw) or 4 DOF (3 DOF and the roll motion) mathematical models are used to design the autopilots (controllers) for maritime surface ships. In literature, there are rather scarce to adopt the 6 DOF manoeuvring mathematical model, due to the fact that the model is very complex, and a large number of parameters need to be adjusted. However, the 6 DOF model can describe the ship's behaviour in all degrees of freedom more accurately, which is especially suitable for ship manoeuvring simulators. Since the numerical simulations in this research were carried out in a ship manoeuvring simulator, it is necessary to describe the 6 DOF mathematical model used in the simulators.

3.2.3.2 Kinematic equations

The motion of the marine surface ship in 6 DOF can be described by the following vectors (Fossen, 1994, 2011):

$$\eta = [x, y, z, \phi, \theta, \psi]^T \quad (3.30)$$

$$v = [u, v, w, p, q, r]^T \quad (3.31)$$

where η represents the position (x, y, z) and orientation vector (ϕ, θ, ψ) in the earth-bound coordinate system; v is the linear (u, v, w) and angular velocity vector (p, q, r) in the body-bound coordinate system.

The transformation from the body-fixed velocity vector (v) to the earth-fixed position vector ($\dot{\eta}$) can be written as:

$$\dot{\eta} = J(\eta) \cdot v \quad (3.32)$$

where $J(\eta)$ is the transformation matrix.

Eq. (3.32) can be rewritten in component form:

$$\dot{x} = u \cos(\psi) \cos(\theta) + v[\cos(\psi) \sin(\theta) \sin(\phi) - \sin(\psi) \cos(\phi)] + w[\sin(\psi) \sin(\phi) + \cos(\psi) \sin(\theta) \cos(\phi)] \quad (3.33)$$

$$\dot{y} = u \sin(\psi) \cos(\theta) + v[\cos(\psi) \cos(\phi) + \sin(\psi) \sin(\theta) \sin(\phi)] \quad (3.34)$$

$$+w[\sin(\psi) \sin(\theta) \cos(\phi) - \cos(\psi) \sin(\phi)]$$

$$\dot{z} = -u \sin(\theta) + v \cos(\theta) \sin(\phi) + w \cos(\theta) \cos(\phi) \quad (3.35)$$

$$\dot{\phi} = p + q \tan(\theta) \sin(\phi) + r \tan(\theta) \cos(\phi) \quad (3.36)$$

$$\dot{\theta} = q \cos(\phi) - r \sin(\phi) \quad (3.37)$$

$$\dot{\psi} = q \frac{\sin(\phi)}{\cos(\theta)} + r \frac{\cos(\phi)}{\cos(\theta)}, \theta \neq \pm 90^\circ \quad (3.38)$$

3.2.3.3 Equations of motion

In this section, the equations of motion proposed by Delefortrie et al., (2016) is presented. Assume the ship longitudinal plane is symmetrical ($y_G = 0$), the ship's dynamic equations in 6 DOF are formulated as:

$$X = m[\dot{u} - vr + wq - x_G(q^2 + r^2) + z_G(\dot{q} + pr)] \quad (3.39)$$

$$Y = m[\dot{v} + ur - wp + x_G(\dot{r} + pq) + z_G(-\dot{p} + qr)] \quad (3.40)$$

$$Z = m[\dot{w} + uq - vp + x_G(-\dot{q} + pr) - z_G(p^2 + q^2)] \quad (3.41)$$

$$K = -mz_G(\dot{v} + ur - wp) + (I_{xx}\dot{p} - I_{xz}\dot{r}) - I_{xz}pq + (I_{zz} - I_{yy})qr \quad (3.42)$$

$$M = m[-x_G(\dot{w} + vp - uq) + z_G(\dot{u} - vr + wq)] + I_{yy}\dot{q} \\ + (I_{xx} - I_{zz})pr + I_{xz}(p^2 - r^2) \quad (3.43)$$

$$N = mx_G(\dot{v} + ur - wp) + (-I_{xz}\dot{p} + I_{zz}\dot{r}) + I_{xz}qr + (I_{yy} - I_{xx})pq \quad (3.44)$$

where X , Y , and Z are the surge, sway, and heave forces, K , M , and N represent the roll, pitch, and yaw moments; m is the ship mass; u , v , and w are the linear velocities of ship, p , q , and r are the angular velocities of ship; I_{xx} , I_{yy} and I_{zz} are moments of inertia, and I_{xz} is the product of inertia.

The inertia and centrifugal terms are supposedly included with hull forces. Adding the effect of hydrodynamic inertia terms to be modelled, results in the recorded equations:

$$X_{IC} = (X_{\dot{u}} - m)\dot{u} + (X_{\dot{q}} - mz_G)\dot{q} + m(vr - wq) + mx_G(q^2 + r^2) \\ - mz_Gpr \quad (3.45)$$

$$Y_{IC} = (Y_{\dot{v}} - m)\dot{v} + (Y_{\dot{p}} + mz_G)\dot{p} + (Y_{\dot{r}} - mx_G)\dot{r} + m(wp - ur) \\ - mx_Gpq - mz_Gqr \quad (3.46)$$

$$Z_{IC} = (Z_{\dot{w}} - m)\dot{w} + (Z_{\dot{q}} + mx_G)\dot{q} + m(vp - uq) - mx_G pr + mz_G(p^2 + q^2) \quad (3.47)$$

$$K_{IC} = (K_{\dot{v}} + mz_G)\dot{v} + (K_{\dot{p}} - I_{xx})\dot{p} + (K_{\dot{r}} + I_{xz})\dot{r} + I_{xz}pq - (I_{zz} - I_{yy})qr + mz_G(ur - wp) \quad (3.48)$$

$$M_{IC} = (M_{\dot{u}} - mz_G)\dot{u} + (M_{\dot{w}} + mx_G)\dot{w} + (M_{\dot{q}} - I_{yy})\dot{q} - (I_{xx} - I_{zz})pr - I_{xz}(p^2 - r^2) + mx_G(vp - uq) - mz_G(wq - vr) \quad (3.49)$$

$$N_{IC} = (N_{\dot{v}} - mx_G)\dot{v} + (N_{\dot{p}} + I_{xx})\dot{p} + (N_{\dot{r}} - I_{zz})\dot{r} - I_{xz}qr - (I_{yy} - I_{xx})pq - mx_G(ur - wp) \quad (3.50)$$

As mentioned before, various models have been developed for analysis the forces X , Y , and Z and moments K , M , and N (the left hand side of Eqs. (3.45)-(3.50)). This work adopted the MMG model to present a detailed representation of the physical phenomena. The modelling for forces and moments are separated into the effects of the hull, propeller, and rudder:

$$\begin{bmatrix} X \\ Y \\ Z \\ K \\ M \\ N \end{bmatrix} = \begin{bmatrix} X_H + X_P + X_R \\ Y_H + Y_P + Y_R \\ Z_H + Z_P + Z_R \\ K_H + K_P + K_R \\ M_H + M_P + M_R \\ N_H + N_P + N_R \end{bmatrix} \quad (3.51)$$

The subscripts H , P , and R represent the hull, propeller, and rudder effects.

3.2.3.3.1 Hull forces

The effects of the hydrodynamic forces and moments on the hull can be divided into the ideal fluid terms, retardation terms, hydrostatic terms, and additional fluid terms (Tello Ruiz, 2018).

The ship's squat shows retardation during acceleration of the ship model. The retardation (*ret*) terms are presented for heave and pitch only by:

$$Z_{ret} = Z_{\dot{u}}\dot{u} + Z_{\dot{v}}|\dot{v}| + Z_{\dot{r}}|\dot{r}| \quad (3.52)$$

$$M_{ret} = M_{\dot{v}}|\dot{v}| + M_{\dot{r}}|\dot{r}| \quad (3.53)$$

It should be mentioned that the other degrees of freedom did not include retardation in Delefortrie et al., (2016). $M_{\dot{u}}$ is already included in Eq. (3.49) but is expected to have implicit retardation.

Assume the vertical motions are small, the hydrostatic (*hyd*) equilibrium in the vertical degrees of freedom is obtained by:

$$Z_{hyd} = -\rho g A_w z \quad (3.54)$$

$$K_{hyd} = -\Delta \overline{GM}_T \phi \quad (3.55)$$

$$M_{hyd} = -\Delta \overline{GM}_L \theta \quad (3.56)$$

Consequently, the models using tabular functions for the total hydrodynamic forces on ship's hull can be expressed as:

$$\begin{aligned} X_H = X_{IC} + \frac{1}{2} \rho L_{PP} T_M (u^2 + v^2) X^{(\beta)} + \frac{1}{2} \rho L_{PP} T_M \left(u^2 + \left(\frac{1}{2} r L_{PP} \right)^2 \right) X^{(\gamma)} \\ + \frac{1}{2} \rho L_{PP} T_M \left(v^2 + \left(\frac{1}{2} r L_{PP} \right)^2 \right) X^{(\chi)} \end{aligned} \quad (3.57)$$

$$\begin{aligned} Y_H = Y_{IC} + \frac{1}{2} \rho L_{PP} T_M (u^2 + v^2) Y^{(\beta)} + \frac{1}{2} \rho L_{PP} T_M \left(u^2 + \left(\frac{1}{2} r L_{PP} \right)^2 \right) Y^{(\gamma)} \\ + \frac{1}{2} \rho L_{PP} T_M \left(v^2 + \left(\frac{1}{2} r L_{PP} \right)^2 \right) Y^{(\chi)} \end{aligned} \quad (3.58)$$

$$\begin{aligned} Z_H = Z_{IC} + Z_{ret} + Z_{hyd} + \Delta T_{u_h} Z^{(\beta)} + \frac{1}{2} \rho L_{PP} T_M \left(u^2 + \left(\frac{1}{2} r L_{PP} \right)^2 \right) Z^{(\gamma)} \\ + \frac{1}{2} \rho L_{PP} T_M \left(v^2 + \left(\frac{1}{2} r L_{PP} \right)^2 \right) Z^{(\chi)} + Z_w w + Z_q q \end{aligned} \quad (3.59)$$

$$\begin{aligned} K_H = K_{IC} + K_{hyd} + K_p p + K_{up} u p - \left(|\phi| \sqrt{\Delta \overline{GM}_T (-K_p + I_{xx})} \right) p \\ + \frac{1}{2} \rho L_{PP} T_M^2 (u^2 + v^2) K^{(\beta)} + \frac{1}{2} \rho L_{PP} T_M^2 \left(u^2 + \left(\frac{1}{2} r L_{PP} \right)^2 \right) K^{(\gamma)} \\ + \frac{1}{2} \rho L_{PP} T_M^2 \left(v^2 + \left(\frac{1}{2} r L_{PP} \right)^2 \right) K^{(\chi)} \end{aligned} \quad (3.60)$$

$$\begin{aligned} M_H = M_{IC} + M_{ret} + M_{hyd} + M_w w + M_q q + \Delta L_{PP} T_{u_h} M^{(\beta)} + \frac{1}{2} \rho L_{PP} T_M^2 \cdot \\ \left(u^2 + \left(\frac{1}{2} r L_{PP} \right)^2 \right) M^{(\gamma)} + \frac{1}{2} \rho L_{PP} T_M^2 \left(v^2 + \left(\frac{1}{2} r L_{PP} \right)^2 \right) M^{(\chi)} \end{aligned} \quad (3.61)$$

$$\begin{aligned} N_H = N_{IC} + \frac{1}{2} \rho L_{PP} T_M^2 (u^2 + v^2) N^{(\beta)} + \frac{1}{2} \rho L_{PP} T_M^2 \left(u^2 + \left(\frac{1}{2} r L_{PP} \right)^2 \right) N^{(\gamma)} \\ + \frac{1}{2} \rho L_{PP} T_M^2 \left(v^2 + \left(\frac{1}{2} r L_{PP} \right)^2 \right) N^{(\chi)} \end{aligned} \quad (3.62)$$

where ρ , L_{PP} , T_M are the water density, the ship's length, the ship's draft; u, v, w represent the surge, sway and heave velocities in the body-bound coordinate system; p, q, r are the roll, pitch and yaw angular velocities in the body-bound

coordinate system. The coefficients $X^{(\beta)}$ to $N^{(\chi)}$ in Eq. (3.57) to Eq. (3.62) are the tabular functions, they are given as function of the hydrodynamic angles:

$$\beta = \text{atan}\left(\frac{-v}{u}\right) \quad (3.63)$$

$$\gamma = \text{atan}\left(\frac{rL_{PP}/2}{u}\right) \quad (3.64)$$

$$\chi = \text{atan}\left(\frac{rL_{PP}/2}{v}\right) \quad (3.65)$$

where β, γ, χ indicate the drift, yaw, and yaw-drift correlation angles.

The heave force (Z_H) and pitch force (M_H) are also given as function of the Tuck parameter (Tuck, 1966):

$$Tu_h = \frac{Fr_h}{\sqrt{1 - Fr_h^2}} \quad (3.66)$$

where Fr_h is the depth-related Froude number, which is expressed as:

$$Fr_h = \frac{V}{\sqrt{gh}} \quad (3.67)$$

where V is the ship's speed; g is the gravity acceleration; h is the water depth.

3.2.3.3.2 Propeller induced forces

The longitudinal force induced by the propeller action can be expressed as a function of a thrust deduction factor:

$$X_P = (1 - t(\varepsilon^*, \phi^*, \gamma^*))T_P \quad (3.68)$$

The thrust deduction fraction t is defined as a function of propeller loading angles ($\varepsilon^*, \phi^*, \gamma^*$):

$$t = f(\varepsilon^*) + q_1(\varepsilon^*)\phi^*\xi_1 + q_3(\varepsilon^*)\phi^*\xi_3 + q_4(\varepsilon^*)\phi^*\xi_4 \quad (3.69)$$

where ε^* is the hydrodynamic advance angle; ϕ^* and γ^* are given as:

$$\phi^* = \text{atan}\left(\frac{|v|}{0.7\pi n D_P}\right) \quad (3.70)$$

$$\gamma^* = \text{atan}\left(\frac{|rL_{PP}/2|}{0.7\pi n D_P}\right) \quad (3.71)$$

The terms $q_j(\varepsilon^*)$ are equal to one in quadrant j and equal to zero in the other quadrants.

The propeller induced forces and moments in other degrees of freedom are given as:

$$Y_P = \left| \frac{n}{n_{max}} \right| (Y_{\dot{v}}^n \dot{v} + Y_{\dot{r}}^n \dot{r}) + K_1 T_P (Y_{PT}(\beta, \varepsilon^*) + Y_{PT}(\gamma, \varepsilon^*)) + K_2 T_P Y_{PTA} \cos(\omega(\varepsilon^*)t + \phi_Y(\varepsilon^*)) \quad (3.72)$$

$$Z_P = K_3 T_P (Z_{PT}(\beta, \varepsilon^*) + Z_{PT}(\gamma, \varepsilon^*)) + K_2 T_P Z_{PTA} \cos(\omega(\varepsilon^*)t + \phi_Z(\varepsilon^*)) \quad (3.73)$$

$$K_P = \left| \frac{n}{n_{max}} \right| (K_{\dot{v}}^n \dot{v} + K_{\dot{r}}^n \dot{r}) + T_M T_P (K_{PT}(\beta, \varepsilon^*) + K_{PT}(\gamma, \varepsilon^*)) + K_2 T_M T_P K_{PTA} \cos(\omega(\varepsilon^*)t + \phi_K(\varepsilon^*)) \quad (3.74)$$

$$M_P = L_{PP} T_P (M_{PT}(\beta, \varepsilon^*) + M_{PT}(\gamma, \varepsilon^*)) + K_2 L_{PP} T_P M_{PTA} \cos(\omega(\varepsilon^*)t + \phi_M(\varepsilon^*)) \quad (3.75)$$

$$N_P = \left| \frac{n}{n_{max}} \right| (N_{\dot{v}}^n \dot{v} + N_{\dot{r}}^n \dot{r}) + L_{PP} T_P (N_{PT}(\beta, \varepsilon^*) + N_{PT}(\gamma, \varepsilon^*)) + K_2 L_{PP} T_P N_{PTA} \cos(\omega(\varepsilon^*)t + \phi_N(\varepsilon^*)) \quad (3.76)$$

where $T_P, Y_{PTA}, Z_{PTA}, K_{PTA}, M_{PTA}, N_{PTA}$ are all functions of ε^* .

3.2.3.3.3 Rudder induced forces

The rudder induced forces on the hull can be obtained by:

$$X_R = F_X \quad (3.77)$$

$$Y_R = (1 + a_H(\varepsilon^*, \beta)) F_Y \quad (3.78)$$

$$Z_R = 0 \quad (3.79)$$

$$K_R = -(z_R + a_H(\varepsilon^*, \beta) z_H(\beta)) F_Y \quad (3.80)$$

$$M_R = z_{HX}(\beta) F_X \quad (3.81)$$

$$N_R = (x_R + a_H(\varepsilon^*, \beta) x_H(\beta)) F_Y \quad (3.82)$$

The longitudinal force induced by the rudder can be directly transferred to the ship's longitudinal force. The sway force and moments rely on the rudder forces and the extra asymmetries induced by the hull. The heave force is not affected by the rudder action.

3.3 Parameter identification methods

3.3.1 Overview

The manoeuvring mathematical model of a ship is fundamental for simulating the ship's motions and designing the ship's controllers. Accurate identification of the ship model's linear and nonlinear parameters has become the key research issue in the fields of system identification and numerical simulations. In present work, a novel Nonlinear Least Squares-Support Vector Machine (NLSSVM) is introduced to identify unknown parameters of the ship's models (Chen, et al., 2019a). It is a new generation machine learning method and can accurately identify model parameters by means of the radial basis function (RBF) kernel. Compared with other intelligent approaches, using large samples of data to estimate unknown parameters, the NLSSVM only depends on limited support vectors based on small samples. Besides, the structure risk minimization theory instead of empirical risk minimization is adopted by the NLSSVM to solve optimisation problems. A global optimisation result is obtained, and local optimisation issues are avoided. Thus, the NLSSVM approach is used to identify the ship's model parameters in this work.

In order to demonstrate the characteristics of the NLSSVM algorithm, traditional methods, such as Nonlinear Least Squares (NLS) and Fitting Least Squares (FLS) algorithms are considered for comparisons (Stigler, 1981). These algorithms will be elaborated in the following sections.

3.3.2 Nonlinear Least Squares method

The Nonlinear Least Squares algorithm has been considered as one of the most common methods used to identify unknown parameters before intelligent methods appeared, because of its simple structure and high accuracy (Merriman, 1877). The NLS method is proposed based on the experience risk minimization theory.

Assume a system with multiple input and single output:

$$Y = \theta_p X, (X \in R^m, Y \in R) \quad (3.83)$$

where X represents the input samples; Y refers to the output sample; θ_p is the unknown model parameters; m indicates the dimension of the input samples.

The estimated parameters can be calculated by:

$$\hat{\theta}_p = X^{-1}Y \quad (3.84)$$

The corresponding error can be derived by:

$$\varepsilon = Y - \hat{\theta}_p X \quad (3.85)$$

Then the objective is to obtain the set of unknown parameters through minimizing the error ε . The object function J is given as:

$$J = \sum_{i=1}^n \varepsilon_i^2 = \varepsilon^T \varepsilon \tag{3.86}$$

where n denotes the number of samples.

In order to minimize the object function, Eq. (3.86) is partially differentiated and the result is set as zero:

$$\left. \frac{\partial J}{\partial \theta_p} \right|_{\theta_p = \hat{\theta}_p} = \frac{\partial}{\partial \theta_p} (Y - \hat{\theta}_p X)^T (Y - \hat{\theta}_p X) = -2X^T Y + 2X^T X \hat{\theta}_p = 0 \tag{3.87}$$

Finally, the parameters can be obtained by solving the equation:

$$\hat{\theta}_p = (X^T X)^{-1} X^T Y \tag{3.88}$$

The detailed procedure is presented in Figure 3.4.

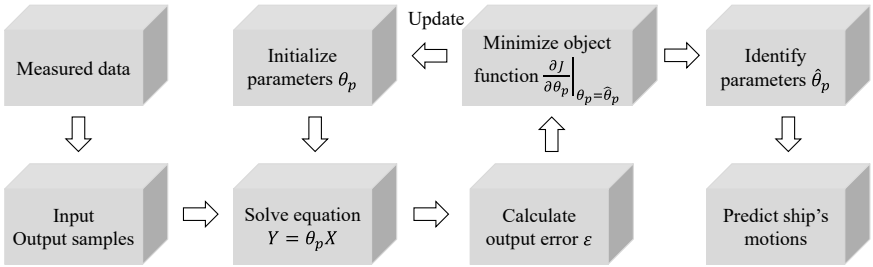


Figure 3.4 Nonlinear least squares (NLS) system identification method.

3.3.3 Fitting Least Squares method

Apart from the NLS, the Fitting Least Squares (FLS) algorithm has also been successfully applied for system identification (Merriman, 1877). The main difference is that in the FLS approach the curve fitting (e.g. Fourier fitting) is first applied to the measured data, then a basic least squares algorithm is applied to identify the unknown parameters. For better illustration purposes, Figure 3.5 sketches the detailed process.

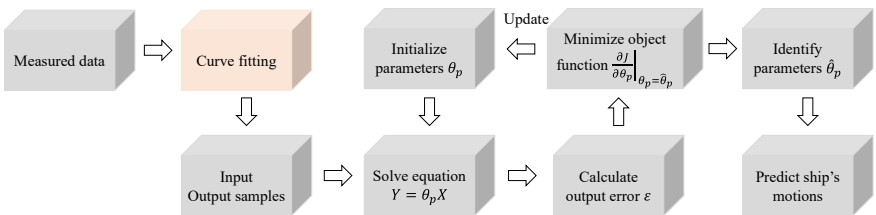


Figure 3.5 Fitting least squares (FLS) system identification method.

3.3.4 Nonlinear Least Squares Support Vector Machine

3.3.4.1 Problem statement

Assume that a parametric system in state-form is available as follows:

$$\frac{dX}{dt} = g(X, T, \theta_p) \quad (3.89)$$

where $X = [x_1, x_2, \dots, x_i]^T$ is the state variable, $\frac{dX}{dt} = \left[\frac{d}{dt} x_1, \frac{d}{dt} x_2, \dots, \frac{d}{dt} x_i \right]^T$ are the derivatives of each state variable, $T = [t_1, t_2, \dots, t_i]^T$ is the time variable, $\theta_p = [\theta_{p1}, \theta_{p2}, \dots, \theta_{pi}]^T$ is an unknown set of parameters.

For the parametric system, the main goal is to identify the unknown parameters θ_p from observed data $Y = [y_1, y_2, \dots, y_i]^T$ at time variable $T = [t_1, t_2, \dots, t_i]^T$.

$$e_i = Y(t_i) - X(t_i), i = 1, 2 \dots n \quad (3.90)$$

where $e_i = [e_1, e_2, \dots, e_i]^T$ is error between the observed data Y and the outputs of the estimated state variable X . The final goal is shifted to get the set of unknown parameters by minimizing the error e_i .

3.3.4.2 Identification procedure

Step 1: Obtain sample data

Sample data $\{(t_i, y_i), i = 1, 2, \dots, n\}$ can be obtained from full scale measurements, model tests or numerical simulations. The sample data is divided into the training data and the testing data in order to train the model and to validate the effectiveness of the identified parameters.

Step 2: Approximate the state variable

Approximate the state variable X based on the sample data $\{(t_i, y_i), i = 1, 2, \dots, n\}$. The k -th state variable x_k is given by:

$$\hat{x}_k(t) = w_k^T \varphi(t) + b_k \quad (3.91)$$

where t is the input data, \hat{x}_k is the output data, w is the weight value, $\varphi(\cdot)$ is the nonlinear function mapping the input data t to the Euclidean space, and b_k is the bias.

To solve the convex optimization problem according to the minimization of structure risk theory (David et al., 2013), the following cost function needs to be solved:

$$\min_{w, b, e} f(w, e) = \frac{1}{2} w^T w + \frac{1}{2} \gamma \|e_i\|_2^2 \quad (3.92)$$

subject to:

$$y_i = w^T \varphi(t_i) + b + e_i \quad (3.93)$$

where $i = 1, 2, \dots, n$, γ is the penalty factor, and e_i is the error.

The optimization problem is solved by the Lagrangian function defined as:

$$L(w, b, e, a) = \frac{1}{2} w^T w + \frac{1}{2} \gamma \|e_i\|_2^2 - \sum_{i=1}^n a_i [w^T \varphi(t_i) + b + e_i - y_i] \quad (3.94)$$

where a_i is the Lagrange multiplier. The optimal conditions can be obtained by partially differentiating with respect to w, b, e, a :

$$\frac{\partial L}{\partial w} = 0 \rightarrow w = \sum_{i=1}^n a_i \varphi(t_i) \quad (3.95)$$

$$\frac{\partial L}{\partial b} = 0 \rightarrow \sum_{i=1}^n a_i = 0 \quad (3.96)$$

$$\frac{\partial L}{\partial e_i} = 0 \rightarrow a_i = \gamma e_i \quad (3.97)$$

$$\frac{\partial L}{\partial a_i} = 0 \rightarrow w^T \varphi(t_i) + b + e_i - y_i = 0 \quad (3.98)$$

Subsequently, the variables w and e_i are eliminated from Eq. (3.95) to Eq. (3.98), and the kernel trick is employed for working in high-dimensional feature spaces without explicit computations on them (David et al., 2013). Finally, the regression model can be expressed as:

$$\hat{x}_k(t) = w_k^T \varphi(t) + b_k = \sum_{i=1}^n \alpha_i^k K(t_i, t) + b_k \quad (3.99)$$

where $K(t_i, t) = \varphi(t_i) \varphi(t)$ is the kernel function.

Step 3: Approximate the derivative of the state variable

Differentiating $\hat{x}_k(t)$ in Eq. (3.99) with respect to time, yields:

$$\hat{\dot{x}}_k(t) = w_k^T \dot{\varphi}(t) = \sum_{i=1}^n \alpha_i^k \varphi(t_i)^T \dot{\varphi}(t) \quad (3.100)$$

According to Mercer's Theorem (Steinwart and Scovel, 2012), the derivative of the kernel is equal to the derivative of the feature (Mehrkanoon et al., 2012):

$$K_1(t_i, t) = \frac{\partial K(t_i, t)}{\partial t} = \varphi(t_i)^T \dot{\varphi}(t) \quad (3.101)$$

Thus, introducing Eq. (3.101) in Eq. (3.100), the latter can be rewritten as:

$$\hat{x}_k(t) = \sum_{i=1}^n \alpha_i^k K_1(t_i, t) \quad (3.102)$$

Step 4: Identify the unknown parameters

After obtaining the approximated values of the k -th state variable $\hat{x}_k(t)$ and its derivative and $\hat{\dot{x}}_k(t)$ in Eq. (3.99) and Eq. (3.102), all the state variables \hat{X} and their time derivatives $\hat{\dot{X}}$ can be obtained by using the above same procedure.

Finally, substituting \hat{X} and $\hat{\dot{X}}$ in the parametric system Eq. (3.89), the unknown parameters can be obtained by solving the optimization problem:

$$\min_{\theta_p} \frac{1}{2} \sum_i^n \|e_i\|_2^2 \quad (3.103)$$

subject to:

$$e_i = \hat{X} - f(\hat{X}(t_i), T, \theta_p), i = 1, 2, \dots, n \quad (3.104)$$

3.3.5 Optimised NLSSVM by BAS method

To further improve the performance of the NLSSVM method, a new optimization approach called Beetle Antennae Search (BAS) algorithm is introduced and applied to optimize the penalty factor γ in Eq. (3.92) of the NLSSVM model, and the kernel parameter σ . The BAS method is an efficient meta-heuristic optimization algorithm (Jiang and Li, 2018), which is similar to other intelligent optimization algorithms such as Particle Swarm Optimization (PSO) and Cross Validation (CV) (Hegazy et al., 2015). However, the BAS algorithm has more advantages, such as a simpler structure, a shorter computational time and superior optimization ability with higher accuracy (Chen et al., 2019b). Therefore, the BAS optimization algorithm is selected and adopted in this work.

In order to obtain the optimal parameter values in the NLSSVM model, an objective function is defined as:

$$f(x) = RMSE(\mu) \quad (3.105)$$

where $x = [\gamma; \sigma]$ is the position matrix of beetle at each penalty factor γ and the RBF kernel parameter σ ; μ is the state variable. The $f(x)$ is the concentration of odor (fitness function), which is defined as the Root Mean Square Error (RMSE) of the state variable μ .

The goal is to obtain optimal penalty factor γ and RBF kernel parameter σ by minimizing RMSE when $x_{best} = [\gamma_{best}; \sigma_{best}]$ is selected in the following form:

$$f_{best}(x_{best}) = \min RMSE(\mu) \quad (3.106)$$

When employing the BAS algorithm to optimize the NLSSVM model parameters, two different processes are defined: a). the parameter search, and b). the parameter detection according to the value of the fitness function. These steps are better illustrated in Figure 3.6 and discussed in more detail in the following subsections.

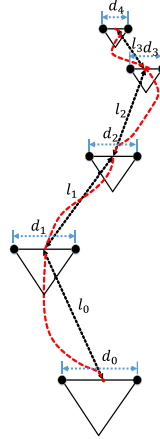


Figure 3.6 Beetle Antennae Search (BAS) optimization trajectory: d_i represents the distance between two antennae; l_i is the iterative step length.

Parameter search

In the first process, the BAS algorithm's parameters including the beetle's initial position $x_0 = [\gamma_0; \sigma_0]$, the distance between two antennae d_0 and the initial step length l_0 are initialized. At the beginning, a randomly generated initial position x_0 is regarded as the best position x_{best} , which is used to calculate the best fitness f_{best} . Additionally, the searching direction of the beetle is assumed to be random and expressed as:

$$\vec{D} = \frac{rands(n,1)}{\|rands(n,1)\|} \quad (3.107)$$

where \vec{D} is the random searching direction. $rands(\cdot)$ represents the random function, and n is denoted as the searching space dimensions, in this case $n = 2$.

Subsequently, the left antennae and the right antennae coordinates of the beetle are assigned as x_l and x_r respectively. x^t is defined as the beetle's centroid coordinate at time t . Then, two antennae coordinates are calculated by the form of:

$$x_l = x^t + d^t \vec{D} \quad (3.108)$$

$$x_r = x^t - d^t \vec{D} \quad (3.109)$$

where d is the distance between two antennae. Then, the left and right antennae coordinate x_l and x_r are substituted in the fitness function Eq. (3.105) as follows:

$$f_l = f(x_l) = RMSE_l(r_{error}) \quad (3.110)$$

$$f_r = f(x_r) = RMSE_r(r_{error}) \quad (3.111)$$

Parameter detection

After the beetle's search parameters, the parameter detection is formulated by setting an iterative system (see Figure 3.6).

If $f_l \leq f_r$, the beetle will search toward the left direction with the step length l . The beetle's centroid coordinate is updated at time t as:

$$x^t = x^{t-1} + l^t \vec{D}_l \quad (3.112)$$

If $f_l \geq f_r$, the beetle will search toward the right direction with the step length l . The beetle's centroid coordinate is updated at time t as:

$$x^t = x^{t-1} - l^t \vec{D}_r \quad (3.113)$$

Therefore, according to the iterative model, the state variables (see Eq. (3.112) and Eq. (3.113)), are rewritten as:

$$x^t = x^{t-1} + l^t \vec{D} \text{sign}(f(x_l) - f(x_r)) \quad (3.114)$$

where $\text{sign}(\cdot)$ is the sign function.

After the state variable x^t is updated, the fitness value $f(x^t)$ at time t is obtained. $f(x^t)$ is then compared with the memorized $f_{best}(x_{best})$ to update the best state variable x_{best} and minimum fitness value f_{best} .

$$\begin{cases} f_{best} = f(x^t) \\ x_{best} = x^t \end{cases}, f_{best} \geq f(x^t) \quad (3.115)$$

It is worth mentioning that the update rules of searching parameters d and l are described as:

$$l^t = c_1 l^{t-1} + l_0 \quad (3.116)$$

$$d^t = l^t / c_2 \quad (3.117)$$

where c_1 and c_2 are attenuation coefficients, which are normally assigned as 0.95.

Finally, the processes of parameter search and parameter detection are circularly executed until ending iterations with minimum RMSE. The NLSSVM-BAS regression process is displayed in Figure 3.7.

3.4 Application of identification methods

3.4.1 Application on roll motion model

3.4.1.1 Overview

Roll motion is one of the most critical responses the ship experiences in her lifespan. An accurate prediction of roll motion in real scenarios is then deemed necessary so to understand better the ship behaviour and to avoid any hazardous condition. The damping components of a roll model play a key role in properly predicting the ship's roll response. The estimation of these parameters is, however, difficult because of their nonlinear characteristics as a result of their viscous and fiction dependency. An efficient approach to obtain accurately the damping terms is still absent, especially in the estimation of the nonlinear term and to avoid parameter drifting.

In order to accurately identify the ship's roll model parameters and solve the problems of difficult estimating nonlinear damping coefficients by traditional methods, the NLSSVM is used. To illustrate the validity and applicability of the proposed method, simulation and decay tests data are combined and utilized to estimate unknown parameters and predict the roll motions. Firstly, simulation data is applied in the NLSSVM model to obtain estimated damping parameters, compared with pre-defined parameters to verify the validity of the proposed method. In order to illustrate the advantages of the proposed NLSSVM method, free decay model test data are used in identifying unknown parameters, and comparisons between the proposed method and traditional methods are presented. Finally, to show the application potentials of the proposed method in shallow water, experimental data from various speeds and Under Keel Clearances (UKCs) are applied to identify the damping coefficients.

3.4.1.2 Ship roll motion model

In a sense, an accurate definition and prediction of damping parameters (especially nonlinear damping coefficients) in the ship roll model is a very necessary task. On the basis of the rigid body theory, the 1 DOF roll motion model can be written as:

$$(I_{xx} + A_{44}^{\infty})\ddot{\phi} + B(\dot{\phi}) + C_{44}\phi = 0 \quad (3.118)$$

where I_{xx} is the mass moment of inertia, A_{44}^{∞} is the added mass moment of inertia (at infinite frequency), $B(\cdot)$ is the moment due to the damping phenomena, C_{44} is the roll restoring coefficient, and ϕ is the roll angle. The single dotted and double dotted variables represent the first and second order derivatives.

The total damping coefficients are divided into a linear ($b_{\dot{\phi}}$), a nonlinear ($b_{\dot{\phi}|\dot{\phi}|}$) (Himeno, 1981; Ikeda et al., 1977), and a potential contribution component in the following form:

$$B(\dot{\phi}) = b_{\dot{\phi}}\dot{\phi} + b_{\dot{\phi}|\dot{\phi}}|\dot{\phi}| + \int_{-\infty}^{+\infty} h_{44}(t - \tau)\dot{\phi}(\tau)d\tau \tag{3.119}$$

where $\dot{\phi}$ is the roll rate and h_{44} is the Impulse Response Function (IRF). Substituting $B(\dot{\phi})$ into Eq. (3.118), the final model in the time domain is expressed as follows:

$$(I_{xx} + A_{44}^{\infty})\ddot{\phi} + b_{\dot{\phi}}\dot{\phi} + b_{\dot{\phi}|\dot{\phi}}|\dot{\phi}| + \int_{-\infty}^{+\infty} h_{44}(t - \tau)\dot{\phi}(\tau)d\tau + C_{44}\phi = 0 \tag{3.120}$$

3.4.1.3 Experimental program

3.4.1.3.1 Ship model

A 1/90 scale model of Ultra Large Container Vessel (ULCV) was chosen to carry out free roll decay tests (Tello Ruiz, 2018). Model tests were carried out at the Towing Tank for Manoeuvres in Confined Water (co-operation Flanders Hydraulics Research and Ghent University) in Antwerp, Belgium. The main particulars and cross-sectional view of the ship model are shown in the Table 3.2 and Figure 3.8.

Table 3.2 Main particulars of model scale and full scale for the Ultra Large Container Vessel (ULCV).

Items	Model scale (1/90)		Full scale	
	Value	Units	Value	Units
L_{OA}	4.418	m	397.6	m
L_{PP}	4.191	m	377.2	m
B	0.627	m	56.4	m
D	0.330	m	29.7	m
T_M	0.145	m	13.1	m
m	226.4	kg	165046	ton
C_b	0.6	-	0.6	-

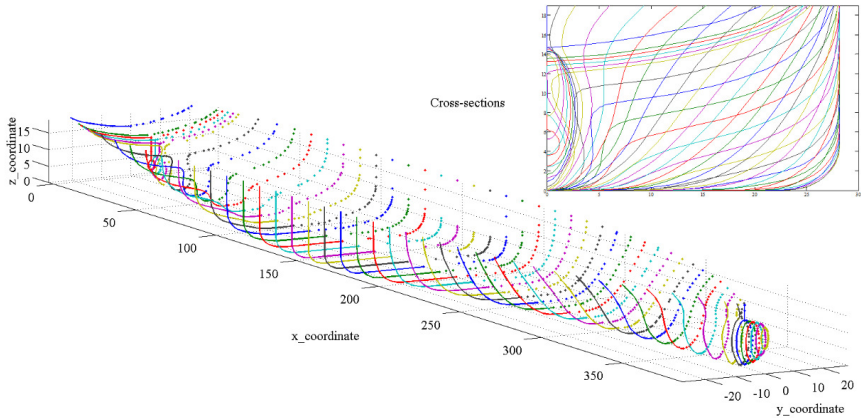


Figure 3.8 Cross-sectional view of the Ultra Large Container Vessel (ULCV).

3.4.1.3.2 Free decay tests

Free decay tests were performed by providing an initial roll angle for the ship model. Then, the ship model was held at this initial position until the towing carriage reached its desired speed and immediately released by pulling the cord attached to a wooden stick. An illustration of the model test setup and mechanism is displayed in Figure 3.9.



Figure 3.9 Model test setup and mechanism of free decay tests.

Free decay model tests were carried out at different UKCs (from 10% to 190% UKCs) and speeds (from 0 to 12 knots). In present study, the experimental data obtained from the UKCs of 10%, 20%, 35%, 190% and the speeds at 0, 3, 6, 9, 12 knots are selected as study cases. The initial roll angles at the chosen conditions are presented in Table 3.3 and Figure 3.10.

Table 3.3 Initial roll angles at different speeds and UKCs.

UKCs	Speeds (knots)				
	0	3	6	9	12
10% UKC (deg)	2.21	1.60	1.89	1.54	1.77
20% UKC (deg)	2.70	3.04	2.71	3.51	2.74
35% UKC (deg)	3.11	3.32	3.27	2.68	1.95
190% UKC (deg)	6.96	6.66	6.45	5.69	6.23

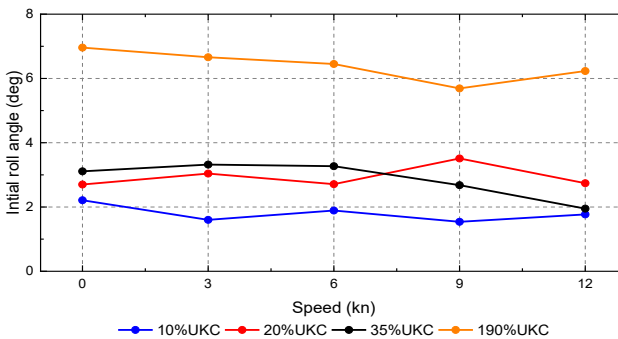


Figure 3.10 The initial roll angles at different speeds for 10%UKC (blue line), 20%UKC (red line), 35%UKC (black line), 190%UKC (orange line).

3.4.1.4 Parameter identification procedure

Taking into consideration of the parameters estimation method in section 3.3.4, the NLSSVM approach is introduced to estimate the linear ($b_{\dot{\phi}}$) and nonlinear ($b_{\phi|\dot{\phi}}$) viscous damping parameters in the nonlinear roll model (Eq. (3.120)). The identification processes are, in more detail, described in Table 3.4 and Figure 3.11.

Table 3.4 Identification processes of the NLSSVM algorithm for the roll model.

Parameter identification using the NLSSVM method for the roll model
1. Obtain the sample data $\{(t_i, \phi_i), i = 1, 2, \dots, n\}$ based on numerical simulation tests or free decay tests. where t_i is the time series and ϕ_i is the roll angles.
2. Estimate the trajectory of the roll angle ϕ (the state variable) by using the NLSSVM model, Eq. (3.99).
3. Differentiate the NLSSVM predicting model with respect to time, Eq. (3.102); And the closed-form approximation for the first ($\dot{\phi}$) and second ($\ddot{\phi}$) derivatives of the state variable are obtained, respectively.
4. Identify the linear ($b_{\dot{\phi}}$) and nonlinear ($b_{\phi \dot{\phi}}$) viscous damping coefficients by solving the optimisation problem in Eq. (3.103).
5. Substitute the identified linear and nonlinear viscous damping coefficients in the roll model, Eq. (3.120). After applying a fourth-order Runge-Kutta approach to solve the ship's roll response equation Eq. (3.120), the ship roll motions are predicted.

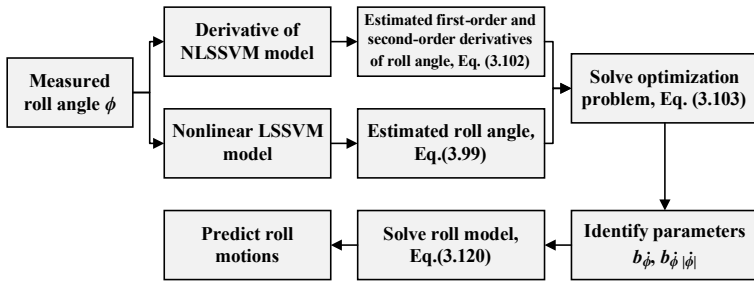


Figure 3.11 Identification process of NLSSVM for the roll model.

3.4.1.5 Effectiveness of NLSSVM method

To investigate the effectiveness of the NLSSVM method, in this subsection, the roll motions with known linear ($b_{\dot{\phi}}$) and nonlinear ($b_{\phi|\dot{\phi}}$) viscous damping coefficients (Table 3.5) are selected to simulate a free roll decay test. The known linear and nonlinear damping parameters are substituted into the roll model, Eq. (3.120). It is worth noting that other parameters in Eq. (3.120) are regarded as known values, which can be found in Tello Ruiz, (2018). Using the Runge-Kutta approach to solve the differential equation, the simulated roll angles (sample data) are obtained.

Subsequently, simulated sample data are divided into two sets, the first set as a training sample (blue circles) is used to train the NLSSVM model and the second set as a test sample (green circles) is selected to test the model. The results are displayed in Figure 3.12.

After the NLSSVM model being trained, unknown damping coefficients are identified by the proposed model and are shown in Table 3.5. Comparing the identified parameters with the known parameters, the results show that the relative errors of the linear ($b_{\dot{\phi}}$) and nonlinear ($b_{\dot{\phi}|\dot{\phi}|}$) viscous damping coefficients are about 0.33% and 1.00%, respectively. These very small errors reveal that the NLSSVM approach can accurately identify unknown parameters and can be well applied in identifying the roll model.

Furthermore, the identified damping parameters are used to predict the roll motions and compared against the sample data. Satisfactory agreement between predicted values and original values can be found in Figure 3.13, with maximum errors between predicted values and original values of around 0.001 deg. This illustrates the potential of the NLSSVM as it performs well with high prediction accuracy. Therefore, the novel NLSSVM algorithm can be applied in identifying the ship roll model.

Table 3.5 Known parameters and identified parameters using the NLSSVM approach.

Parameters	Known	Identified	Error (%)
$b_{\dot{\phi}}$ ($\text{kgm}^2/\text{s}, 10^8$)	6.0	6.02	0.33
$b_{\dot{\phi} \dot{\phi} }$ ($\text{kgm}^2, 10^7$)	4.0	4.04	1.00

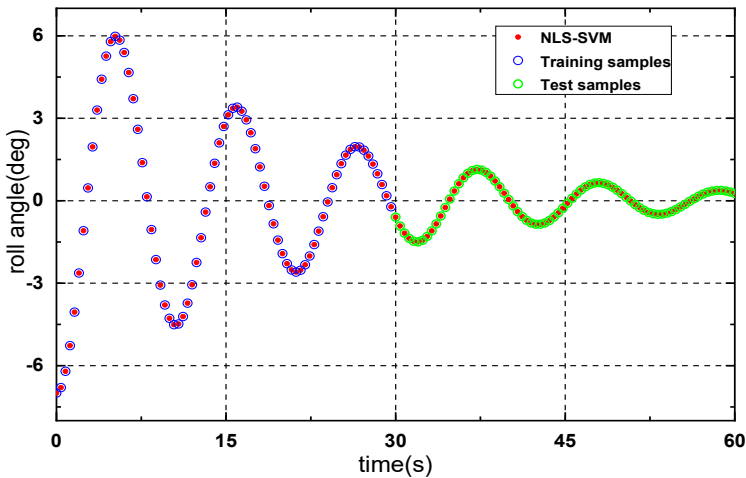


Figure 3.12 Train and test roll angles with known damping coefficients using NLSSVM method at 190% UKC.

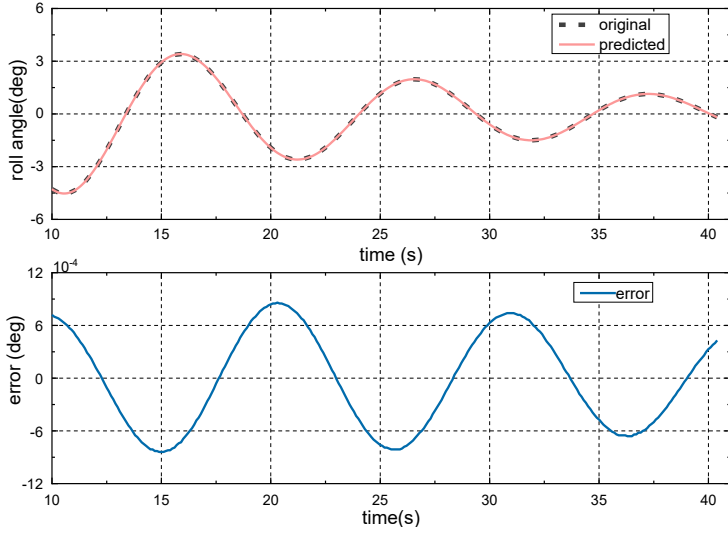


Figure 3.13 Predicted roll angles and errors with known damping coefficients using NLSSVM method at 190% UKC.

3.4.1.6 Comparison with different identification methods

In order to illustrate the advantages of the NLSSVM algorithm, traditional methods, such as Nonlinear Least Squares (NLS) and Fitting Least Squares (FLS) algorithms are selected for comparisons. The process of NLS and FLS methods for identifying the roll model are shown in Figure 3.14 and Figure 3.15.

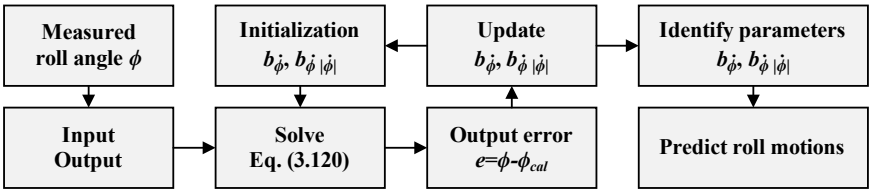


Figure 3.14 Nonlinear Least Squares (NLS) identification method for the roll model.

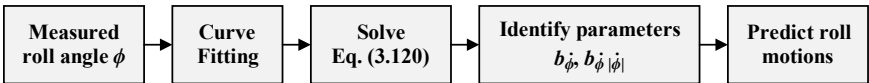


Figure 3.15 Fitting Least Squares (FLS) identification method for the roll model.

Aiming at comparing the performance of the three identification approaches, three evaluation indexes are selected: the Mean Absolute Error (MAE), the Root Mean Square Error (RMSE), and the Computational time (CPU time). The MAE is employed to assess the performance of the model; the RMSE is utilized to measure

the accuracy of the model; the CPU time is represented as calculation time. The MAE and the RMSE are, respectively given by:

$$MAE = \frac{\sum_{i=1}^n |\phi_i - \hat{\phi}_i|}{n} \quad (3.121)$$

$$RMSE = \sqrt{\frac{\sum_{i=1}^n (\phi_i - \hat{\phi}_i)^2}{n}} \quad (3.122)$$

In this case study, the free decay tests data at the speed of 12 knots and the UKC of 20% are presented as an example. The parameters of the roll model are identified by the NLS, FLS, and NLSSVM method, respectively, and their comparisons can be found in Table 3.6. From the results, it can be seen that the linear damping coefficient ($b_{\dot{\phi}}$) can be identified by all methods within the same magnitude (10^9). The nonlinear term, however, has some discrepancies, the traditional NLS method estimates a magnitude of $b_{\dot{\phi}|\dot{\phi}|}$ which is around 100 times smaller than the other two approaches. The latter draws the main attention to consider the use of an intelligent method, the NLSSVM, for improving the performance in practice.

Moreover, the MAE is around 0.0405 deg for the NLSSVM model, which decreased by 27.9% from 0.0562 deg for the NLS model and by 17.2% from 0.0489 deg for the FLS model, respectively. For accuracy analysis, the RMSE (0.0502 deg) of the NLSSVM is reduced by 20.6% (0.0632 deg) compared to the NLS model and by 17.4% (0.0608 deg) compared to the FLS model, which demonstrates that the NLSSVM model's errors are smaller, and the accuracy is higher than traditional methods. Moreover, comparing the CPU times, less time is taken by the proposed model.

Table 3.6 Comparisons of identification results among NLS, FLS and NLSSVM identification methods.

Parameters	Methods		
	NLS	FLS	NLSSVM
$b_{\dot{\phi}}$ (kgm ² /s, 10 ⁹)	3.30	3.43	3.38
$b_{\dot{\phi} \dot{\phi} }$ (kgm ² , 10 ⁷)	0.0493	5.14	3.55
MAE (deg, 10 ⁻²)	5.62	4.89	4.05
RMSE (deg, 10 ⁻²)	6.32	6.08	5.02
CPU time (s)	97	13	12

$$\text{error} = \phi_{\text{known}} - \phi_{\text{pred}} \quad (3.123)$$

Subsequently, the identified linear and nonlinear damping coefficients are employed to predict the ship's roll motions separately. The predicted results and errors (Eq. (3.123)) are presented in Figure 3.16 and Figure 3.17, respectively. From Figure 3.16, there are small but not significant deviations between the original data and predicted data for the three identification approaches. It is noted that the predicted values by the NLSSVM method are closer to the original values

than the other two approaches. Furthermore, the overall errors of the NLSSVM model in Figure 3.17 are smaller than that of NLS and FLS methods.

The analysed results demonstrate that the new NLSSVM model has better identification performance and time saving ability as well as higher accuracy compared to traditional algorithms. The advantages of the NLSSVM are validated.

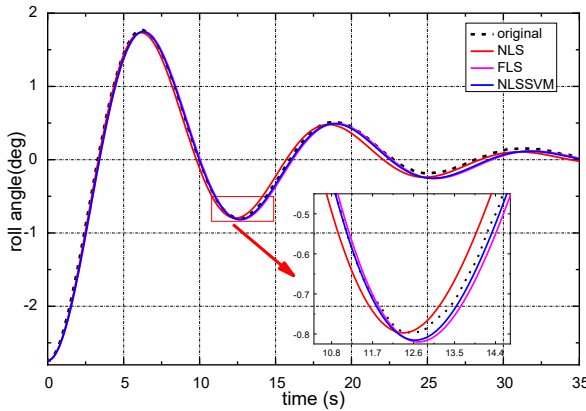


Figure 3.16 Predicted roll angles using NLS, FLS, NLSSVM approaches.

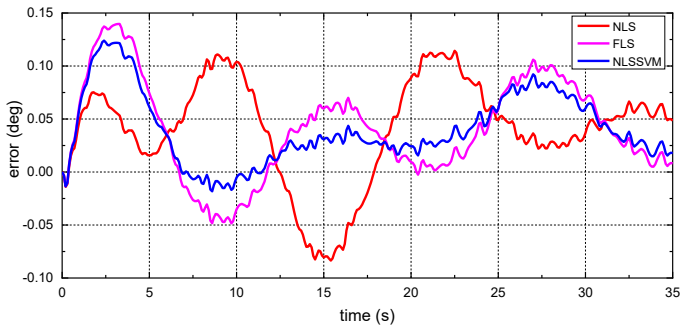


Figure 3.17 Predicted roll angle errors using NLS, FLS, NLSSVM approaches

3.4.1.7 Applicability analysis of NLSSVM

3.4.1.7.1 Applicability analysis for different UKCs

Considering the effect of water depth on the damping coefficients, the different UKCs (10%, 20%, 35% and 190% UKCs) at a speed of 6 knots are considered as case studies. After the NLSSVM model being trained by the decay tests data in different UKCs, Table 3.7 presents a quantitative comparison of the identified results. It is noted that the MAE (around 0.015-0.051 deg) and the RMSE (the values around 0.017-0.073 deg) are pretty small, and computational time is very short (10-20 s), which reveal furtherly good generality and applicability of the NLSSVM model both in shallow water and deep water.

Table 3.7 Comparisons identification results for different UKCs at a speed of 6 knots.

Parameters	UKC (6 knots)			
	10% UKC	20% UKC	35% UKC	190% UKC
$b_{\dot{\phi}}$ (kgm ² /s, 10 ⁹)	2.56	1.97	1.70	0.95
$b_{\phi \dot{\phi}}$ (kgm ² , 10 ⁷)	2.58	3.01	3.26	4.03
MAE (deg, 10 ⁻²)	1.51	1.77	1.24	5.10
RMSE (deg, 10 ⁻²)	1.70	2.23	1.43	7.29
CPU time (s)	15	15	11	18

To have a better idea of the effect of the UKCs, substituting the identified parameters in the roll model, Eq. (3.120), the ship’s roll motion for different UKCs are predicted. The results are displayed in Figure 3.18 to Figure 3.21, for 10%, 20%, 35% and 190% UKC, respectively. In Figure 3.18 to Figure 3.21 it can be observed that the predicted roll angles agree well with the experiments for all tests and that the maximum errors for all UKCs are about 0.30 (at 10% UKC), 0.06 (at 20% UKC), 0.02 (at 35% UKC) and 0.20 (at 190% UKC) deg. Note that the larger error is obtained when a smaller initial roll angle is chosen (see 10% UKC). The latter can be associated to the model formulation needed to satisfy such magnitudes and not of the identification method itself. In spite of the relative larger errors obtained for the lower UKC the overall results show that the NLSSVM method can successfully be used to identify parameters of the roll model in the shallow and deep water with small errors.

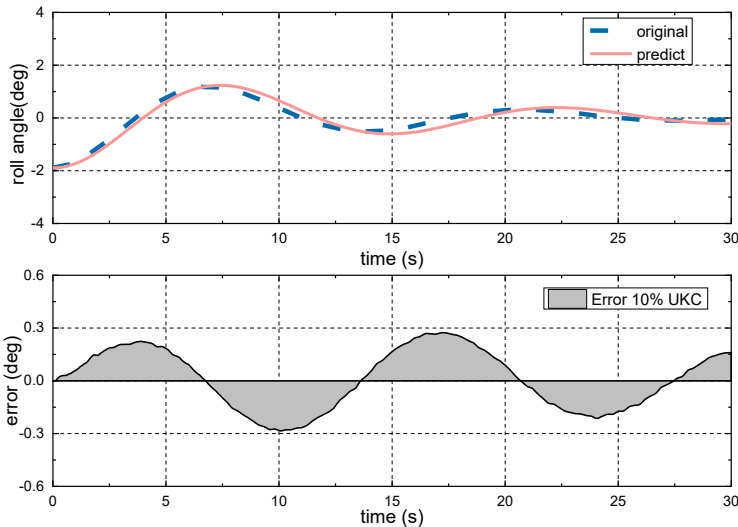


Figure 3.18 Predicted roll angles and errors for 10% UKC.

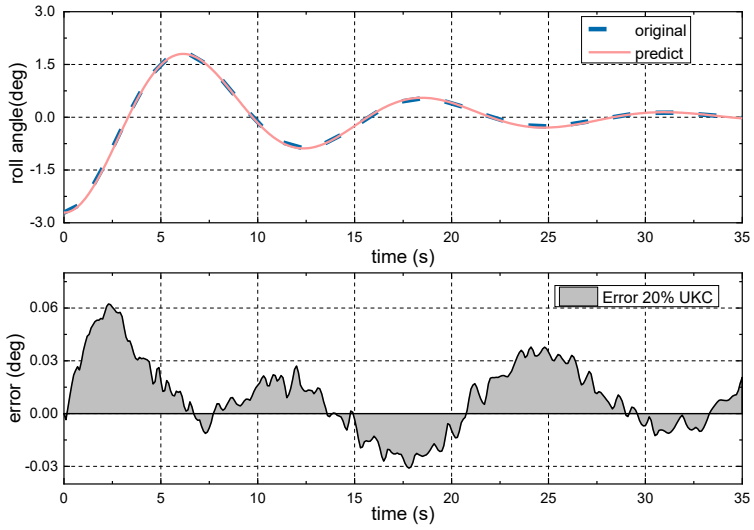


Figure 3.19 Predicted roll angles and errors for 20% UKC.

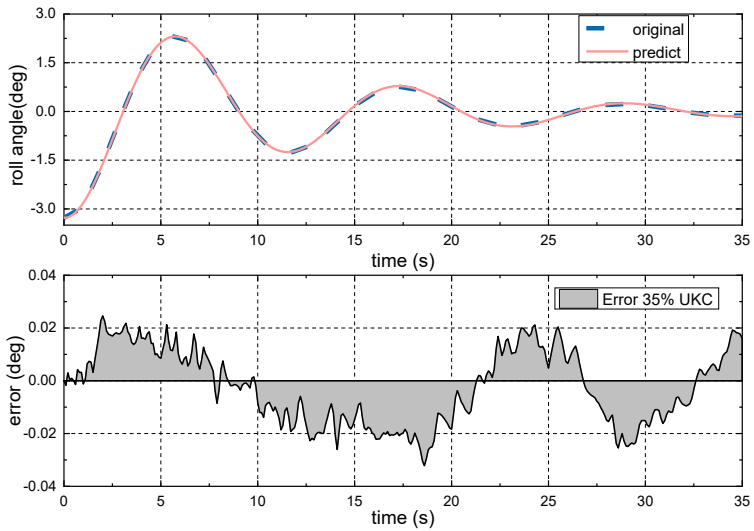


Figure 3.20 Predicted roll angles and errors for 35% UKC.

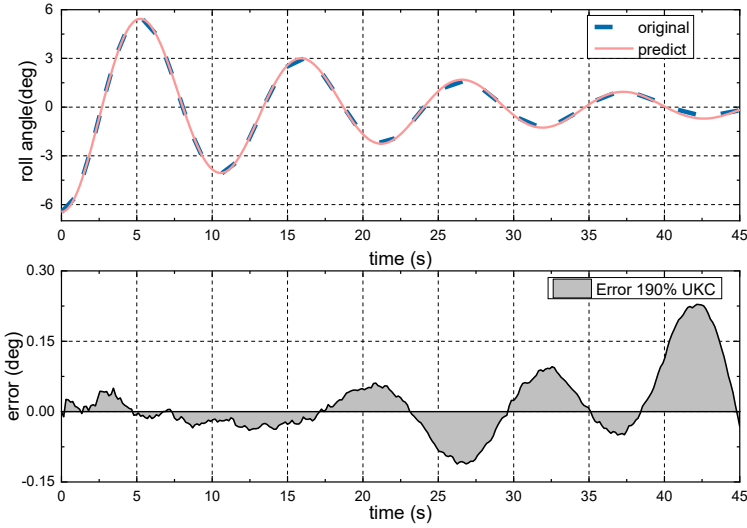


Figure 3.21 Predicted roll angles and errors for 190% UKC.

3.4.1.7.2 Applicability analysis for different speeds

Similarly, the applicability in shallow water (20% UKC) at different speeds is investigated. The experimental data at 0 to 12 knots are taken as examples to train the NLSSVM model and to identify the unknown linear and nonlinear damping coefficients at different speeds. The identified results are shown in Table 3.8. The RMSE is around 0.0185 to 0.0891 deg, whose values are speed dependent. Moreover, the MAE at different speeds are with small values about 0.0185 to 0.0739 deg. For the CPU time, they are around 15 to 17 s. It can be seen that the three evolution indexes are very small. After quantitative comparison, it can be concluded that the NLSSVM model has good applicability in shallow water at different speeds.

Table 3.8 Comparisons identification results for different speeds (20% UKC).

Parameters	Speed (knots)				
	0	3	6	9	12
$b_{\dot{\phi}}$ (kgm ² /s, 10 ⁹)	1.93	1.94	1.97	2.84	3.38
$b_{\phi \dot{\phi}}$ (kgm ² , 10 ⁷)	2.66	2.93	3.01	3.45	3.55
MAE (deg, 10 ⁻²)	1.85	1.92	1.77	7.39	4.05
RMSE (deg, 10 ⁻²)	1.85	2.20	2.23	8.91	5.02
CPU time (s)	15	17	15	17	15

Furthermore, the predicted results in shallow water at speeds of 0, 6, 12 knots are obtained in Figure 3.22 to Figure 3.24. It can be observed that the predicted values have satisfactory agreement with the original data at different speeds. The predicted roll angles at a speed of 12 knots are a little bit higher than the original ones, but the predicted results are still valid, because the overall errors are very

small and the effect on the ship is not significant. Thus, the effectiveness and applicability of the NLSSVM approach applied in shallow water at different speeds are verified.

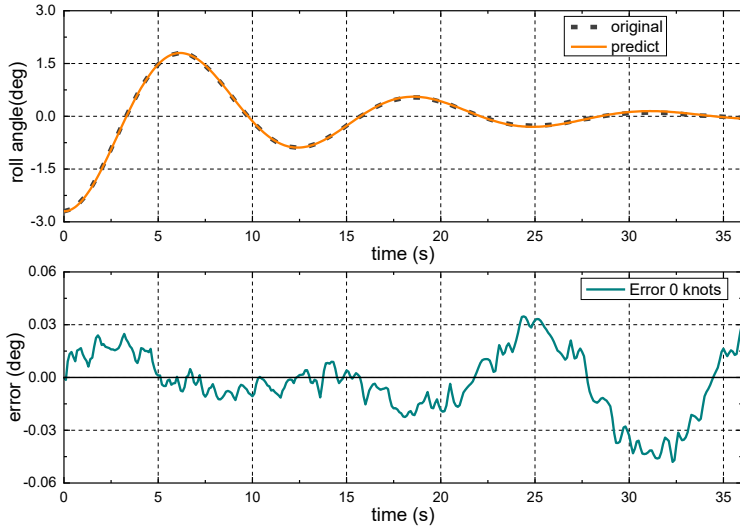


Figure 3.22 Predicted roll angles and errors at 0 knots.

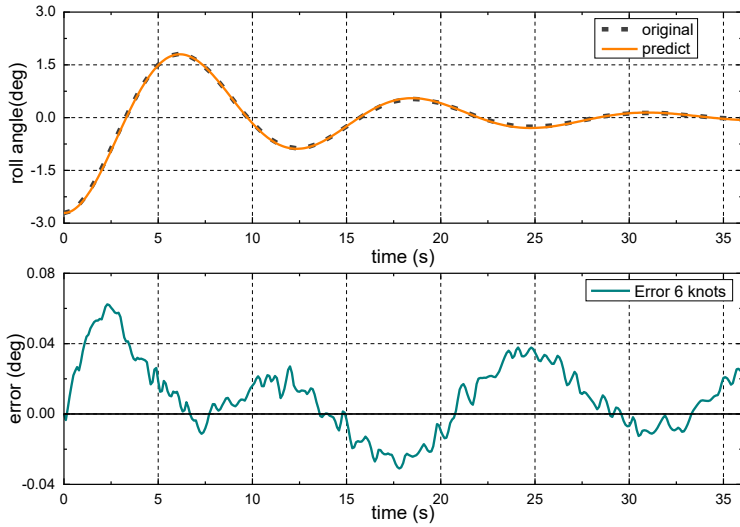


Figure 3.23 Predicted roll angles and errors at 6 knots.

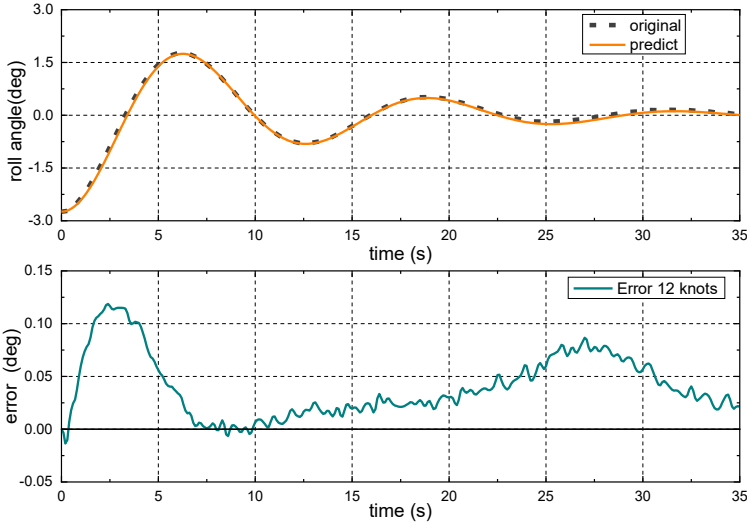


Figure 3.24 Predicted roll angles and errors at 12 knots.

To summarize, the novel NLSSVM parameter identification approach for estimating unknown damping coefficients in shallow water is investigated in this section. Firstly, comparisons between numerical simulation roll angles based on the known damping coefficients and predicted roll angles using estimated damping coefficients present satisfactory agreement (section 3.4.1.5), which illustrate the proposed identification algorithm can be effectively applied in identifying the roll model. Subsequently, comparing traditional identification approaches (NLS and FLS) with the intelligent method (section 3.4.1.6), the NLSSVM algorithm can perform better with higher accuracy, and overcome the weakness of conventional methods for identifying nonlinear damping coefficients. Moreover, free decay tests data in different UKCs and speeds were prepared for the purpose of demonstrating the shallow water effect in parametric identification based on the NLSSVM method (section 3.4.1.7). The good agreement between decay tests results and predicted results suggests the satisfactory applicability of the proposed algorithm in shallow water. Therefore, the effectiveness, accuracy, and applicability of the NLSSVM model applied in identifying the nonlinear roll model in shallow water, have been verified by qualitative and quantitative analysis.

3.4.2 Application on ship response model

3.4.2.1 Overview

In order to investigate the accuracy and applicability of the optimised NLSSVM by the BAS algorithm (section 3.3.5), the approach is utilized to identify a ship motion model. Firstly, numerical simulations and experimental data are collected for parameter identification. Then, the optimized NLSSVM-BAS is applied to identify the linear and nonlinear parameters for the ship nonlinear response model.

Finally, the accuracy and validity of the NLSSVM-BAS are investigated by comparing the original data with predicted data.

3.4.2.2 Ship nonlinear response model

According to Eq. (3.8), the well-known 1st order linear Nomoto model is expressed as (Nomoto et al., 1957):

$$T\dot{r} + r = K\delta \quad (3.124)$$

where T is the time constant, K is the gain, r is the yaw rate, and δ is the rudder angle.

Including a static nonlinearity in the 1st order linear Nomoto model, the following nonlinear form is obtained:

$$T\dot{r} + r + ar^3 = K\delta \quad (3.125)$$

where a is the nonlinear constant.

3.4.2.3 Parameter identification by NLSSVM-BAS method

3.4.2.3.1 Optimise parameters by BAS algorithm

In this subsection, the BAS optimisation algorithm described in section 3.3.5 is adopted to search for the optimal penalty factor and kernel parameter of the NLSSVM model. In the optimisation process, the RMSE of the ship yaw rate is assigned as the objective function (Eq. (3.105)). Then, global optimal parameters are found by the BAS optimisation algorithm.

Figure 3.25 and Figure 3.26 present the optimisation trajectories of the beetle searching in two-dimensional (2D) and three-dimensional (3D) space. It can be seen that the beetle gradually moves to the optimal parameters point and quickly converges to the optimal value. Moreover, the convergence curve is found in Figure 3.27, it can be seen that the convergence rate of the fitness (objective function) is very fast, and the minimum value of the objective function is obtained after around 40 iterations. The optimisation results illustrate that the BAS algorithm has excellent optimisation ability and can quickly provide optimal parameters for the NLSSVM model.

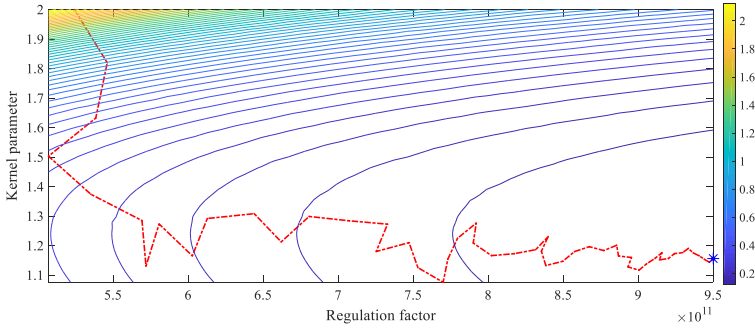


Figure 3.25 Optimisation trajectories of the beetle searching in 2D space.

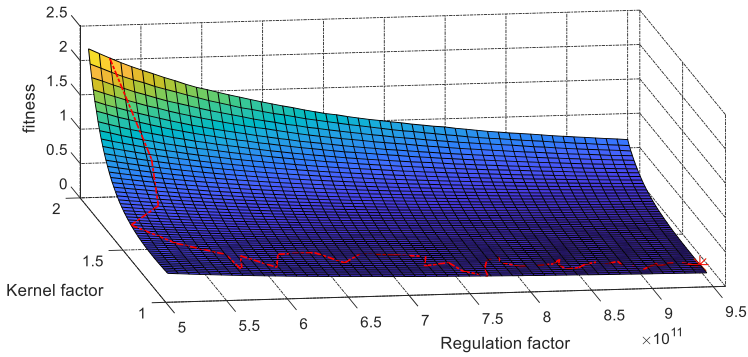


Figure 3.26 Optimisation trajectories of the beetle searching in 3D space.

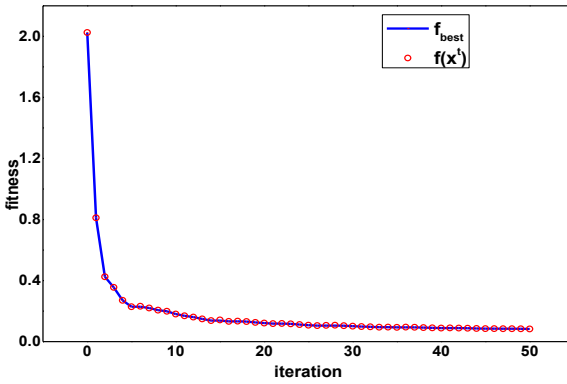


Figure 3.27 Convergence curve of parametric optimisation.

3.4.2.3.2 Effectiveness and accuracy of NLSSVM-BAS algorithm

In this section, the first-order nonlinear Nomoto model Eq. (3.125) is selected as a case study. The validation process in detail is as follows:

The first step is to generate sample data and identify unknown parameters. The sample data are generated based on $20^\circ/20^\circ$ zigzag test using a 1/37.89 scale model of the KRISO Container Ship (KCS) in the MARIN towing tank (SIMMAN, 2014). The three parameters of the 1st order nonlinear Nomoto model including time constant (T), gain (K) and nonlinear constant (a) are pre-defined as the known values. Then, the fourth-order Runge-Kutta algorithm is used to solve the Nomoto mathematical model, and training sample data are obtained. Subsequently, the NLSSVM-BAS is employed to identify the parameters of the Nomoto model. The results are displayed in Table 3.9. By comparing the predefined parameters with the identified parameters, small errors are observed with values of 0.6% for the time constant T , 0.1% for the gain K and 1.1% for the nonlinear constant a . It means that the proposed approach can successfully identify the nonlinear Nomoto model with high accuracy.

Table 3.9 Pre-defined parameters and identified parameters using the NLSSVM-BAS model

Parameters	Known	Identified	Error (%)
T (s)	66.0	66.38	0.6
K (1/s)	0.10	0.10	0.1
a (s ² /deg ²)	1.00	0.99	1.1

Furthermore, the identified parameters are applied to predict the ship yaw rates (Figure 3.28). It is easily seen that the predicted values of the ship yaw rate agree well with the actual values with only small deviations. It is worth noting that the maximum error between predicted data and actual data is around 0.01 deg/s, which illustrates that the predicted results match well with the simulation results with high precision. After qualitative and quantitative analysis, the effectiveness and accuracy of the NLSSVM-BAS model in identifying the ship response model are verified.

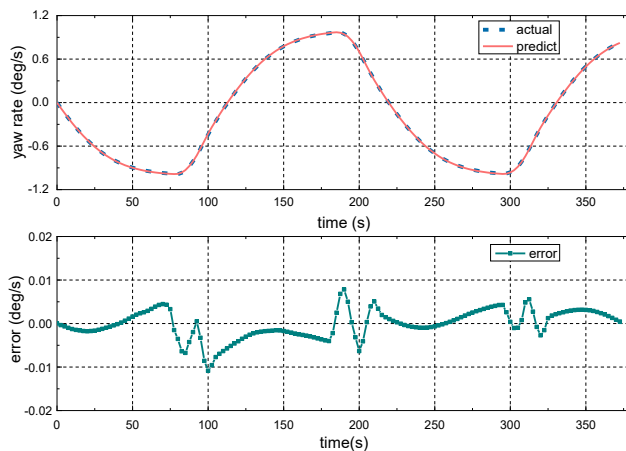


Figure 3.28 Predicted yaw rates and errors with pre-defined parameters using simulation data.

3.4.2.3.3 Comparison among different optimisation approaches

The aim of this section is to study the advantages of the NLSSVM-BAS model by comparing the NLSSVM model optimised by other techniques such as CV (Cross Validation) and PSO (Hegazy et al., 2015). The sample data are obtained from 20°/20° zigzag tests on the 1/37.89 scale model of the KRISO Container Ship (KCS) in the MARIN towing tank (SIMMAN, 2014).

After setting the same parameters and conditions of the NLSSVM model, three intelligent algorithms are adopted to optimise the parameters of the NLSSVM model, and their performances are compared and described in detail as follows:

For quantitative analysis, two characteristic indexes including the CPU time and the Root-Mean-Square Error (RMSE) of the ship yaw rate are selected for comparisons. The results including estimated parameters, the RMSE, the CPU time by three different optimised algorithms are listed in Table 3.10. From Table 3.10, it can be found that there are similar results among the three optimisation methods, but there are differences for the estimated parameters and two characteristic indexes (RMSE and CPU time). Compared with other optimisation approaches, the BAS algorithm has the smallest RMSE (0.061deg/s) and the shortest CPU time (6.2 s), which means the proposed model outperforms the other two algorithms.

Table 3.10 Comparison results among different optimisation methods.

Parameters	CV	BAS	PSO
T (s)	61.75	62.38	62.27
K (1/s)	0.113	0.114	0.114
a (s ² /deg ²)	0.719	0.725	0.713
RMSE (deg/s)	0.064	0.061	0.063
CPU Time (s)	7.5	6.2	15.4

For qualitative analysis, the identified parameters by the three methods are applied in predicting the ship yaw rates. The predicted results are shown in Figure 3.29. On one hand, the three identification algorithms perform similarly with small derivations compared to the measured data (red), but not significant. On the other hand, comparing the partial enlargement of the BAS, CV and PSO optimisation algorithms in Figure 3.29, it can be seen that the curve predicted by the BAS method (blue) is closer to the actual data curve compared to the CV and the PSO approaches.

Moreover, errors at each predicted point of three approaches are presented in Figure 3.30. The overall trend of errors for the BAS algorithm is the lowest, and the maximum error of the BAS method is the smallest. As seen, the error curves illustrate that the NLSSVM model optimised by the BAS algorithm performs better than the other two approaches. Thus, the advantages of the NLSSVM-BAS approach are illustrated in detail by comparison with other optimisation methods.

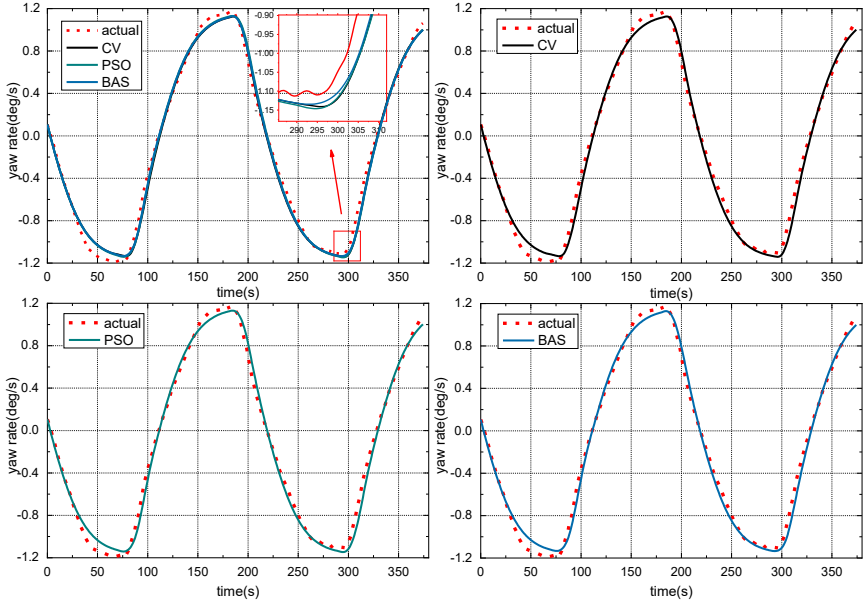


Figure 3.29 Predicted yaw rates of the NLSSVM model optimised by the BAS, CV and PSO.

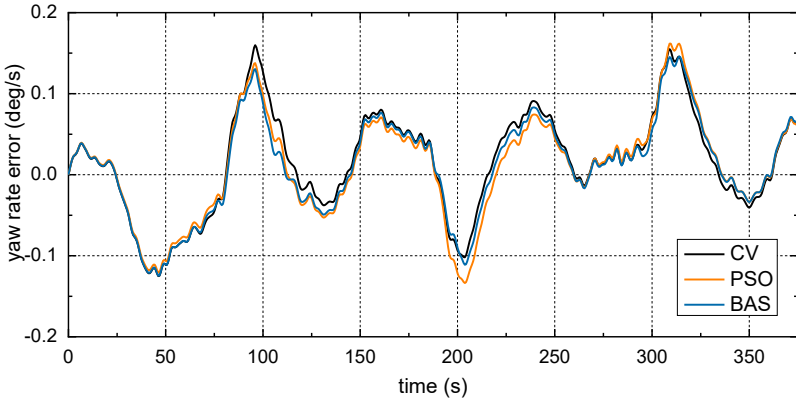


Figure 3.30 Yaw rate errors of the NLSSVM model optimised by the BAS, CV and PSO.

3.4.2.3.4 Robustness and stability analysis

In order to analyse the robustness and stability of the proposed model. Gaussian white noises are added in the original sample data. The noise level is defined as the standard deviation of noises ranging from 0.057 to 0.172 deg/s. The identification results for different parameters and their relative errors in different noise levels are displayed in Table 3.11. To better illustrate the stability of the model, the comparison results are plotted in Figure 3.31 to Figure 3.33. From the

results in Table 3.11, the errors between predefined parameters and estimated parameters for the time constant c , gain constant K and nonlinear constant a increase gradually with noise level rising. The relative errors get bigger as well.

Table 3.11 Comparison of the identified time constant T , gain K and nonlinear constant a by the BAS method after adding different Gaussian white noises.

Noise (deg/s)	T (s)			K (1/s)			a (s ² /deg ²)		
	True	Estimate	Error (%)	True	Estimate	Error (%)	True	Estimate	Error (%)
0.000	66.00	66.38	0.57	0.10	0.10010	0.10	1.00	0.99	1.13
0.057	66.00	66.54	0.82	0.10	0.10035	0.35	1.00	0.98	1.63
0.172	66.00	66.62	0.94	0.10	0.10061	0.58	1.00	0.98	1.85

Take time constant T as an example. The identified parameter value is around 66.38 s and its relative error is about 0.57% when there is no Gaussian white noise in the original sample data. Then, add Gaussian white noise with the levels of 0.057 deg/s and 0.172 deg/s to the sample data, the relative errors increase to around 0.82% and 0.94% respectively, and the identified parameters with small deviations, but not significant. Small errors mean that the identification results can be accepted and used to predict.

Therefore, the proposed NLSSVM-BAS model can accurately identify model parameters with small Gaussian white noise. The robustness and stability of the proposed model are verified.

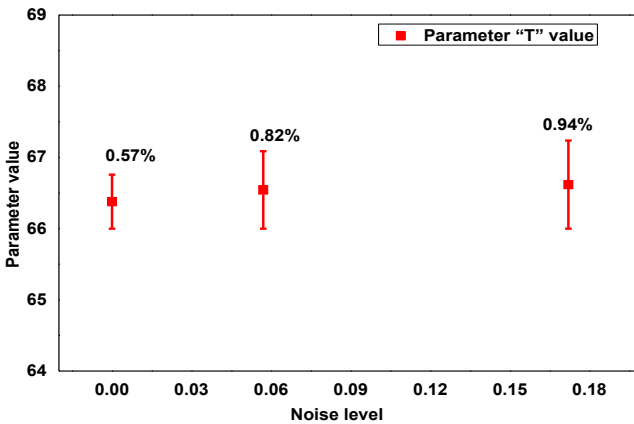


Figure 3.31 Identification results for the time constant T and its relative errors in different noise levels.

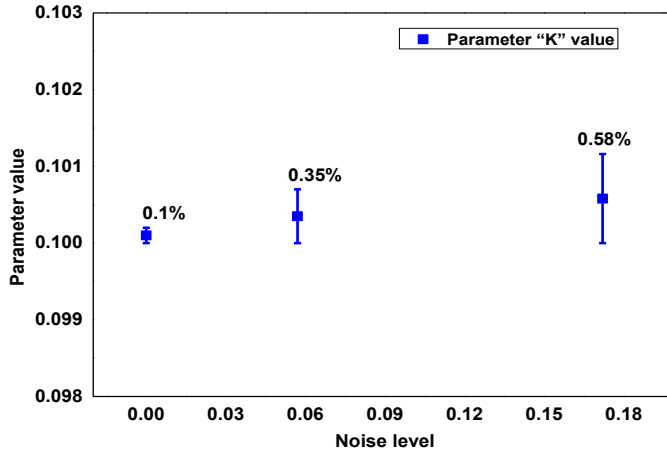


Figure 3.32 Identification results for the gain K and its relative errors in different noise levels.

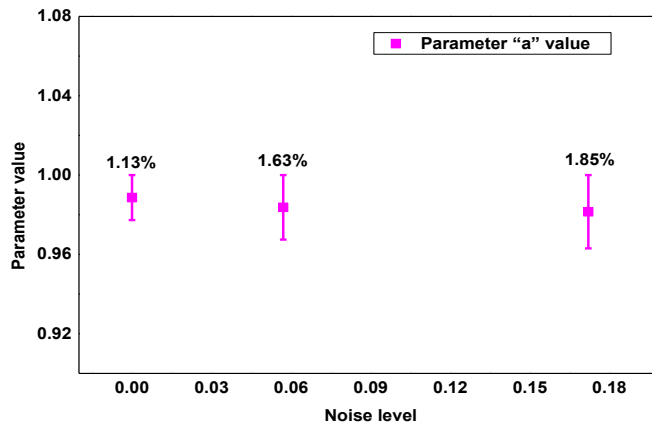


Figure 3.33 Identification results for the nonlinear constant a and its relative errors in different noise levels.

To summarize, the new NLSSVM-BAS method is proposed to improve the performance of parameters identification in the field of the ship motion models. Numerical simulation data and experimental data are used to identify the model and to predict the ship yaw motions. The comparison of the results demonstrates that the proposed model presents better performance. Comparing the numerical simulation data with the predicted data by identified model, good agreement and high accuracy are observed, which illustrate that the developed model can be applied in estimating parameters of the ship motions model. Meanwhile, compared with CV and PSO, the NLSSVM approach, optimised by the BAS algorithm, outperforms and can improve the accuracy of parameter identification. Based on comparisons among identified results disturbed by various Gaussian white noises, the stability and robustness are verified.

3.5 Reference

- Chen, C. Y., Tello Ruiz, M., Delefortrie, G., Mei, T. L. T. L., et al.,** 2019a. *Parameter estimation for a ship's roll response model in shallow water using an intelligent machine learning method*. *Ocean Engineering*, 191, 1–10.
- Chen, C. Y., Tello Ruiz, M., Lataire, E., Delefortrie, G., et al.,** 2019b. *Ship manoeuvring model parameter identification using intelligent machine learning method and the beetle antennae search algorithm*. In *Proceedings of the ASME 2019 38th International Conference on Ocean, Offshore and Arctic Engineering*. Glasgow, Scotland.
- David, M. S., Dictino, C., Jesus Manuel, D. L. C., and Joaquin, A.,** 2013. *Identification of a surface marine vessel using LS-SVM*. *Journal of Applied Mathematics*, 2013, 1–11.
- Delefortrie, G., Eloot, K., Lataire, E., Van Hoydonck, W., et al.,** 2016. *Captive model tests based on 6 DOF shallow water manoeuvring model*. In *International conference on ship manoeuvring in shallow and confined water with special focus on ship bottom interaction (4th MASHCON)*. Hamburg, Germany.
- Do, K. D., and Pan, J.,** 2009. *Control of ships and underwater vehicles*. Springer, London.
- Ejaz, M., and Chen, M.,** 2017. *Sliding mode control design of a ship steering autopilot with input saturation*. *International Journal of Advanced Robotic Systems*, 14(3), 1–13.
- Fossen, T. I.,** 1994. *Guidance and control of ocean vehicles*. New York, United States: John Wiley & Sons Inc.
- Fossen, T. I.,** 2011. *Handbook of marine craft hydrodynamics and motion control*. John Wiley & Sons Ltd. United Kingdom.
- Hegazy, O., Soliman, O. S., and Salam, M. A.,** 2015. *Comparative study between FPA, BA, MCS, ABC, and PSO algorithms in training and optimizing of LS-SVM for stock market prediction*. *International Journal of Advanced Computer Research*, 5(18), 35–45.
- Himeno, Y.,** 1981. *Prediction of ship roll damping – state of the art*. *Technical Report of Department of Naval Architecture and Marine Engineering*. University of Michigan, Michigan, USA.
- Ikeda, Y., Himeno, Y., and Tanaka, N.,** 1977. *On eddy making component of roll damping force on naked hull*. *Journal of the Society of Naval Architects of Japan*, 1977(142), 54–64.
- Jiang, X. Y., and Li, S.,** 2018. *BAS: Beetle antennae search algorithm for*

- optimization problems*. International Journal of Robotics and Control., 1(1), 1–5.
- Johansen, T. A., Fossen, T. I., and Tøndel, F.,** 2005. *Efficient optimal constrained control allocation via multiparametric programming*. Journal of Guidance, Control, and Dynamics, 28(3), 506–515.
- Merriman, M.,** 1877. *A list of writings relating to the method of least squares: with historical and critical notes*. Kessinger Publishing, LLC.
- Mehrkanoon, S., Falck, T., and Suykens, J. A. K.,** 2012. *Parameter estimation for time varying dynamical systems using least squares support vector machines*. IFAC Proceedings Volumes, 45(16), 1300–1305.
- Nomoto, K., Taguchi, T., Honda, K., and Hirano, S.,** 1957. *On steering qualities of ships*. Technical Report. International Shipbuilding Progress, 4(35), 57–66.
- SIMMAN 2014.** *The workshop on benchmark the capabilities of different ship manoeuvring simulation methods*. In *The workshop on benchmark the capabilities of different ship manoeuvring simulation methods*. Lyngby, Denmark, (<https://simman2014.dk/>).
- Skjetne, R., Fossen, T. I., and Kokotović, P. V.,** 2005. *Adaptive maneuvering, with experiments, for a model ship in a marine control laboratory*. Automatica, 41, 289–298.
- Skjetne, R., Smogeli, Ø. N., and Fossen, T. I.,** 2004. *A nonlinear ship manoeuvring model: identification and adaptive control with experiments for a model ship*. Modeling, Identification and Control, 25(1), 3–27.
- Steinwart, I., and Scovel, C.,** 2012. *Mercer’s theorem on general domains: on the interaction between measures, kernels, and RKHSs*. Constructive Approximation, 35(3), 363–417.
- Stigler, S. M.,** 1981. *Gauss and the invention of least squares*. Annals of Statistics, 9(3), 465–474.
- Tello Ruiz, M.,** 2018. *Manoeuvring model of a container vessel in coastal waves*. Ghent University, Belgium (PhD thesis).
- Tuck, E. O.,** 1966. *Shallow-water flows past slender bodies*. Journal of Fluid Mechanics, 26(1), 81–95.

Ship motion control systems

4	<i>Path plan, guidance, navigation, and control</i>	103
4.1	General discussion	103
4.2	Path planning system	105
4.2.1	Overview	105
4.2.2	Manually planning method	105
4.2.3	Automatically planning method	105
4.3	Guidance system	117
4.3.1	Overview	117
4.3.2	Determination of LOS angle	117
4.3.3	Selection of current waypoint	118
4.3.4	Sign of cross track error	120
4.4	Navigation system	121
4.5	Reference	123

I can't change the direction of the wind, but I can adjust my sails to always reach my destination.

--Jimmy Dean

4

Path plan, guidance, navigation, and control

4.1 General discussion

A ship motion system is usually constructed as three independent subsystems, namely, a guidance system, a navigation system, and a control system. In addition, a path planning module is used to generate waypoints to be used by the guidance system. These subsystems interact with each other through data and signal transmission (Fossen, 2011). Figure 4.1 displays the structure of the ship's motion system used in this research. In the next sections, the path planning, guidance and navigation systems will be elaborated, while the motion control system will be elaborated in Chapter 5.

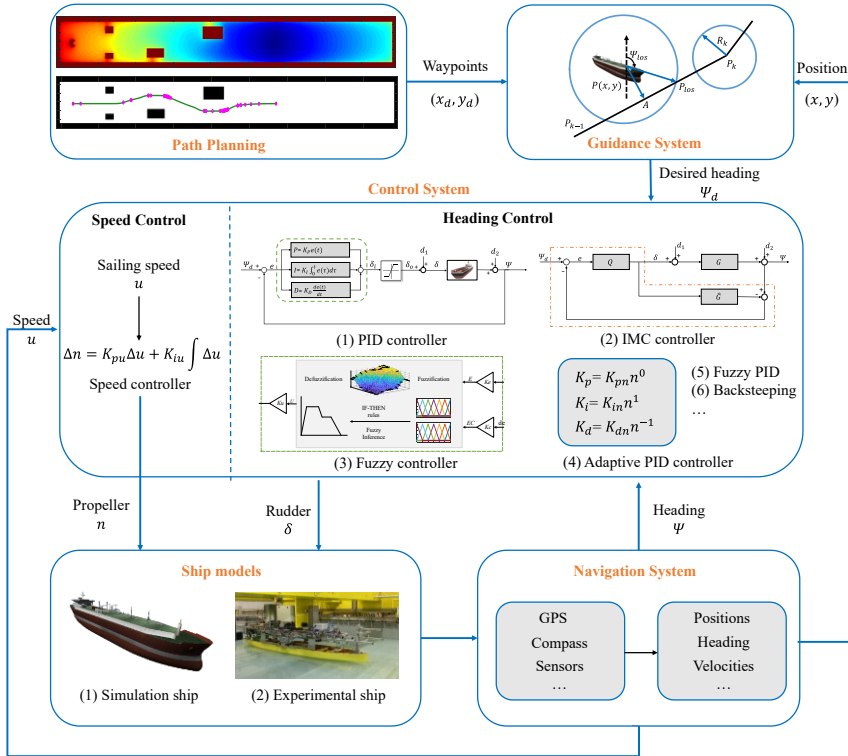


Figure 4.1 Schematic of path planning, guidance, navigation, and control system.

4.2 Path planning system

4.2.1 Overview

Path planning system, also motion planning system, is used to generate the shortest or optimal path from the start position to the destination, passing through a sequence of the predefined waypoints. The path planning techniques are divided into two categories: 1) manually planning method; 2) automatically planning method.

4.2.2 Manually planning method

Planning a desired path by the manual approach is relatively simple. It is to manually select appropriate waypoints according to the bathymetry, sailing environment and experience, etc. Meanwhile, the waypoints can be feasibly adjusted by the designer according to the actual sailing requirements. Figure 4.2 displays an example of manually planning a desired route. Yet, this path planning approach is more complex than the automatic way. Hence more advanced planning methods should be considered to improve the applicability.

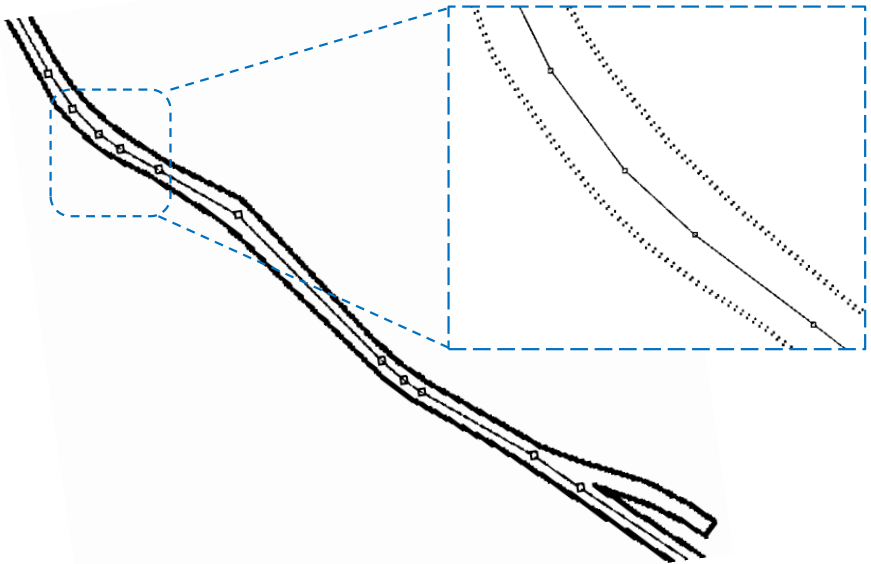


Figure 4.2 Plan a desired path by the manual approach.

4.2.3 Automatically planning method

A number of path planning algorithms, e.g. A* algorithm (Xie et al., 2019) and artificial potential field (APF) (Lyu and Yin, 2018), etc. have been proposed and applied in ship path planning field. In this research, on basis of the fast marching method (FMM) and fast marching square (FMS) method, a new path planning algorithm, called Angle-guidance and Tuned-distance Fast Marching Square

(ATFMS), is proposed. the ATFMS method can generate a smooth and optimal path in complex environment taking into account of the ship’s navigation safety, economy and manoeuvring. The development of the ATFMS algorithm will be presented in sections 4.2.3.1 to 4.2.3.4.

4.2.3.1 Fast marching method (FMM)

The fast marching method (FMM) is a grid search algorithm to generate (plan) a desired route. The method is used to solve the Eikonal equation (Eq. (4.1)) for a grid map and model any phenomena evolving as a wave front that propagates along its normal direction (Sethian, 1996; Garrido et al., 2020). The Eikonal equation is formulated as:

$$|\nabla T(x, y)|V(x, y) = 1 \tag{4.1}$$

where $T(x, y)$ is the interface arrival time at point (x, y) , $V(x, y)$ is the interface propagating speed at point (x, y) .

The solution of Eikonal equation (Eq. (4.1)) can be derived by using the upwind difference scheme to approximate the partial derivatives of $T(x, y)$. Suppose the grid point as (x, y) where the arrival time $T(x, y)$ needs to be solved. The neighbor of (x, y) is a point set consisting of four elements (Figure 4.3): $(x - \Delta x, y)$, $(x + \Delta x, y)$, $(x, y - \Delta y)$, $(x, y + \Delta y)$.

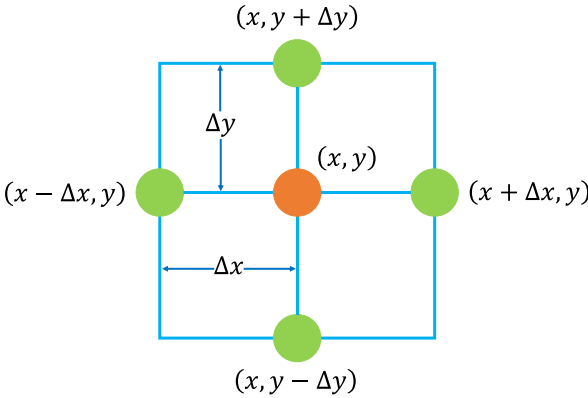


Figure 4.3 Grid point (x, y) and its neighbors.

The gradient $\nabla T(x, y)$ is discretized according to Sethian (1999), then Eq. (4.1) yields:

$$\max(D_{(x,y)}^{-x}T, -D_{(x,y)}^{+x}, 0)^2 + \max(D_{(x,y)}^{-y}T, -D_{(x,y)}^{+y}, 0)^2 = \frac{1}{V_{(x,y)}^2} \tag{4.2}$$

where

$$\begin{aligned}
D_{(x,y)}^{-x} &= \frac{T_{(x,y)} - T_{(x-\Delta x,y)}}{\Delta x} \\
D_{(x,y)}^{+x} &= \frac{T_{(x+\Delta x,y)} - T_{(x,y)}}{\Delta x} \\
D_{(x,y)}^{-y} &= \frac{T_{(x,y)} - T_{(x,y-\Delta y)}}{\Delta y} \\
D_{(x,y)}^{+y} &= \frac{T_{(x,y+\Delta y)} - T_{(x,y)}}{\Delta y}
\end{aligned} \tag{4.3}$$

where $D_{(x,y)}^{-x}$, $D_{(x,y)}^{+x}$, $D_{(x,y)}^{-y}$, $D_{(x,y)}^{+y}$ represent the one-side partial difference operator in $-x$, $+x$, $-y$ and $+y$ directions, respectively; Δx and Δy are the grid spacing in x and y directions.

Substitute Eq. (4.3) into Eq. (4.2) and assume:

$$T_x = \min(T_{(x-\Delta x,y)}, T_{(x+\Delta x,y)}) \tag{4.4}$$

$$T_y = \min(T_{(x,y-\Delta y)}, T_{(x,y+\Delta y)}) \tag{4.5}$$

Then, for a discrete two dimensions (2D) space, the Eikonal equation is reformulated:

$$\max\left(\frac{T_{(x,y)} - T_x}{\Delta x}, 0\right)^2 + \max\left(\frac{T_{(x,y)} - T_y}{\Delta y}, 0\right)^2 = \frac{1}{V_{(x,y)}^2} \tag{4.6}$$

The quadratic solution of Eq. (4.6) is derived as:

$$\frac{1}{v(x,y)} = \begin{cases} \sqrt{\left(\frac{T_{(x,y)} - T_x}{\Delta x}\right)^2 + \left(\frac{T_{(x,y)} - T_y}{\Delta y}\right)^2} & \max(T_x, T_y) \leq T_{(x,y)} \\ \frac{T_{(x,y)} - T_x}{\Delta x} & T_x \leq T_{(x,y)} \leq T_y \\ \frac{T_{(x,y)} - T_y}{\Delta y} & T_y \leq T_{(x,y)} \leq T_x \end{cases} \tag{4.7}$$

To simplify the notation, the grid is assumed as the unit square cell:

$$\Delta x = \Delta y = 1 \tag{4.8}$$

The final solution is written as:

$$T_{(x,y)} = \begin{cases} \text{Quadratic solution of Eq. (4.6)} & \max(T_x, T_y) \leq T \\ T_x + \frac{1}{V(x,y)} & T_x \leq T \leq T_y \\ T_y + \frac{1}{V(x,y)} & T_y \leq T \leq T_x \end{cases} \quad (4.9)$$

In order to better understand the FMM algorithm, Figure 4.4 presents an example of the development of the FMM algorithm in a 7×7 grid map. When running the FMM algorithm, the grid points in the map are classified into three groups (Figure 4.4):

- **Known** is the set of grid points at which the arrival time value $T(x, y)$ has been calculated and determined. The value will not be changed.
- **Trial** represents the set of next grid points to be examined, where the arrival time value $T(x, y)$ has been calculated and may be changed later.
- **Unvisited** is the set of all other points with undecided arrival time value $T(x, y)$.

The updating procedure includes four steps:

Step 1: all the grid points in the map are initialized as unvisited points except for the start point, which is assigned in the middle of the map with the interface propagating speed as “1” at each grid point (Figure 4.4(a)).

Step 2: the start point is considered as the known point with the arrival time T as “0”. Then the neighbours of the start point become the trial points with the calculated arrival time T as step 1 (Figure 4.4(b)).

Step 3: the point with the smallest arrival time (T) is set as a new known point. Yet, according to the results in Figure 4.4(b), the four neighbour (trial) points have the same arrival time (“1”). In this case, the point below the start point is identified as the known point and other neighbour points are considered as the trial points (Figure 4.4(c)).

Step 4: The updating process of step 3 is repeated and shown in Figure 4.4(d)-(g). The procedure continues until all points are set as known, and the final result is depicted in Figure 4.4(h).

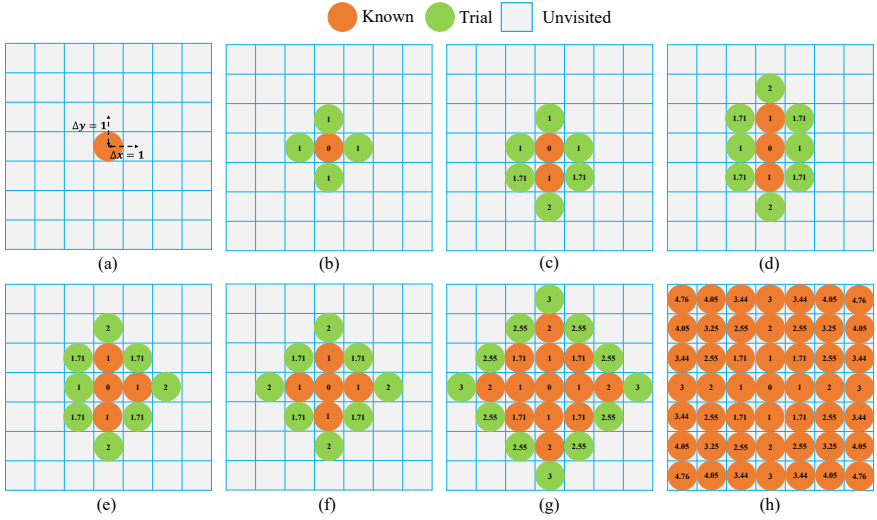
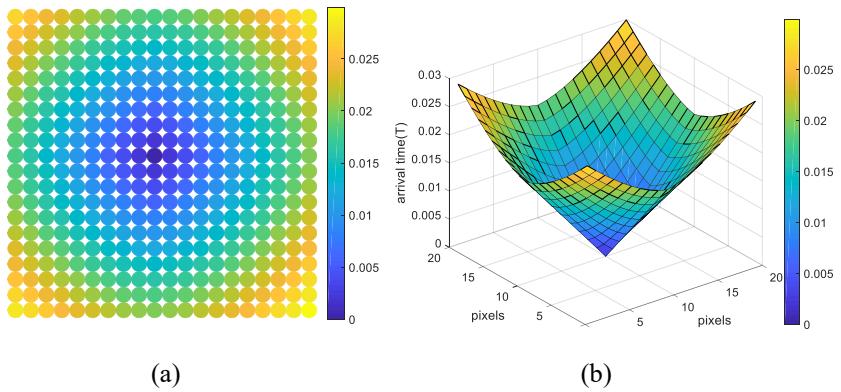


Figure 4.4 Updating process of fast marching method (FMM).

According to the above updating process, the FMM method is applied in the 20×20 and 60×60 grid maps. Figure 4.5 shows the arrival time (T) in two dimensions (2D) and three dimensions (3D). It can be seen from Figure 4.5 that the arrival time function has a funnel-like shape, the desired path is finally generated by using the gradient descent method.



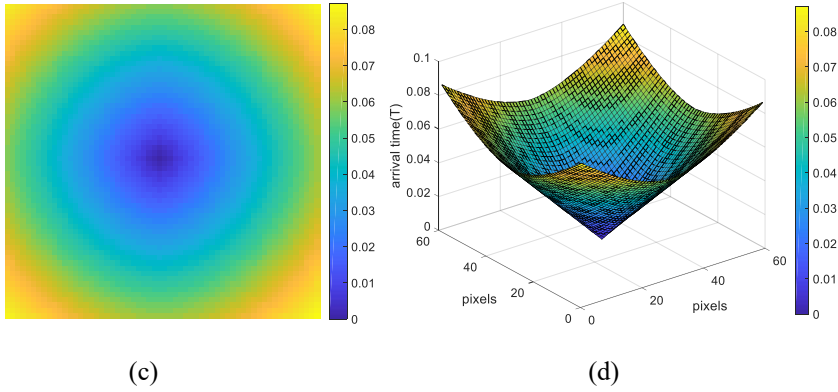


Figure 4.5 Arrival time (T) calculated by fast marching method (FMM) in two grid maps: (a) arrival time in a 20×20 grid map (2D); (b) arrival time in a 20×20 grid map (3D); (c) arrival time in a 60×60 grid map (2D); (d) arrival time in a 60×60 grid map (3D).

Table 4.1 elaborates the FMM based path planning algorithm. Assume a planning space as a grid map (M), which is shown in Figure 4.6(a). In Figure 4.6(a), the black circles represent the obstacles, while the white zone is the navigable area. The FMM algorithm firstly reads the map information to identify the obstacles and navigable area and calculates the propagating speed matrix $V(x, y)$ at each grid point (x, y) . The arrival time matrix $T(x, y)$ is derived based on the calculated speed matrix $V(x, y)$. Figure 4.6(b) and Figure 4.6(d) visualize the arrival time potential field in 2D and 3D where different colour represents the different arrival time. Meanwhile, the potential value indicates the distance from the start point. Based on the calculated arrival time potential field, the desired path is finally obtained by using the gradient descent method and presented in Figure 4.6(c).

Table 4.1 FMM algorithm for planning a desired path.

Path planning by FMM algorithm
Procedure $FMM(M, P_S, P_E)$
Require: A grid map (M), start point (P_S) and end point (P_E)
1. Read map information (M)
2. Calculate propagating speed matrix $V \leftarrow FMM(M)$
3. Calculate arrival time matrix $T \leftarrow FMM(V, P_S, P_E)$
4. Generate optimal path \leftarrow Gradient Descent(T, P_S, P_E)
End

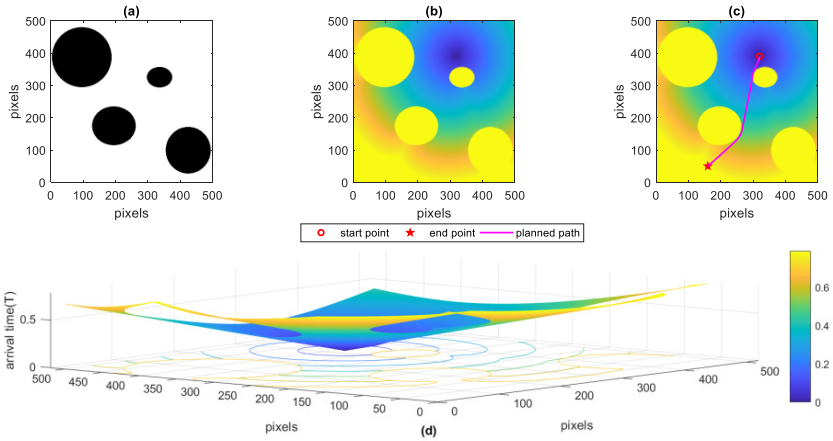


Figure 4.6 Fast marching method (FMM) for path planning: (a) grid map; (b) output of the FMM, arrival time matrix (T); (c) arrival time potential field and planned path; (d) 3D plot for arrival time matrix (T).

4.2.3.2 Fast marching square method (FMS)

Even though the FMM algorithm is quite advanced, a number of shortcomings have been detected during recent applications. In particular, the planned path by the FMM algorithm is too close to the obstacles, see Figure 4.6(c) for better illustration. In such scenarios, there is a risk of running aground in shallow water or collision with obstacles near coastlines or islands.

To address this problem, a new planning algorithm called fast marching square (FMS) was proposed by Gómez et al. (2013), which added one step to the FMM algorithm. Specifically, a safety potential map (M_s) is firstly generated via applying the FMM algorithm to propagate interfaces from all grid points in the obstacle area (Figure 4.7(b)). On basis of the safety potential map (M_s), the FMM algorithm is adopted to generate a desired path from the start point to the end point. The procedure of planning an optimal path by the FMS algorithm is listed in Table 4.2. Figure 4.7 shows the planning results, where the generated path keeps a safe distance from the obstacles.

Table 4.2 FMS algorithm for planning a desired path.

Path planning by FMS algorithm
Procedure $FMS(M, P_S, P_E)$
Require: A grid map (M), start point (P_S) and end point (P_E)
1. Read map information (M)
2. Generate a safety potential map $M_s \leftarrow FMM(M)$
5. Calculate propagating speed matrix $V \leftarrow FMM(M_s)$
3. Calculate arrival time matrix $T \leftarrow FMM(V, P_S, P_E)$
4. Generate optimal path \leftarrow Gradient Descent(T, P_S, P_E)
End

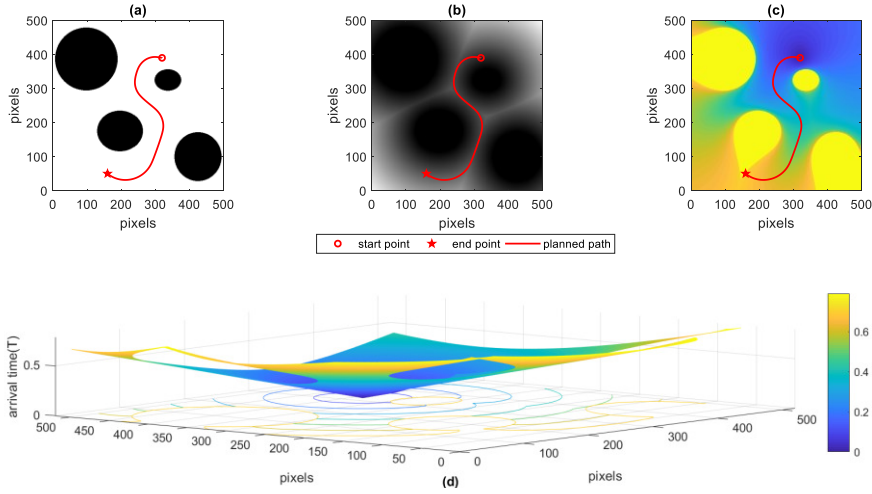


Figure 4.7 Fast marching square (FMS) method for path planning: (a) grid map and planned path; (b) velocity map and planned path; (c) arrival time matrix (T) and planned path; (d) 3D plot for arrival time matrix (T).

4.2.3.3 Tuned fast marching square method (TFMS)

Figure 4.8 shows a comparison between the FMM algorithm and the FMS algorithm. It can be found in Figure 4.8 that the path (purple line) generated by the FMM algorithm is close to the obstacles, while the planned path (green line) by the FMS algorithm is away from the obstacles. Closing to the obstacles will increase the stranding risk and staying away from obstacles will increase the sailing distance. To achieve a balance between the safety and sailing distance, a tuned-distance fast marching square algorithm (TFMS) is developed. The approach integrates a saturation adjustment mechanism into the FMS algorithm to tune the velocity potential map (V). The saturation mechanism is used to scale the velocity potential map V into V_s with the range between $[0, 1]$ according to Eq. (4.10). The TFMS-based path planning algorithm is described in Table 4.3.

$$V_s = \text{rescale}(\min(\text{scale}(V), \text{sat})) \quad (4.10)$$

where V_s is the scaled velocity potential map; sat is the saturation value with a value between $[0, 1]$. The saturation value is employed to optimize the planned path.

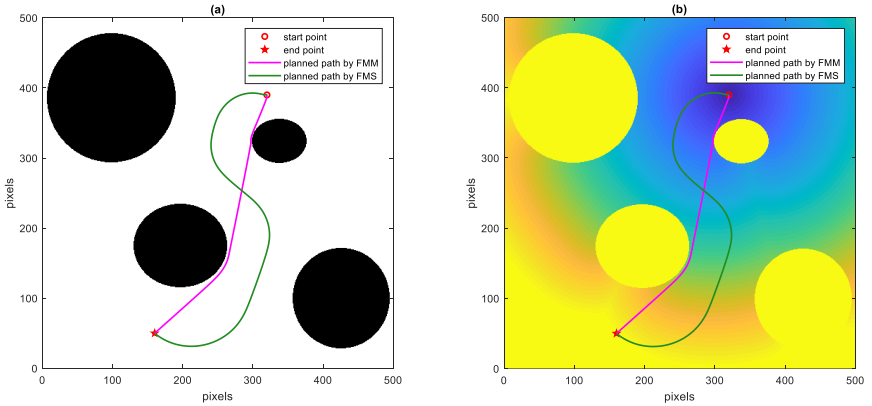


Figure 4.8 Comparison between the FMM method and the FMS method for path planning.

Table 4.3 TFMS algorithm for planning a desired path.

Path planning by TFMS algorithm
Procedure TFMS(M, P_S, P_E, sat)
Require: A grid map (M), start point (P_S), end point (P_E), saturation value (sat)
1. Read map information (M)
2. Generate a safety potential map $M_s \leftarrow$ FMM (M, sat)
3. Calculate propagating speed matrix $V \leftarrow$ FMM(M_s)
4. Calculate arrival time matrix $T \leftarrow$ FMM (V, P_S, P_E)
5. Generate optimal path \leftarrow Gradient Descent(T, P_S, P_E)
End

Figure 4.9 exhibits the paths generated by the TFMS algorithm with different saturation values from 0.2 to 0.8. The distances between the planned paths and obstacles vary with the saturation values, which improve the flexibility of path planning and trade off the safety and sailing distance. We can adjust the saturation value to meet actual engineering requirements. Note that when the saturation value is 0, the TFMS becomes the FMM method, which will generate the path closest to obstacles. On the contrary, when the saturation value is 1, the TFMS becomes the FMS method, which will plan the safest path (but far away from obstacles).

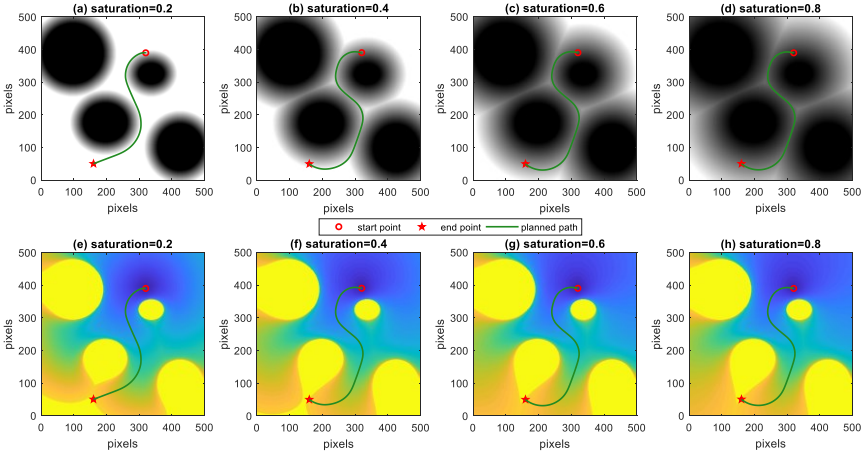


Figure 4.9 Tuned Fast marching square (TFMS) method for path planning with different saturations. (1) *Safety potential map*: (a) saturation 0.2; (b) saturation 0.4; (c) saturation 0.6; (d) saturation 0.8; (2) *Arrival time matrix*: (e) saturation 0.2; (f) saturation 0.4; (g) saturation 0.6; (h) saturation 0.8.

4.2.3.4 Angle-guidance tuned fast marching square method (ATFMS)

The angle-guidance tuned-distance fast marching square method (ATFMS) is introduced to further improve the path planning performance. The procedure of the ATFMS algorithm for planning a desired path is presented in Table 4.4. The ATFMS algorithm is developed based on the TFMS method and added a guidance range (GR) module (Figure 4.10).

Table 4.4 ATFMS algorithm for planning a desired path.

Path planning by ATFMS algorithm
Procedure ATFMS(M, P_S, P_E, sat)
Require: A grid map (M), start point (P_S), end point (P_E), saturation value (sat), heading angle (Ψ), turning angle (θ_A), range distance (d)
1. Read map information (M)
2. Range \leftarrow GuidanceRange ($M, P_S, \Psi, \theta_A, d$)
3. Generate a safety potential map $M_s \leftarrow$ FMM(M, sat)
4. Calculate propagating speed matrix $V \leftarrow$ FMM(M_s)
5. Calculate arrival time matrix $T \leftarrow$ FMM(V, P_S, P_E)
6. Generate optimal path \leftarrow Gradient Descent(T, P_S, P_E)
End

The structure of GR module is shown in Figure 4.10, where the turning range is in white sector and the obstacle is in black grid sector. The turning range sector is modelled by three parameters: i.e. turning angle θ_A , range distance d and heading angle Ψ . The range distance (d) is the radius of the cone shape which is used to

control the influence range, and it is related to the forward speed of the ship. The turning angle is calculated according to ship yaw constraint:

$$\theta_A = r_{max}\Delta t \tag{4.11}$$

where r_{max} is the maximum yaw rate, Δt is the time step.

It is necessary to mention that these parameters can be adjusted according to the ship dynamics in real application.

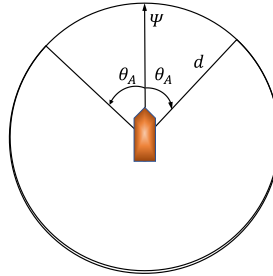


Figure 4.10 Illustration of guidance range.

Figure 4.11(a) presents the colour map with the designed guidance range. The guidance range has an initial heading angle (Ψ) of 180 deg, a range distance (d) of 10 m and a turning angle (θ_A) of 30 deg. To better illustrate the advantage of the ATFMS performance, a comparison between the TFMS method and the ATFMS method for path planning is displayed in Figure 4.11(b). It can be seen from Figure 4.11(b) that the TFMS algorithm did not consider the initial turning direction of ship, generated a path based on the smallest sailing distance, and avoided obstacles from the upper part (purple line). Yet, it is not realistic to follow such a planned path at the start point due to the large heading change (180 deg). On the contrary, the path generated by the ATFMS took into account the preferred direction and avoided obstacles from the bottom part (green line). Note that both the distance factor and the dynamic requirements of the ship are considered in the ATFMS method, which makes it more practical.

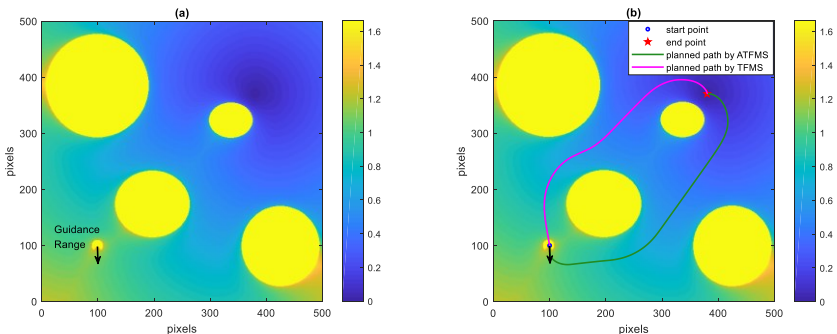


Figure 4.11 Comparison of TFMS and ATFMS methods for path planning.

4.2.3.5 Application of ATFMS in towing tank

According to the principle of the ATFMS algorithm, a desired path was planned in FHR towing tank. The simulation environment includes the towing tank wall and four obstacles (Figure 4.12(a)). The dimension of towing tank grid map is 45×450 pixels (including towing tank walls), and each pixel represents 0.2 m. The start point and the end point are located in (22, 22) and (290, 22) (pixels). The guidance range was set as an initial heading angle of 90 deg (north bound is 0 degs), a range distance of 4 m and a turning angle of 30 deg, while the saturation value was selected as 0.8. The results including the velocity map, the arrival time map and the planned path are shown in Figure 4.12(b)-(d).

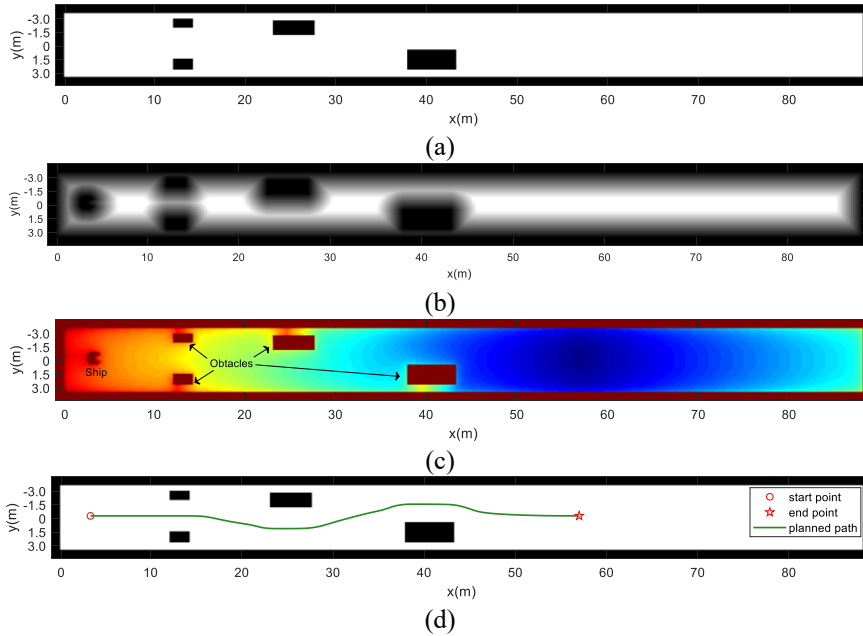


Figure 4.12 Application of ATFMS method to plan a desired path in towing tank environment (a) grid map, (b) velocity map, (c) time map, (d) planned path.

$$x_A = x_{k-1} + \frac{[(x-x_{k-1})(x_k-x_{k-1})+(y-y_{k-1})(y_k-y_{k-1})]}{[(x_k-x_{k-1})^2+(y_k-y_{k-1})^2]}(x_k - x_{k-1}) \quad (4.12)$$

$$y_A = y_{k-1} + \frac{[(x-x_{k-1})(x_k-x_{k-1})+(y-y_{k-1})(y_k-y_{k-1})]}{[(x_k-x_{k-1})^2+(y_k-y_{k-1})^2]}(y_k - y_{k-1}) \quad (4.13)$$

The cross track error Δy is defined as the distance between the ship current position P and the orthogonal projection position A :

$$\Delta y = \sqrt{(x - x_A)^2 + (y - y_A)^2} \quad (4.14)$$

The LOS position P_{los} is determined by a look ahead distance L_A formulated as:

$$L_A = \sqrt{(\Delta y + cL_{PP})^2 - (\Delta y)^2} \quad (4.15)$$

$$x_{los} = x_A + \frac{x_k - x_{k-1}}{\sqrt{(x_k - x_{k-1})^2 + (y_k - y_{k-1})^2}} L_A \quad (4.16)$$

$$y_{los} = y_A + \frac{y_k - y_{k-1}}{\sqrt{(x_k - x_{k-1})^2 + (y_k - y_{k-1})^2}} L_A \quad (4.17)$$

where c is a parameter with the default value 0.5.

Then, the desired course angle (LOS angle) Ψ_{los} is calculated by:

$$\Psi_{los} = atan \frac{y_{los} - y}{x_{los} - x} \quad (4.18)$$

4.3.3 Selection of current waypoint

The selection of the current waypoint is a key factor to perform the LOS guidance system and needs to be elaborated. When the ship is travelling along the segmented track, the following possible options for the current waypoint are considered:

The previous P_{k-1} , current P_k and next P_{k+1} waypoints are collinear.

If the distance (AP_k) between the orthogonal projection position A and the current waypoint P_k is larger than the radius ($R_k = \omega_{los}L_{PP}$) of acceptance circle for the current waypoint P_k (Figure 4.14), the LOS angle (Ψ_{los}) can be determined by:

$$\Psi_{los} = atan \frac{y_{los} - y}{x_{los} - x} \quad (4.19)$$

where ω_{los} is the parameter that needs to be tuned according to test conditions, its default value is 0.5.

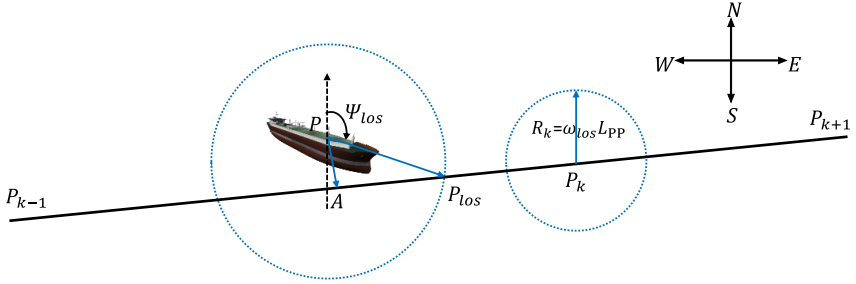


Figure 4.14 A ship converging to a collinear straight-line using the LOS guidance approach ($AP_k > R_k$).

If the distance (AP_k) between the orthogonal projection position A and the current waypoint P_k is smaller than the radius ($R_k = \omega_{los} L_{PP}$) of acceptance circle for the current waypoint P_k (Figure 4.15), the LOS position P_{los} is replaced by the current waypoint P_{k+1} , the LOS angle (ψ_{los}) can be determined by:

$$\psi_{los} = \text{atan} \frac{y_{k+1} - y}{x_{k+1} - x} \quad (4.20)$$

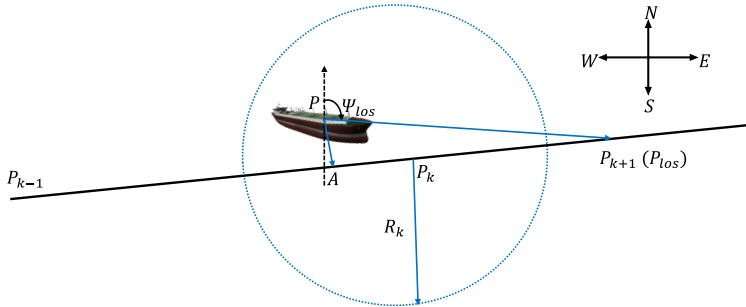


Figure 4.15 A ship converging to a collinear straight-line using LOS guidance approach ($AP_k \leq R_k$).

The previous P_{k-1} , current P_k and next P_{k+1} waypoints are not collinear.

If the distance between the ship position P and the current waypoint P_k is larger than $2R_k$ (Figure 4.13):

- If the look ahead distance L_A is not exceeding the position of the current waypoint P_k , then the desired course can be determined by Eq. (4.19).
- Else

$$L'_A = L_A - \sqrt{(x_k - x_A)^2 + (y_k - y_A)^2} \quad (4.21)$$

$$x'_{los} = x_k + \frac{x_{k+1} - x_k}{\sqrt{(x_{k+1} - x_k)^2 + (y_{k+1} - y_k)^2}} L'_A \quad (4.22)$$

$$y'_{los} = y_k + \frac{y_{k+1} - y_k}{\sqrt{(x_{k+1} - x_k)^2 + (y_{k+1} - y_k)^2}} L'_A \quad (4.23)$$

Then the desired course angle is calculated by:

$$\Psi_{los} = atan \frac{y'_{los} - y}{x'_{los} - x} \quad (4.24)$$

If the distance between the ship position P and the current waypoint P_k is smaller than $2R_k$: the next waypoint becomes the current waypoint. The orthogonal projection position A and the LOS position P_{los} are evaluated versus the new current waypoint and a reevaluated Eq. (4.19) can be used to determine the desired course.

4.3.4 Sign of cross track error

The sign of cross track error Δy depends on the ship position versus the segmented track. When considering the vectors defined by the cross track and the track in Figure 4.13, their cross sign yields:

$$\begin{vmatrix} x_{los} - x_A & x - x_A \\ y_{los} - y_A & y - y_A \end{vmatrix} \quad (4.25)$$

The above equation illustrates the ship position with respect to the segmented track.

If the ship locates on the starboard side of track, the sign of cross track error Δy will be positive, then a more negative value of the LOS angle Ψ_{los} should be considered to minimise the Δy . Otherwise, the sign of cross track error Δy will be negative, and a more positive LOS angle Ψ_{los} will be needed.

4.4 Navigation system

Typically, the navigation system is adopted to measure ship motion states such as absolute positions, velocities, and heading, etc., which are usually done by using the positioning system combining with some motion sensors, for instance, gyros and accelerometers. Furthermore, a traditional ship control system is implemented with a state estimator for dealing with the navigation and sensor data. The raw measured data are processed by a signal processing unit for quality checking and wild-point removal. The processed data are fed back to the navigation unit and the sensors, which adopts a motion state estimator to filter noise, predict and reconstruct the unmeasured states (Fossen, 2011).

In the present work, towing tank tests were conducted to investigate the performance of the whole ship motion system, including the navigation subsystem. The navigation system of the experimental ship model is presented in Figure 4.16 and Figure 4.17. During experiments, the free running model tests are executed in the towing tank, without a rigid connection between the towing carriage and the ship model. The position, rudder and propeller information are measured by the lasers and gauges, see Figure 4.16 and Figure 4.17 for better illustration. Because the acceleration and deceleration of the ship model by using its own propulsion system occupy a significant portion of the towing tank, the ship model is launched to the desired initial speed by the carriage in a captive way (Delefortrie et al., 2016). The ship model is released once it reaches the desired speed. At the end of the free running tests, the ship model is stopped by the towing carriage in a safe way by the clamping mechanism.

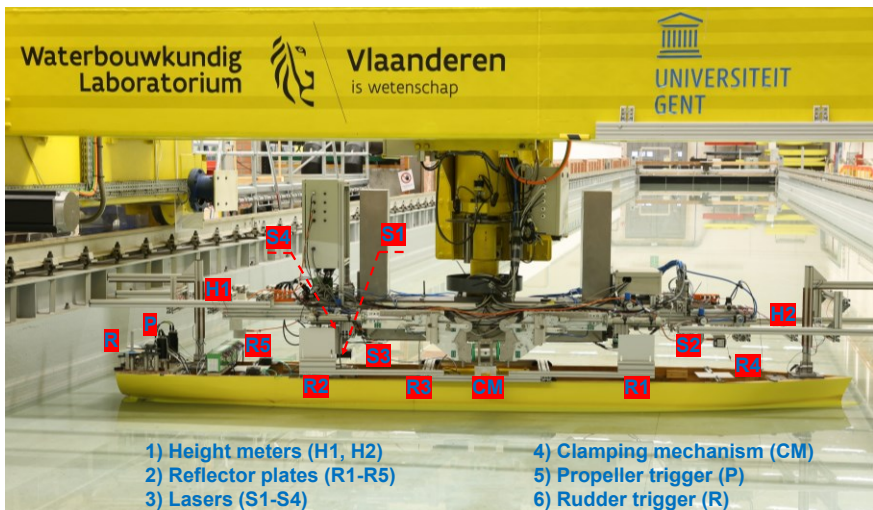


Figure 4.16 Navigation system of experimental ship model.

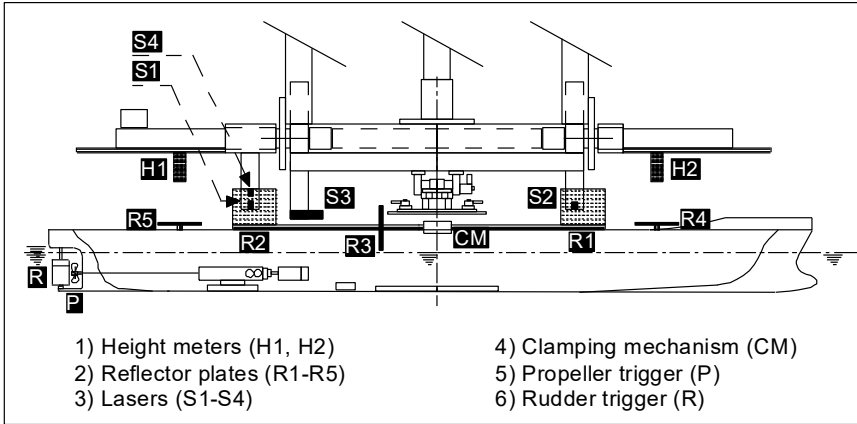


Figure 4.17 Navigation system of experimental ship model (sketch).

4.5 Reference

- Breivik, M.**, 2003. *Nonlinear Maneuvering Control of Underactuated Ships*. Norwegian University of Science and Technology, Trondheim, Norway (Master thesis).
- Delefortrie, G., Geerts, S., and Vantorre, M.**, 2016. *The towing tank for manoeuvres in shallow water*. In *Proceedings of 4th MASHCON*. Hamburg, Germany.
- Fossen, T. I.**, 2011. *Handbook of marine craft hydrodynamics and motion control*. John Wiley & Sons Ltd. United Kingdom.
- Garrido, S., Alvarez, D., and Moreno, L. E.**, 2020. *Marine applications of the fast marching method*. *Frontiers in Robotics and AI*, 7(2), 1–12.
- Gómez, J. V., Lumbier, A., Garrido, S., and Moreno, L.**, 2013. *Planning robot formations with fast marching square including uncertainty conditions*. *Robotics and Autonomous Systems*, 61, 137–152.
- Lyu, H. G., and Yin, Y.**, 2018. *Ship's trajectory planning for collision avoidance at sea based on modified artificial potential field*. In *2017 2nd International Conference on Robotics and Automation Engineering, ICRAE 2017*. Shanghai, China.
- Moreira, L., Fossen, T. I., and Guedes Soares, C.**, 2007. *Path following control system for a tanker ship model*. *Ocean Engineering*, 34, 2074–2085.
- Sethian, J. A.**, 1996. *A fast marching level set method for monotonically advancing fronts*. *Applied Mathematics*, 93, 1591–1595.
- Sethian, J. A.**, 1999. *Level set methods and fast marching methods*. Cambridge University Press.
- Xie, L., Xue, S., Zhang, J., Zhang, M., et al.**, 2019. *A path planning approach based on multi-direction A* algorithm for ships navigating within wind farm waters*. *Ocean Engineering*, 184, 311–322.

Ship motion control systems

5	<i>Motion control systems</i>	125
5.1	General discussion	125
5.2	PID controller	127
5.2.1	Controller structure.....	127
5.2.2	Determination of time constant T and gain K	128
5.2.3	Determination of PID parameters.....	130
5.3	Internal model controller	131
5.3.1	Controller structure.....	131
5.3.2	Controller design	132
5.4	Adaptive PID controller	134
5.4.1	Controller structure.....	134
5.4.2	Controller design	135
5.5	Fuzzy controller	136
5.5.1	Controller structure.....	136
5.5.2	Controller design	136
5.6	Fuzzy PID controller	140
5.6.1	Controller structure.....	140
5.6.2	Controller design	140
5.7	Backstepping controller	144
5.7.1	Controller structure.....	144
5.7.2	Controller design	144
5.8	Nonlinear feedback and nonlinear decoration filters	148
5.8.1	Nonlinear feedback filter.....	148
5.8.2	Nonlinear decoration filter.....	149
5.9	Speed controller	151
5.9.1	Controller structure.....	151
5.9.2	Determination of K_{pu} and K_{iu}	151
5.9.3	Tolerance interval and propeller rate limiter	151
5.10	Controller performance evaluation	153
5.10.1	Evaluation procedure.....	153
5.10.2	Evaluation mechanism.....	153
5.10.3	Model selection mechanism	154
5.11	Reference	156

If a craftsman wants to do good work, he must first sharpen his tools.

--Confucius

5

Motion control systems

5.1 General discussion

The ship motion control system is used to determine the necessary control forces and moments in order to achieve a certain control objective. This work focus on the design of the course and path following controllers. According to whether or not replying on the ship mathematical model, controllers used in this research can be classified:

- Model-based controllers
 - Proportional Integral Derivative controller (PID)
 - Internal model controller (IMC)
 - Adaptive PID controller
 - Fuzzy PID controller
 - Backstepping controller
- Model-free controllers
 - Fuzzy controller

The above controllers were tested in towing tank and a fast-time manoeuvring simulator to accomplish the following control missions:

- Course control
 - Course keeping
 - Course changing
 - Nonlinear feedback
 - Nonlinear decoration
- Path following control
 - Straight line
 - Step line
 - Folding line
 - Curved line

- Obstacle avoidance

In addition to the aforementioned heading controllers, a new speed controller was proposed to obtain desired forward speeds during path following control missions.

5.2 PID controller

5.2.1 Controller structure

The Proportional-Integral-Derivative (PID) controller is a classical control method that is most widely applied in ship control systems (Minorsky, 1922), due to its simple structure, ease of design, and low cost in implementation. In spite of the existence of more advanced controllers, the performance of the PID controller can be considered as a benchmark for the future implementation of more sophisticated control approaches (Peeters et al., 2020). In the PID control law, the controller is employed to reduce the error between the measured and desired heading angles, which is shown in continuous-time form as:

$$\delta = K_p(\Psi_d - \Psi) + K_i \int_0^t (\Psi_d - \Psi) d\tau - K_d \dot{\Psi} \tag{5.1}$$

where δ is the rudder angle, Ψ is the measured heading angle, Ψ_d is the desired heading angle. K_p , K_i and K_d are the proportional, integral, and derivative coefficients, respectively.

Figure 5.1 shows the structure of PID controller, while the Matlab Simulink design for PID controller is displayed in Figure 5.2, where δ_i and δ_0 are rudder angle, d_1 and d_2 are the input and output disturbances.

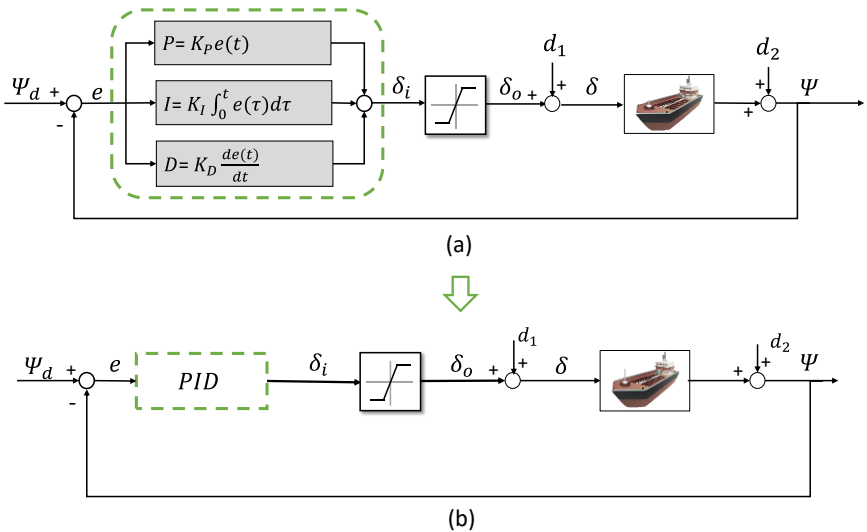


Figure 5.1 Structure of PID controller.

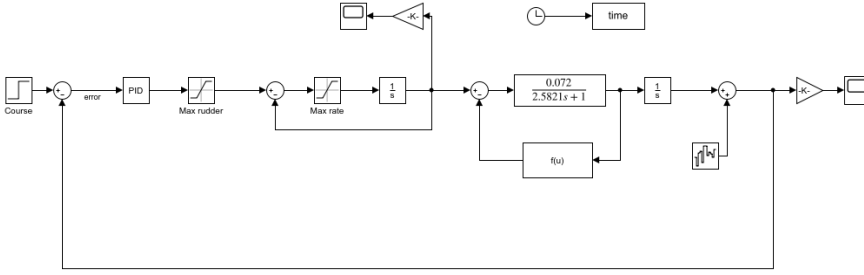


Figure 5.2 Matlab Simulink design for PID controller.

5.2.2 Determination of time constant T and gain K

The PID controller parameters need to be well tuned to obtain an accurate and robust performance. Generally, the PID constants are expressed as a function of the time constant T and the gain K of the Nomoto model, hence the first step is to determine the T and K .

5.2.2.1 Based on the step test

The easiest way to determine the time constant T and the gain K is to perform a step test (Delefortrie et al., 2020), where the rudder angle changes according to the step response δ_s , so that the yaw rate follows the function:

$$r = K\delta_s \left(1 - e^{-\frac{t}{T}}\right) \quad (5.2)$$

When the yaw rate reaches the maximum value, Eq. (5.2) is rewritten as:

$$\lim_{t \rightarrow \infty} r = K\delta_s \quad (5.3)$$

Then, the gain K yields:

$$K = \frac{\lim_{t \rightarrow \infty} r}{\delta_s} \quad (5.4)$$

If $t = T$, Eq. (5.2) yields:

$$r = K\delta_s (1 - e^{-1}) \approx 0.63K\delta_s \quad (5.5)$$

The relationships in Eq. (5.4) and Eq. (5.5) allow to graphically determine K and T . Figure 5.3 shows an example for a simulated step test ($\delta_s=10$ deg) at 8 knots and 100% UKC (Green line) using an LNG ship (see Figure 7.6). In the presented example, the limiting value of yaw rate is -0.261 deg/s (Figure 5.3(a)), then:

$$K = \frac{\lim_{t \rightarrow \infty} r}{\delta_s} = \frac{-0.261}{10} = -0.0261 \text{ s}^{-1} \quad (5.6)$$

Substitute the K value in Eq. (5.6) to Eq. (5.5):

$$r \approx 0.63K\delta_s = -0.63 * 0.0261 * 10 = -0.164 \text{ deg/s} \tag{5.7}$$

The time constant $T \approx 48 \text{ s}$ can be derived from Figure 5.3(b).

To check the accuracy of K and T , the yaw rate is predicted by solving Eq. (5.2) with the calculated K and T . The prediction result is displayed in Figure 5.3 (Orange line), in which the predicted yaw rate is as good as that from the simulation.

Note that a step test is also possibly executed in the towing tank, yet it is dangerous to conduct the step test due to the limited width of the FHR confined towing tank. Thus, the zigzag test is a safer option.

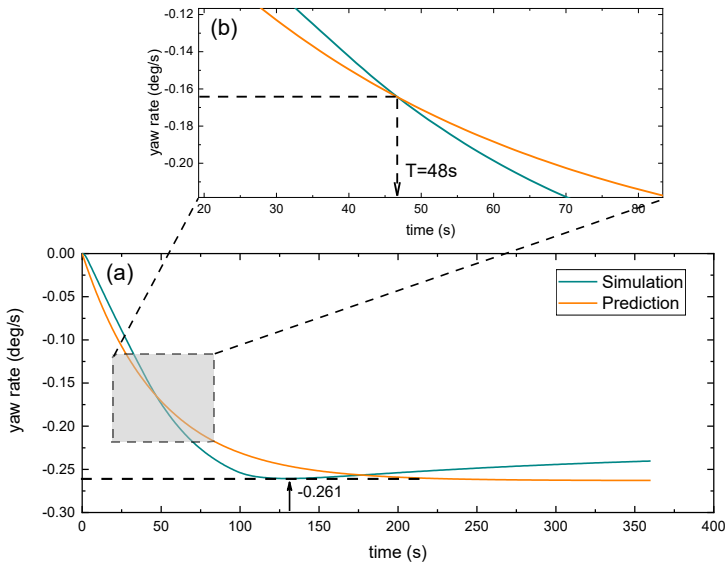


Figure 5.3 Determination of K and T based on a step test ($\delta_s=10 \text{ deg}$) at 8 knots and 100% UKC.

5.2.2.2 Based on the zigzag test

The zigzag manoeuvres executed in this work are slightly different from those recommended by the ITTC (ITTC, 2017) and IMO criteria (IMO, 2002), where the standard test is either a $10^\circ/10^\circ$ or $20^\circ/20^\circ$ zigzag manoeuvre. Due to the limitation of size and vicinity of the tank walls in the test facility, the alternative manoeuvres executed in the FHR towing tank are $10^\circ/2.5^\circ$ or $20^\circ/5^\circ$ zigzag tests (please refer to section 6.6.2 for more information). Figure 5.4 depicts an example for the $20^\circ/5^\circ$ zigzag manoeuvre experiment at speed of 8 knots and 100%UKC. From the zigzag tests, we can obtain the time, yaw rate and rudder deflection data.

A regression method is then used to determine the gain K and the time constant T based on Eq. (5.1).

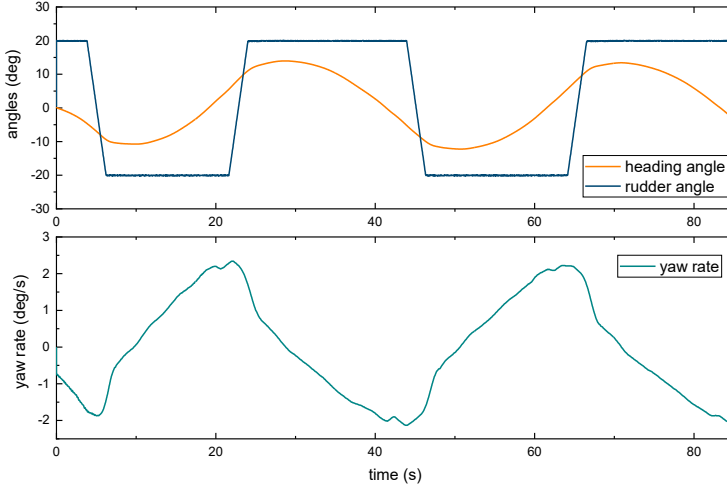


Figure 5.4 20°/5° zigzag manoeuvre experiment at speed of 8 knots and 100% UKC.

5.2.3 Determination of PID parameters

The method proposed by Fossen (1994) is used to determine PID controller parameters in this section. Assume the relative damping ratio $\zeta = 1$ and a bandwidth equal to:

$$\omega_b = \frac{1}{T} \quad (5.8)$$

The natural frequency is then:

$$\omega_n = \frac{\omega_b}{\sqrt{1 - 2\zeta^2 + \sqrt{4\zeta^4 - 4\zeta^2 + 2}}} \quad (5.9)$$

The controller coefficients can be calculated as:

$$K_p = \frac{\omega_n^2 T}{K} \quad (5.10)$$

$$K_i = \frac{\omega_n^3 T}{10K} \quad (5.11)$$

$$K_d = \frac{2\zeta\omega_n T - 1}{K} \quad (5.12)$$

5.3 Internal model controller

5.3.1 Controller structure

The internal model control (IMC) approach is a model-based method, which is characterized by a clear dependency on the control plant parameters (Morari and Zafiriou, 1989). The IMC structure is displayed in Figure 5.5, where ψ_d is the desired heading angle, Q is the design transfer function, δ is the rudder angle, G is the plant to be controlled, \hat{G} is the plant model, Ψ is the system output (actual heading angle), d_1 and d_2 are the input and output disturbances. The actual controller is represented by the box delimited by the dashed dot contour line in Figure 5.5. Note that in Figure 5.5 (dash-dot line) the plant model \hat{G} is embedded in the controller, which is the so-called Internal Model Controller.

After some simplification, the IMC controller (see the box in Figure 5.6(a)) is changed into a classical feedback structure, which is further reduced to a simple transfer function form in Figure 5.6(b).

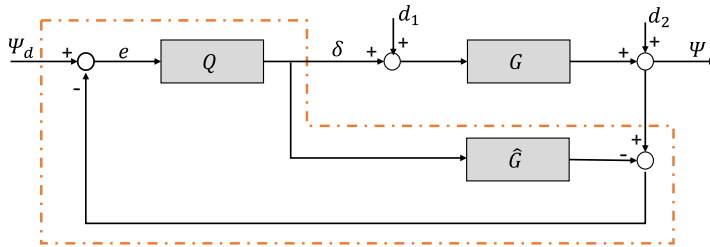


Figure 5.5 Internal model controller structure.

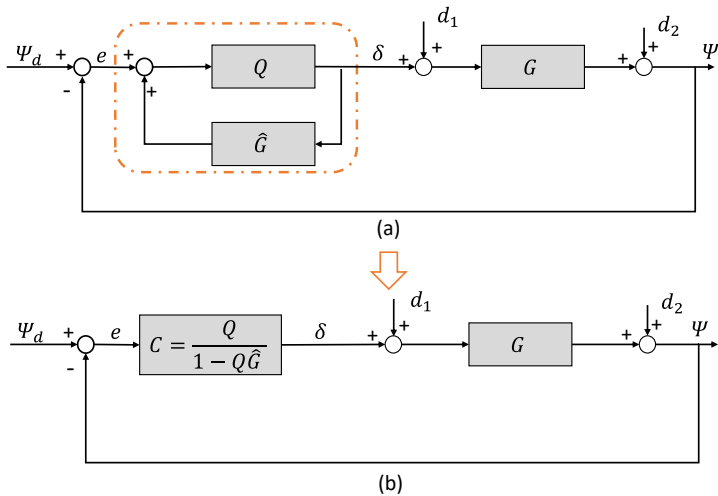


Figure 5.6 Simplified internal model controller structure: (a) classical feedback form; (b) transfer function form.

5.3.2 Controller design

It can be seen from Figure 5.6(b) that the IMC controller is expressed as:

$$C = \frac{Q}{1 - Q\hat{G}} \quad (5.13)$$

where Q is the design transfer function, which is defined as:

$$Q = F\hat{G}_{inv} \quad (5.14)$$

where \hat{G}_{inv} is the inverse model of the plant model \hat{G} , F is the modulating filter defined as:

$$F(s) = \frac{1}{(1 + \beta_c s)^m} \quad (5.15)$$

where β_c is the designed parameter, used to determine the close-loop system response speed, m is a positive integer.

According to the research in Lee et al. (2010) and Saari and Djemai (2012), the plant model \hat{G} is chosen as the first-order Nomoto model:

$$\hat{G} = \frac{\Psi(s)}{\delta(s)} = \frac{K}{s(1 + Ts)} \quad (5.16)$$

while the design transfer function Q of Eq. (5.14) is considered as:

$$Q(s) = \frac{3\beta_c s + 1}{(1 + \beta_c s)^3} \frac{s(1 + Ts)}{K} \quad (5.17)$$

Substituting Eq. (5.16) and Eq. (5.17) in Eq. (5.13) yields:

$$C(s) = \frac{3\beta_c Ts^2 + (3\beta_c + T)s + 1}{\beta_c^3 K s^2 + 3\beta_c^2 K s} \quad (5.18)$$

The controller in Eq. (5.18), can be expressed into a PID format:

$$C(s) = K_p + \frac{K_i}{s} + \frac{K_d s}{\gamma s + 1} \quad (5.19)$$

where $\gamma s + 1$ is employed to eliminate the unwanted differentiating influence in the high frequency region.

When substituting Eq. (5.18) into Eq. (5.19), the PID controller coefficients, derived from the IMC, are:

$$K_p = \frac{(8/3)\beta_c + T}{3\beta_c^2 K} \quad (5.20)$$

$$K_i = \frac{1}{3\beta_c^2 K} \quad (5.21)$$

$$K_d = \frac{(8/3)\beta_c T - (8/9)\beta_c^2}{3\beta_c^2 K} \quad (5.22)$$

$$\gamma = \frac{\beta_c}{3} \quad (5.23)$$

5.4 Adaptive PID controller

5.4.1 Controller structure

Despite the traditional PID controller is widely used, it cannot obtain satisfactory control performance when the navigation environment changes, for instance, the forward speed and the water depth, etc. To solve the speed dependency problem of the PID controller, a new adaptive PID controller was proposed. Determination of speed dependency was done based on the PID parameters (derived by the IMC algorithm) for different forward speeds and checked if a relationship between these set of PID values per sailing speed could be found. The design of the adaptive PID controller was based on the experimental results carried out in the towing tank. To demonstrate the development procedures, the experimental results at 100% UKC were presented as examples. Due to the constant propeller rate per speed was used during experimental studies, the relationship between the controller's coefficients and the propeller rates were investigated and shown in Table 5.1 and Figure 5.7.

Table 5.1 Propeller rate versus PID controller coefficients at 100% UKC.

100% UKC				
Speed (m/s)	n (rps)	K_p	K_i	K_d
0.2376	3.2833	6.9665	0.2597	36.6839
0.3564	4.9250	6.3744	0.3403	24.4352
0.4752	6.5667	6.1329	0.4230	18.6082
0.6534	9.0357	6.5080	0.6485	13.9571
0.7722	10.6774	6.4132	0.7107	12.6429
0.9500	13.1333	6.8850	0.8598	12.2435

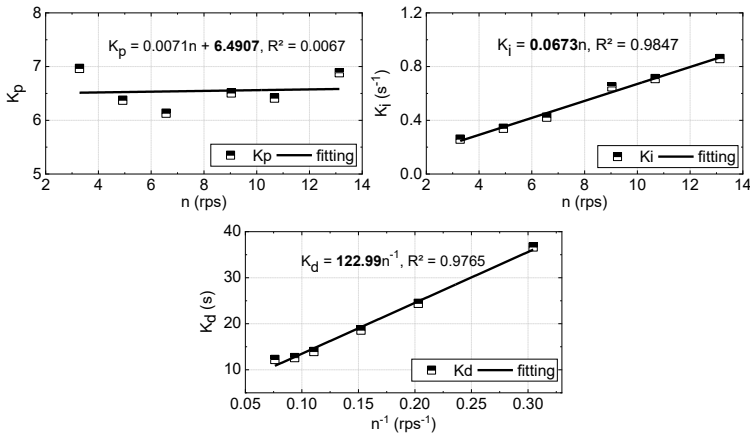


Figure 5.7 Propeller rate versus PID controller coefficients at 100% UKC.

5.4.2 Controller design

As is shown in Figure 5.7, the regression results between the propeller rates and the PID coefficients are summarized as:

$$K_p = K_{pn}n^0 \quad (5.24)$$

$$K_i = K_{in}n^1 \quad (5.25)$$

$$K_d = K_{dn}n^{-1} \quad (5.26)$$

where K_p , K_i , K_d are the proportional, integral, and derivative coefficients, respectively; K_{pn} , K_{in} , K_{dn} are the propeller rate adaptive proportional, integral, and derivative coefficients, respectively, n is the propeller rate.

One can observe in Eq. (5.24) to Eq. (5.26), the proportional coefficient (K_p) is not dependent on the propeller rate, the integral coefficient (K_i) is proportional to the propeller rotating rate (n), and the derivative coefficient (K_d) is inversely proportional to the propeller rotating rate (n) but limited below 1.5 rps (model scale) to avoid excessive derivative action.

5.5 Fuzzy controller

5.5.1 Controller structure

The fuzzy controller gives an appropriate output value for the rudder angle according to the current situation. The current situation is evaluated in terms of heading angle deviation $e = \psi_e$ and the change in time of this deviation $\frac{de}{dt} = \dot{\psi}_e$. Figure 5.8 shows an overview of the fuzzy controller and Figure 5.9 exhibits its Matlab Simulink design.

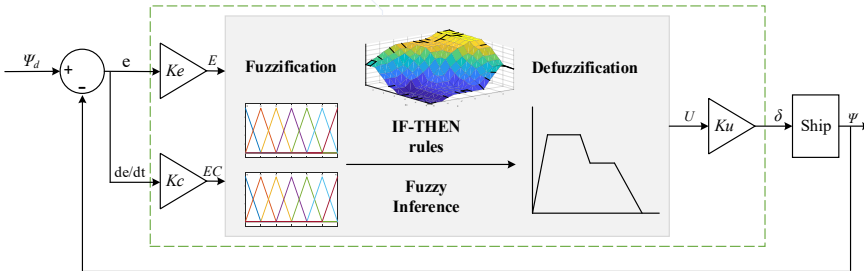


Figure 5.8 Overview of the fuzzy controller.

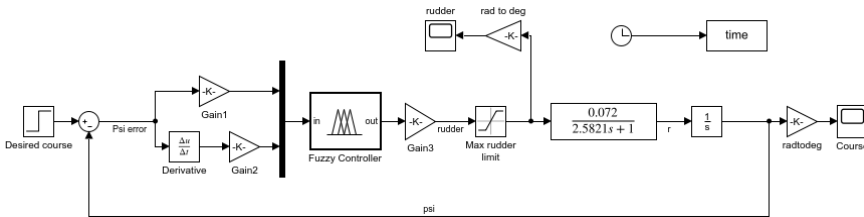


Figure 5.9 Matlab Simulink design for fuzzy controller.

5.5.2 Controller design

It can be seen from Figure 5.8 that the fuzzy control system consists of four blocks, i.e., fuzzification, fuzzy rules, fuzzy inference, and defuzzification (Zadeh, 1965).

Fuzzification: The inputs e and $\frac{de}{dt}$ are multiplied with approximate scale factors K_e and K_c respectively to normalize the errors with a given interval. An error can have different denominations, for instance:

- Negative Big (NB): -3;
- Negative Medium (NM): -2;
- Negative Small (NS): -1;
- Zero (ZO): 0;
- Positive Small (PS): +1;
- Positive Medium (PM): +2;
- Positive Big (PB): +3;

The scaling will then transform e and $\frac{de}{dt}$ to respectively E and EC both having a value between $[-3,+3]$.

If E or EC is an integer value, the process is straightforward. To deal with the problem of intermediate values of E and EC , three membership functions are used in this research:

- Triangle membership function (Figure 5.10);
- Trapezoidal membership function (Figure 5.11);
- Gaussian membership function (Figure 5.12).

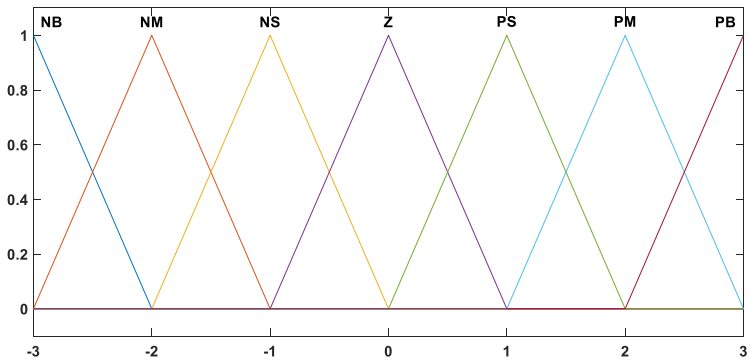


Figure 5.10 Triangle membership function of the fuzzy controller.

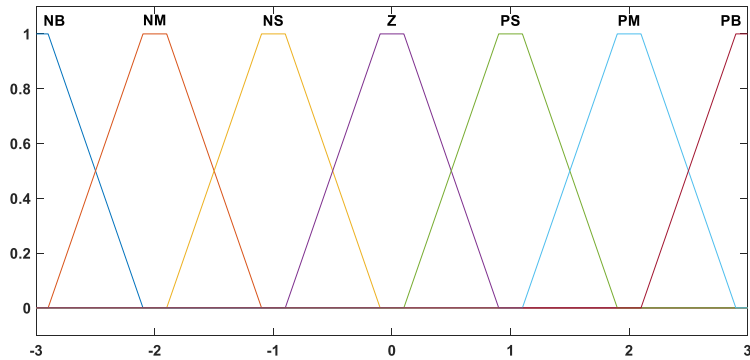


Figure 5.11 Trapezoidal membership function of the fuzzy controller.

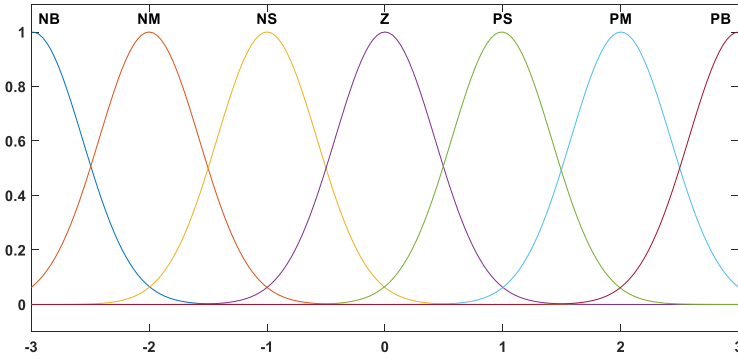


Figure 5.12 Gaussian membership function of the fuzzy controller.

Fuzzy rules: The If-Then rules are adopted to describe the relationship between the fuzzy inputs and outputs, for instance:

If E is PB and EC is PB, then U is PB.

The whole rule matrix is shown in Table 5.2.

Table 5.2 Fuzzy rule matrix.

$E \backslash EC$	NB	NM	NS	ZO	PS	PM	PB
NB	NB	NB	NB	NB	NM	NS	ZO
NM	NB	NB	NB	NM	NS	ZO	PS
NS	NB	NB	NM	NS	ZO	PS	PM
ZO	NB	NM	NS	ZO	PM	PM	PB
PS	NM	NS	ZO	PS	PM	PB	PB
PM	NS	ZO	PS	PM	PB	PB	PB
PB	ZO	PS	PM	PB	PB	PB	PB

Fuzzy Inference: The Sugeno inference system is used to determine the fuzzy relationship R (Figure 5.13) (Sugeno, 1985):

$$R = \cup \left((E_i \times EC_j) \times U_{ij} \right) \tag{5.27}$$

where E_i and EC_j are the fuzzy inference inputs, U_{ij} is the output of the inference, \cup is the union set, i, j are the positive integers.

The output of fuzzy inference U yields:

$$U = (E \times EC)^T \cdot R \tag{5.28}$$

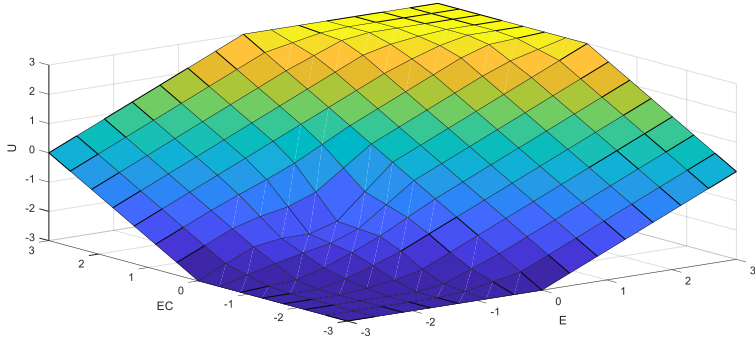


Figure 5.13 Fuzzy inference system.

Defuzzification: The fuzzy output U is converted into crisp value δ by defuzzification process:

$$\delta = \frac{\sum_{k=1}^n U_k \mu_U(U_k)}{\sum_{k=1}^n \mu_U(U_k)} \quad (5.29)$$

where μ_U is the membership of the fuzzy output, k, n are the positive integers.

5.6 Fuzzy PID controller

5.6.1 Controller structure

Fuzzy PID controller is adopted to improve the system adaptability and robustness (Feng, 2006; Khan and Rapal, 2006). The controller structure is depicted in Figure 5.14 and Figure 5.15, where the fuzzy logic controller is used to online tune the gains of the PID control law.

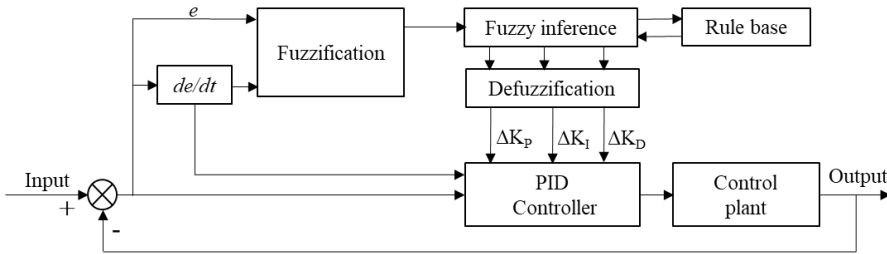


Figure 5.14 Structure of Fuzzy-PID controller.

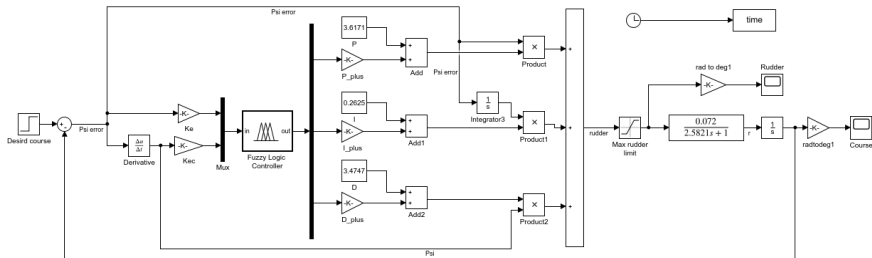


Figure 5.15 Matlab Simulink design for fuzzy PID controller.

5.6.2 Controller design

The procedure of tuning the PID controller gains by the fuzzy logic method is elaborated described as following four modules:

Fuzzification: The heading angle error (e) and the error derivative ($\frac{de}{dt}$) are chosen as fuzzy system inputs, the tuning gains ΔK_p , ΔK_I and ΔK_D are assigned as three outputs. Each input and output are defined as seven fuzzy sets: Negative Big (NB), Negative Medium (NM), Negative Small (NS), Zero (ZO), Positive Small (PS), Positive Medium (PM), Positive Big (PB). For input and output variables, their membership degrees for every fuzzy set are calculated by one of following membership functions:

- Triangle membership function (Figure 5.10);
- Trapezoidal membership function (Figure 5.11);
- Gaussian membership function (Figure 5.12);

Fuzzy rules: The fuzzy rules are defined based on nautical practice. In the present study, the If-then rules are utilized to describe the relationships between the antecedents and consequents:

If E is NB and EC is NB, then ΔK_P is PB, ΔK_I is NB and ΔK_D is PS

The fuzzy rule matrices for ΔK_P , ΔK_I and ΔK_D are shown in Table 5.3-Table 5.5.

Table 5.3 Fuzzy rules for ΔK_P .

EC \ E	NB	NM	NS	ZO	PS	PM	PB
NB	PB	PB	PM	PM	PS	ZO	ZO
NM	PB	PB	PM	PS	PS	ZO	NS
NS	PM	PM	PM	PS	ZO	NS	NS
ZO	PM	PM	PS	ZO	NS	NM	NM
PS	PS	PS	ZO	NS	NS	NM	NM
PM	PS	ZO	NS	NM	NM	NM	NB
PB	ZO	ZO	NM	NM	NM	NM	NB

Table 5.4 Fuzzy rules for ΔK_I .

EC \ E	NB	NM	NS	ZO	PS	PM	PB
NB	NB	NB	NM	NM	NS	ZO	ZO
NM	NB	NB	NM	NS	NS	ZO	ZO
NS	NM	NM	NS	NS	ZO	PS	PS
ZO	NM	NM	NS	ZO	PS	PM	PM
PS	NM	NS	ZO	PS	PS	PM	PB
PM	ZO	ZO	PS	PS	PM	PB	PB
PB	ZO	ZO	PS	PM	PM	PB	PB

Table 5.5 Fuzzy rules for ΔK_D .

EC \ E	NB	NM	NS	ZO	PS	PM	PB
NB	PS	NS	NB	NB	NB	NM	PS
NM	PS	NS	NB	NM	NM	NS	ZO
NS	ZO	NS	NM	NM	NS	NS	ZO
ZO	ZO	NS	NS	NS	NS	NS	ZO
PS	ZO						
PM	PB	NS	PS	PS	PS	PS	PB
PB	PB	PM	PM	PM	PS	PS	PB

Fuzzy Inference: In this process, the Sugeno reasoning method is selected to map the given inputs to the fuzzy outputs (Sugeno, 1985). The fuzzy inference results are displayed in Figure 5.16-Figure 5.18.

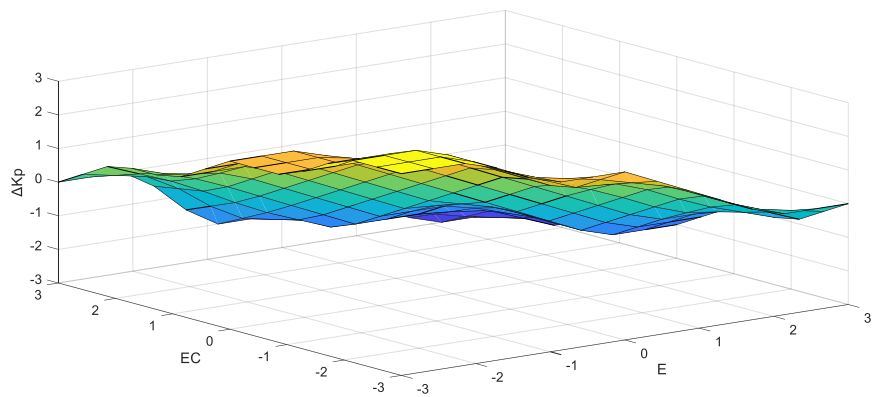


Figure 5.16 Fuzzy inference for ΔK_p .

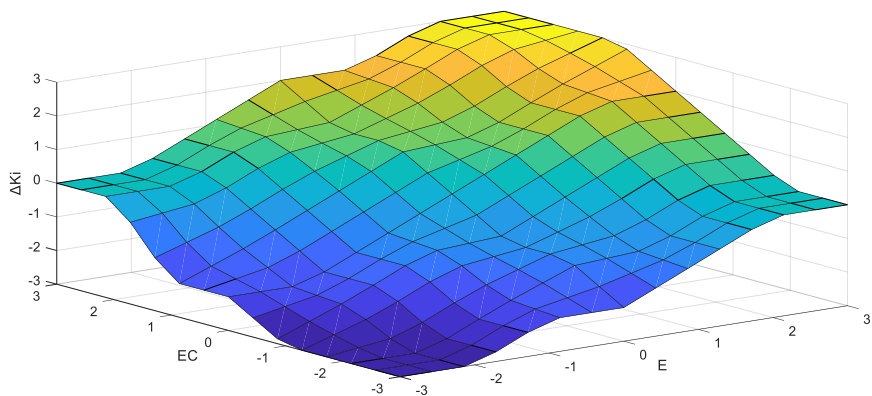


Figure 5.17 Fuzzy inference for ΔK_i .

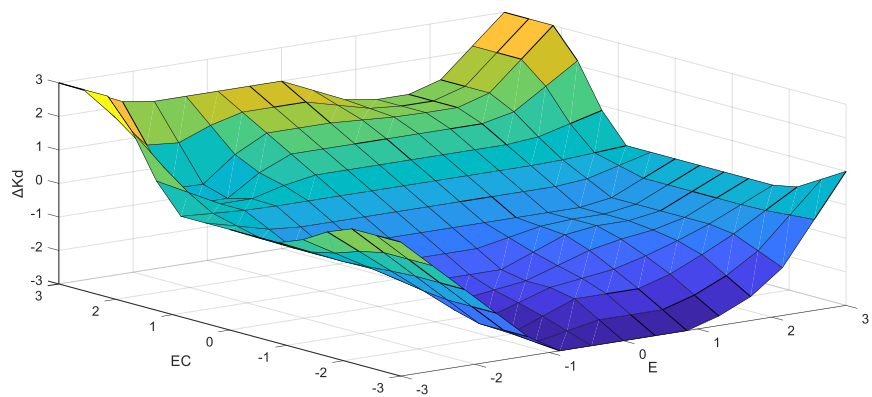


Figure 5.18 Fuzzy inference for ΔK_d .

Defuzzification: The fuzzy outputs are converted into crisp values ΔK_p , ΔK_I and ΔK_D by the defuzzification process. Then, the tuned gains ΔK_p , ΔK_I and ΔK_D are added in the PID controller.

5.7 Backstepping controller

5.7.1 Controller structure

The backstepping algorithm is a systematic method for designing stabilizing controls for nonlinear systems (Pettersen and Nijmeijer, 2001; Zhang et al., 2018). The control mechanism is built to decompose the complex nonlinear systems into some simple and irreducible subsystems, which can be stabilized by employing some special techniques, such as the Lyapunov stabilization approach (Lypunov, 1992). In each subsystem, the virtual control law can be obtained on the premise of ensuring the convergence of subsystems. When designing the next subsystem, the virtual control term of the former subsystem is used as a control target for the next subsystem. The same manner can be taken by the rest subsystems. Finally, the actual control term of the whole nonlinear system can be obtained, at the same time, the system stability can be guaranteed by the Lyapunov analysis method. Figure 5.19 shows the structure of the backstepping controller.

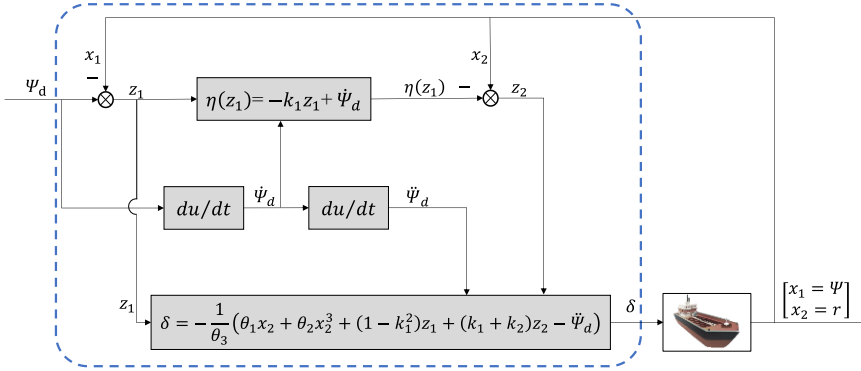


Figure 5.19 Structure of backstepping controller.

5.7.2 Controller design

To illustrate the procedure of the backstepping control algorithm, the Nomoto nonlinear ship math model is used to describe a ship nonlinear system, reflecting the relationship between the rudder angle and the heading angle. The ship math model is expressed as:

$$T\ddot{\Psi} + \dot{\Psi} + \alpha\Psi^3 = K\delta \quad (5.30)$$

Or

$$T\dot{r} + r + \alpha r^3 = K\delta \quad (5.31)$$

$$\dot{r} = -\frac{1}{T}r - \frac{\alpha}{T}r^3 + \frac{K}{T}\delta \quad (5.32)$$

where Ψ is the heading angle, T is the time constant, α is the nonlinear parameter, K is the gain, r is the yaw rate. The single dotted and double dotted variables represent the first and second order derivatives.

Define $x_1 = \Psi$, $x_2 = \dot{x}_1 = r$, then the nonlinear ship model is transformed as:

$$\begin{cases} \dot{x}_1 = x_2 \\ \dot{x}_2 = \dot{r} = -\frac{1}{T}r - \frac{\alpha}{T}r^3 + \frac{K}{T}\delta \end{cases} \quad (5.33)$$

Denote $\theta_1 = -\frac{1}{T}$, $\theta_2 = -\frac{\alpha}{T}$, $\theta_3 = \frac{K}{T}$, then

$$\begin{cases} \dot{x}_1 = x_2 \\ \dot{x}_2 = \theta_1 r + \theta_2 r^3 + \theta_3 \delta \end{cases} \quad (5.34)$$

Define Ψ is the actual heading, Ψ_d is the desired heading, then the error is:

$$z_1 = \Psi - \Psi_d = x_1 - \Psi_d \quad (5.35)$$

At the same time, introduce a new variable z_2 , which is used to stabilize the control system:

$$z_2 = x_2 - \eta(z_1) \quad (5.36)$$

where $\eta(z_1)$ is the virtual control law.

Differentiate the error z_1 as:

$$\dot{z}_1 = \dot{x}_1 - \dot{\Psi}_d = x_2 - \dot{\Psi}_d = z_2 + \eta(z_1) - \dot{\Psi}_d \quad (5.37)$$

Construct the first Lyapunov function:

$$V_1 = \frac{1}{2}z_1^2 \quad (5.38)$$

Differentiate the Lyapunov function V_1 :

$$\dot{V}_1 = z_1 \dot{z}_1 = z_1(z_2 + \eta(z_1) - \dot{\Psi}_d) \quad (5.39)$$

Design the virtual control law $\eta(z_1)$ as:

$$\eta(z_1) = -k_1 z_1 + \dot{\Psi}_d \quad (5.40)$$

where k_1 is the design parameter.

Insert $\eta(z_1)$ in Eq. (5.39), then:

$$\dot{V}_1 = -k_1 z_1^2 + z_1 z_2 \quad (5.41)$$

Construct the second Lyapunov function:

$$V_2 = V_1 + \frac{1}{2}z_2^2 \quad (5.42)$$

Differentiate the Lyapunov function V_2 :

$$\begin{aligned} \dot{V}_2 &= \dot{V}_1 + z_2\dot{z}_2 \\ &= -k_1z_1^2 + z_1z_2 + z_2\dot{z}_2 \\ &= -k_1z_1^2 + z_2(z_1 + \dot{z}_2) \\ &= -k_1z_1^2 + z_2(z_1 + \dot{x}_2 - \dot{\eta}(z_1)) \end{aligned} \quad (5.43)$$

where:

$$\dot{x}_2 = \theta_1x_2 + \theta_2x_2^3 + \theta_3\delta \quad (5.44)$$

$$\begin{aligned} \dot{\eta}(z_1) &= -k_1\dot{z}_1 + \ddot{\Psi}_d \\ &= -k_1(z_2 + \eta(z_1) - \dot{\Psi}_d) + \ddot{\Psi}_d \\ &= -k_1(z_2 - k_1z_1 + \dot{\Psi}_d - \dot{\Psi}_d) + \ddot{\Psi}_d \\ &= -k_1(-k_1z_1 + z_2) + \ddot{\Psi}_d \\ &= k_1^2z_1 - k_1z_2 + \ddot{\Psi}_d \end{aligned} \quad (5.45)$$

Then:

$$\begin{aligned} \dot{V}_2 &= -k_1z_1^2 + z_2(z_1 + \theta_1x_2 + \theta_2x_2^3 + \theta_3\delta - k_1^2z_1 + k_1z_2 - \ddot{\Psi}_d) \\ &= -k_1z_1^2 + z_2(\theta_1x_2 + \theta_2x_2^3 + \theta_3\delta + (1 - k_1^2)z_1 + k_1z_2 - \ddot{\Psi}_d) \end{aligned} \quad (5.46)$$

To guarantee the system stability, the \dot{V}_2 should be negative ($\dot{V}_2 < 0$), then the final control input δ is selected as:

$$\delta = -\frac{1}{\theta_3}(\theta_1x_2 + \theta_2x_2^3 + (1 - k_1^2)z_1 + (k_1 + k_2)z_2 - \ddot{\Psi}_d) \quad (5.47)$$

where k_2 is the design parameter. Substitute Eq. (5.47) into Eq. (5.46):

$$\dot{V}_2 = -k_1z_1^2 - k_2z_2^2 < 0 \quad (5.48)$$

According to the Lyapunov theory, the designed control law can make the nonlinear system asymptotically stable at the equilibrium point $x_1 = \Psi_d$, $x_2 = \dot{\Psi}_d$.

Based on the calculation of Eq. (5.33) and Eq. (5.34), the final control input is:

$$\begin{aligned}
 \delta &= -\frac{T}{K} \left[-\frac{1}{T}x_2 - \frac{\alpha}{T}x_2^3 + (1 + k_1k_2)(x_1 - \Psi_d) + (k_1 + k_2)(x_2 - \Psi_d) \right. \\
 &\quad \left. - \dot{\Psi}_d \right] \\
 &= \frac{T}{K} \left[\frac{1}{T}x_2 + \frac{\alpha}{T}x_2^3 - (1 + k_1k_2)(x_1 - \Psi_d) - (k_1 + k_2)(x_2 - \Psi_d) + \dot{\Psi}_d \right] \\
 &= \frac{T}{K} \left[\frac{1}{T}r + \frac{\alpha}{T}r^3 - (1 + k_1k_2)(x_1 - \Psi_d) - (k_1 + k_2)(r - \Psi_d) + \dot{\Psi}_d \right] \\
 &= \frac{T}{K} \left[\frac{1}{T}x_2 + \frac{\alpha}{T}x_2^3 - (1 + k_1k_2)(x_1 - \Psi_d) - (k_1 + k_2)(x_2 - \Psi_d) + \dot{\Psi}_d \right] \\
 &= \frac{1}{K} (x_2 + \alpha x_2^3) - \frac{T}{K} [(1 + k_1k_2)(x_1 - \Psi_d) + (k_1 + k_2)(x_2 - \Psi_d) - \dot{\Psi}_d]
 \end{aligned} \tag{5.49}$$

5.8 Nonlinear feedback and nonlinear decoration filters

5.8.1 Nonlinear feedback filter

In this section, two types of filters are used to improve the controller performance. The first filter $f(e)$ is applied to the control input e (heading angle error) in order to eliminate high-frequency noise or oscillations of the heading angle. This process is defined as a nonlinear feedback mechanism (Zhang et al., 2016), see Figure 5.20.

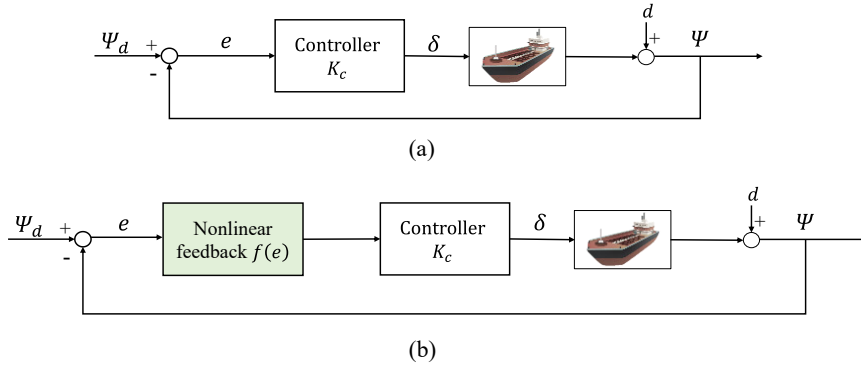


Figure 5.20 Standard feedback control (a); Nonlinear feedback control (b).

Compared with the standard feedback configuration, a nonlinear function $f(e)$ is introduced into the control system to regulate the heading angle error (e), then the control output δ yields:

$$\delta = K_c(f(e)) \quad (5.50)$$

where δ is rudder angle; $K_c(\cdot)$ is the controller function; $f(\cdot)$ is the nonlinear feedback function; e is the heading angle error.

In this work, three functions are adopted to nonlinear feedback design as follows:

- Sinusoidal:

$$f(e) = \sin(ce) \quad (5.51)$$

- Inverse tangent:

$$f(e) = \text{atan}(ce) \quad (5.52)$$

- tanh or exponential:

$$f(e) = \frac{1 - e^{-2ce}}{1 + e^{-2ce}} \quad (5.53)$$

where c is a tuning factor.

Each of the above filters can be applied on heading angle error e , provided its value is transformed to radians first and before applying any of the controller described in sections 5.2 to 5.7. To have a clearer understanding of the nonlinear feedback mechanism, taking the PID controller (section 5.2) as an example, the sinusoidal function (Eq. (5.51)) is used to adjust the heading angle error e , the nonlinear feedback PID controller is presented in Figure 5.21.

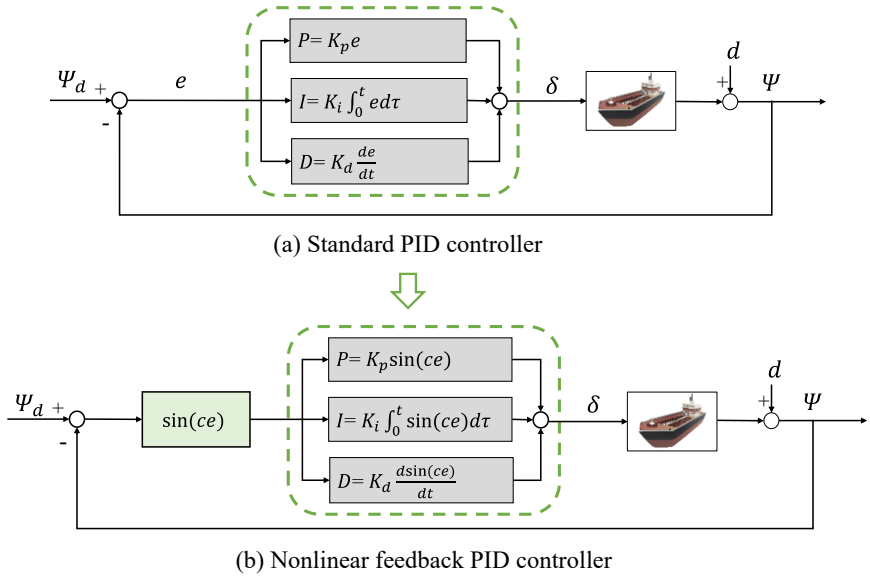


Figure 5.21 Standard PID controller and nonlinear feedback PID controller.

5.8.2 Nonlinear decoration filter

The control output or rudder angle δ can also be attenuated by a nonlinear decoration algorithm $h(\delta)$, see Figure 5.22. The purpose of using the nonlinear decorator is to reduce the rudder efforts and enhance rudder efficiency while the controller system’s performance is not significantly changed (Zhang et al., 2018). Three functions are also applied to the nonlinear decoration design as follows:

- Sinusoidal:

$$h(\delta) = \sin(c\delta) \tag{5.54}$$

- Inverse tangent:

$$h(\delta) = \text{atan}(c\delta) \tag{5.55}$$

- tanh or exponential:

$$h(\delta) = \frac{1 - e^{-2c\delta}}{1 + e^{-2c\delta}} \tag{5.56}$$

where c is a tuning factor.

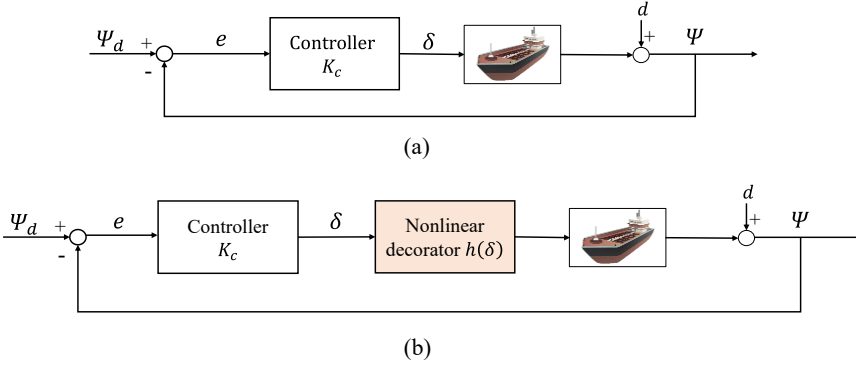


Figure 5.22 Structure of nonlinear decoration design: (a) standard controller; (b) controller with nonlinear decorator.

After applying one of the control methods described in sections 5.2 to 5.7, the output can be filtered according to the nonlinear decoration algorithm. One example of the PID controller decorated by the sinusoidal function is shown in Figure 5.23. Mind that the control output δ should be transformed to radians first and before using any of the controllers.

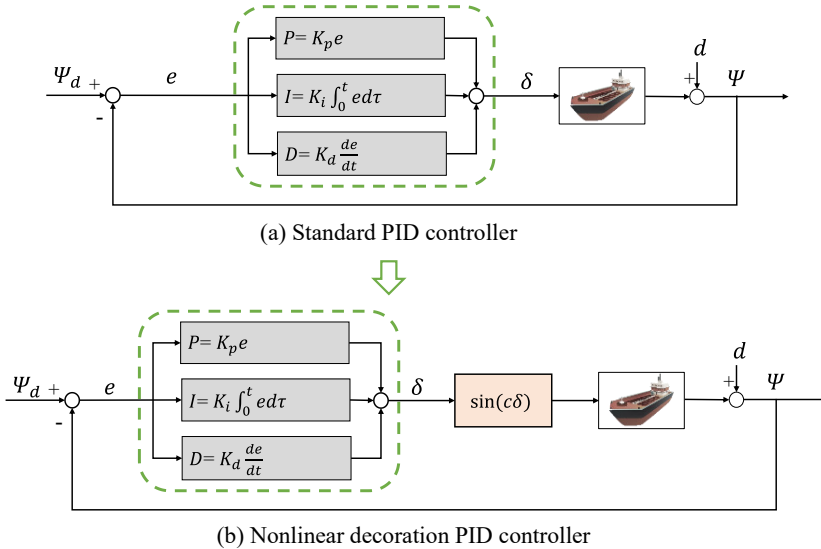


Figure 5.23 Standard PID controller (a) and nonlinear decoration PID controller (b).

5.9 Speed controller

5.9.1 Controller structure

In order to be able to perform tests at a constant forward velocity, a speed controller is deemed necessary. Because when the ship is making a turn, she will decelerate due to the increased resistance. In this section, a PI (Proportional Integral) speed controller is introduced, which has been validated via experiments and simulations by Maes (2020). The PI control law has been implemented in the towing tank autopilot system and ship manoeuvring simulators at FHR. The control algorithm is formulated as:

$$\Delta n = K_{pu}\Delta u + K_{iu} \int \Delta u \quad (5.57)$$

where Δu is the difference between the actual forward speed and the desired speed, Δn represents the change of propeller rate to counteract the forward speed error, K_{pu} and K_{iu} are the P and I gains of the PI speed controller.

5.9.2 Determination of K_{pu} and K_{iu}

To determine a value of K_{pu} in PI speed controller, the relationship between the propeller rates n and forward speed u should be known, which can be obtained based on the results of straight line acceleration tests (self-propulsion tests). After execution of such acceleration tests with the different propeller rates, a linear relationship can be found by using a regression method. The relationship can be expressed as:

$$u = \alpha n \quad (5.58)$$

where u is the forward speed, α is the regression coefficient, n is the propeller rate.

The determined α -value is of importance for the determination of K_{pu} , according to Eq. (5.58), the parameter K_{pu} can be derived as:

$$K_{pu} \sim \Delta n / \Delta u \sim n / u = \alpha^{-1} \quad (5.59)$$

For K_{iu} , there is no information available in literature about how to obtain the optimal value. According to the experimental and simulation results, $K_{iu} = K_{pu} / 10 = 1 / (10\alpha)$ gives satisfactory results.

5.9.3 Tolerance interval and propeller rate limiter

On one hand, the speed measuring equipment is subject to small inaccuracies, on the other hand, it is difficult to achieve a perfectly constant speed. Combination of both results in a continuously fluctuating forward speed, consequently resulting in a continuously fluctuating value for the desired propeller rate. To avoid heavy oscillations on the propeller, a tolerance interval is specified. Then, the speed

controller is only activated when the forward speed drops out this tolerance interval. A tolerance interval $[0.99u_d, 1.01u_d]$ has been proved proper working, where u_d represents the desired forward speed.

In addition, during simulated speed increase tests by using the first design of the speed controller, it is observed that large propeller rates are used, and significant overshoots of forward speed occur. Large propeller rates result in the increase of the fuel consumption, which should be avoided. Thus, a propeller rate limiter is used as well:

$$0.9n_{expect} < n_{actual} < 1.1n_{expect} \quad (5.60)$$

where n_{expect} and n_{actual} are the expected and actual propeller rates, respectively. The above propeller rate limits are determined based on simulation studies, and they can be tuned according to the actual needs.

5.10 sController performance evaluation

5.10.1 Evaluation procedure

A new evaluation procedure was proposed to assess the specified controllers' path following performance. Firstly, the numerical simulations or model tests are conducted to collect the controller related data, e.g. ship position, heading angle, rudder angle, etc. Based on test data, an evaluation mechanism is developed to calculate the performance specifications of controllers. According to the calculated evaluation indexes, the Grey Relational Decision-Making (GRDM) approach is used to select the best controller. The detailed procedure displays in Figure 5.24.

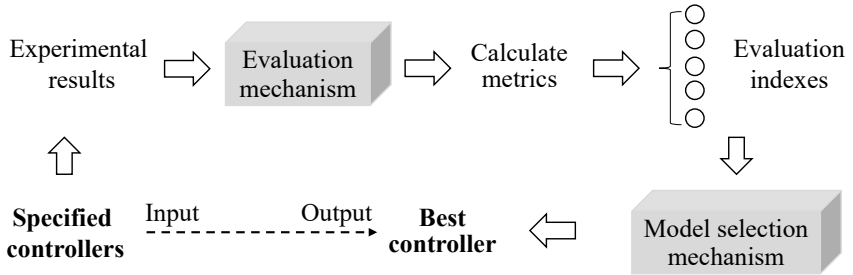


Figure 5.24 Controller performance evaluation procedure.

5.10.2 Evaluation mechanism

In this section, five performance specifications are selected to describe and compare controller performance, they are:

- mean Track Error Integral (mTEI):

$$\text{mTEI} = \frac{1}{t_{\infty} - t_0} \int_{t_0}^{t_{\infty}} |T_e(t)| dt \quad (5.61)$$

- Maximum Track Error (MTE):

$$\text{MTE} = \text{Max}|T_e(t)| \quad (5.62)$$

- mean Rudder Integral (mRI):

$$\text{mRI} = \frac{1}{t_{\infty} - t_0} \int_{t_0}^{t_{\infty}} |\delta(t)| dt \quad (5.63)$$

- mean Rudder Total Variation (mRTV):

$$\text{mRTV} = \frac{1}{t_\infty - t_0} \int_{t_0}^{t_\infty} |\delta(t) - \delta(t - 1)| dt \quad (5.64)$$

- mean Heading Error Integral (mHEI):

$$\text{mHEI} = \frac{1}{t_\infty - t_0} \int_{t_0}^{t_\infty} |\Psi_e(t)| dt \quad (5.65)$$

where t is the time, T_e is the cross track error, δ is the rudder angle, Ψ_e is the heading angle error.

mTEI and MTE are used to measure the mean and maximum of cross track error, while mRI and mRTV are employed to describe the amplitude and smoothness of rudder angle. Moreover, mHEI represents the mean heading angle error.

5.10.3 Model selection mechanism

Based on the above evaluation indexes, the grey relational decision-making method is adopted to determine the optimum controller. It is a classic multi-criteria decision-making approach, which can select the best control algorithm according to the controller properties (Yang, 2013; Zhao and Kang, 2007). The procedure is described as follows:

Define initial decision matrix:

n different alternatives and m attributes compose the initial decision matrix. In initial decision matrix, the reference series $X_0 = (x_0(1), x_0(2), \dots, x_0(m))^T$ is determined, $x_0(j)$ is the best performance value in the j^{th} attribute. Then the initial decision matrix yields:

$$(X_0, X_1, \dots, X_n) = \begin{pmatrix} x_0(1) & x_1(1) & \dots & x_n(1) \\ x_0(2) & x_1(2) & \dots & x_n(2) \\ \vdots & \vdots & \ddots & \vdots \\ x_0(m) & x_1(m) & \dots & x_n(m) \end{pmatrix}, (0 \leq i \leq n, 1 \leq j \leq m) \quad (5.66)$$

Non-dimensional initial matrix:

$$X'_i(j) = \frac{X_i(j)}{X_0(j)} (0 \leq i \leq n, 1 \leq j \leq m) \quad (5.67)$$

$$(X'_0, X'_1, \dots, X'_n) = \begin{pmatrix} x'_0(1) & x'_1(1) & \dots & x'_n(1) \\ x'_0(2) & x'_1(2) & \dots & x'_n(2) \\ \vdots & \vdots & \ddots & \vdots \\ x'_0(m) & x'_1(m) & \dots & x'_n(m) \end{pmatrix} \quad (5.68)$$

Calculate the difference $\Delta_i(j)$ between the alternative series and the reference series:

$$\Delta_i(j) = |x'_0(j) - x'_i(j)|, (0 \leq i \leq n, 1 \leq j \leq m) \quad (5.69)$$

$$\Delta = \begin{pmatrix} \Delta_1(1) & \Delta_2(1) & \cdots & \Delta_n(1) \\ \Delta_1(2) & \Delta_2(2) & \cdots & \Delta_n(2) \\ \vdots & \vdots & \ddots & \vdots \\ \Delta_1(m) & \Delta_2(m) & \cdots & \Delta_n(m) \end{pmatrix} \quad (5.70)$$

Calculate the grey relational coefficient:

The grey relational coefficient between the alternative series and the reference series are calculated by:

$$\xi_i(j) = \frac{\min_i \min_j \Delta_i(j) + \rho \max_i \max_j \Delta_i(j)}{\Delta_i(j) + \rho \max_i \max_j \Delta_i(j)} \quad (5.71)$$

where the identification coefficient $\rho = 0.5$, which provides good stability for calculation.

Then, the grey relational coefficient matrix is formulated as:

$$\xi = \begin{pmatrix} \xi_1(1) & \xi_2(1) & \cdots & \xi_n(1) \\ \xi_1(2) & \xi_2(2) & \cdots & \xi_n(2) \\ \vdots & \vdots & \ddots & \vdots \\ \xi_1(m) & \xi_2(m) & \cdots & \xi_n(m) \end{pmatrix} \quad (5.72)$$

Calculate the grey relational degree γ_i :

$$\gamma_i = \frac{1}{m} \sum_{j=1}^m \xi_i(j) \quad (5.73)$$

The grey relational degree γ_i can be used to rank the alternatives (controllers) by the similarity between the alternative series and the reference series (the best control performance). The best controller can be determined according to the maximum grey relational degree γ_i . Mind that it is assumed that all five criteria have the same importance.

5.11 Reference

- Delefortrie, G., Eloot, K., and Mostaert, F.,** 2020. *Ship manoeuvring behaviour subreport 13: execution of free running tests with the Q-flex (report)*.
- Feng, G.,** 2006. *A survey on analysis and design of model-based fuzzy control systems*. IEEE Transactions on Fuzzy Systems, 14(5), 676–697.
- Fossen, T. I.,** 1994. *Guidance and control of ocean vehicles*. New York, United States: John Wiley & Sons Inc.
- IMO.,** 2002. *Explanatory notes to the standards for ship manoeuvrability*.
- ITTC.,** 2017. *Full scale manoeuvring trials. ITTC – Recommended Procedures and Guidelines*.
- Khan, A. A., and Rapal, N.,** 2006. *Fuzzy PID controller: Design, tuning and comparison with conventional PID controller*. In *IEEE International Conference on Engineering of Intelligent Systems, ICEIS 2006*. Islamabad, Pakistan.
- Lee, S. D., Yu, C. H., Hsiu, K. Y., Hsieh, Y. F., et al.,** 2010. *Design and experiment of a small boat track-keeping autopilot*. Ocean Engineering, 37, 208–217.
- Lypunov, A.,** 1992. *General problem of the stability of motion*. International Journal of Control, 55(3), 521–527.
- Maes, K.,** 2020. *Update of an autopilot for free running model tests with a twin screw/twin rudder tanker*. Ghent University (Master thesis).
- Minorsky, N.,** 1922. *Directional stability of automatically steered bodies*. Journal of the American Society for Naval Engineers, 34(2), 280–309.
- Morari, M., and Zafiriou, E.,** 1989. *Robust Process Control*. Englewood Cliffs (N.J.): Prentice-Hall.
- Peeters, G., Kotzé, M., Afzal, M. R., Catoor, T., et al.,** 2020. *An unmanned inland cargo vessel: Design, build, and experiments*. Ocean Engineering, 201, 107056.
- Pettersen, K. Y., and Nijmeijer, H.,** 2001. *Underactuated ship tracking control: Theory and experiments*. International Journal of Control, 74(14), 1435–1446.
- Saari, H., and Djemai, M.,** 2012. *Ship motion control using multi-controller structure*. Ocean Engineering, 55, 184–190.
- Sugeno, M.,** 1985. *An introductory survey of fuzzy control*. Information Sciences, 36, 59–83.

- Yang, Z.**, 2013. *The multi-objective decision-making model based on grey correlation degree*. In *Proceedings of 2013 IEEE International Conference on Grey systems and Intelligent Services (GSIS)*. Macao, China.
- Zadeh, L. A.**, 1965. *Fuzzy sets*. *Information and Control*, 8(3), 338–353.
- Zhang, X. K., Zhang, G. Q., and Chen, X. J.**, 2016. *A novel nonlinear feedback control and its application to course-keeping autopilot*. *Journal of Marine Science and Technology (Taiwan)*, 24(2), 192–198.
- Zhang, X. K., Zhang, Q., Ren, H. X., and Yang, G. P.**, 2018. *Linear reduction of backstepping algorithm based on nonlinear decoration for ship course-keeping control system*. *Ocean Engineering*, 147, 1–8.
- Zhao, J., and Kang, Z.**, 2007. *A model based on the grey system for multi-objective decision-making and its application in the shipbuilding project*. *Chinese Journal of Management Science*, 16, 187–191.

Ship motion control systems

6	Experimental program	159
6.1	General discussion	159
6.2	Experimental setup	160
6.2.1	Towing tank.....	160
6.2.2	Ship model.....	162
6.3	Beam and coordinate systems	164
6.3.1	Captive and free running model tests	164
6.3.2	Coordinate systems in towing tank.....	166
6.4	Test conditions	168
6.4.1	Water depths.....	168
6.4.2	Forward speeds.....	170
6.5	Post processing	172
6.5.1	Postprocessing theory.....	172
6.5.2	Postprocessing by softwares.....	173
6.6	Experimental results	176
6.6.1	Self-propulsion tests	176
6.6.2	Zigzag tests.....	178
6.6.3	Course tests.....	182
6.6.4	Path following tests	186
6.7	Shallow water and speed effects	202
6.7.1	Effects on manoeuvring indices K and T	202
6.7.2	Effects on controller parameters.....	207
6.7.3	Effects on controller performance	211
6.7.4	Improvement of controllers' performance.....	217
6.8	Reference	223

All life is an experiment. The more experiments you make the better.

--Ralph Waldo Emerson

6

Experimental program

6.1 General discussion

Although great efforts have been made to design advanced control algorithms, most studies concentrated on theoretical analysis, but these are often too complex to apply in practical engineering. Moreover, controllers were mostly investigated in numerical simulation runs, there is only a very limited amount of test results dedicated to the controller development available in publications, and such tests were conducted in deep water. Yet, most harbours and inland canals are located in shallow water areas. The finite water depth reduces the under keel clearance (UKC), hence changing the ship hydrodynamics and increasing the control difficulty. Therefore, the investigation of ship autopilots in shallow water becomes even more necessary and critical.

To investigate the controller performance in shallow water, a comprehensive experimental research program has been carried out, consisting of about 5000 model tests. These tests can be categorized into two main groups, i.e. course control tests and path following control tests. All tests were carried out in free running mode, and four different autopilot algorithms were tested using a scale model of a Liquefied Natural Gas (LNG) carrier in the confined towing tank at Flanders Hydraulics Research (FHR). The program covered different forward speeds and UKCs focusing on the autopilot performance in shallow water.

6.2 Experimental setup

6.2.1 Towing tank

6.2.1.1 Overview

The experimental investigation of ship autopilots was carried out in the Towing Tank for Manoeuvres in Confined Water (co-operation Flanders Hydraulics Research and Ghent University) in Antwerp, Belgium. The towing tank has a total length of 87.5 m, a width of 7.0 m, and a maximum water depth of 0.5 m. The useful length of the towing tank is limited to 68.0 m due to the presence of a wave maker and a harbour (see Table 6.1 and Figure 6.1). These dimensions are sufficient for the execution of manoeuvring and autopilot tests with ship scale models ranging from 3.5 m to 4.5 m at moderate or low speeds. In addition, a wave maker is installed at the end of the towing tank (Figure 6.1), which can be used to generate long crested regular and irregular waves. As such, the forces acting on the ship model due to wave action and the influence of wave action on the manoeuvring behaviour of a ship model can be determined. Detailed information about this towing tank can be obtained in Delefortrie et al. (2016).

Table 6.1 Main dimensions of towing tank for Manoeuvres in Confined Water.

Items	Value	Units
Total length	87.5	(m)
Useful length	68.0	(m)
Width	7.0	(m)
Maximum water depth	0.50	(m)
Length of the ship models	3.5-4.5	(m)



Figure 6.1 Bird's eye view of towing tank for Manoeuvres in Confined Water.

6.2.1.2 Motion mechanism

The ship model is controlled by a main carriage (Figure 6.2), which can run over the rails. The motion mechanism consists of a longitudinal carriage (main carriage), a lateral carriage, a yawing table, and a roll mechanism, allowing an arbitrary movement in the horizontal plane as well as roll motion (Delefortrie et al., 2016). The main kinematic characteristics in the horizontal plane are presented in Table 6.2.

The towing tank application software allows the operator to manually control the carriage, to calibrate the ship position, and to adjust the settings to execute the tests, etc. During tests, the towing carriage is fully computer-controlled and operates so that test programs run unmanned and automatically 24 hours a day, 7 days a week. This is a huge advantage over manually controlled carriages. Due to the necessity of a waiting time between two test runs for water to calm down, an average of 35 tests can be carried out in 24 hours.



Figure 6.2 Motion mechanism of towing tank carriage.

Table 6.2 Range of positions, velocities, and accelerations of towing tank motion mechanism at FHR.

	Main carriage	Lateral carriage	Yawing table
Minimal position	0.00 m	-2.55 m	-130.0 deg
Maximal position	68.00 m	2.55 m	220.0 deg
Maximal velocity	2.01 m/s	1.30 m/s	16.0 deg/s
Maximal acceleration	0.40 m/s ²	0.70 m/s ²	8.0 deg/s ²

6.2.2 Ship model

6.2.2.1 Overview

The model tests have been carried out in the towing tank with a 1/75 scale model of the Q-Flex LNG carrier (Figure 6.3). The main characteristics on model and full scale are presented in Table 6.3.

Table 6.3 Main particulars on model and full scale of the Q-Flex LNG carrier (1/75).

Items	Model scale	Full scale	Units
L_{OA}	4.205	315.3	(m)
L_{PP}	4.122	309.1	(m)
B	0.667	50.0	(m)
T_M	0.160	12.0	(m)
∇	0.337	142,129	(m ³)
GM	0.121	9.06	(m)
KM	0.314	23.54	(m)
D_p	0.101	7.600	(m)
A_R	0.012	64.69	(m ²)
H_R	0.139	10.40	(m)
C_B	0.762	0.762	(-)
I_{zz}	310.0	7.356e+11	(kg m ²)
I_{xx}	17.95	4.259e+10	(kg m ²)



Figure 6.3 The Q-Flex LNG carrier scale model.

6.2.2.2 Propellers and rudders distribution

The ship is equipped with two propellers and two rudders. The propeller model was designed according to the real ship's propellers (right hand propeller on port and left hand propeller on starboard), and the rudders was a Mariner-type design. Each rudder could be operated independently, but in this research the coupled mode was used. During each time step the same rudder angle was steered to port and starboard rudder. At the same time, both rudder angles were measured, and any difference monitored. Moreover, the maximum rudder deflection and rudder rate allowed were set as 35 deg and 22.5 deg/s, respectively. Figure 6.4 presents the propellers and rudders distribution of the scale model, and their characteristics are described in Table 6.4.

Table 6.4 Propeller and rudder characteristics (model scale).

Single propeller			Single rudder		
Items	Value	Units	Items	Value	Units
Number of blades	5	(-)	Number of rudders	2	(-)
Diameter	101	(mm)	Side area	115	(cm ²)
Pitch ratio	0.954	(-)	Height	139	(mm)
Expanded area ratio	0.964	(-)	Mean chord	83	(mm)
Rake angle	0.44	(deg)			
Rotation direction	Inwards	(-)			

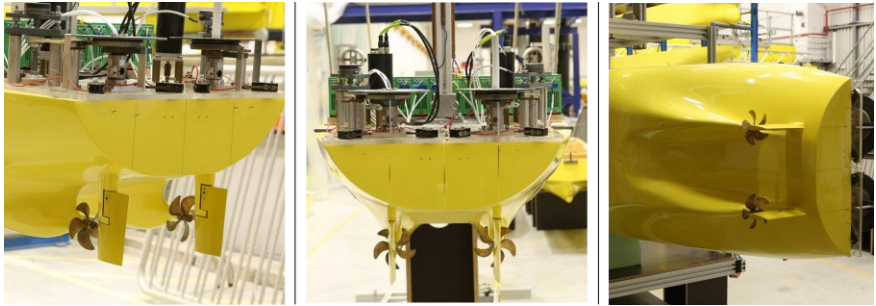


Figure 6.4 Twin propeller and twin rudder installed on the scale model.

$$z = \frac{1}{2(x_{fp} - x_{ap})} [x_{fp} \quad x_{fp} \quad -x_{ap} \quad -x_{ap}] \begin{bmatrix} \text{P1} \\ \text{P2} \\ \text{P3} \\ \text{P4} \end{bmatrix} \quad (6.1)$$

$$\theta = \frac{1}{2(x_{fp} - x_{ap})} [1 \quad 1 \quad -1 \quad -1] \begin{bmatrix} \text{P1} \\ \text{P2} \\ \text{P3} \\ \text{P4} \end{bmatrix} \quad (6.2)$$

$$\phi = \frac{1}{4y_{ap}} [-1 \quad 1 \quad -1 \quad 1] \begin{bmatrix} \text{P1} \\ \text{P2} \\ \text{P3} \\ \text{P4} \end{bmatrix} \quad (6.3)$$

where x_{fp} , x_{ap} and y_{ap} represent the longitudinal and transversal position of potentiometers P1 to P4.

- 2) Load cells (LC1, LC2) are installed to record the surge, sway forces and yaw moments, which can be derived by:

$$\begin{bmatrix} X \\ Y \\ N \end{bmatrix} = \begin{bmatrix} 1 & 1 & 0 & 0 \\ 0 & 0 & 1 & 1 \\ 0 & 0 & x_{aLC} & x_{fLC} \end{bmatrix} \begin{bmatrix} X_{LC1} \\ X_{LC2} \\ Y_{LC1} \\ Y_{LC2} \end{bmatrix} \quad (6.4)$$

where x_{aLC} and x_{fLC} are the longitudinal positions of the load cells.

- 3) Pitch and roll mechanism are used to release or restrain the pitch or roll motion or both motions.
- 4) Vertical guidance is implemented for the heave motion.

6.3.1.2 Free running mode

Since 2009, free running model tests can be executed in the towing tank at FHR too. In this work, the autopilot tests were mainly carried out in this free running mode. During free running tests, the scale model is manoeuvring completely free using nothing but its own control mechanism, rudders and propellers. There is no rigid connection between the towing carriage and the scale model, and the carriage follows the scale model as a tracking device and the position (deviations) of the vessel with respect to the carriage is measured by lasers. The combination of the exact position of the carriage and the relative position between scale model and carriage, results in an accurate position, in time, in the Earth bound coordinate system. See Figure 6.6 for a better illustration. Figure 6.6(a) presents the beam frame and instrumentation arrangement. During tests, S1 and S2 lasers capture lateral displacement (with R2 and R1 reflector plates) and yaw angle; S1 and S4 lasers capture roll motion (with R2 reflector plate), S1 and S4 lasers are at a vertical distance of 10 cm apart; S3 laser captures forward motion (with R3 reflector plate); H1, H2 capture vertical motion (with R5 and R4 reflector plates).

Note that the numbering corresponds with the setup of the system by the manufacturer and there is no one to one agreement between the lasers (S) and the reflector plates (R).

Additionally, free running tests are conducted with a combination of a software library for the ship model autopilot and the carriage control mechanism. The autopilot library is used to control the ship model to follow a predefined course or trajectory. The autopilot library includes different control algorithms, e.g. a PID, a fuzzy, a fuzzy PID, an IMC, and an adaptive PID, etc. The library is developed in such a way that new control algorithms can be added easily. The towing carriage is used in a captive way to bring the ship to an initial state (position and velocity), after which the ship model is released and the autopilot library fully controls the ship model, while the carriage is used only as a position tracking device.

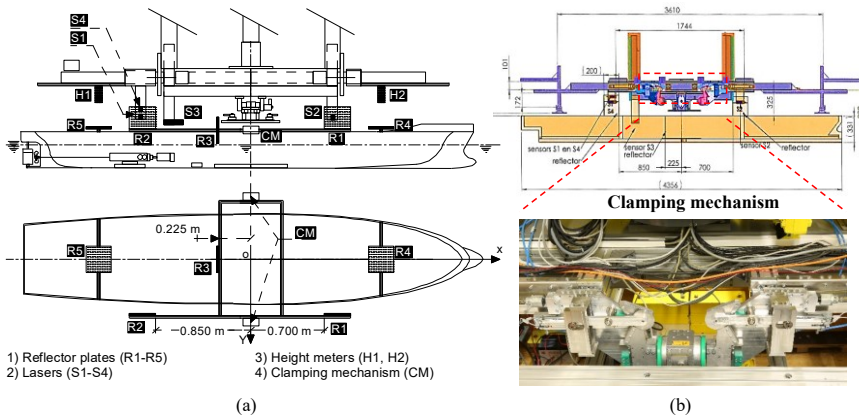


Figure 6.6 Ship model setup during free running tests: (a) beam frame and instrumentation arrangement. (b) clamping mechanism.

6.3.2 Coordinate systems in towing tank

6.3.2.1 Earth fixed coordinate system

During model tests, two coordinate systems are defined to describe the ship's position and orientation along towing tank, an earth-fixed axes system $O_0x_0y_0z_0$ and a body-fixed axes system $Oxyz$. A sketch describing the coordinate systems is displayed in Figure 6.7.

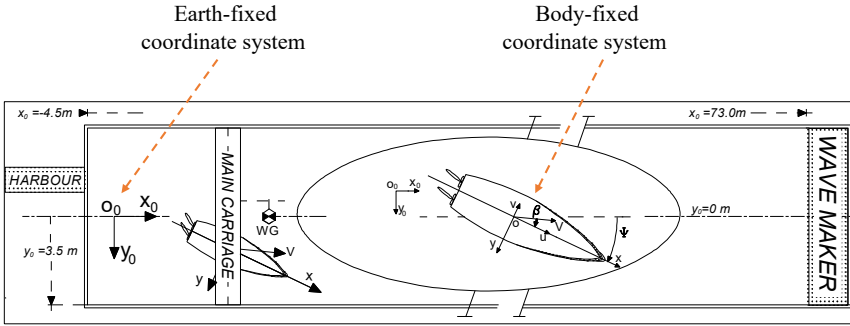


Figure 6.7 Towing tank main dimensions and its coordinate systems.

In the earth-fixed coordinate system (Figure 6.7), the longitudinal axis O_0x_0 is aligned with the towing tank's centre line and positive to forward. The transverse axis O_0y_0 is perpendicular to the centre line and positive towards the right. The O_0z_0 axis is positive to downward. The longitudinal position of the origin ($x_0 = 0$ m) is located at the home position of towing carriage, which is 4.0 m away from the rear wall of the tank (harbour side).

6.3.2.2 Body fixed coordinate system

During model tests, the ship model is attached in the towing carriage but allows free heave and pitch (Figure 6.8). In the body-fixed coordinate system, the origin O is located at the intersection (midship, $1/2L_{PP}$ and $1/2B$) of the longitudinal vertical symmetry plane (Oxy). The longitudinal axis Ox coincides with the ship's centre line and is positive from stern to bow. The transverse axis Oy is positive towards starboard, while the Oz axis is positive to downward.

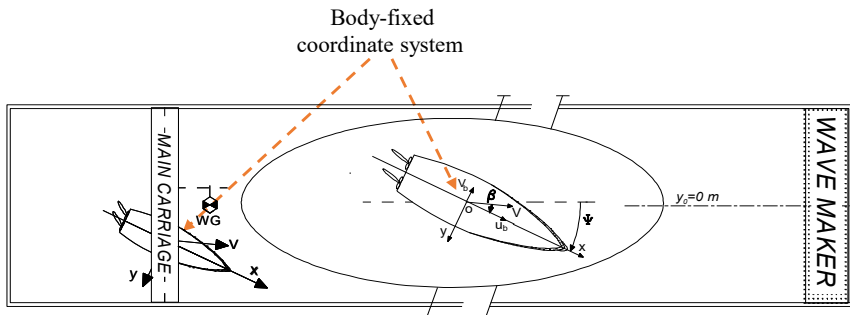


Figure 6.8 Body-fixed coordinate system of ship model.

6.4 Test conditions

6.4.1 Water depths

Model tests were performed at four different water depths from 176.0 mm to 320 mm (model scale), corresponding to the UKCs from 10% to 100%. The tested water depths are shown in Table 6.5 and Figure 6.9. A series of sample photos for experimental water depths are shown in Figure 6.10 and Figure 6.11. It can be seen from Figure 6.10 and Figure 6.11 that the space between the bottom of the ship model and the towing tank floor decreases significantly with the decrease of UKC, especially the 10% UKC test condition.

Table 6.5 Water depths of tests on model scale (h_M) and full scale (h_F).

Test series	h_M (mm)	h_F (m)	UKC	h/T_M	Execution period
G0102A01(G01)	320.0	24.0	100%	2.0	2019.09.16-2019.11.25
G0102A02 (G02)	216.0	16.2	35%	1.35	2019.11.25-2019.12.09
G0102A03 (G03)	192.0	14.4	20%	1.2	2019.12.12-2019.12.23
G0102A04 (G04)	176.0	13.2	10%	1.1	2019.12.23-2020.01.03

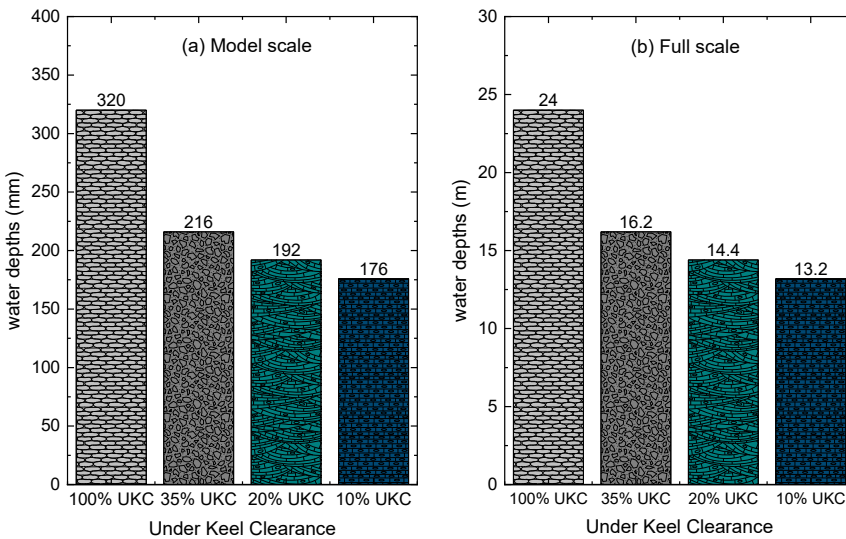


Figure 6.9 Under keel clearances (UKCs) versus water depths of tests: (a) model scale; (b) full scale.

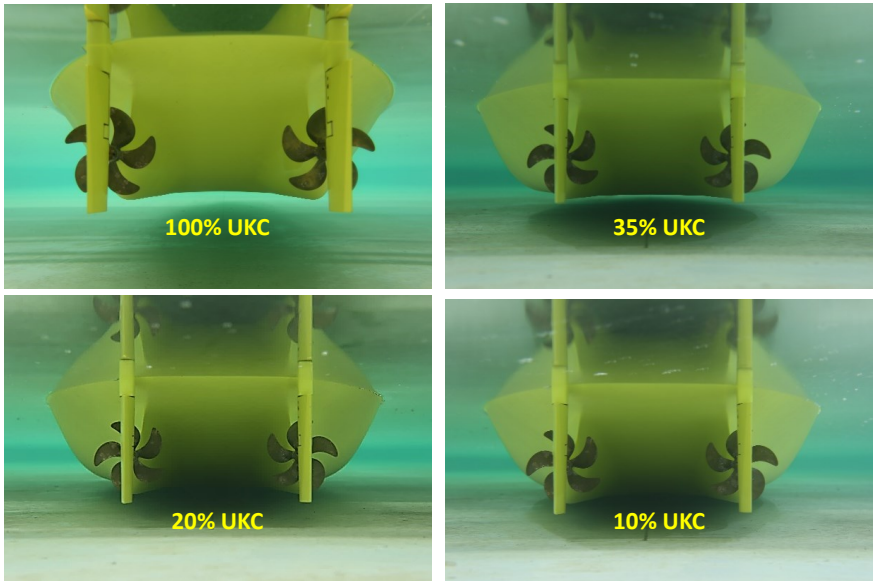


Figure 6.10 Sample photos for different experimental water depths (back view).

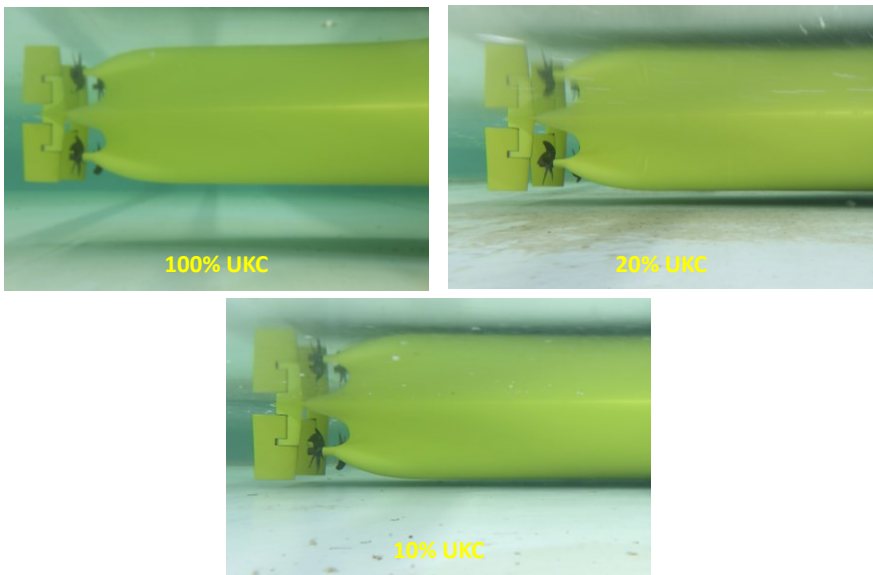


Figure 6.11 Sample photos for different experimental water depths (side view).

According to the criteria about the shallowness of a fairway related to the vessels' draft (PIANC, 1992), the water depth can be categorized into four main groups:

- 1) $3.0 < \frac{h}{T_M}$ Deep

- 2) $1.5 < \frac{h}{T_M} < 3.0$ Medium deep
- 3) $1.2 < \frac{h}{T_M} < 1.5$ Shallow
- 4) $1.0 < \frac{h}{T_M} < 1.2$ Very shallow

Figure 6.12 shows all water depth to draft ratios (h/T_M) with the amount of model tests executed for each ratio. Most of tests were conducted in medium deep and shallow water conditions, respectively account for 67.4% and 30.4% of total model tests. Due to time constraints, only a few tests were carried out under very shallow water condition (2.2%).

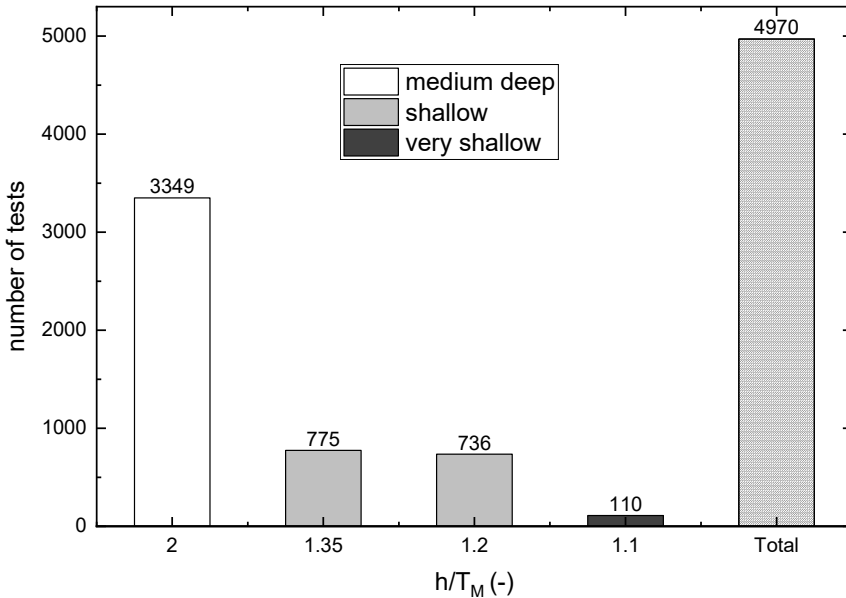


Figure 6.12 Number of model tests for each water depth to draft ratio (h/T_M).

6.4.2 Forward speeds

Free running model tests were performed at speeds from 4 knots up to 16 knots according to full scale or 0.24 and 0.95 m/s on model scale, Table 6.6 and Figure 6.13 present the speed changes at different UKCs or water depth to draft ratio (h/T_M). In very shallow water ($h/T_M=1.1$ or 10% UKC), the ship model was tested at 4, 6 and 8 knots full scale. In shallow water ($h/T_M=1.2$ and 1.35 or 20% UKC and 35% UKC), tests at 11 knots and 13 knots were added to the experimental program. In medium deep water ($h/T_M=2$ or 100% UKC), tests at 16 knots were also added.

Figure 6.13 shows that the maximum test speeds decrease with decreasing water depth, due to larger grounding risk and poorer propulsion efficiency at lower water depths.

Table 6.6 Test speeds at different UKCs.

Speed label	Full scale (kn)	Model scale (m/s)	Fr (-)	100% UKC	35% UKC	20% UKC	10% UKC
S1	4	0.2376	0.037	√	√	√	√
S2	6	0.3564	0.056	√	√	√	√
S3	8	0.4752	0.074	√	√	√	√
S4	11	0.6534	0.102	√	√	√	×
S5	13	0.7722	0.120	√	√	×	×
S6	16	0.9500	0.148	√	×	×	×

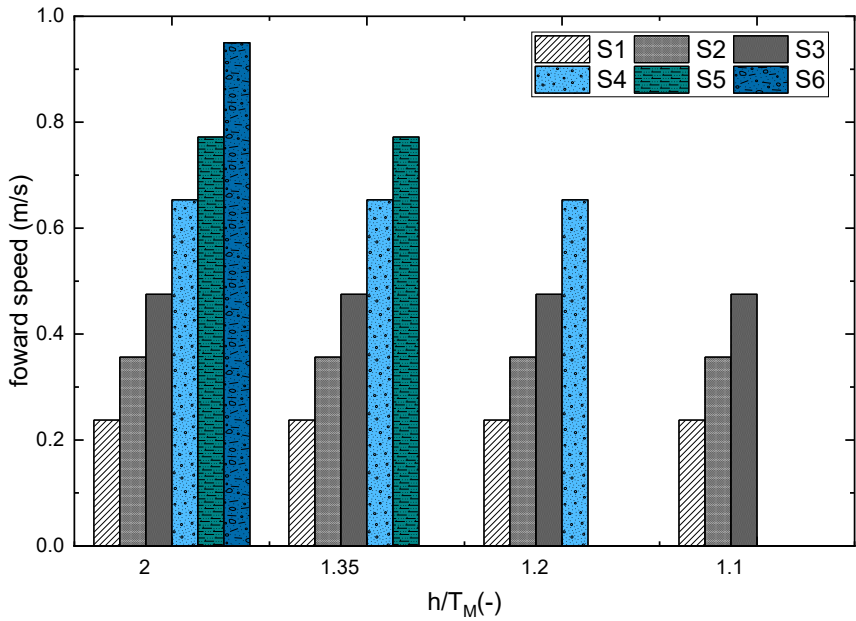


Figure 6.13 Test speeds (model scale) at different water depths.

6.5 Post processing

6.5.1 Postprocessing theory

Kinematics in the horizontal plane

During free running tests, the measured position and orientation information of the ship model consists of $x_m(t)$, $y_m(t)$, $\Psi_m(t)$. Their derivatives are expressed as:

$$\dot{x}_m(t_i) = \frac{x_m(t_i) - x_m(t_{i-1})}{t_i - t_{i-1}} \quad (6.5)$$

$$\dot{y}_m(t_i) = \frac{y_m(t_i) - y_m(t_{i-1})}{t_i - t_{i-1}} \quad (6.6)$$

$$\dot{\Psi}_m(t_i) = \frac{\Psi_m(t_i) - \Psi_m(t_{i-1})}{t_i - t_{i-1}} \quad (6.7)$$

where t represents time, and i is an integer. Then, the speed is calculated as:

$$U(t_i) = \sqrt{\dot{x}_m(t_i)^2 + \dot{y}_m(t_i)^2} \quad (6.8)$$

Meanwhile, the instantaneous heading angle $\Psi'_m(t_i)$ is described as the derivative of ship's track:

$$\Psi'_m(t_i) = \text{atan} \frac{\dot{y}_m(t_i)}{\dot{x}_m(t_i)} \quad (6.9)$$

The drift angle $\beta(t_i)$ is the difference between the ship's heading angle $\Psi_m(t_i)$ and the instantaneous heading angle $\Psi'_m(t_i)$:

$$\beta(t_i) = \Psi_m(t_i) - \Psi'_m(t_i) \quad (6.10)$$

Then, the bound velocities of ship model are:

$$u(t_i) = U(t_i)\cos\beta(t_i) \quad (6.11)$$

$$v(t_i) = -U(t_i)\sin\beta(t_i) \quad (6.12)$$

$$r(t_i) = \dot{\Psi}_m(t_i) \quad (6.13)$$

The bound accelerations of ship model are:

$$\dot{u}(t_i) = \frac{u(t_i) - u(t_{i-1})}{t_i - t_{i-1}} \quad (6.14)$$

$$\dot{v}(t_i) = \frac{v(t_i) - v(t_{i-1})}{t_i - t_{i-1}} \quad (6.15)$$

$$\dot{r}(t_i) = \frac{r(t_i) - r(t_{i-1})}{t_i - t_{i-1}} \quad (6.16)$$

Finally, the ship position coordinates are obtained as:

$$x(t_i) = \int_0^t [u(t_i)\cos(\Psi_m(t_i)) - v(t_i)\sin(\Psi_m(t_i))]dt \quad (6.17)$$

$$y(t_i) = \int_0^t [u(t_i)\sin(\Psi_m(t_i)) + v(t_i)\cos(\Psi_m(t_i))]dt \quad (6.18)$$

Kinematics in the vertical plane

There are two lasers to measure the running sinkage of the ship model. One is near the bow (at x_b from midship), and another one is near the stern (at x_s from midship). The mean sinkage and the trim angle can be calculated based on the measurement of two lasers:

$$z(t_i) = \frac{z_b(t_i)|x_s| + z_s(t_i)|x_b|}{|x_s| + |x_b|} \quad (6.19)$$

$$\vartheta(t_i) = \text{atan} \frac{z_s(t_i) - z_b(t_i)}{|x_s| + |x_b|} \quad (6.20)$$

where z is the ship's mean sinkage, z_b and z_s are the sinkage of bow and stern, ϑ is the trim angle. It is worth mentioning that the roll velocity and acceleration should be calculated as well in theory analysis, but the roll motion was not post processed owing to very small orders of magnitude.

6.5.2 Postprocessing by softwares

6.5.2.1 Zeeman software (version 1.3.5)

The measurement data of free running tests are recorded in an "Autolog" and "Doc" format files (No link to MSWord file format whatsoever). The "Autolog" file is a 10 Hz log file. The measured data are firstly post processed by Zeeman software (Figure 6.14), which is employed to transform the "Doc" files to HDR and KRT files to be used for further post processing.



Figure 6.14 Zeeman post processing software.

6.5.2.2 Regstatx (version 4.3.0)

The Regstatx software is used to further post process the free running measured data based on the files generated by the inhouse developed Zeeman software (Figure 6.15). The analysis results can be exported in MS Excel format or visualized in the software directly. For illustration purposes, one example of the post processing results is visualized in Figure 6.16. One can select one or more analysis results, at the same time the different information can be shown in the graph. In this example, the position information (x, y) of all listed post processing results are presented in Figure 6.16.



Figure 6.15 Regstatx software for free running test analysis.

6.6 Experimental results

6.6.1 Self-propulsion tests

The self-propulsion tests were carried out for the purpose of obtaining the relationship between the propeller rates and the forward speeds. The scale model of the LNG carrier was equipped with two propellers, and the propeller rates were imposed. The ship model was controlled to sail in the free running mode on a straight line using a default PID controller with coefficients $K_p=10$, $K_I=0.1$, $K_D=25$ (Delefortrie et al., 2020). The propeller rates were fixed percentages of the propeller rate corresponding to telegraph position full ahead, and the following conventions have been used (Table 6.7).

Table 6.7 Propeller rates at corresponding telegraph positions for the tested LNG ship.

Telegraph position	Full scale (rpm)	Model scale (rpm)	rpm/max rpm (-)
Full	91	788	100%
Harbour full	47.5	411	52%
Half	37.5	325	41%
Slow	27.5	238	30%
Dead slow	23	199	25%

In this work, the propeller rate was tested systematically from 20%, 40%, 60%, 80% up to 100% of the maximal propeller rate in medium deep and shallow water (20%, 35% and 100% UKCs). However, owing to the excessive squat, in very shallow water (10% UKC), it was not possible to conduct tests using the maximal propeller rate (100% rpm).

Table 6.8 and Figure 6.17 show the relationship between the propeller rates and the forward speeds in different water depths (UKCs). From Table 6.8 and Figure 6.17, one can observe that in the same water depth, the propeller rate is proportional to the forward speed, in other words, the propeller rate (self-propulsion point) should be increased in order to achieve higher speed.

Table 6.8 Relationship between the propeller rates and the forward speeds at different water depths (UKCs).

Forward speeds		100% UKC	35% UKC	20% UKC	10% UKC
Full scale (knots)	Model scale (m/s)	Propeller rates (rpm)			
4	0.2376	197.00	236.40	249.01	269.50
6	0.3564	295.50	353.81	373.51	404.24
8	0.4752	394.00	472.01	498.02	538.99
11	0.6534	542.14	649.31	685.56	
13	0.7722	640.64	788.00		
16	0.9500	788.00			

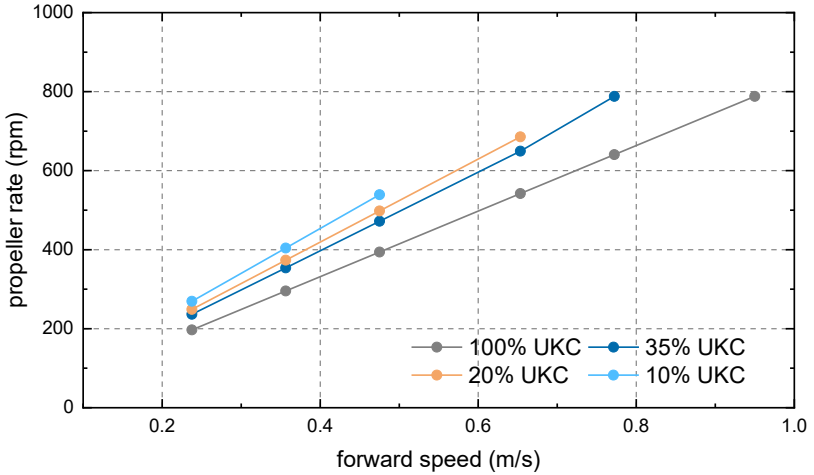


Figure 6.17 Relationship between the propeller rates and the forward speeds at different water depths (UKCs).

Table 6.9 and Figure 6.18 present the effects of water depths on the propeller rates. From Figure 6.18, one can find that the propeller rates increased with decreasing water depths (UKCs) in order to reach the same speed. Taken the results at speed of 4 knots (full scale) as examples, the propeller rate in medium deep water (100% UKC) is 197.00 rpm, which is increased by 20% to 236.40 rpm in shallow water (35% UKC), and increased by 36.8% to 269.50 rpm in very shallow water (10% UKC). The effects of water depths on propeller rates can be attributed to higher resistance and lower propulsive efficiency in shallow water, thus a bigger propeller rate is needed to reach a same speed.

Table 6.9 The effects of water depths on the propeller rates at same speed.

UKC	h/T_M	0.2376	0.3564	0.4752	0.6534
		(4 knots)	(6 knots)	(8 knots)	(11 knots)
Propeller rates (rpm)					
100%	2.0	197.00	295.50	394.00	542.14
35%	1.35	236.40	353.81	472.01	649.31
20%	1.2	249.01	373.51	498.02	685.56
10%	1.1	269.50	404.24	538.99	

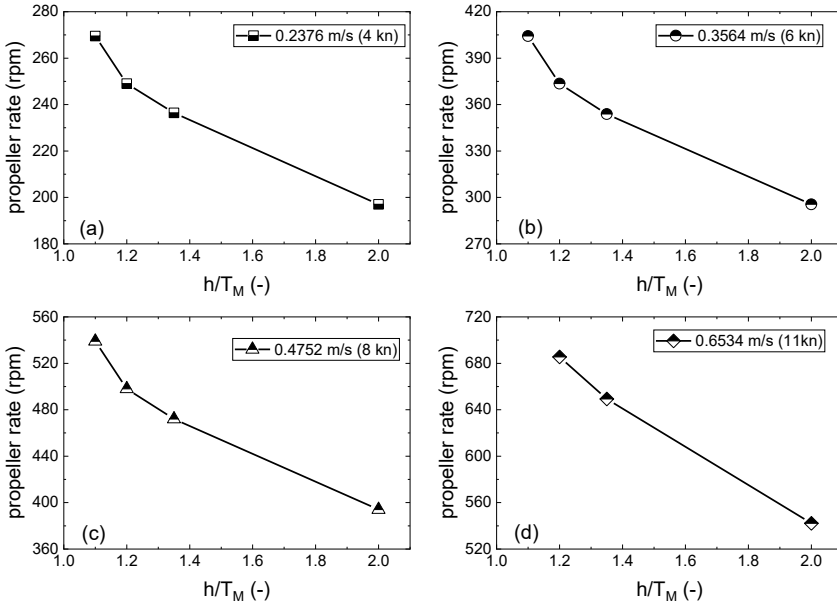


Figure 6.18 The effects of water depths on the propeller rates at same speed.

6.6.2 Zigzag tests

6.6.2.1 Overview

In order to determine the parameters of ship mathematical models, zigzag or turning circle manoeuvre data are commonly used in combination with the system identification methods (Luo et al., 2016; Wang et al., 2020). Due to the limitation of size and vicinity of the tank wall in the test facility of Flanders Hydraulics Research (FHR towing tank) (Eloot et al., 2015), only partial turning circles can be executed, but the data from the partial turning circles are not enough to obtain the ship model parameters. Thus, the zigzag manoeuvre tests are considered in present study. The zigzag manoeuvres executed in this work are slightly different from those recommended by the ITTC (ITTC, 2017) and IMO (IMO, 2002) criteria, where the standard test is either a $10^\circ/10^\circ$ or $20^\circ/20^\circ$ zigzag manoeuvre. Due to the limited width of the towing tank, the alternative manoeuvre executed in the FHR towing tank is $\pm 10^\circ/2.5^\circ$ or $\pm 20^\circ/5^\circ$ zigzag. The zigzag tests were conducted at the following forward speeds:

- 4 knots full scale, for all UKCs.
- 6 knots full scale, for all UKCs.
- 8 knots full scale, for all UKCs.
- 11 knots full scale, only for $UKC \geq 20\%$.
- 13 knots full scale, only for $UKC \geq 35\%$.
- 16 knots full scale, only for 100% UKC.

Figure 6.19 and Figure 6.20 exhibit examples of $-10^\circ/2.5^\circ$, $10^\circ/2.5^\circ$, $-20^\circ/5^\circ$, $20^\circ/5^\circ$ zigzag manoeuvres at 8 knots and 35% UKC. A clear difference can be found between the phase shift and spread for the $\pm 10^\circ/2.5^\circ$ zigzag tests compared with the $\pm 20^\circ/5^\circ$ zigzag manoeuvres.

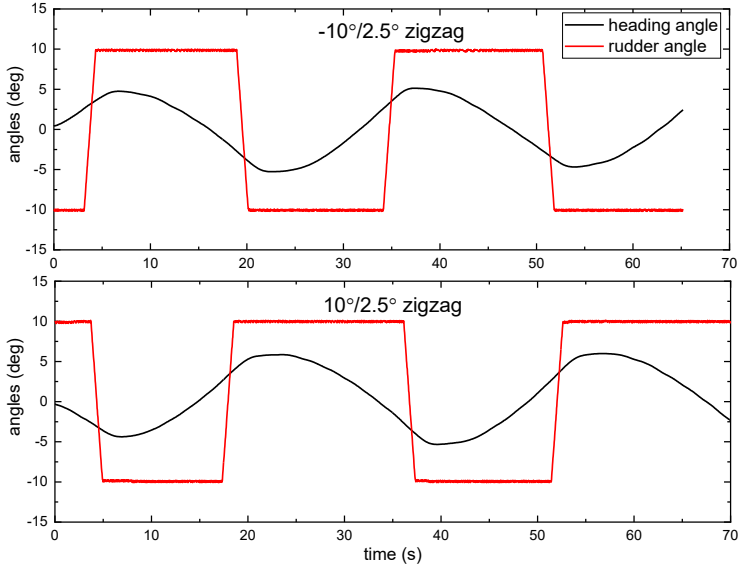


Figure 6.19 $\pm 10^\circ/2.5^\circ$ zigzag manoeuvres at 8 knots and 35% UKC.

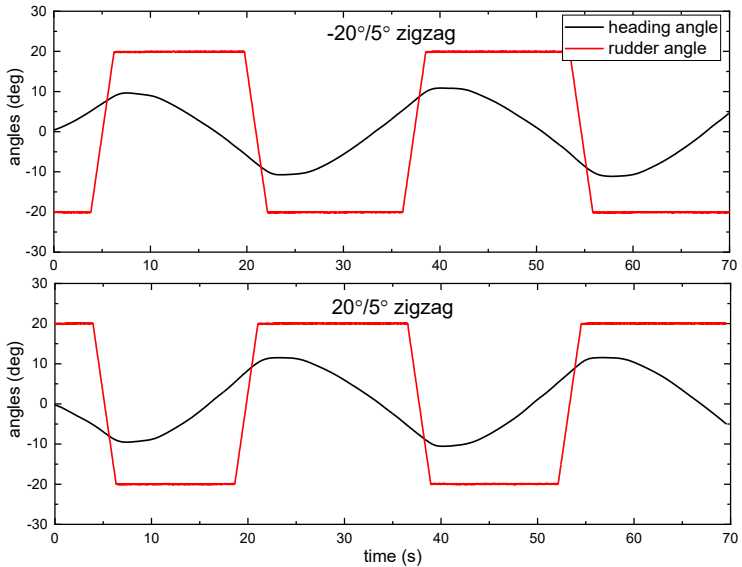


Figure 6.20 $\pm 20^\circ/5^\circ$ zigzag manoeuvres at 8 knots and 35% UKC.

6.6.2.2 Shallow water effects on zigzag manoeuvres

To illustrate the effects of water depth on zigzag manoeuvres, Figure 6.21 and Figure 6.22 present the trajectories and the motion response of $20^\circ/5^\circ$ zigzag manoeuvres at 8 knots in different water depths. From Figure 6.21 one can observe that in (very) shallow water (10%, 20% and 35% UKCs) the lateral displacement during zigzag tests was smaller compared to the medium deep case (100% UKC). Moreover, it can be seen from Figure 6.22(a) and Figure 6.22(b) that the overshoot angle and yaw rate presented a nonlinear decrease with decreasing water depth (UKC), meanwhile the ship model took a smaller drift angle at a smaller UKC (Figure 6.22(c)). Forward speed loss was more obvious at larger UKC's (Figure 6.22(e)), while sinkage became smaller with increasing UKC (Figure 6.22(f)).

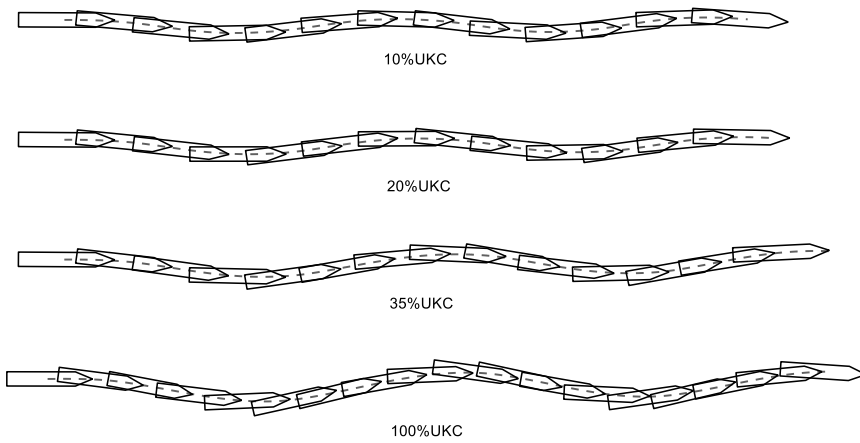


Figure 6.21 Trajectories of $20^\circ/5^\circ$ zigzag tests at 10%, 20%, 35% and 100% UKCs for the speed of 8 knots.

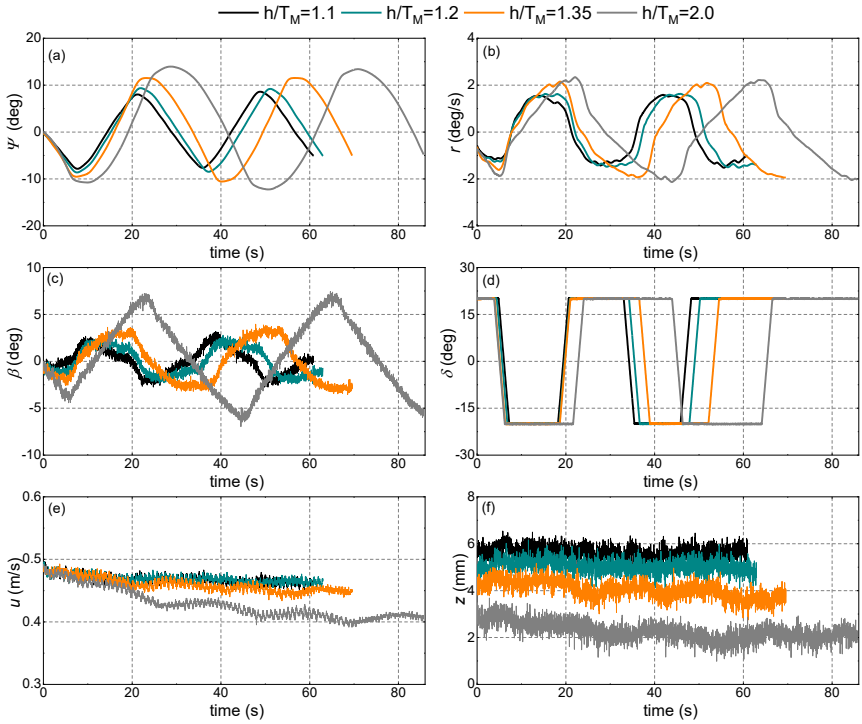


Figure 6.22 Time histories of heading angle (Ψ), yaw rate (r), drift angle (β), rudder angle (δ), forward speed (u), sinkage (z) of $20^\circ/5^\circ$ zigzag manoeuvres in different water depths for the speed of 8 knots.

Figure 6.23 shows the phase plot of yaw rate (r) over rudder angle (δ) and heading angle (Ψ) to provide further insight into the hydrodynamic damping characteristics during zigzag manoeuvres. It is obvious that the phase trajectories expanded as the water depth (h/T_M) increased. One can observe from Figure 6.23(a)-(d) that when the same rudder angles were applied, in (very) shallow water, the yaw rate (r) was significantly smaller compared to the medium deep water case. This is caused by smaller hydrodynamic damping during zigzag manoeuvres in deeper water. Table 6.10 quantitatively compares the overshoot angles during zigzag tests in different water depths. One can note that the first and second overshoot angles presented a decreasing trend as decreasing water depths, due to larger hydrodynamic damping in the sway direction. According to zigzag results, it can be confirmed that the water depth has an effect on the ship’s course-checking ability, which is reduced as the water depth increases. This effect can be seen in the increase of the overshoot angles from 10% UKC to 100% UKC. In other words, the ship’s heading stability becomes better in more shallow water.

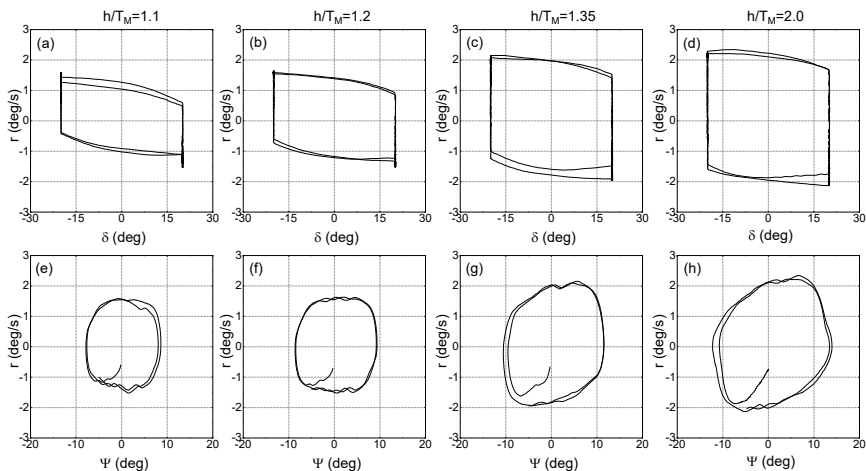


Figure 6.23 Phase diagram yaw rate (r) over rudder angle (δ) and heading angle (Ψ) of $20^\circ/5^\circ$ zigzag manoeuvres in different water depths for the speed of 8 knots.

Table 6.10 Statistics of $20^\circ/5^\circ$ zigzag model tests at the speed of 8 knots in different water depths.

UKC(%)	h/T_M (-)	first overshoot(deg)	second overshoot(deg)
100	2.0	5.8	9.0
35	1.35	4.5	6.5
20	1.2	3.6	4.4
10	1.1	2.8	3.0

6.6.3 Course tests

Ship autopilots are mostly designed to perform course keeping manoeuvres in open sea and course changing manoeuvres near coastal waters. For course keeping, it is desirable to maintain minimum course deviation from its set course with smaller control effort; for a course changing manoeuvre, it is desirable to track the target course as swift as possible with minimum course angle overshoot.

In this work, course keeping and changing performance of the designed controllers (see Chapter 5 for information about control strategies) were tested extensively at different forward speeds and UKCs. All course keeping tests were conducted at the same speeds and UKCs as the test conditions in section 6.4. The tests considered not only keeping a course at 0 deg, but also changing a course with 10 deg (Figure 6.24).

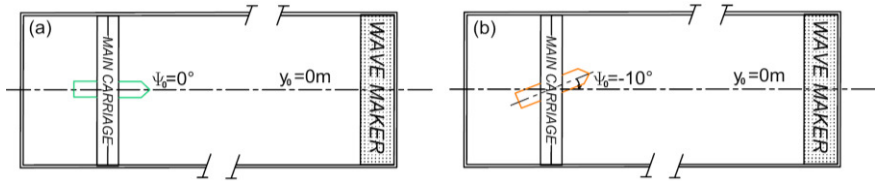


Figure 6.24 Initial conditions for course keeping (a) and course changing (b).

6.6.3.1 Course keeping tests

In the course keeping manoeuvre, the main goal is to maintain a constant set course, namely, to follow a straight course. If the actual heading angle of the ship deviates slightly from the set course, the rudders are activated to correct for the heading deviation. In case of the model tests, the desired course angle was assigned as 0 deg, and the ship model tried to maintain the set course and follow a straight course. Three types of course keeping tests were studied, they are:

- Course keeping with constant speed.
- Course keeping with acceleration.
- Course keeping with deceleration.

For illustration purposes, taking the fuzzy controller as an example, and its course keeping performance with constant speed, acceleration and deceleration are depicted in Figure 6.25 to Figure 6.27.

Figure 6.25 shows the course keeping performance of the fuzzy controller at 8 knots (0.4752 m/s) and 35% UKC. It can be observed in Figure 6.25(a) and Figure 6.25(b) that the ship model maintained its heading Ψ within ± 0.5 deg using small rudder angles ($|\delta| = 5$ deg). The results indicate a good course keeping ability of the fuzzy controller for constant speed. Similar results for acceleration and deceleration are shown in Figure 6.26 and Figure 6.27.

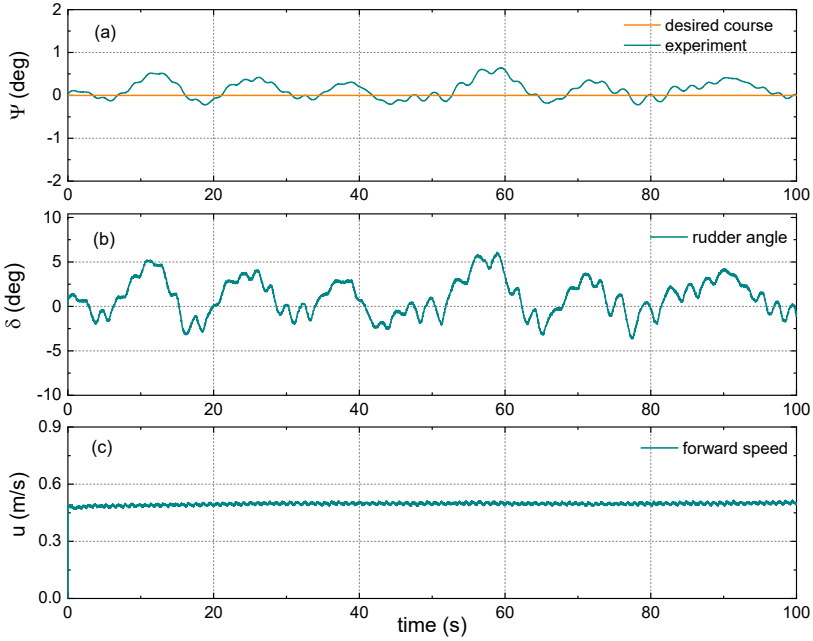


Figure 6.25 Course keeping test with constant speed at 8 knots (0.4752 m/s) and 35% UKC.

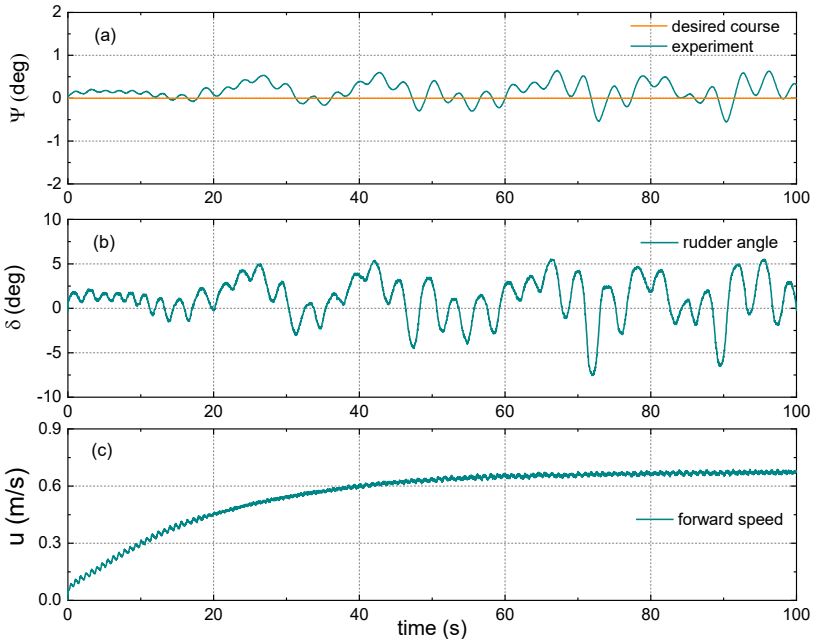


Figure 6.26 Course keeping test with acceleration from 0 to 11 knots (0.6534 m/s) at 35% UKC.

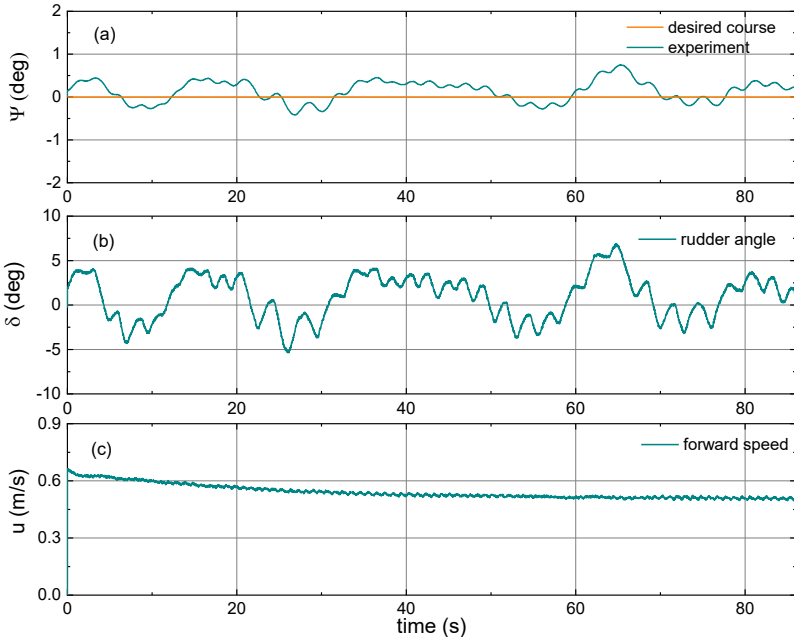


Figure 6.27 Course keeping test with deceleration from 11 knots (0.6534 m/s) to 8 knots (0.4752 m/s) at 35% UKC.

6.6.3.2 Course changing

A modern autopilot must not only have course keeping abilities, but also turning capabilities, namely, course changing capacities. In this work, the course changing abilities of the designed controllers were also investigated. Figure 6.28 exhibits an example of course changing performance of the fuzzy controller at 8 knots and 35% UKC. The ship model can change the heading angle from the initial -10 deg to the desired 0 deg despite some overshoots are seen. The overshoot angle at initial turning phase can be attributed to that the ship started with a drift angle (Figure 6.24). The aim of a setting initial drift angle is to create more space for course changing manoeuvring in the confined towing tank and avoid approaching the tank sidewall too soon. The overshoot angle at the end of the turning phase can be explained by the selected controller parameters. The results imply that the fuzzy controller achieved good course changing performance.

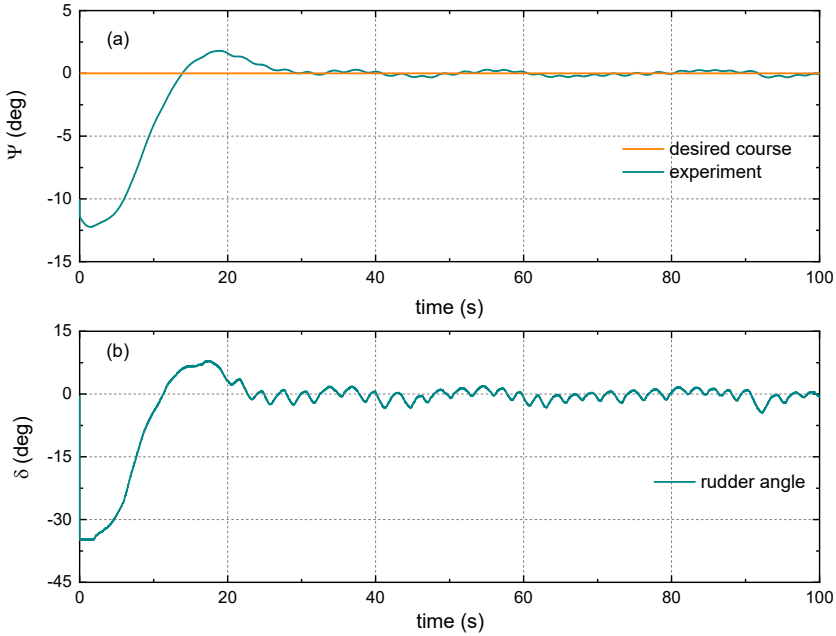


Figure 6.28 Course changing test at 8 knots and 35% UKC.

6.6.4 Path following tests

In the path following tests, the ship model follows a predefined path composed of several waypoints. Four types of paths were used to carry out path following tests (Figure 6.29):

- 1) Straight line path
- 2) Curved path with obstacles
- 3) Step line path
- 4) Folding line path

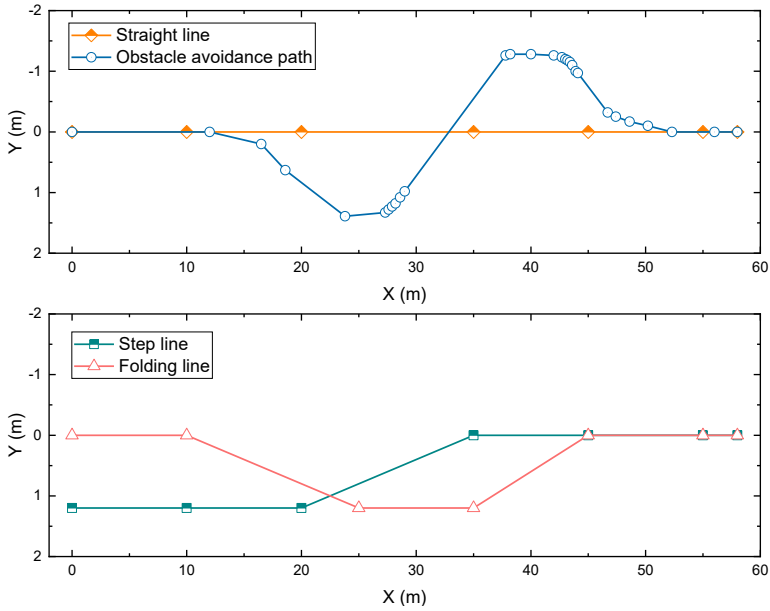


Figure 6.29 Pre-planned paths and their waypoints: straight line (orange); path with obstacles (blue); step line (green); folding line (red).

It is necessary to mention that the waypoints of the straight line, step line, and folding line paths were manually selected considering the towing tank environment. Each path consists of a total of 7 waypoints, which is a minimal number of waypoints required in the towing tank system (software configuration), even when a straight line is considered. The curved path with obstacles was planned by the ATFMS path planning algorithm (section 4.2), and the desired path and its waypoints are shown in Figure 6.29 and Figure 6.30. Note that the obstacles were not physically present in the towing tank (but the model thought they were).

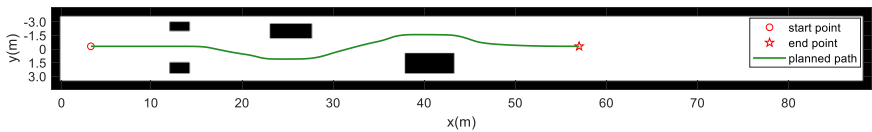


Figure 6.30 Planned curved path with four virtual obstacles.

During tests, the tracking ability of PID, IMC, fuzzy and adaptive PID controllers were investigated. The PID controller parameters K_p , K_i , and K_d were calculated according to the time constant T and the gain K of the Nomoto model, which were obtained using a system identification approach based on zigzag tests (Chen, et al., 2019), then the PID controller coefficients were determined by Eqs. (5.10)-(5.12). Regarding the IMC, the controller can be expressed into a PID format (Eqs. (5.20)-(5.22)). Except for the time constant T and the gain K , one more parameter β_c needs to be tuned. In this work, the parameter β_c was determined by testing

different options, and the value of β_c that led to satisfactory results was directly used in experiments to further examine its applicability. More specifically, firstly, an initial value of β_c ($1 \leq \beta_c \leq 10$) was used to determine the parameter K_p , K_i , and K_d , then the performance of the controller was evaluated by the evaluation indexes in section 5.10. If the performance of controller is optimal, then the β_c is determined. If not, then a new β_c will be tested. According to experimental results, a tuning parameter $1 \leq \beta_c \leq 10$ was used. For the adaptive PID controller, the first step to determine the parameters K_p , K_i , and K_d at a certain speed (the procedure is the same as for the PID controller), then the parameters of other speeds (propeller rates) can be derived according to the relationship between the propeller rate and the controller parameters in Eqs. (5.24)-(5.26). The fuzzy controller is a model-free controller, the performance of which only relies on the maximum heading angle deviation Ψ_e^{max} and the maximum change in time of this deviation $d\Psi_e^{max}/dt$. The reasonable range of Ψ_e^{max} was 8-10 deg, and $d\Psi_e^{max}/dt$ was 4-5 deg/s.

Because the thesis will become too large if all tests are shown, and the same methodologies were used for all tests, not all results are fully described. For illustrative purposes, the straight line and curved line with obstacles path following results are presented as case studies in sections 6.6.4.1 and 6.6.4.2. But the results for all tested conditions were summarized in section 6.6.4.3.

6.6.4.1 Straight line path following control

6.6.4.1.1 Overview

In this subsection, the experimental results at a speed of 11 knots and 20% UKC are presented as a case study. The PID controller coefficients were selected as $K_p=10.7568$, $K_i=0.7771 \text{ s}^{-1}$, $K_d=20.1729 \text{ s}$. The IMC controller coefficients were $\beta_c=2.94$, $K_p=3.6992$, $K_i=0.3705 \text{ s}^{-1}$, $K_d=3.3850 \text{ s}$. The fuzzy controller coefficients were $Ke=0.38 \text{ deg}^{-1}$, $Kc=0.75 \text{ deg}^{-1}$, $Ku=11.66 \text{ deg}$, and the adaptive PID controller coefficients were $K_{pn}=3.7075$, $K_{in}=0.0324$, $K_{dn}=43.1770$.

6.6.4.1.2 Controller performance

Figure 6.31 demonstrates the performance of the PID controller. Figure 6.31(a) shows that the ship (green pentagon) can follow the predefined straight line successfully. The measured trajectory agreed well with the desired trajectory with very small deviations. Figure 6.31(b) and Figure 6.31(c) display the cross track errors and heading angle errors. The cross track errors fluctuated within 0.05 m (7.5% breadth), while the heading angle errors kept within ± 2 deg. Figure 6.31(d) and Figure 6.31(f) show the longitudinal and lateral position errors. The longitudinal position errors were around zero (less than 0.01%), and the lateral position errors were within ± 0.05 m (7.5% breadth). These small errors imply a good control effect. Additionally, the time history of rudder angles is plotted in Figure 6.31(e). In the rudder behaviour, obvious oscillations can be seen. Similar results for the IMC, fuzzy, and adaptive PID controllers are presented in Figure 6.32-Figure 6.34.

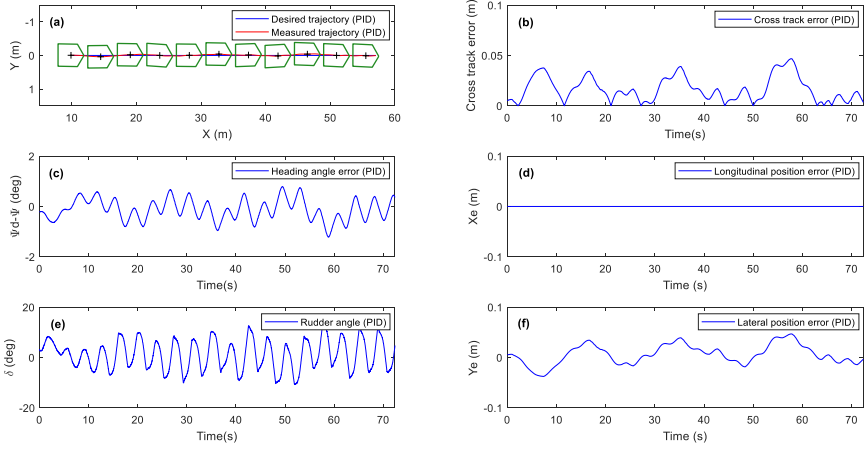


Figure 6.31 PID controller performance at 11 knots and 20% UKC: (a) desired and measured trajectories; (b) cross track error; (c) heading angle error; (d) longitudinal position error; (e) rudder angle; (f) lateral position error.

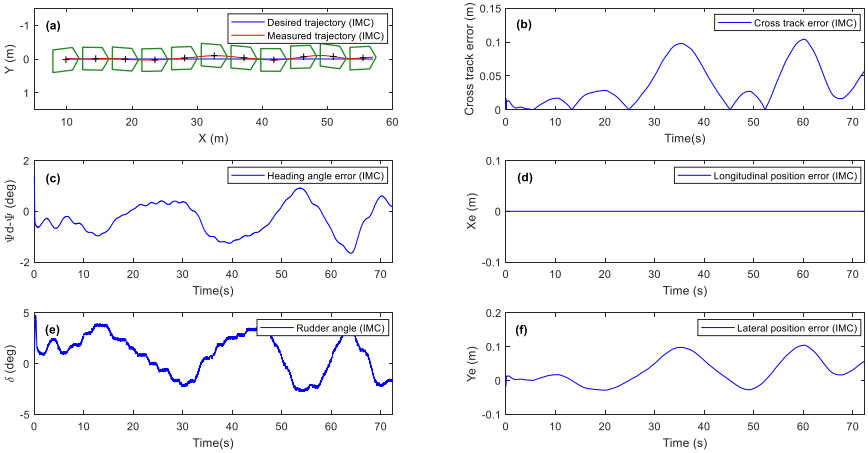


Figure 6.32 IMC controller performance at 11 knots and 20% UKC: (a) desired and measured trajectories; (b) cross track error; (c) heading angle error; (d) longitudinal position error; (e) rudder angle; (f) lateral position error.

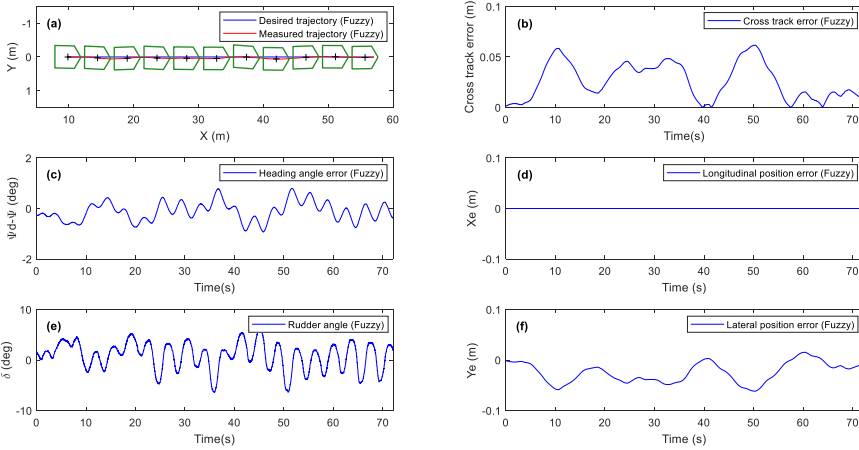


Figure 6.33 Fuzzy controller performance at 11 knots and 20% UKC: (a) desired and measured trajectories; (b) cross track error; (c) heading angle error; (d) longitudinal position error; (e) rudder angle; (f) lateral position error.

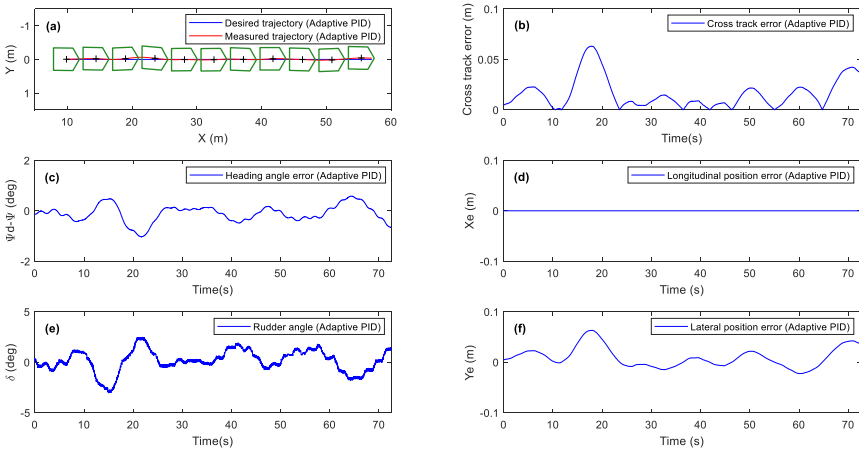


Figure 6.34 Adaptive PID controller performance at 11 knots and 20% UKC: (a) desired and measured trajectories; (b) cross track error; (c) heading angle error; (d) longitudinal position error; (e) rudder angle; (f) lateral position error.

6.6.4.1.3 Qualitative comparison

For the qualitative analysis of the controllers' performance, the results including trajectory error, heading angle error, and rudder angle are compared in Figure 6.35-Figure 6.37.

All controllers could stabilize the ship within 0.1043 m (~15% breadth), as is shown in Figure 6.35(a) and Figure 6.35(b). Small trajectory errors of four controllers indicate their good tracking capability. According to Figure 6.35(c)-

(f), the errors for the PID and adaptive PID controllers centred at zero, but those of the IMC and fuzzy controllers deviated off zero. Additionally, errors of the adaptive PID controller were denser around zero than the PID controller. Therefore, the adaptive PID controller presents the most satisfactory trajectory errors.

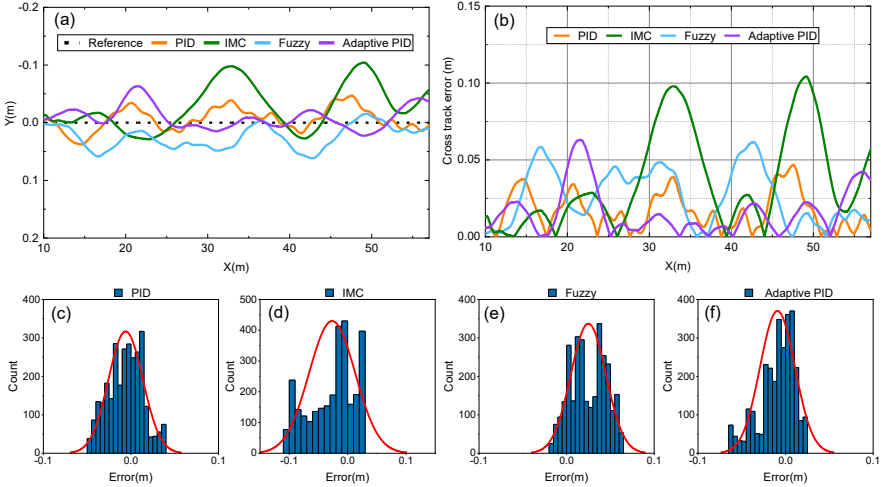


Figure 6.35 Comparison results for the trajectory error at 11 knots and 20% UKC: (a) reference and measured trajectories; (b) cross track error; (c) position error histogram of PID controller; (d) position error histogram of IMC controller; (e) position error histogram of fuzzy controller; (f) position error histogram of adaptive PID controller.

Figure 6.36 presents the heading angle errors of four controllers. The heading angle errors were small and within 1.5 deg. Note that the heading angle errors of the PID and fuzzy controllers fluctuated at higher frequencies, while those of the IMC and adaptive PID controllers showed a relatively smooth evolution. Figure 6.36 displays the rudder behaviour of the four controllers. The amplitude of rudder angles for the PID controller was obviously larger. Furthermore, the PID and fuzzy controllers presented larger oscillations than that of the IMC and adaptive PID controllers, indicating that they used the rudder more frequently.

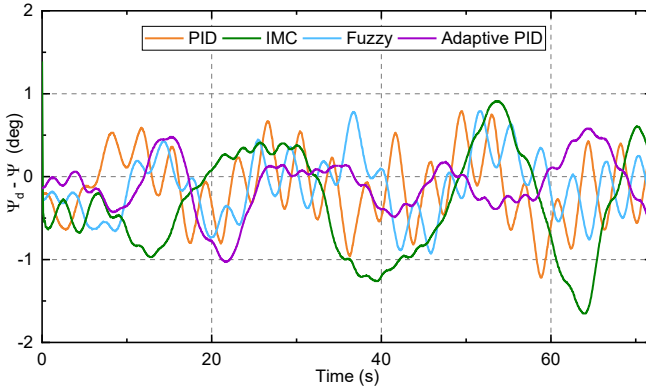


Figure 6.36 Comparison results for the heading angle error at 11 knots and 20% UKC.

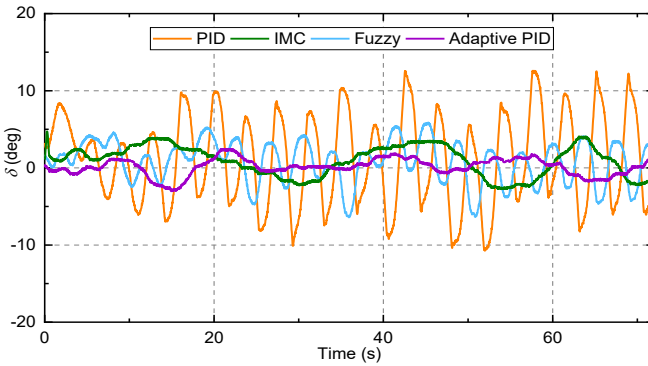


Figure 6.37 Comparison results for the rudder angle at 11 knots and 20% UKC.

6.6.4.1.4 Quantitative comparison

The model evaluation and selection mechanisms described in section 5.10 were adopted to compare four controllers based on five properties including mTEI, MTE, mRI, mRTV, and mHEI (Table 6.11). Adaptive PID controller presented the minimum cross track error (mTEI=0.0161) and heading angle error (mHEI=0.2710) and used the smallest and smoothest rudder (mRI=0.8524, mRTV=0.1070). However, the PID controller obtained the smallest value of the maximum cross track error (MTE=0.0468).

Table 6.11 Control performance of four controllers for following straight line.

Properties	PID	IMC	Fuzzy	Adaptive PID
mTEI	0.0166	0.0361	0.0265	0.0161
MTE	0.0468	0.1043	0.0617	0.0631

mRI	5.0307	1.9212	2.4237	0.8524
mRTV	0.2324	0.1210	0.1317	0.1070
mHEI	0.3616	0.5862	0.3177	0.2710

Note: Numbers in bold indicate the smallest value of each evaluation index, corresponding to better performance.

Then, the grey relational decision-making method (refer to section 5.10) was used to determine the best controller based on the results in Table 6.11.

1) Construct an initial decision matrix

Assume four controllers as alternative series and five evaluation indexes as attribute series. According to the results in Table 6.11, the initial decision matrix is described as:

$$(X_0, X_1, \dots X_n) = \begin{pmatrix} 0.0161 & 0.0166 & 0.0361 & 0.0265 & 0.0161 \\ 0.0468 & 0.0468 & 0.1043 & 0.0617 & 0.0631 \\ 0.8524 & 5.0307 & 1.9212 & 2.4237 & 0.8524 \\ 0.1070 & 0.2324 & 0.1210 & 0.1317 & 0.1070 \\ 0.2710 & 0.3616 & 0.5862 & 0.3177 & 0.2710 \end{pmatrix} \quad (6.21)$$

2) Non-dimensional initial matrix:

$$(X'_0, X'_1 \dots X'_n) = \begin{pmatrix} 1.0000 & 1.0311 & 2.2422 & 1.6460 & 1.0000 \\ 1.0000 & 1.0000 & 2.2286 & 1.3184 & 1.3483 \\ 1.0000 & 5.9018 & 2.2539 & 2.8434 & 1.0000 \\ 1.0000 & 2.1720 & 1.1308 & 1.2308 & 1.0000 \\ 1.0000 & 1.3343 & 2.1631 & 1.1723 & 1.0000 \end{pmatrix} \quad (6.22)$$

3) Calculate the difference $\Delta_i(j)$ matrix between the alternative series and the reference series:

$$\Delta = \begin{pmatrix} 0.0311 & 1.2422 & 0.6460 & 0.0000 \\ 0.0000 & 1.2286 & 0.3184 & 0.3483 \\ 4.9018 & 1.2539 & 1.8434 & 0.0000 \\ 1.1720 & 0.1308 & 0.2308 & 0.0000 \\ 0.3343 & 1.1631 & 0.1723 & 0.0000 \end{pmatrix} \quad (6.23)$$

4) Grey relational coefficient matrix yields:

$$\xi = \begin{pmatrix} 0.9875 & 0.6636 & 0.7914 & 1.0000 \\ 1.0000 & 0.6661 & 0.8850 & 0.8756 \\ 0.3333 & 0.6616 & 0.5707 & 1.0000 \\ 0.6765 & 0.9493 & 0.9139 & 1.0000 \\ 0.8800 & 0.6782 & 0.9343 & 1.0000 \end{pmatrix} \quad (6.24)$$

5) Finally, the grey relational degree γ_i is obtained:

$$\gamma_i = (0.7755 \quad 0.7238 \quad 0.8191 \quad 0.9751) \tag{6.25}$$

Table 6.12 Grey relational degree and rank of four controllers.

Controllers	PID	IMC	Fuzzy	Adaptive PID
γ_i	0.7755	0.7238	0.8191	0.9751
Rank	3	4	2	1

The adaptive PID controller obtained the maximum grey relational degree, followed by the fuzzy and the PID controllers, and the IMC controller had the smallest grey relational degree (Table 6.12). Therefore, the adaptive PID controller presented the optimal performance in this case study.

Comparison results imply that four controllers can be applied in the towing tank environment with success to follow a desired straight line. The adaptive PID controller presented a better performance from the perspective of cross track error, heading angle and rudder deflection, etc.

6.6.4.2 Curved line path following control and obstacle avoidance

6.6.4.2.1 Controller performance

Controllers were evaluated to follow a curved path with four virtual obstacles in shallow water. The results at a speed of 8 knots and 20% UKC were presented as a case study. Figure 6.38 demonstrates the performance of the PID controller. The measured trajectory agreed well with the desired trajectory despite small deviations near bends (Figure 6.38(a)). The cross track errors fluctuated within 0.3 m (45% breadth) and the big cross track errors appeared near curve bends (Figure 6.38(b)), while the heading angle errors kept within ± 10 deg (Figure 6.38(c)). Furthermore, obvious oscillations were observed for rudder angles (Figure 6.38(e)). Similar results of the IMC, fuzzy and adaptive PID controllers are shown in Figure 6.39-Figure 6.41.

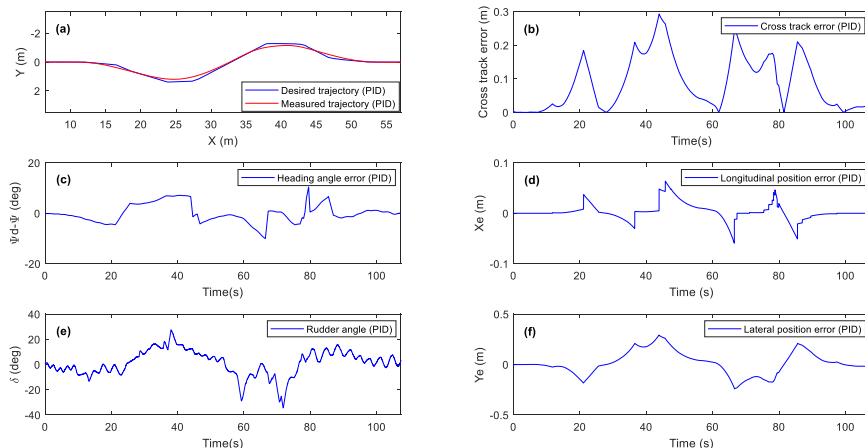


Figure 6.38 PID controller performance at 8 knots and 20% UKC: (a) desired and measured trajectories; (b) cross track error; (c) heading angle error; (d) longitudinal position error; (e) rudder angle; (f) lateral position error.

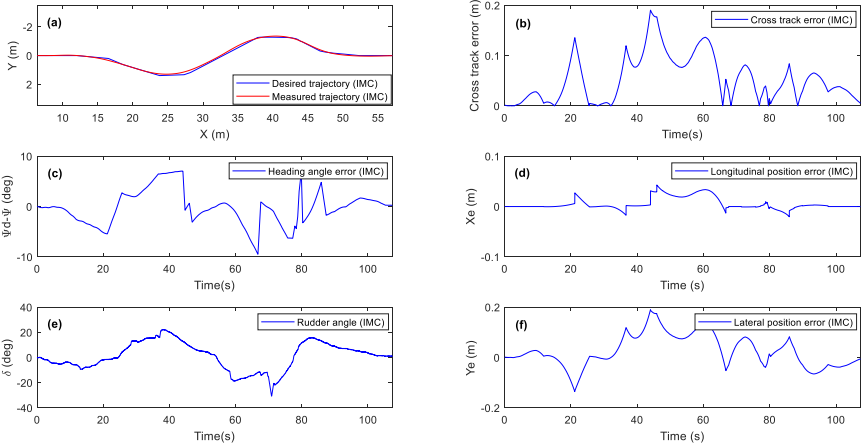


Figure 6.39 IMC controller performance at 8 knots and 20% UKC: (a) desired and measured trajectories; (b) cross track error; (c) heading angle error; (d) longitudinal position error; (e) rudder angle; (f) lateral position error.

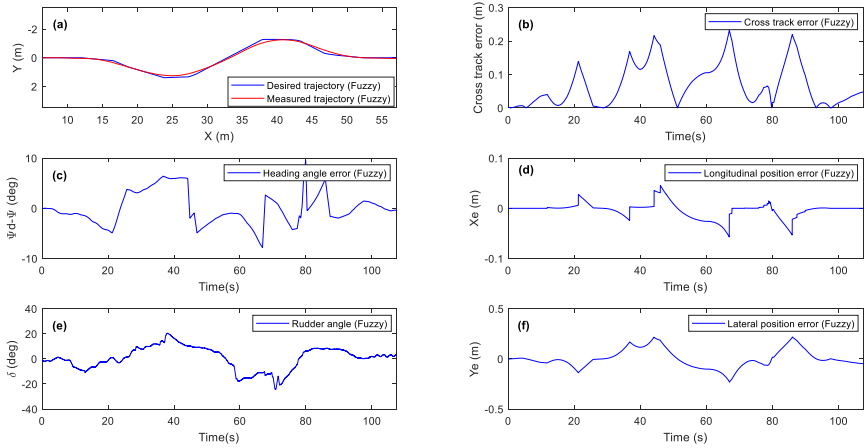


Figure 6.40 Fuzzy controller performance at 8 knots and 20% UKC: (a) desired and measured trajectories; (b) cross track error; (c) heading angle error; (d) longitudinal position error; (e) rudder angle; (f) lateral position error.

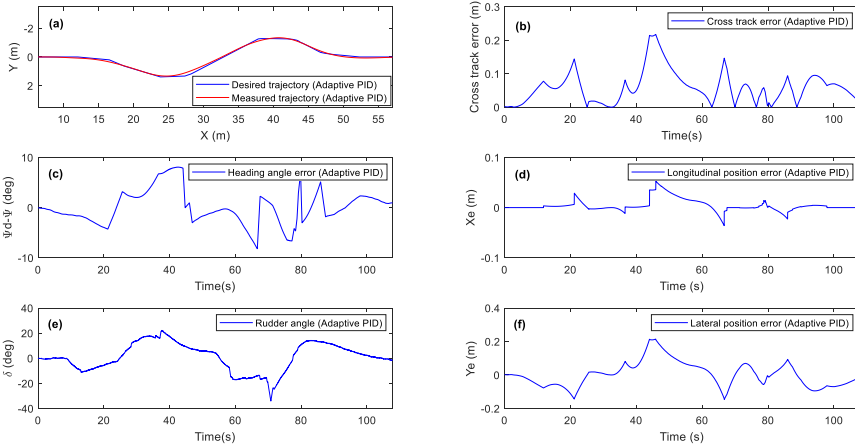


Figure 6.41 Adaptive PID controller performance at 8 knots and 20% UKC: (a) desired and measured trajectories; (b) cross track error; (c) heading angle error; (d) longitudinal position error; (e) rudder angle; (f) lateral position error.

6.6.4.2.2 Qualitative comparison

Cross track error, heading angle error, and rudder angle of controllers are plotted in Figure 6.42-Figure 6.44. All four controllers were able to stabilize the ship within 0.25 m (38% breadth), except for the value around 45 seconds for the PID controller (0.30 m) (Figure 6.42). The small trajectory errors of four controllers demonstrate their good tracking capability for the curved path, and the minimum trajectory error was obtained by the IMC controller. The heading angle error of four controllers ranged between -10 deg and 10 deg (Figure 6.43). The PID controller used the rudder more frequently with big oscillations while the IMC, fuzzy, and adaptive PID controllers changed the rudders less and smoothly (Figure 6.44).

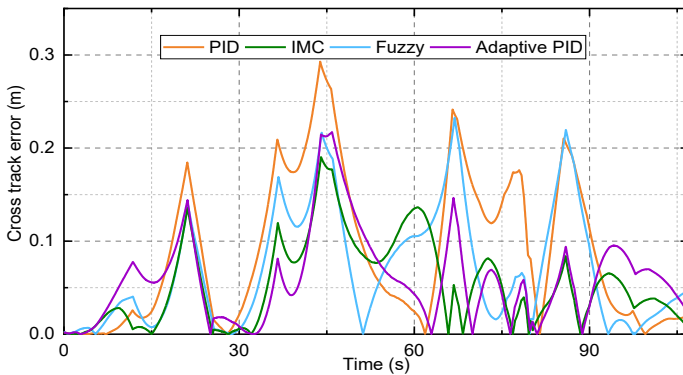


Figure 6.42 Comparison results for the cross track error at 8 knots and 20% UKC.

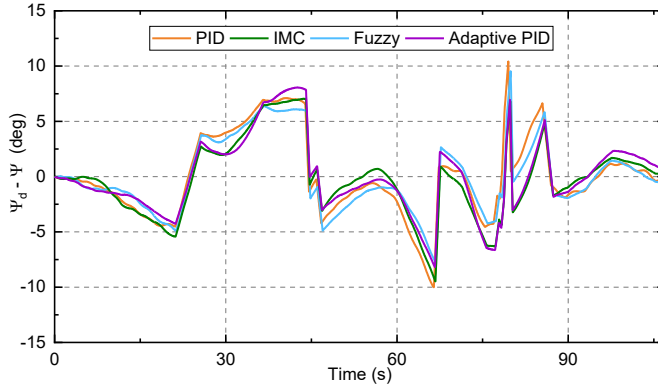


Figure 6.43 Comparison results for the heading angle error at 8 knots and 20% UKC.

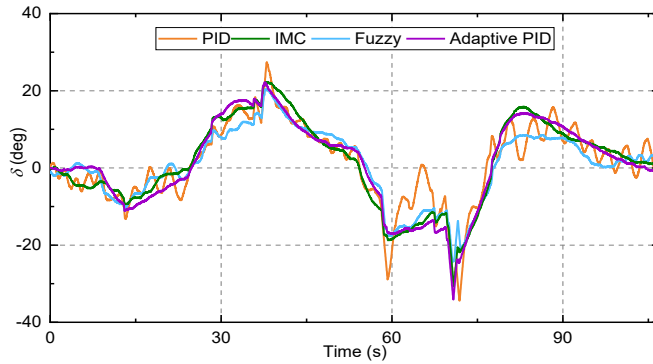


Figure 6.44 Comparison results for the rudder angle at 8 knots and 20% UKC.

6.6.4.2.3 Quantitative comparison

The model evaluation and selection mechanisms described in section 5.10 were used to compare four controllers based on five properties including mTEI, MTE, mRI, mRTV, and mHEI (Table 6.13). IMC controller obtained the maximum grey relational degree (γ_i) due to its smaller trajectory error (mTEI and MTE), heading angle error (mHEI), and smoother rudder angle (mRTV). It was followed by the adaptive PID and the fuzzy controllers with similar results, while the PID controller had the smallest grey relational degree. Additionally, the performance of the four controllers to follow a path with four obstacles is presented in Figure 6.45-Figure 6.48. All four controllers succeeded to follow the reference curved trajectory and avoid obstacles, and the real trajectory of the IMC controller was closer to the reference trajectory especially near bends.

Qualitative and quantitative results indicate that the IMC presents better performance than other controllers in this case study.

Table 6.13 Control performance of four controllers for following a path with obstacles.

Properties	PID	IMC	Fuzzy	Adaptive PID
mTEI	0.0880	0.0536	0.0693	0.0592
MTE	0.2929	0.1903	0.2327	0.2173
mRI	8.0998	9.1391	7.3523	9.0234
mRTV	0.1714	0.1118	0.1280	0.1182
mHEI	2.7703	2.4666	2.5352	2.5383
Y_i	0.5130	0.9139	0.7443	0.7594
Rank	4	1	3	2

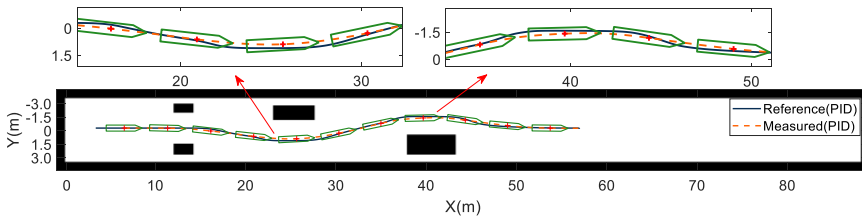


Figure 6.45 PID controller performance for following a path with four obstacles at 8 knots and 20% UKC.

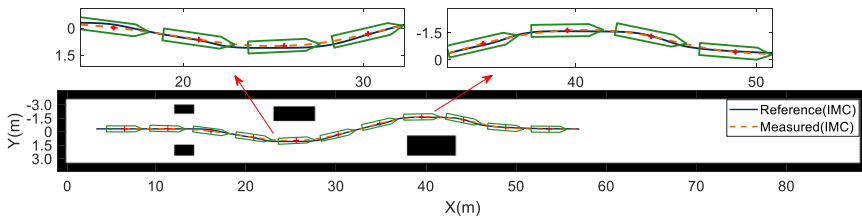


Figure 6.46 IMC controller performance for following a path with four obstacles at 8 knots and 20% UKC.

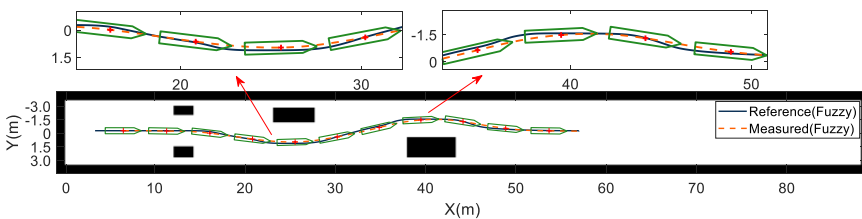


Figure 6.47 Fuzzy controller performance for following a path with four obstacles at 8 knots and 20% UKC.

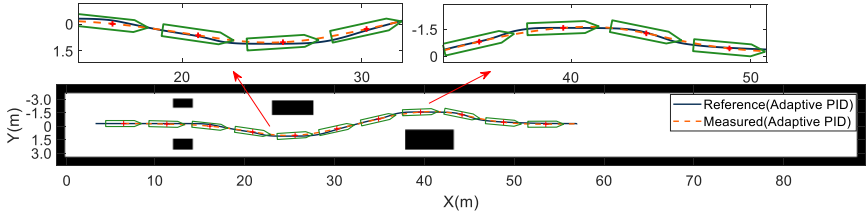


Figure 6.48 Adaptive PID controller performance for following a path with four obstacles at 8 knots and 20% UKC.

Similar to the results at 8 knots and 20% UKC, Figure 6.49 and Figure 6.50 show the controllers’ performance at 11 knots and 20% UKC. Four controllers could control the ship following the desired trajectory, but the trajectory obtained by the IMC controller was a closer fit compared to the other three controllers (Figure 6.49(b)), in particular, near the bend at $35 \text{ m} \leq X \leq 50 \text{ m}$. The trajectory error of the four controllers was stabilized within 0.30 m (45% breadth), except for the value around 28 s for the PID controller (0.34 m), and the IMC controller obtained the smallest trajectory deviation (Figure 6.50(a)). Besides, the amplitude and frequency of rudder deflection for the PID controller were higher than for the other three controllers (Figure 6.50(c)).

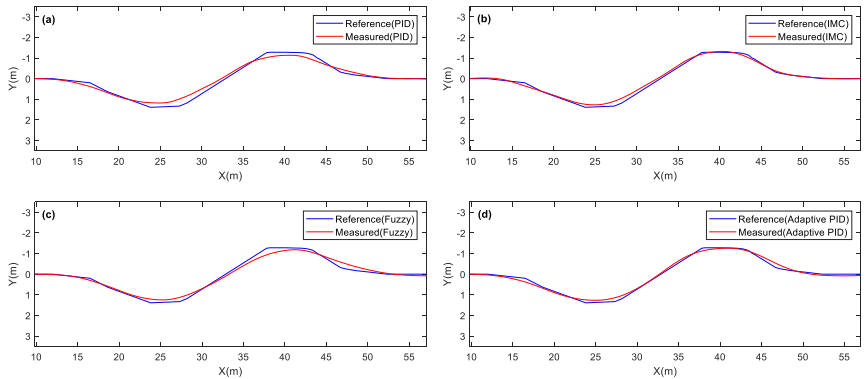


Figure 6.49 Controller performance at 11 knots and 20% UKC: (a) PID controller; (b) IMC controller; (c) Fuzzy controller; (d) Adaptive PID controller.

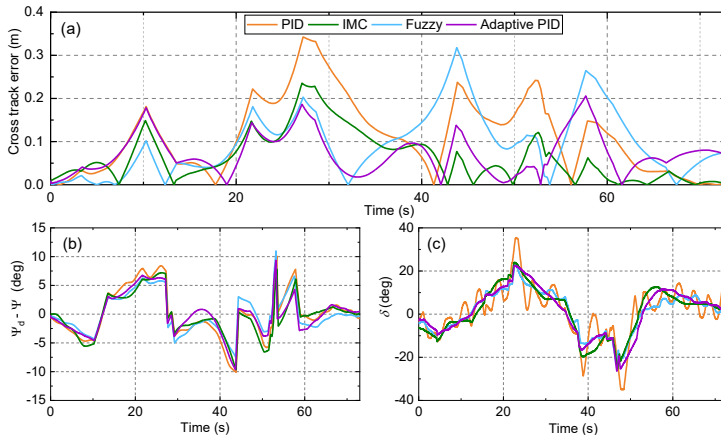


Figure 6.50 Comparison results at 11 knots and 20% UKC: (a) cross track error; (b) heading angle error; (c) rudder angle.

6.6.4.3 Summary of all experimental results

In this section, the average performance from repeated tests of each controller are compared, Table 6.14 shows the experimental conditions of the repeated tests. The four controllers were compared at the same experimental condition including forward speed, water depth, and temperature, etc. The best performance controller of each test condition was selected. The frequencies for each controller obtaining the best performance at all test conditions are summarized in Table 6.15 and visualized in Figure 6.51. It is worth mentioning that a large amount of model tests (about 5000 tests) were conducted. Within the number of tests considered, the same methodology has been used and is statistically relevant.

For the straight line control task, compared with the PID, IMC, and fuzzy controllers, the adaptive PID controller had the highest frequency (43%) of obtaining the best performance. The performance of the PID (21%) and the IMC (21%) controllers was similar, which were slightly better than the fuzzy controller (15%). Results suggest that the adaptive PID presents better tracking capability for the straight line trajectory.

As for the curved path with obstacles, the adaptive PID controller remained to obtain the best performance (47%) most frequently. It was followed by the IMC controller (41%), which was more than three times that of the fuzzy controller (12%). The results indicate that the adaptive PID controller can achieve more satisfactory performance for the curved trajectory and obstacle avoidance.

Regarding the step line control task, the fuzzy controller showed the highest frequency of obtaining the optimal performance (50%), followed by adaptive PID (29%) and the IMC (21%) controllers. Similar results were observed for the folding line trajectory.

Summarized, the adaptive PID performed the best in most experiments (36%), followed by the fuzzy (30%) and IMC (29%) controllers whilst the PID controller presented the worst control effect (5%).

According to the statistical results, we can observe that the performance of the PID controller is inferior compared to the other controllers. It might be attributed to the constant bandwidth frequency adopted by the PID controller during tests. In addition, Table 6.15 shows that the frequencies for each controller obtaining the best performance varied according to the desired path, which might be explained by the influence of the number of waypoints and the look ahead distance, etc.

Table 6.14 Experimental conditions of the repeated tests.

Speeds (knots)	10%UKC				20% UKC				35% UKC				100% UKC			
	St	C	S	F	St	C	S	F	St	C	S	F	St	C	S	F
4	√	√	x	x	√	√	√	√	√	√	√	√	x	√	√	√
6	√	√	x	x	√	√	√	√	√	√	√	√	x	√	√	√
8	√	√	x	x	√	√	√	√	√	√	√	√	√	√	√	√
11					√	√	√	√	√	√	√	√	√	√	√	√
13									√	√	√	√	x	√	√	√

Note: St: Straight line; C: Curved line with obstacles; S: Step line; F: Folding line.

Table 6.15 Frequencies for each controller obtaining the best performance at all test conditions.

Desired path	No. (Percentage)			
	PID	IMC	Fuzzy	Adaptive PID
Straight line	3 (21%)	3 (21%)	2 (15%)	6 (43%)
4 obstacles	0 (0%)	7 (41%)	2 (12%)	8 (47%)
Step line	0 (0%)	3 (21%)	7 (50%)	4 (29%)
Folding line	0 (0%)	4 (29%)	7 (50%)	3 (21%)
Total	3 (5%)	17 (29%)	18 (30%)	21 (36%)

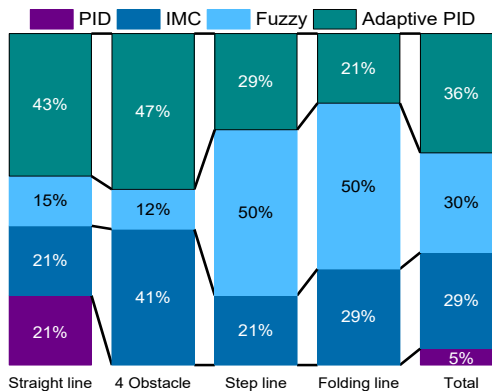


Figure 6.51 Frequencies for each controller obtaining the best performance at all test conditions.

6.7 Shallow water and speed effects

6.7.1 Effects on manoeuvring indices K and T

6.7.1.1 Effect of water depth on K and T

The research about ship manoeuvrability in restricted water is of crucial importance when ships are accessing or navigating in shallow and confined water which changes the ship hydrodynamic forces. Mathematical models are widely employed to describe the ship dynamic characteristics, such as MMG model, Abkowitz model, etc. The structure of those mathematical models is relatively complex and difficult to be used to design ship autopilots. Most of autopilots are designed based on a simple response model. In this section, it is assumed that no manoeuvring models are available for towing tank tests, and the 1st Nomoto model is used to have an idea of the ship's manoeuvring behaviour.

The origin of the 1st Nomoto model is the uncoupled linear yaw motion model:

$$(I_{zz} - N_{\dot{r}})\dot{r} - N_r r = N_\delta \delta \quad (6.26)$$

Eq. (6.26) is rewritten in the format:

$$-\frac{(I_{zz} - N_{\dot{r}})}{N_r} \dot{r} + r = -\frac{N_\delta}{N_r} \delta \quad (6.27)$$

Or

$$T\dot{r}(t_i) + r(t_i) = K\delta(t_i) \quad (6.28)$$

Then the time constant T and the gain K of the Nomoto model are derived as:

$$T = -\frac{(I_{zz} - N_{\dot{r}})}{N_r} \quad (6.29)$$

$$K = -\frac{N_\delta}{N_r} \quad (6.30)$$

where r is yaw rate, δ is the rudder angle.

To study the shallow water effect on the ship steering model, the Eqs. (6.29)-(6.30) should be considered. With decreasing water depth, $N_{\dot{r}}$ and N_r will monotonously increase (Delefortrie et al., 2020). Because the water depth effect on N_r is stronger and I_{zz} is constant, hence T will decrease with decreasing water depth. Due to that Y_δ tends to be bigger value at lower water depth, but N_δ is not necessary owing to the forward shift of the application point with water depth. Therefore, K will present a smaller value at lower water depth.

To verify the theoretic analysis, the $\pm 10^\circ/2.5^\circ$ and $\pm 20^\circ/5^\circ$ zigzag experimental results for different speeds (4 knots to 8 knots) and UKCs (10% UKC to 100%

UKC) are used. Based upon the zigzag experimental results, the novel system identification technique NLSSVM is adopted to determine ship manoeuvring indices T and K . More information about the NLSSVM machine learning approach can be obtained in section 3.3.4 and Chen et al. (2019). The regression results are presented in Table 6.16, and visualized in Figure 6.52-Figure 6.54. One can observe that the time constant T and the gain K increase with increasing water depths, which is consistent with theoretical analysis.

Table 6.16 The Nomoto model parameters T and K with different water depth at 4, 6, 8 knots forward speed.

UKC	Zigzag (4 knots)							
	20°/5°		-20°/5°		10°/2.5°		-10°/2.5°	
	T	K	T	K	T	K	T	K
10%	4.6467	0.0345	4.5940	0.0317	5.0267	0.0361	6.2803	0.0421
20%	6.2822	0.0356	6.3107	0.0359	8.4759	0.0461	8.8850	0.0497
35%	10.3774	0.0543	10.2219	0.0550	19.4615	0.0885	24.4253	0.1019
100%	17.2803	0.0623	16.1676	0.0607	28.8879	0.1060	37.6782	0.1295
UKC	Zigzag (6 knots)							
	20°/5°		-20°/5°		10°/2.5°		-10°/2.5°	
	T	K	T	K	T	K	T	K
10%	3.1574	0.0513	2.7946	0.0463	4.6449	0.0639	4.5999	0.0681
20%	4.4984	0.0569	4.3758	0.0593	5.4578	0.0656	5.4332	0.0744
35%	6.9676	0.0846	6.9494	0.0819	10.2005	0.1073	10.6785	0.1091
100%	11.0229	0.0952	11.0037	0.0977	22.774	0.1851	17.4565	0.1368
UKC	Zigzag (8 knots)							
	20°/5°		-20°/5°		10°/2.5°		-10°/2.5°	
	T	K	T	K	T	K	T	K
10%	2.5821	0.0720	2.2735	0.0680	3.3311	0.0797	3.3170	0.0796
20%	3.255	0.0828	3.289	0.0813	4.2762	0.0979	4.0729	0.0942
35%	5.3875	0.1163	5.362	0.1130	7.5504	0.1412	6.4010	0.1277
100%	8.904	0.1380	8.8458	0.1378	17.3859	0.2415	14.3581	0.2128

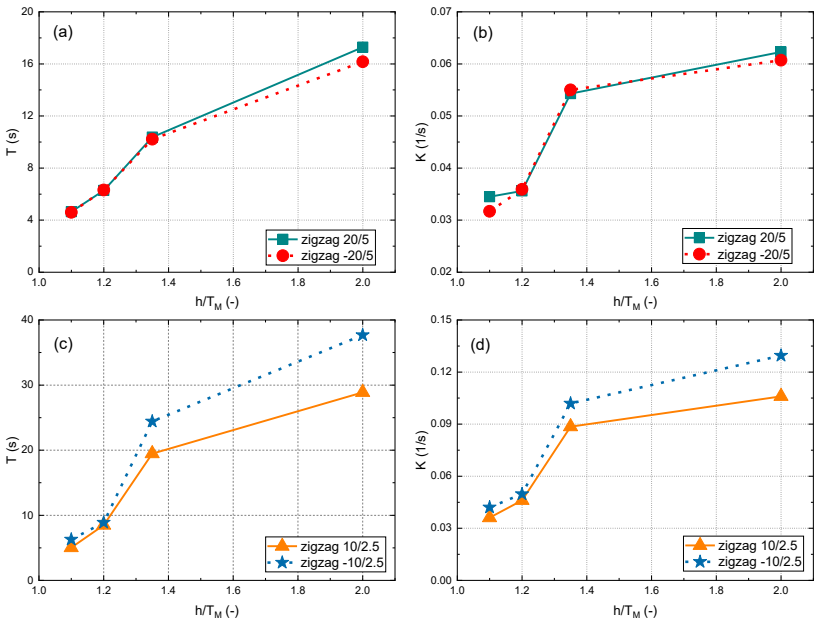


Figure 6.52 The tendency of the Nomoto model parameters T and K with different water depth at 4 knots forward speed.

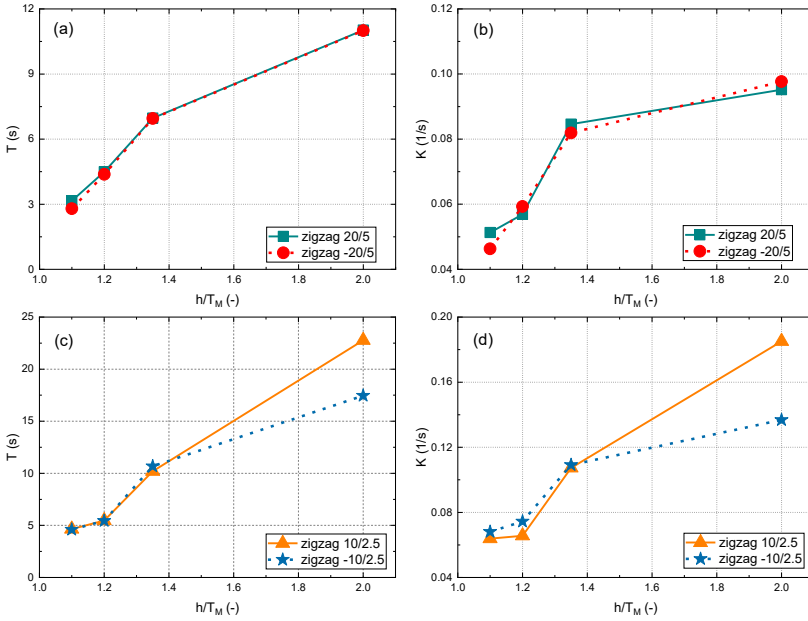


Figure 6.53 The tendency of the Nomoto model parameters T and K with different water depth at 6 knots forward speed.

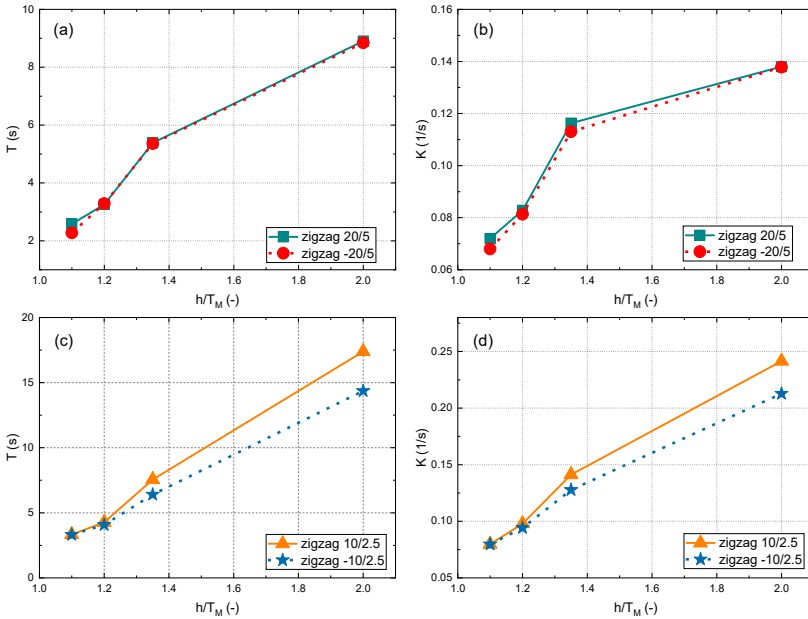


Figure 6.54 The tendency of the Nomoto model parameters T and K with different water depth at 8 knots forward speed.

6.7.1.2 Effect of forward speed or propeller rate on K and T

To have a better understanding of the influence of forward speed on ship manoeuvring model in shallow and medium deep water. Ship manoeuvring indices T and K at different forward speeds for four UKCs are presented in Figure 6.55 to Figure 6.58. Taken the results at 100% UKC as examples (see Figure 6.55). It is not difficult to find in Figure 6.55(a) and Figure 6.55(c) that the time constant T tends to decrease with increasing forward speed, while a larger forward speed results in a larger gain K , which can be found in Figure 6.55(b) and Figure 6.55(d). Similar results can be observed for 35% UKC, 20% UKC and 10% UKC (see Figure 6.56-Figure 6.58). The phenomenon might be attributed to the effect of forward speed or the propeller rate on the response of the rudders. The propeller rate has direct influence on the inflow towards the rudders and thus the manoeuvring force created. Hence, a higher speed or propeller rate will deliver a smaller response time T and a larger gain K , in other words:

$$T \sim n^{-1} \text{ or } T \sim u^{-1} \tag{6.31}$$

$$K \sim n \text{ or } K \sim u \tag{6.32}$$

where n represents the propeller rate, u is the forward speed.

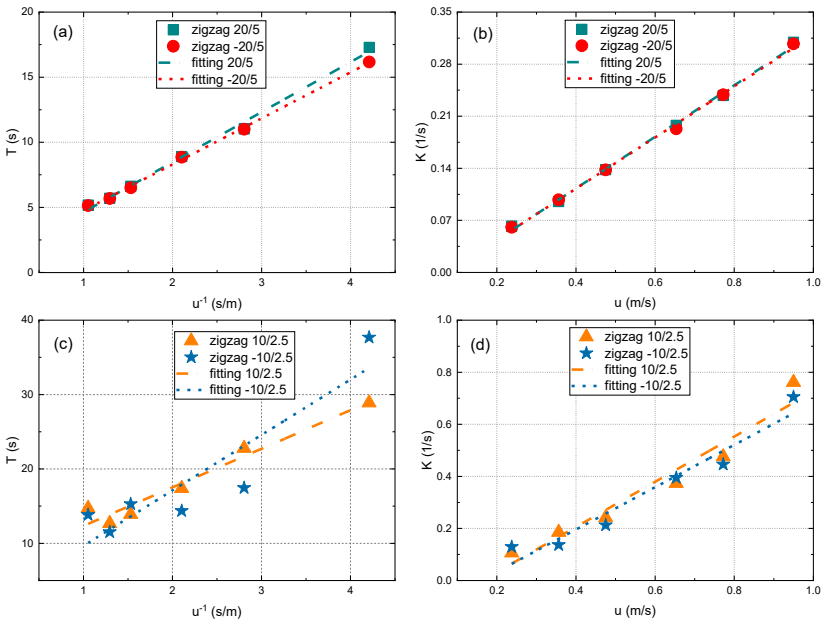


Figure 6.55 The tendency of the Nomoto model parameters T and K with different forward speed at 100% UKC.

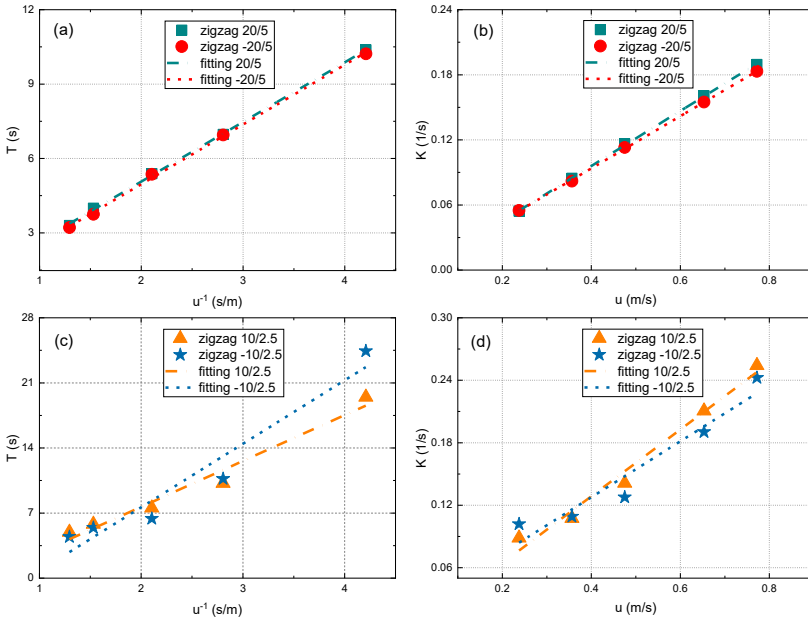


Figure 6.56 The tendency of the Nomoto model parameters T and K with different forward speed at 35% UKC.

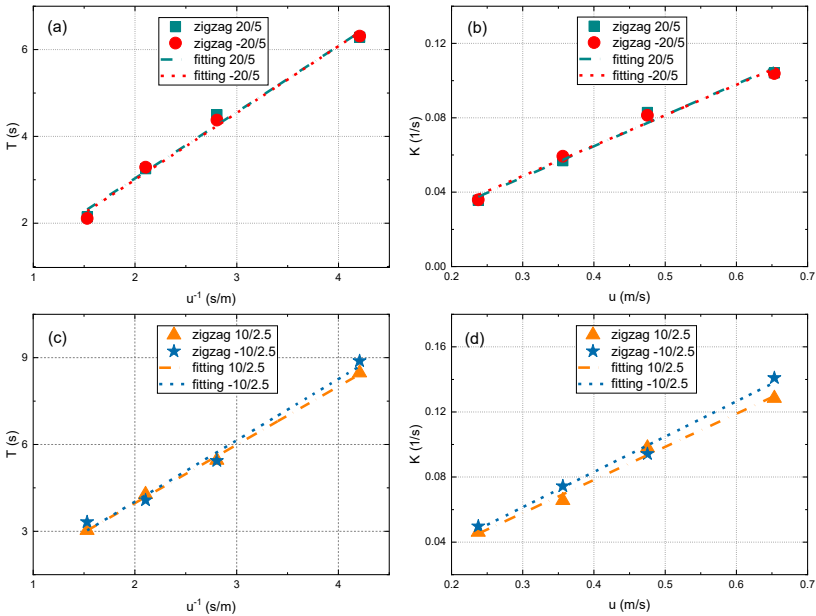


Figure 6.57 The tendency of the Nomoto model parameters T and K with different forward speed at 20% UKC.

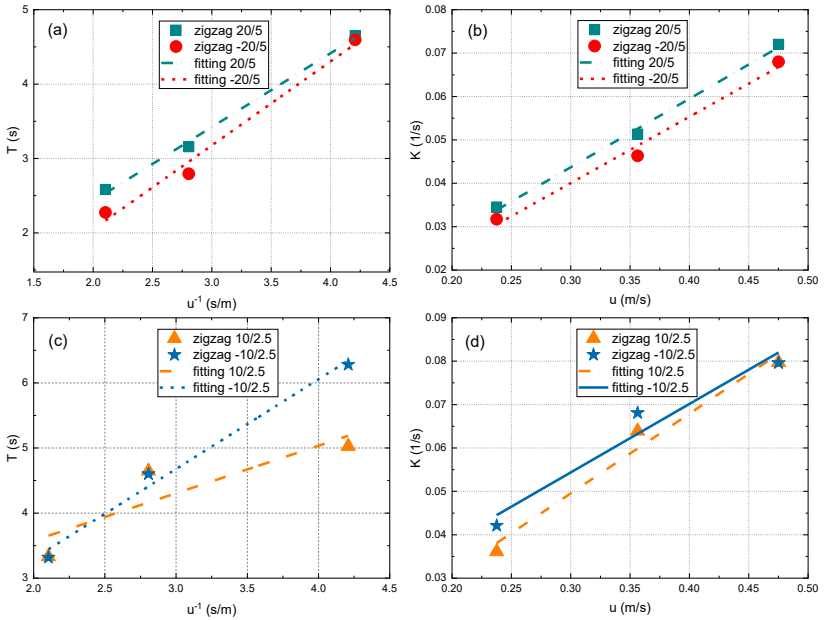


Figure 6.58 The tendency of the Nomoto model parameters T and K with different forward speed at 10% UKC.

6.7.2 Effects on controller parameters

6.7.2.1 Overview

In this section, the effect of water depth and approach speed on the IMC controller’s parameters will be presented, more specifically on the related PID values K_p , K_i and K_d (see Eqs. (5.20)-(5.22)), where the parameters T , K and β_c were determined by the method in section 6.6.4.

6.7.2.2 Effect of water depth on K_p , K_i and K_d

Table 6.17 and Figure 6.59 present the relationship between the PID coefficients and water depths (UKCs) for the speed of 4, 6 and 8 knots. One can observe from Figure 6.59 that the proportional (K_p), integral (K_i), and derivative (K_d) coefficients present descending trends with decreasing water depth (h/T_M). According to the analysis of experimental results, it seems that smaller PID coefficients deliver better results for the lower under keel clearances.

Table 6.17 PID controller coefficients at different water depths (UKCs) for the speed of 4, 6 and 8 knots.

UKC	h/T_M	K_p (-)	K_i (s ⁻¹)	K_d (s)
4 knots				

100%	2.0	6.9665	0.2597	36.6839
35%	1.35	4.7161	0.1825	23.8326
20%	1.2	3.6987	0.1266	9.9165
10%	1.1	3.6128	0.1312	5.3653
6 knots				
100%	2.0	6.3744	0.3403	24.4352
35%	1.35	4.7541	0.2802	16.0199
20%	1.2	3.7115	0.1937	7.5697
10%	1.1	3.7018	0.2028	3.8902
8 knots				
100%	2.0	6.1329	0.4230	18.6082
35%	1.35	4.9489	0.3932	12.7031
20%	1.2	3.7326	0.2788	5.6172
10%	1.1	3.6171	0.2625	3.4747

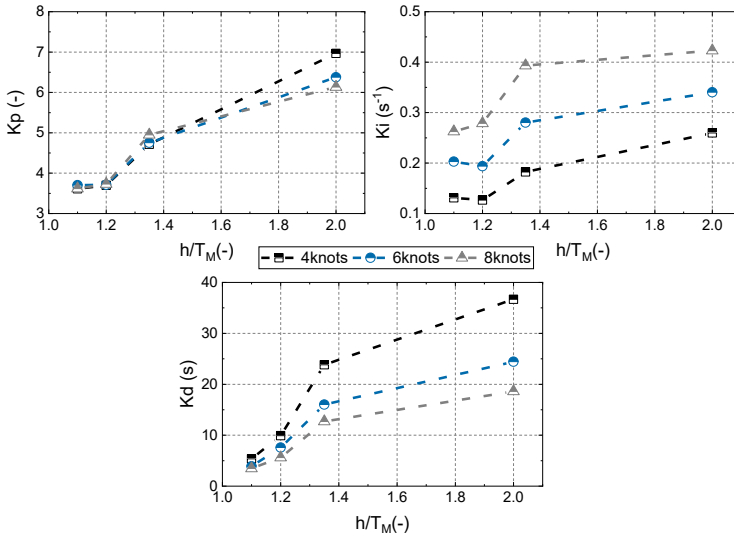


Figure 6.59 Relationship between the PID coefficients and water depths (h/T_M) for the speed of 4, 6 and 8 knots.

6.7.2.3 Effect of speed or propeller rate on K_p , K_i and K_d

To study the effect of forward speed or propeller rate on PID controller coefficients K_p , K_i and K_d . The PID coefficients at different speeds or propeller rates were obtained according to Eqs. (5.20)-(5.22). Because the constant propeller rate was adopted during model tests, thus the relationship between the PID controller's coefficients and the propeller rates were investigated.

Table 6.18 shows the PID coefficients at different propeller rates for four water depths. The values found for the proportional, integral, and derivative coefficients are plotted in function of the propeller rate they correspond with and a trendline is

added for each of the controller parameters (Figure 6.60-Figure 6.62). The relationships between the PID coefficients and propeller rate are summarized in Table 6.19.

From Figure 6.60-Figure 6.62 and Table 6.19, one can find that at the same UKC the proportional coefficient K_p was constant, which was not dependent on the propeller rate. Mind that in Figure 6.60 a constant approximation was obtained for the proportional coefficient K_p , rather than trying to fit a higher order polynomial. Furthermore, the integral coefficient K_i was proportional to the propeller rate, namely, K_i increased with increasing propeller rate. The derivative coefficient K_d was inversely proportional to the propeller rate. Within the bound of the results in Table 6.19, the following relationships can be obtained:

$$K_p = K_{pn}n^0 \tag{6.33}$$

$$K_i = K_{in}n^1 \tag{6.34}$$

$$K_d = K_{dn}n^{-1} \tag{6.35}$$

where K_p , K_i and K_d are the proportional, integral and derivative coefficients; K_{pn} , K_{in} and K_{dn} are the speed dependent proportional, integral and derivative coefficients. n is the propeller rate.

By realizing this, optimal PID values only need to be determined for one forward speed, other PID values can be determined according to the relationship in Eqs. (6.33)-(6.35), which is so-called the adaptive PID controller. The new development of adaptive PID controller can save time by not having to determine the optimal values for all forward speeds, and more model tests can be carried out. In addition, the speed dependency guarantees proper track keeping behaviour in case speed changes are induced during manoeuvring.

Table 6.18 Propeller rate versus PID controller coefficients at different speeds for 10%, 20%, 35%, and 100% UKCs.

Speed (m/s)	n (rps)	K_p (-)	K_i (s ⁻¹)	K_d (s)
100% UKC				
0.2376 (4 knots)	3.2833	6.9665	0.2597	36.6839
0.3564 (6 knots)	4.9250	6.3744	0.3403	24.4352
0.4752 (8 knots)	6.5667	6.1329	0.4230	18.6082
0.6534 (11 knots)	9.0357	6.5080	0.6485	13.9571
0.7722 (13 knots)	10.6774	6.4132	0.7107	12.6429
0.9500 (16 knots)	13.1333	6.8850	0.8598	12.2435
35% UKC				
0.2376 (4 knots)	3.9400	4.7161	0.1825	23.8326
0.3564 (6 knots)	5.8969	4.7541	0.2802	16.0199
0.4752 (8 knots)	7.8669	4.9489	0.3932	12.7031
0.6534 (11 knots)	10.8219	4.8358	0.5186	9.1971
0.7722 (13 knots)	13.1333	4.7659	0.6087	7.5334

20% UKC				
0.2376 (4 knots)	4.1501	3.6987	0.1266	9.9165
0.3564 (6 knots)	6.2252	3.7115	0.1937	7.5697
0.4752 (8 knots)	8.3003	3.7326	0.2788	5.6172
0.6534 (11 knots)	11.4260	3.6992	0.3705	3.3850
10% UKC				
0.2376 (4 knots)	4.492	3.613	0.131	5.365
0.3564 (6 knots)	6.737	3.702	0.203	3.890
0.4752 (8 knots)	8.983	3.617	0.263	3.475

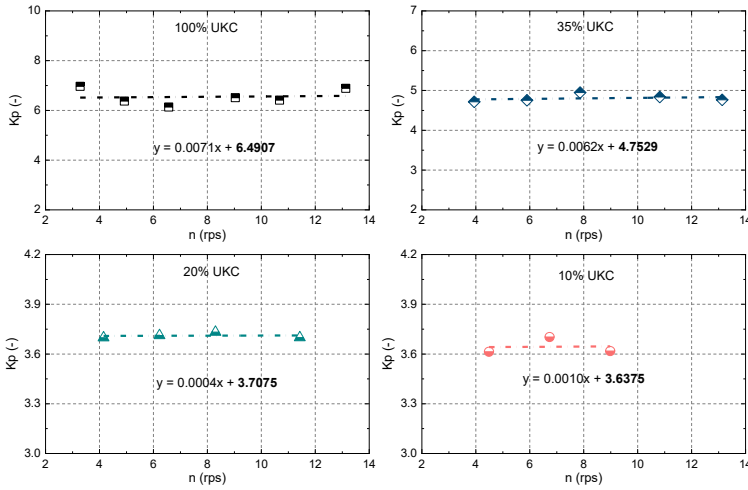


Figure 6.60 Relationship between the proportional coefficient K_p and propeller rate n at 10%, 20%, 35%, and 100% UKCs.

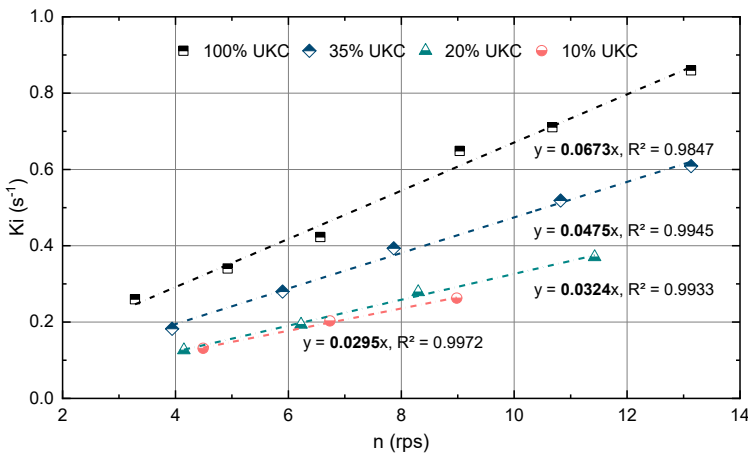


Figure 6.61 Relationship between the integral coefficient K_i and propeller rate n at 10%, 20%, 35%, and 100% UKCs.

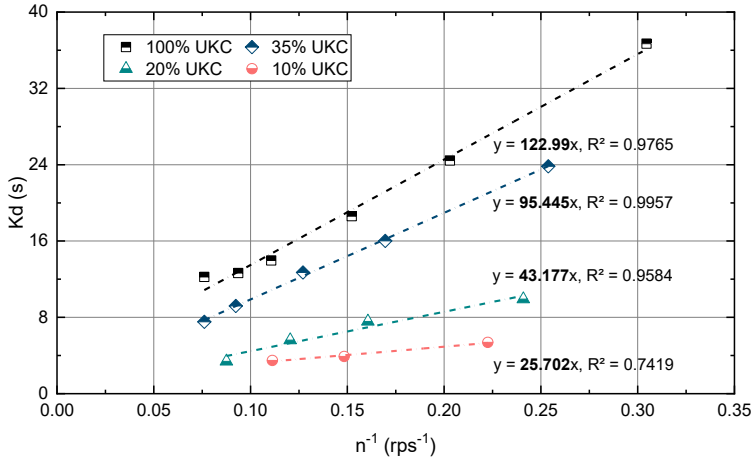


Figure 6.62 Relationship between the derivative coefficient K_i and propeller rate n at 10%, 20%, 35%, and 100% UKCs.

Table 6.19 Relationship between the proportional, integral, derivative coefficients (coef.) and propeller rate at 10%, 20%, 35%, and 100% UKCs.

UKC	Proportional coef.	Integral coef.	Derivative coef.
100%	$K_p = 0.0071n^1 + 6.4907n^0$ Or $K_p \approx 6.4907n^0$	$K_i = 0.0672n^1$ $R^2 = 0.9847$	$K_d = 122.99n^{-1}$ $R^2 = 0.9765$
35%	$K_p = 0.0062n^1 + 4.7529n^0$ Or $K_p \approx 4.7529n^0$	$K_i = 0.0475n^1$ $R^2 = 0.9945$	$K_d = 95.445n^{-1}$ $R^2 = 0.9957$
20%	$K_p = 0.0004n^1 + 3.7075n^0$ Or $K_p \approx 3.7075n^0$	$K_i = 0.0324n^1$ $R^2 = 0.9933$	$K_d = 43.177n^{-1}$ $R^2 = 0.9584$
10%	$K_p = 0.0010n^1 + 3.6375n^0$ Or $K_p \approx 3.6375n^0$	$K_i = 0.0295n^1$ $R^2 = 0.9972$	$K_d = 25.702n^{-1}$ $R^2 = 0.7419$

6.7.3 Effects on controller performance

To study the effect of water depth on the controllers’ performance, free running model tests with the adaptive PID and IMC control algorithms were conducted in FHR towing tank. The performance of controllers was evaluated according to their capacity of tracking a curved path and avoiding obstacles in different test water depths. In the following sections, the results for four different water depths (10%, 20%, 35%, and 100% UKCs) and two speeds (8 and 11 knots) are presented to elaborate the shallow water effect on controllers’ performance. For the different water depths, the same controller used the same coefficients. Because the controllers were first tested in 100% UKC, hence the coefficients of each

controller in 10%, 20% and 35% UKCs were consistent with 100% UKC. Table 6.20 lists the parameters of adaptive PID and IMC controllers.

Table 6.20 Parameters of adaptive PID and IMC controllers at 100% UKC for 8 and 11 knots.

Speed	Adaptive PID			IMC		
	K_{pn} (-)	K_{in} (-)	K_{dn} (-)	K_p (-)	K_i (s^{-1})	K_d (s)
8 knots	6.4907	0.0673	122.99	6.1329	0.4230	18.6082
11knots				6.5080	0.6485	13.9571

Figure 6.63 and Figure 6.64 present the performance of the adaptive PID controller at 8 knots under different water depths. One can observe from Figure 6.63 that the ship could follow the reference path and avoid obstacles, although the same parameters were used in different water depths. Nevertheless, the tracking error increased as the water depth decreased especially near curve bends, see Figure 6.64(a) and Figure 6.64(b) for better illustration. Furthermore, it can be found in Figure 6.64(c) that the ship used bigger rudders in order to change the heading in the shallower water. Similar results for the IMC can be seen in Figure 6.65 and Figure 6.66.

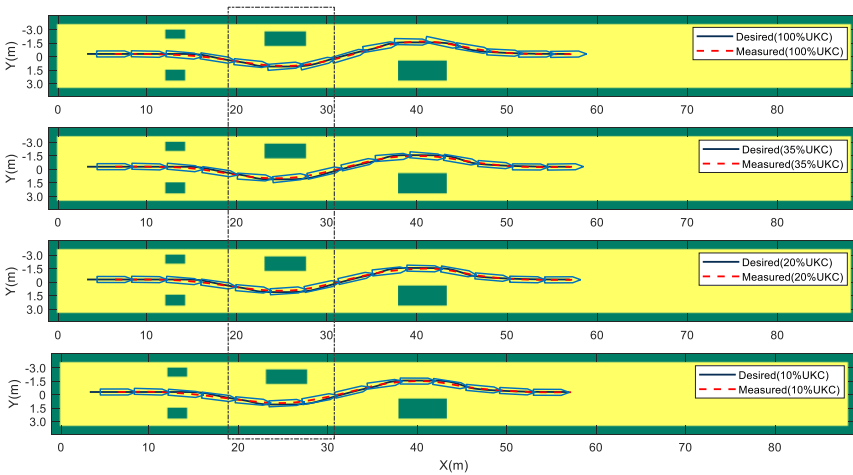


Figure 6.63 Trajectories obtained by the adaptive PID controller in different water depths at 8 knots.

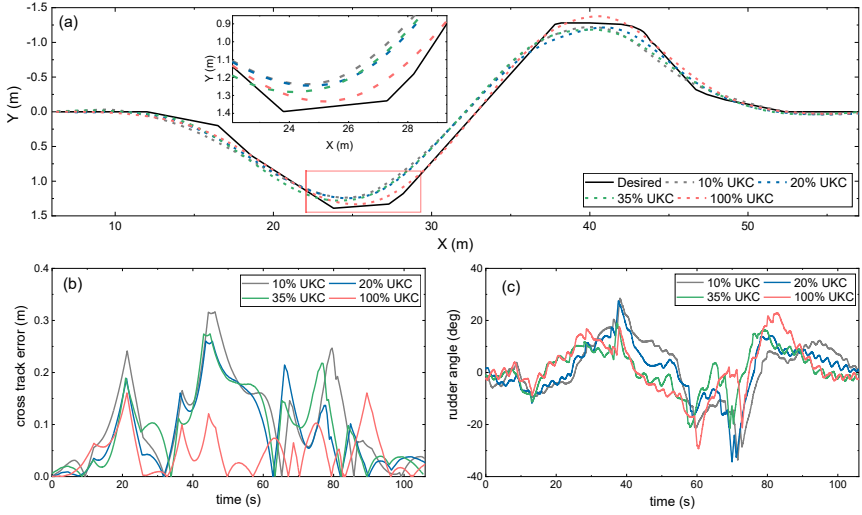


Figure 6.64 Adaptive PID controller performance in different water depths at 8 knots: (a) desired and measured trajectories; (b) cross track error; (c) rudder angle.

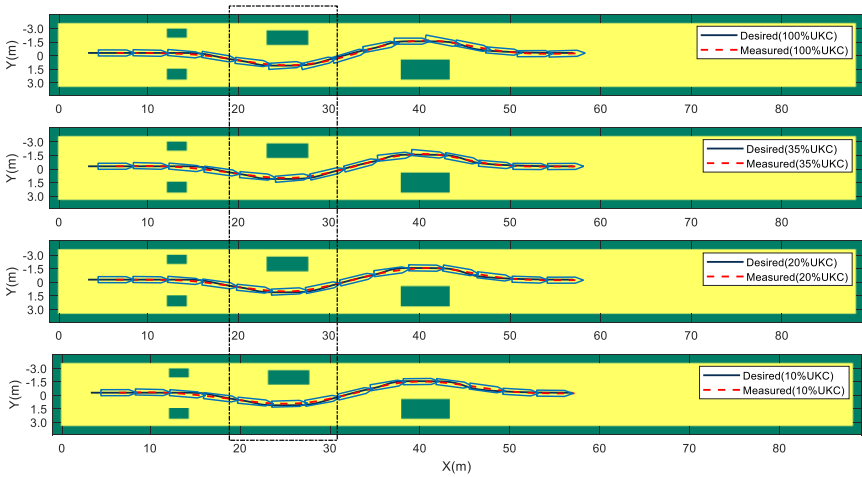


Figure 6.65 Trajectories obtained by the IMC controller in different water depths at 8 knots.

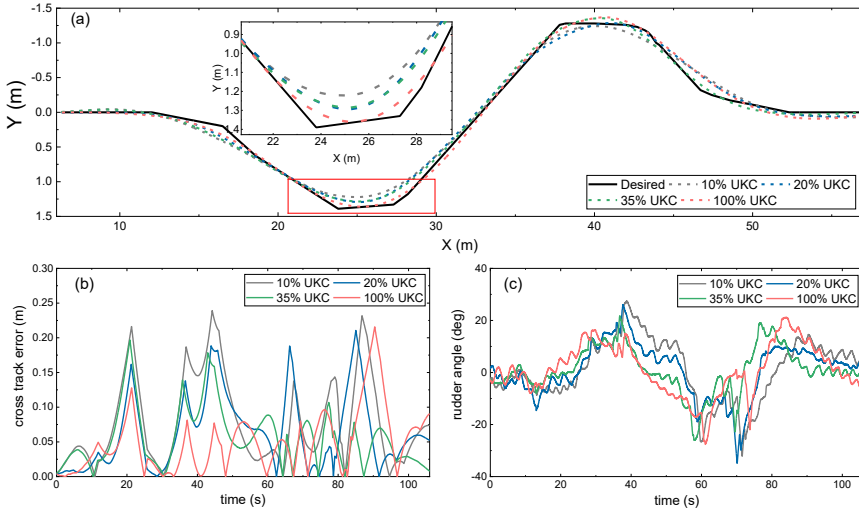


Figure 6.66 IMC controller performance in different water depths at 8 knots: (a) desired and measured trajectories; (b) cross track error; (c) rudder angle.

To provide further quantification, the evaluation indexes mTEI, MTE, mHEI, and mRI in section 5.10 were employed to assess the tracking capacity of controllers. Table 6.21 and Figure 6.67 give a quantitative comparison of the adaptive PID and IMC controllers' performance in different water depths. It is noted that the average and maximal cross track errors (mTEI, MTE) showed an increase with decreasing UKC. For instance, the mTEI of adaptive PID controller at 100% UKC was 0.0437 m, which was increased to 0.0936 m, 0.0842 m, 0.1018 m at 35% UKC, 20% UKC and 10% UKC, respectively. It can be attributed to that the water-depth limitations changed the pressure distribution around the ship and caused an increase of hydrodynamic forces. In addition to an increase in ship's resistance, the propulsive efficiency and manoeuvrability of the ship were reduced when sailing at a small UKC. Thus, the ship was not able to arrive at the desired speed and position, leading to the tracking error increased. Moreover, in shallower water, the directional stability of the ship became better, hence the heading deviation (mHEI) was smaller. Owing to the variations of hydrodynamic forces and propulsive efficiency, a greater rudder (mRI) was needed to change the ship's heading for following the desired trajectory.

Table 6.21 Evaluation indexes of adaptive PID and IMC controllers in different water depths at 8 knots.

UKC (%)	h/T_M (-)	mTEI (m)	MTE (m)	mHEI (deg)	mRI (deg)
Adaptive PID					
100	2.0	0.0437	0.1607	3.2806	7.1987
35	1.35	0.0936	0.2742	3.2321	6.2256
20	1.2	0.0842	0.2605	2.7992	8.0332
10	1.1	0.1018	0.3167	2.9316	9.3783

IMC					
100	2.0	0.0512	0.2157	3.2660	7.4934
35	1.35	0.0564	0.1968	2.7997	6.2929
20	1.2	0.0638	0.2106	2.5154	8.2870
10	1.1	0.0793	0.2392	2.6149	9.5768

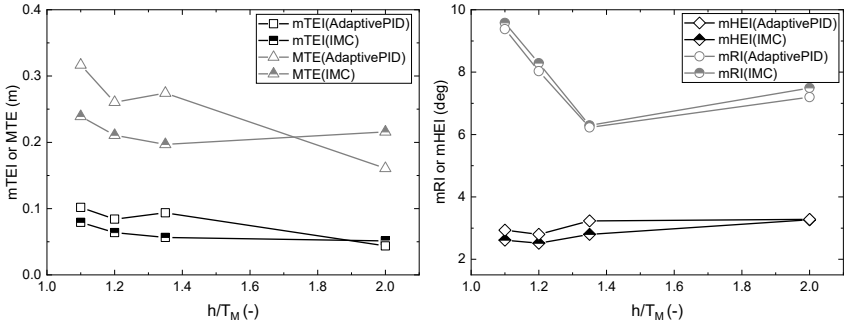


Figure 6.67 Evaluation indexes of adaptive PID and IMC controllers in different water depths at 8 knots.

Figure 6.68 and Figure 6.69 show the effect of water depth on adaptive PID and IMC controllers’ performance at the speed of 11 knots, including trajectories, cross track error, and rudder angle. Table 6.22 and Figure 6.70 present their quantitative comparison. According to the controllers’ performance in different water depths at 11 knots, similar conclusions as the speed of 8 knots can be drawn.

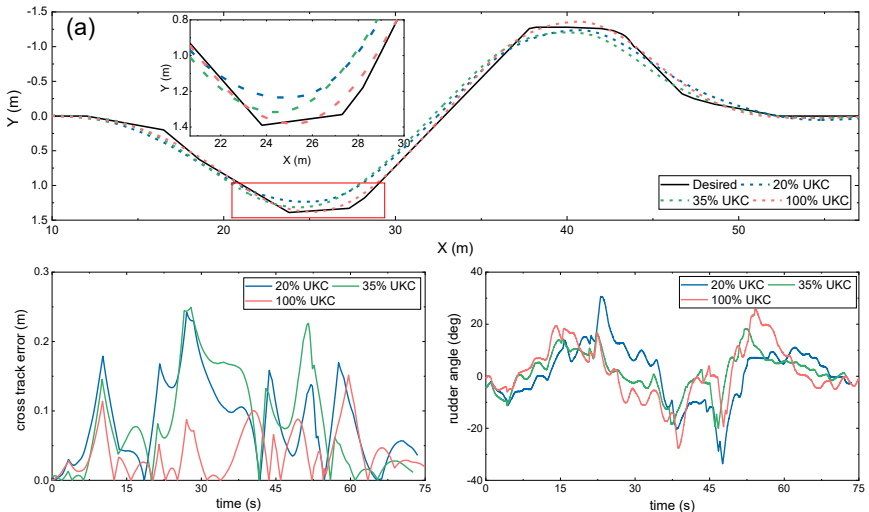


Figure 6.68 Adaptive PID controller performance in different water depths at 11 knots: (a) desired and measured trajectories; (b) cross track error; (c) heading angle error; (d) rudder angle.

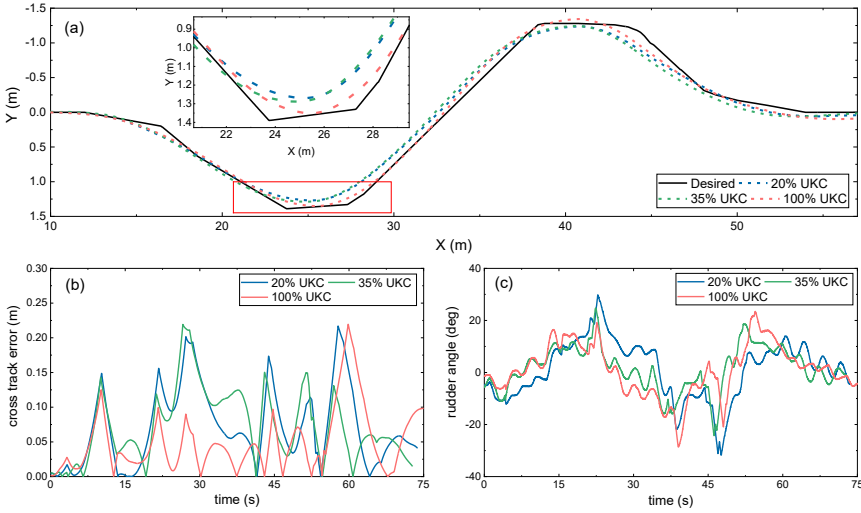


Figure 6.69 IMC controller performance in different water depths at 11 knots: (a) desired and measured trajectories; (b) cross track error; (c) heading angle error; (d) rudder angle.

Table 6.22 Evaluation indexes of the adaptive PID and IMC controllers in different water depths at 11 knots.

UKC (%)	h/T_M (-)	mTEI (m)	MTE (m)	mHEI (deg)	mRI (deg)
Adaptive PID					
100	2.0	0.0384	0.1516	3.5673	8.0161
35	1.35	0.0833	0.2494	3.2750	6.1843
20	1.2	0.0834	0.2419	2.8047	9.0355
IMC					
100	2.0	0.0505	0.2195	3.3171	7.5016
35	1.35	0.0728	0.2192	3.0409	6.8417
20	1.2	0.0711	0.2169	2.6934	9.3167

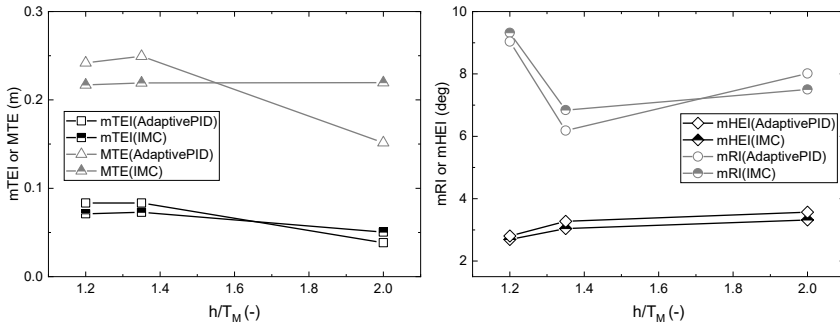


Figure 6.70 Evaluation indexes of adaptive PID and IMC controllers in different water depths at 11 knots.

6.7.4 Improvement of controllers' performance

Based on the above analysis, if the same parameters were used in different water depths, the controllers could not achieve satisfactory performance. Thus, the parameters of controllers should vary in different UKCs. In order to improve the adaptive PID and IMC controllers' performance, different parameters were used in different depths in this work, see Table 6.18 and Table 6.19 for values of these.

Table 6.23, Figure 6.71 and Figure 6.72 compare the performance of adaptive PID controller using the constant and optimized parameters in different water depths at the speed of 8 knots and 11 knots, where "Constant" means the same controllers' parameters were used in different water depths (same with 100% UKC); "Optimized" represents the different parameters were used in different water depths. Under optimized conditions, the trajectories were closer to the desired one (Figure 6.71 and Figure 6.72), especially when sailing near bends. From Table 6.23, one can observe that the mean and maximum cross track errors (mTEI, MTE) obtained using the optimized parameters were generally smaller than that from constant parameters, see Figure 6.71 and Figure 6.72 for better illustration. For instance, at 8 knots and 10% UKC, the mTEI and MTE were 0.1018 m and 0.3167 m obtained using the constant parameters, the optimized values were 0.0783 m and 0.2341 m, the tracking errors mTEI and MTE were reduced by 23.1% and 26.1%, respectively. On the other hand, the heading angle error (mHEI) was also reduced (Table 6.23). In addition, one can observe from Figure 6.71 and Figure 6.72 that the frequency of rudder deflection was less, and the rudder angle was smoother under optimized conditions. Therefore, the performance of controller was improved using the optimized parameters. It is confirmed that the varying controllers' parameters should be adopted in different water depths.

Table 6.23 Adaptive PID controller's performance using the constant and optimized parameters in different water depths at 8 knots and 11 knots.

UKC (%)	h/T_M (-)	Adaptive PID, 8 knots				
		Parameters	mTEI (m)	MTE (m)	mHEI (deg)	mRI (deg)
10%	1.1	Constant	0.1018	0.3167	2.9316	9.3783
		Optimized	0.0783	0.2341	2.6854	9.2301
20%	1.2	Constant	0.0842	0.2605	2.7992	8.0332
		Optimized	0.0592	0.2173	2.5383	9.0234
35%	1.35	Constant	0.0936	0.2742	3.2321	6.2256
		Optimized	0.0628	0.1676	2.8897	7.3858
Adaptive PID, 11 knots						
20%	1.2	Constant	0.0834	0.2419	2.8047	9.0355
		Optimized	0.0622	0.1641	2.1965	9.9652
35%	1.35	Constant	0.0833	0.2494	3.2750	6.1843
		Optimized	0.0642	0.1537	2.9478	7.7955

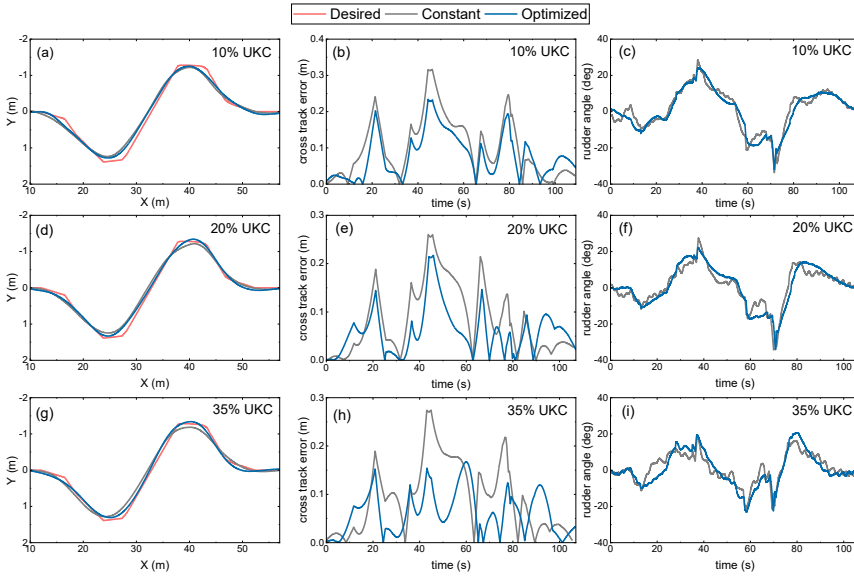


Figure 6.71 Adaptive PID controller's performance using the constant and optimized parameters in different water depths at 8 knots.

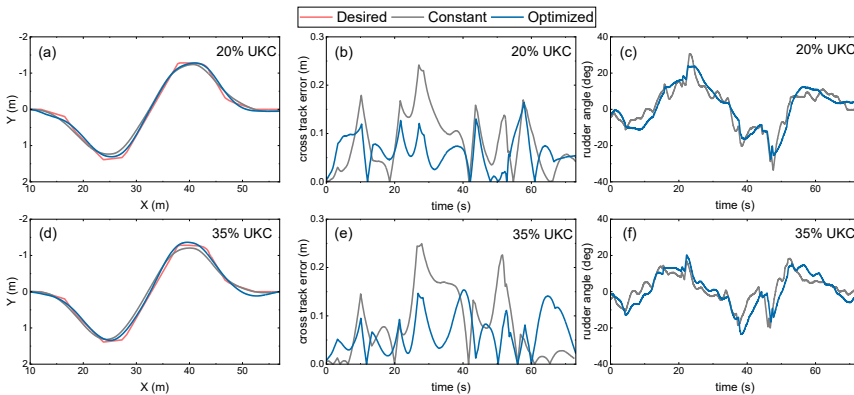


Figure 6.72 Adaptive PID controller's performance using the constant and optimized parameters in different water depths at 11 knots.

Table 6.24 presents quantitative comparisons for the performance of the IMC controller using the constant and optimized parameters in different water depths at the speed of 8 knots and 11 knots. Figure 6.73 and Figure 6.74 compare the trajectories, cross track error, and rudder deflection. According to the IMC controller's performance, similar conclusions to the adaptive PID controller can be obtained.

Table 6.24 IMC controller’s performance using the constant and optimized parameters in different water depths at 8 knots and 11 knots.

UKC (%)	h/T_M (-)	IMC, 8 knots				
		Parameters	mTEI (m)	MTE (m)	mHEI (deg)	mRI (deg)
10%	1.1	Constant	0.0793	0.2392	9.5768	0.1288
		Optimized	0.0643	0.1862	10.0839	0.1186
20%	1.2	Constant	0.0638	0.2106	8.2870	0.1453
		Optimized	0.0536	0.1903	9.1391	0.1118
35%	1.35	Constant	0.0564	0.1968	6.2929	0.1446
		Optimized	0.0648	0.2127	6.4528	0.1294
IMC, 11 knots						
20%	1.2	Constant	0.0711	0.2169	9.3167	0.1571
		Optimized	0.0625	0.2354	9.2697	0.1270
35%	1.35	Constant	0.0728	0.2192	6.8417	0.1698
		Optimized	0.0649	0.1744	6.9266	0.1485

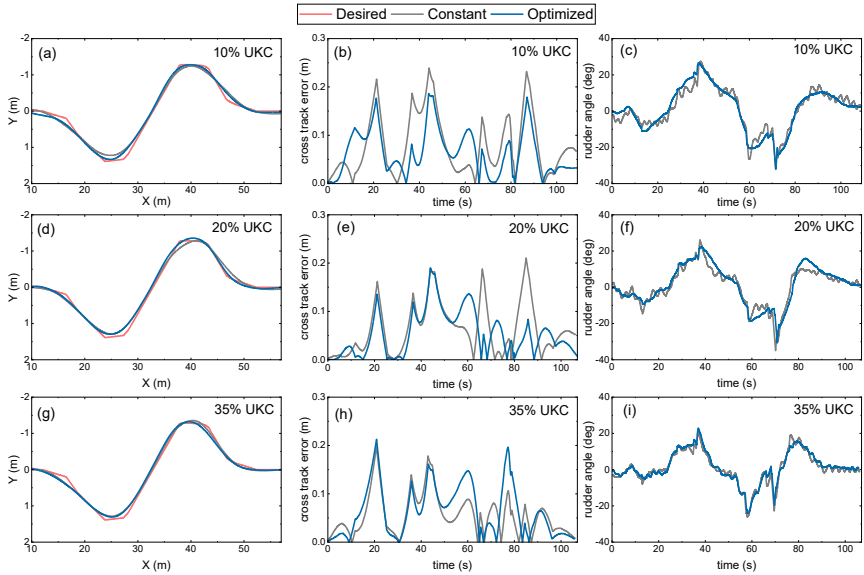


Figure 6.73 IMC controller’s performance using the constant and optimized parameters in different water depths at 8 knots.

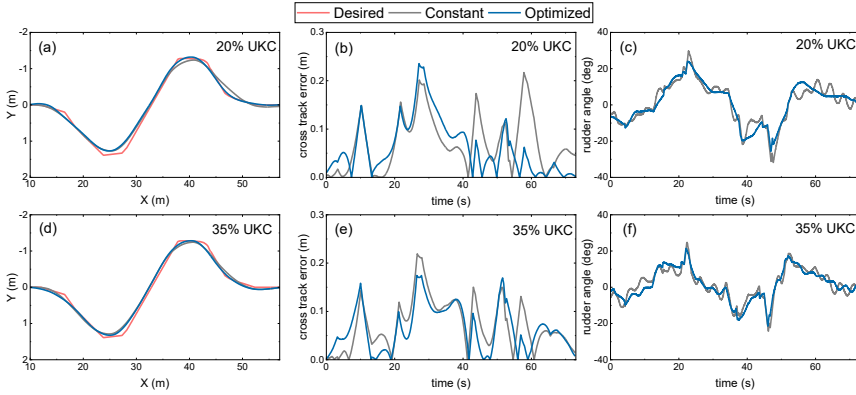


Figure 6.74 IMC controller's performance using the constant and optimized parameters in different water depths at 11 knots.

In order to further improve the adaptability of the controller to different water depths, within the bound of the results in Table 6.18 and Table 6.19, the following relation can be established between deep water (100% UKC) and 20% UKC:

$$K_p = \left[K_{pn,deep} + K_{pn,h} \frac{T_M}{h-T_M} \right] n^0 \quad (6.36)$$

$$K_i = \left[K_{in,deep} + K_{in,h} \frac{T_M}{h-T_M} \right] n^1 \quad (6.37)$$

$$K_d = \left[K_{dn,deep} + K_{dn,h} \frac{T_M}{h-T_M} \right] n^{-1} \quad (6.38)$$

where $K_{pn,deep}$, $K_{pn,h}$ are the adaptive proportional coefficients in deep water and specified water depth; $K_{in,deep}$, $K_{in,h}$ are the adaptive integral coefficients; $K_{dn,deep}$, $K_{dn,h}$ are the adaptive derivative coefficients; T_M is the draft at midship; h is the water depth; n is the propeller rate.

According to the parameters K_{pn} , K_{in} , and K_{dn} at 100% UKC and 20% UKC in Table 6.19, the 6 regression terms in Eq. (6.36)-Eq. (6.38) can be obtained: $K_{pn,deep} = 7.1865$, $K_{pn,h} = -0.6958$, $K_{in,deep} = 0.0759$, $K_{in,h} = -0.0087$, $K_{dn,deep} = 142.9433$, $K_{dn,h} = -19.9533$. Based on the above 6 coefficients, the values of K_{pn} , K_{in} , and K_{dn} in different water depths can be obtained. Table 6.25 compares the experimental parameters and the parameters derived from Eq. (6.36)-Eq. (6.38) (adaptive parameters). Mind that Eq. (6.36)-Eq. (6.38) should be applied up to 20% UKC, and then the parameters remain constant for lower UKCs. One can observe in Table 6.25 that the adaptive parameters are similar to the experimental parameters.

Table 6.25 Comparisons between the experimental parameters and the adaptive parameters.

UKC (%)	$\frac{T_M}{h - T_M}$	Experimental parameters			Adaptive parameters		
		K_{pn}	K_{in}	K_{dn}	K_{pn}	K_{in}	K_{dn}
100	1.0	6.4907	0.0672	122.99	6.4907	0.0672	122.99
35	2.9	4.7529	0.0475	95.445	5.1985	0.0510	85.933
20	5.0	3.7075	0.0324	43.177	3.7075	0.0324	43.177
10	10.0	3.6375	0.0295	25.702	3.7075	0.0324	43.177

To test the developed control algorithm, numerical simulations were conducted using the same ship model in a manoeuvring simulator. Simulations were executed at 6 knots and 35% UKC using the experimental and adaptive parameters, respectively. Table 6.26, Figure 6.75 and Figure 6.76 compare their performance and control effects. It can be seen from Table 6.26 the mean and maximum tracking errors were smaller than 50% B . According to the safety criteria of the ship sailing in the restricted water (PIANC, 2014), the maximum track deviation from the desired trajectory should not be greater than 50% of the own ship’s breadth (B). Thus, both cases meet above requirement. Compared with the simulation results using the experimental parameters, the mean track error increased by 1.1% B for the proposed adaptive algorithm. But the maximum track error was slightly reduced. Although there were slight differences, the overall performance and control effects of the two cases were similar, see Figure 6.75 and Figure 6.76 for better illustration.

Table 6.26 Tracking errors obtained from simulations using experimental and adaptive parameters at 6 knots and 35% UKC.

	Mean track error		Maximum track error	
Experimental parameters	0.0864 m	13.0% B	0.2839 m	42.6% B
Adaptive parameters	0.0940 m	14.1% B	0.2567 m	38.5% B

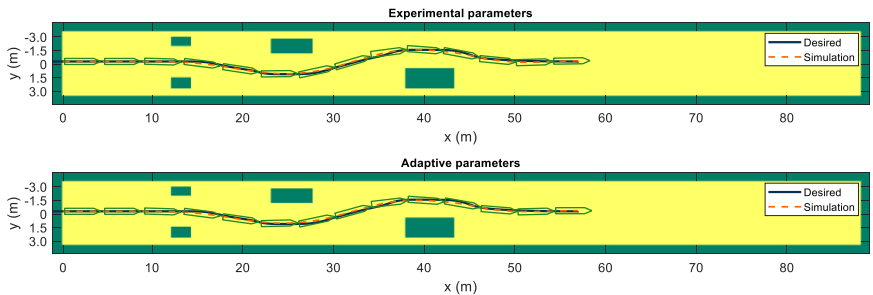


Figure 6.75 Trajectories obtained by simulations using the experimental and adaptive parameters at 6 knots and 35% UKC.

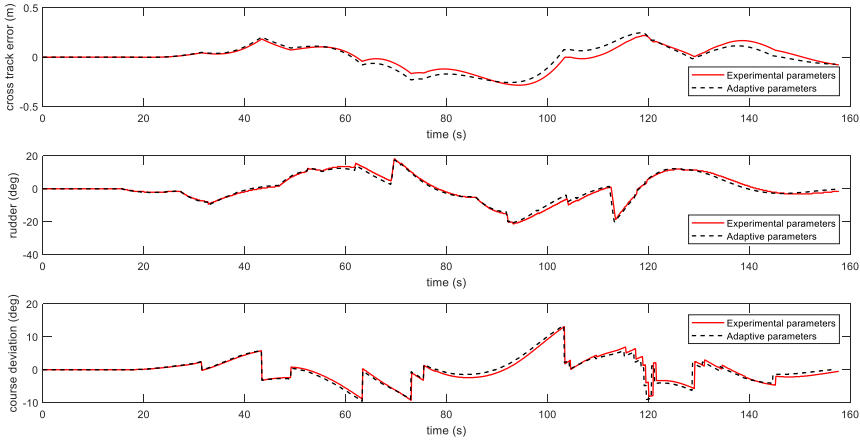


Figure 6.76 Control effects using the experimental and adaptive parameters at 6 knots and 35% UKC.

Finally, to validate the effectiveness of the designed speed and water-depth adaptive algorithm, numerical simulations were executed at 6 knots and 50% UKC, which is a new water depth and was not investigated before. Simulation results are presented in Figure 6.77. The designed controller could control the ship following the desired path and avoid obstacles, and satisfactory performance can be observed in Figure 6.77. The mean and maximum track errors were 0.0842 m (12.6% B) and 0.2377 m (35.7% B) respectively, which still meet the safety criteria ($<50\%$ B). By realizing this, only 6 parameters are needed to control the ship in different water depths and speeds.

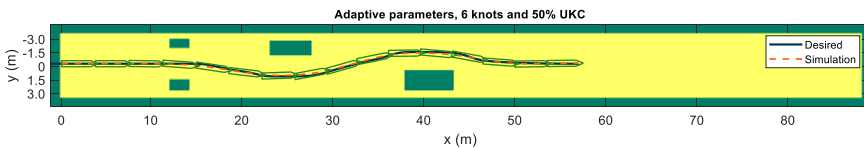


Figure 6.77 Trajectory obtained by simulation using the adaptive parameters at 6 knots and 50% UKC.

6.8 Reference

- Chen, C. Y., Tello Ruiz, M., Delefortrie, G., Mei, T. L., et al.,** 2019a. *Parameter estimation for a ship's roll response model in shallow water using an intelligent machine learning method*. Ocean Engineering, 191, 1–10.
- Chen, C. Y., Tello Ruiz, M., Lataire, E., Delefortrie, G., et al.,** 2019b. *Ship manoeuvring model parameter identification using intelligent machine learning method and the beetle antennae search algorithm*. In *Proceedings of the ASME 2019 38th International Conference on Ocean, Offshore and Arctic Engineering*. Glasgow, Scotland.
- Delefortrie, G., Eloot, K., and Mostaert, F.,** 2020. *Ship manoeuvring behaviour subreport 13: execution of free running tests with the Q-flex (report)*.
- Delefortrie, G., Geerts, S., and Vantorre, M.,** 2016. *The towing tank for manoeuvres in shallow water*. In *Proceedings of 4th MASHCON*. Hamburg, Germany.
- Eloot, K., Delefortrie, G., Vantorre, M., and Quadvlieg, F.,** 2015. *Validation of ship manoeuvring in shallow water through free-running tests*. In *Proceedings of the ASME 2015 34th International Conference on Ocean, Offshore and Arctic Engineering OMAE2015*. Newfoundland, Canada.
- IMO.,** 2002. *Explanatory notes to the standards for ship manoeuvrability*.
- ITTC.,** 2017. *Full scale manoeuvring trials. ITTC – Recommended Procedures and Guidelines*.
- Luo, W. L., Guedes Soares, C., and Zou, Z. J.,** 2016. *Parameter identification of ship maneuvering model based on support vector machines and particle swarm optimization*. Journal of Offshore Mechanics and Arctic Engineering, 138(3), 1–8.
- Milanov, E., Chotukova, V., and Yossifov, K.,** 2010. *FHR LNG vessel free running model maneuvering tests (report)*.
- PIANC.,** 1992. *Capability of ship manoeuvring simulation models for approach channels and fairway in harbours (report)*.
- PIANC.,** 2014. *Harbour approach channels design guidelines (report)*.
- Tello Ruiz, M.,** 2018. *Manoeuvring model of a container vessel in coastal waves*. Ghent University, Belgium (PhD thesis).
- Wang, Z. H., Guedes Soares, C., and Zou, Z. J.,** 2020. *Optimal design of excitation signal for identification of nonlinear ship manoeuvring model*. Ocean Engineering, 196, 106778.

Ship motion control systems

7	<i>Numerical simulation studies</i>	225
7.1	General discussion	225
7.2	Track controller in fast-time simulator	228
7.2.1	Prescience model based track controller.....	228
7.2.2	Proposed track controller.....	229
7.3	Ship model validation	231
7.4	Numerical simulation results	233
7.4.1	Overview.....	233
7.4.2	Folding line path following simulation.....	233
7.4.3	Curved path following and obstacle avoidance simulation.....	235
7.5	Comparison with experimental results	236
7.5.1	Folding line path following.....	236
7.5.2	Curved path and obstacle avoidance.....	238
7.6	Application of the track controller on the Panama Canal	243
7.6.1	Performance of controllers.....	243
7.6.2	Bank effect on controllers' performance.....	246
7.6.3	Influence of speed controller.....	254
7.7	Application of the track controller on the Western Scheldt	258
7.7.1	Overview.....	258
7.7.2	Track Controller Input.....	259
7.7.3	Results and discussions.....	262
7.8	Reference	271

The greatest mathematicians, as Archimedes, Newton, and Gauss, always united theory and applications in equal measure.

--Felix Klein

7

Numerical simulation studies

7.1 General discussion

Systematic investigation of ship motion controllers in shallow and confined water is performed by Flanders Hydraulics Research (FHR) and Ghent University (UGent) through real-time and fast-time manoeuvring simulators. The ship manoeuvring simulation centre at FHR covers three full-mission bridge simulators (real-time simulators): two maritime simulators (SIM 360+ and SIM 225) and one inland simulator (Lara) (www.shallowwater.be). SIM 360+ and SIM 225 allow sailing simulations with various types of ships such as seagoing vessels, coasters and tugboats. Lara is a ship manoeuvring simulator specifically for inland vessels. The real-time simulators can be used for both research and manoeuvre training in different scenarios, typically for designing new navigation areas or for assessing the accessibility of existing navigation areas for larger ships (Figure 7.1).



Figure 7.1 Full-mission bridge simulator (real-time simulator) at Flanders Hydraulics Research (FHR) and its typical application scenarios.

The ship manoeuvring simulator comprises various components, where the ship mathematical model is the calculating core behind ship motions. Most ships in the simulator fleet have in-house developed modular mathematical models of the tabular type. The new developments, updates, improvements and extensions are based upon research carried out in the Towing Tank for Manoeuvres in Confined Water (co-operation Flanders Hydraulics Research and Ghent University) or other test facilities available at FHR (lock access model, flumes, full scale measurements) (Lataire et al., 2018). See Figure 7.2 for better illustration.

The mathematical models and software in the ship manoeuvring simulator can also be applied in fast-time mode (Figure 7.2). During real-time simulator studies, an experienced human like a captain or pilot takes command of the virtual ship, which allows him/her to get acquainted with the future situation, while his/her experience can be incorporated in the study. During fast-time simulation runs, on the other hand, the human element is eliminated and replaced by a control algorithm. This offers a number of advantages: no visuals have to be developed, the simulations do not need to be performed at a full mission bridge simulator, and the computer controller does not have to perform the simulations in real time, so that many runs can be performed in a much shorter time span. Moreover, the involvement of human elements in simulation studies causes an additional spreading of the results, which may make it difficult to find objective tendencies caused by other effects. Therefore, fast-time simulations are quite efficient for performing large series of systematic runs and objectively assess the feasibility of specific manoeuvres. Hence, in present work, the fast time simulator will be used to conduct numerical simulation studies and check the performance of various controllers.



Figure 7.2 Numerical simulation study platforms: real-time simulator and fast-time simulator.

7.2 Track controller in fast-time simulator

7.2.1 Prescience model based track controller

The computer algorithm controlling the virtual vessel during fast-time simulation studies is often referred to as “autopilot”, but in order to avoid confusion with on-board autopilots, the term “track controller” will be used instead. In 1997, Flanders Hydraulics Research (FHR) and Ghent University (UGent) developed the prescience model based track controller (PMTC) (Vantorre et al., 1997). The PMTC is used for track-keeping in confined channels and aims to reproduce the decision making of a real pilot to steer the vessel on a desired trajectory while using the predictive power of math models of hydrodynamic effects.

The principle of the PMTC used in the fast-time simulator is shown in Figure 7.3. Input signals include the ship’s position and orientation (x_0, y_0, Ψ_0) , velocity components (u_0, v_0, r_0) , acceleration components $(\dot{u}_0, \dot{v}_0, \dot{r}_0)$, and the present values of the output signals (rudder angle (δ) and propeller rate (n)). The control algorithm makes its decisions based on a prediction model, which can predict the ship’s position after a lapse of time Δt (Δt equal to ξ/u , ξ is the look ahead distance, u is the longitudinal velocity). At discrete time intervals a discrete number of combinations of δ and n are used to predict the ship’s position after Δt . The effect of each considered control action (rudder and propeller) is evaluated via a cost function (Eq. (7.1)). The optimal control action is selected according to the minimum value of the cost function:

$$C = c_F \eta_F^2 + c_M \eta_M^2 + c_A \eta_A^2 \quad (7.1)$$

where c_F, c_M, c_A are the weight coefficients; η_F, η_M, η_A represent the distances relative to the reference track at ship’s fore perpendicular, amidship and aft perpendicular, respectively. See Figure 7.4 for better illustration.

The control action is defined as a combination of rudder angle δ , taking discrete values $\delta_1, \delta_2, \dots, \delta_k$, between hard port and hard starboard and according to $\Delta\delta = 5$ deg. The rudder angle is updated periodically based on Δt_δ . The propeller rate n is updated every Δt_n taking only 4 discrete values n_1, n_2, n_3, n_4 according to the telegraph positions (dead slow, slow ahead, half ahead, harbour full).

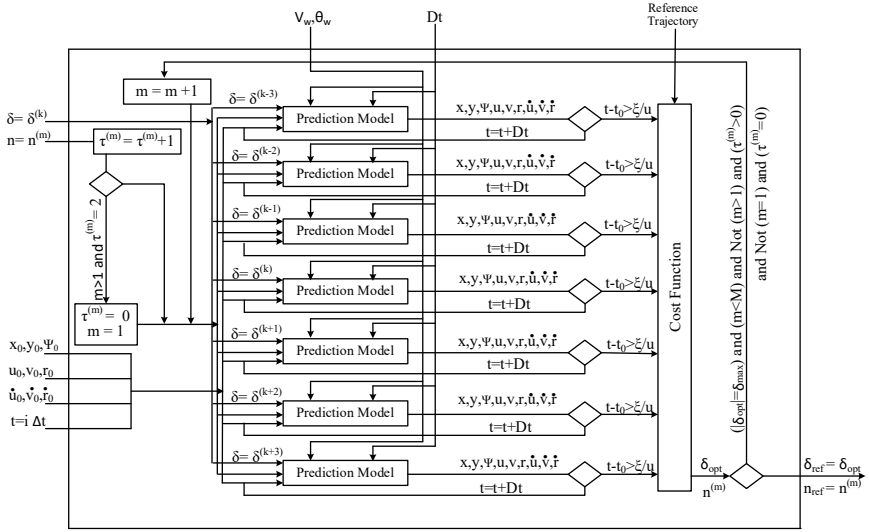


Figure 7.3 Principle of prescience model based track controller in the fast-time simulator (Vantorre et al., 1997).

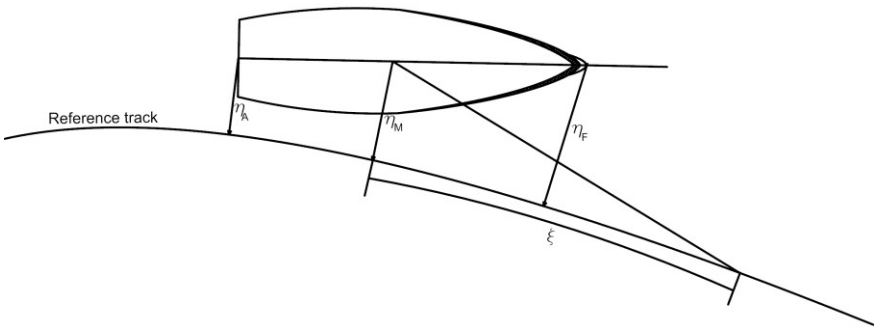


Figure 7.4 Cost function of mathematical pilot model (Vantorre et al., 1997).

7.2.2 Proposed track controller

Even though the PMTC is quite advanced, a number of shortcomings have been detected during recent applications. For instance, the control settings often have to be adapted to the specific environmental conditions, bathymetries and planned interactions with other shipping traffic, etc. In order to simplify the setting and improve the performance of controller, a new ship motion control system was proposed (Figure 7.5). It mainly consists of: (1) Guidance subsystem, (2) Control subsystem, (3) Navigation subsystem. These subsystems interact with each other through data and signal transmission. Moreover, a path planning module is adopted to generate the reference waypoints for use by the guidance system. To simulate the real scenarios, the environmental disturbances including wave, wind and bank effects, among others are considered. On top of that, the controllers

including the PID, the adaptive PID, the fuzzy, the IMC, and the speed controllers (presented in Chapter 5) have also been made available in the simulators.

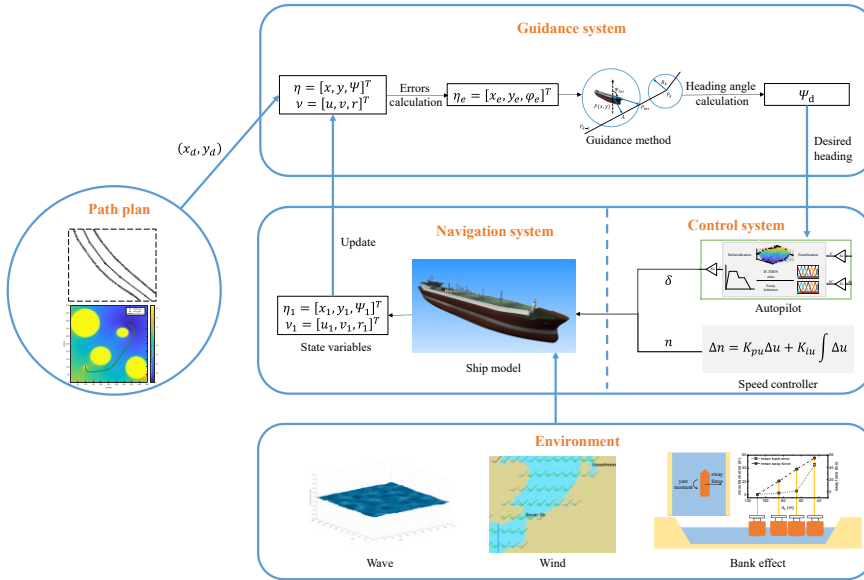


Figure 7.5 Signal flow of the proposed motion control system.

7.3 Ship model validation

In the simulator, the 6 DOF manoeuvring model described in section 3.2.3 has been implemented to provide an accurate description of ship motions in all degrees of freedom. Meanwhile, the LNG manoeuvring model used in the towing tank has been built in the simulator, which is visualized in 3D view in Figure 7.6.

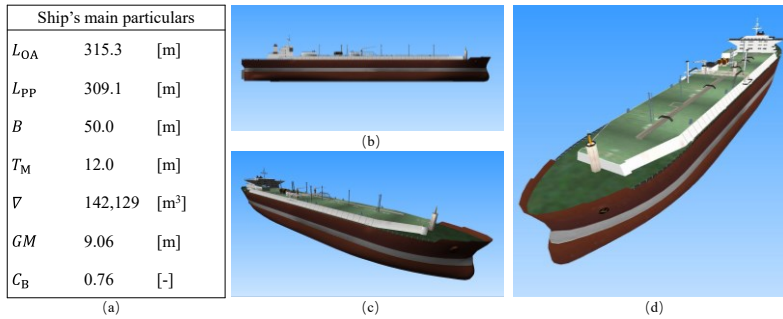


Figure 7.6 3D view of the LNG ship: (a) ship’s particulars; (b) side view; (c) bow view; (d) top view.

To verify the accuracy of the 6 DOF mathematical model, a comparison was conducted between the numerical and the experimental zigzag manoeuvres at the largest speed of each UKC (see Table 6.6 for a value of these). For illustration purposes, Figure 7.7 shows an example for the comparison between the simulated and experimental 20°/5° zigzag manoeuvre at 11 knots and 20% UKC. As is shown in Figure 7.7, the period (defined as the time between the 2nd and 4th zero crossings of the course angle) of the simulated zigzag is around 190 s is very close to the experimental period (189 s). Moreover, the first and the second overshoot angles obtained by the numerical simulation are similar to those of the experimental result. More comparisons for other water depths are shown in Table 7.1 and Figure 7.8. According to the zigzag results, the steering performance of the 6 DOF model matched well with the actual ship (except for 35% UKC). Hence the accuracy of 6 DOF model is proved and satisfactory for further simulations.

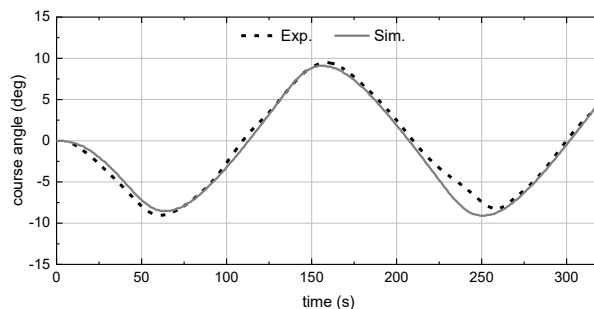


Figure 7.7 Comparison of the simulated (Sim.) and experimental (Exp.) 20°/5° zigzag manoeuvre at 11 knots and 20%UKC.

Table 7.1 Statistics of the simulated and experimental 20°/5° zigzag in medium and shallow water.

UKC (%)	h/T_M (-)	prototype period(s)		first overshoot(deg)		second overshoot(deg)	
		Exp.	Sim.	Exp.	Sim.	Exp.	Sim.
100	2.0	222	205	10.7	10.5	14.7	14.0
35	1.35	197	171	6.2	4.3	9.7	5.5
20	1.2	190	189	4.0	3.5	4.5	4.1
10	1.1	242	230	2.8	2.8	3.0	2.6

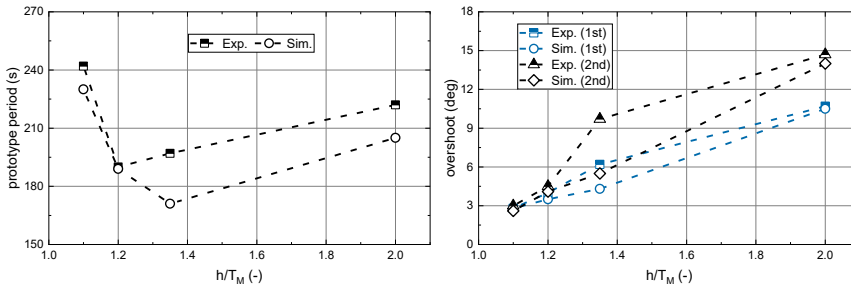


Figure 7.8 Statistics of the simulated and experimental 20°/5° zigzag in medium and shallow water.

7.4 Numerical simulation results

7.4.1 Overview

To evaluate whether the controllers studied in the towing tank exhibit satisfactory performance in simulation settings and whether their application in simulation of complex situations can be improved, the designed controllers are evaluated by the numerical simulations in the fast time simulator. The control effects for path following are analysed in the case of folding and curved paths. For illustration purposes, the results at 8 knots and 20% UKC are presented as examples in this section. Please bear in mind that the simulation studies were carried out in prototype without ITTC correction and then Froude scaled. Moreover, due to the poor performance of the PID controller during model tests, this controller will not be evaluated in simulation runs. Only the performance of adaptive PID, fuzzy, and IMC controllers will be presented in the simulation studies.

7.4.2 Folding line path following simulation

The first case study is the folding line path following simulation, and the reference path consists of 7 waypoints: WP₁(0,0) m, WP₂(10,0) m, WP₃(25,1.2) m, WP₄(35,1.2) m, WP₅(45,0) m, WP₆(55,0) m, WP₇(58,0) m. The control parameters are set as: $K_{pn}=3.71$, $K_{in}=0.03$, $K_{dn}=43.18$, $K_p=3.73$, $K_i=0.03 \text{ s}^{-1}$, $K_d=48.65 \text{ s}$, $K_e=0.33 \text{ deg}^{-1}$, $K_c=0.75 \text{ deg}^{-1}$, $K_u=11.66 \text{ deg}$. Simulation results including trajectories and motion responses of the ship are shown in Figure 7.9 and Figure 7.10.

Figure 7.9 exhibits the reference and the simulated trajectories by the adaptive PID, fuzzy and IMC controllers. It can be seen in Figure 7.9 that all three controllers were able to keep the ship on the reference path with moderate rudder angles (Figure 7.10(b)). The simulated trajectories matched well with the reference one. Figure 7.10(a) shows the cross track errors of three controllers, the maximum trajectory error was 0.16 m (~24% breadth), while the heading deviation kept within $\pm 6 \text{ deg}$ (Figure 7.10(c)). These small errors of three controllers indicate their good tracking capability.

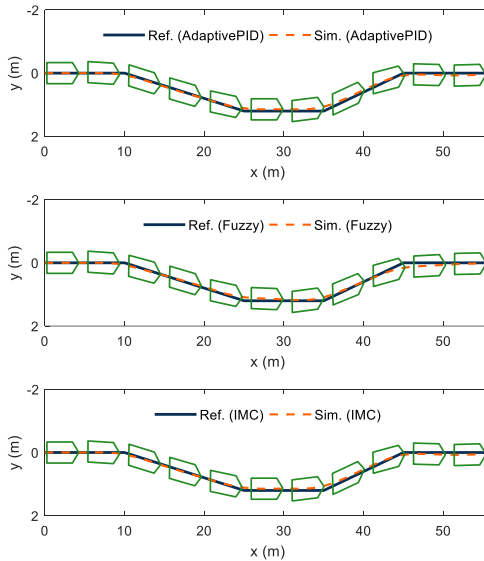


Figure 7.9 Reference and simulated trajectories by the adaptive PID, fuzzy and IMC controllers at 8 knots and 20% UKC.

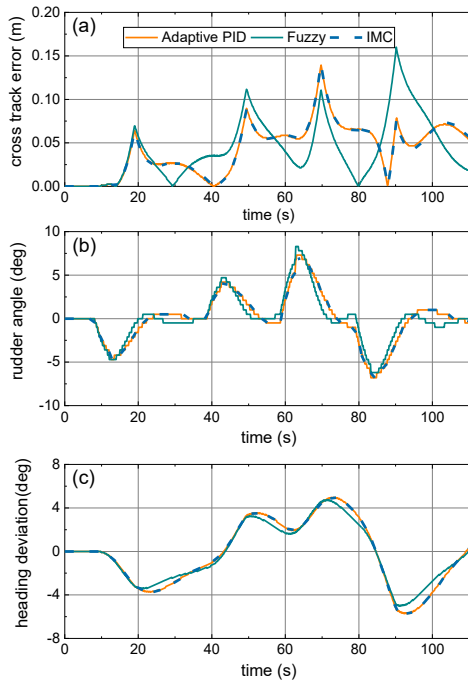


Figure 7.10 Motion responses of ship: (a) cross track error; (b) rudder angle; (c) heading deviation at 8 knots and 20% UKC.

7.4.3 Curved path following and obstacle avoidance simulation

Controllers were also evaluated by controlling the ship following a curved path with four virtual obstacles (Figure 7.11). The reference path is defined in section 6.6.4. All settings except for the reference trajectory are the same as the folding line path following in section 7.4.2.

Figure 7.11 and Figure 7.12 show the simulation results for the curved path. The ship converged well to the desired path and succeeded to avoid the obstacles (Figure 7.11). The track errors of three controllers fluctuated within 0.3 m (~45% breadth, Figure 7.12(a)), note that most deviations appeared near curved bends.

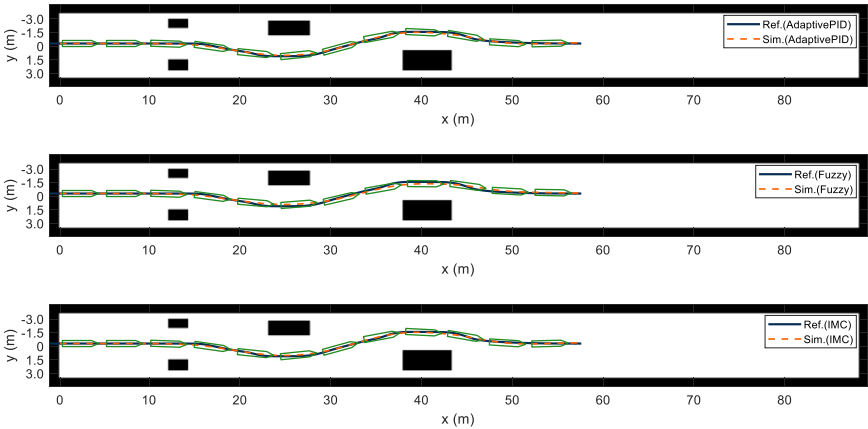


Figure 7.11 Reference and simulated trajectories by the adaptive PID, fuzzy and IMC controllers at 8 knots and 20% UKC.

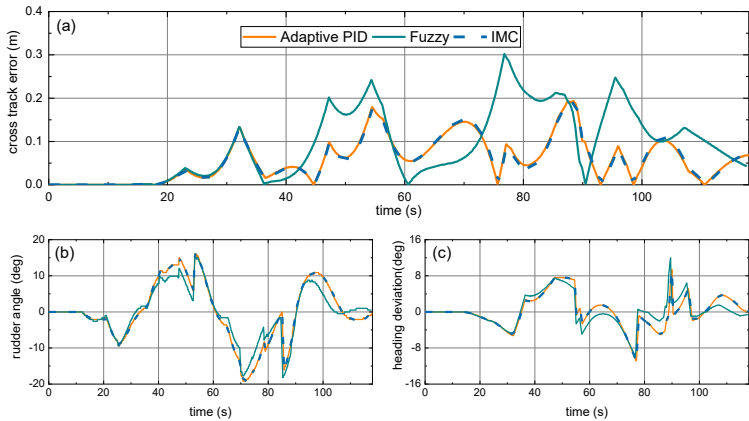


Figure 7.12 Motion responses of ship at 8 knots and 20% UKC: (a) cross track error; (b) rudder angle; (c) heading deviation.

7.5 Comparison with experimental results

7.5.1 Folding line path following

To validate the controller performance, the simulation results were compared with the experiments carried out in the towing tank with exactly the same settings. Figure 7.13 to Figure 7.15 compare the simulation (Sim.) and experimental (Exp.) results of the adaptive PID, fuzzy, and IMC controllers for folding line path following.

Figure 7.13 presents the numerical and experimental performance of the adaptive PID controller. Figure 7.13(a) shows that the trajectory obtained from the numerical simulation agreed well with that from the experiment. In both scenarios, the cross track errors fluctuated within 0.14 m (~21% breadth). In terms of rudder deflection (Figure 7.13(c)) and heading angle (Figure 7.13(d)), the numerical and experimental results display similar trends and amplitudes with slight difference. Similar results for the fuzzy and IMC controllers are displayed in Figure 7.14 and Figure 7.15.

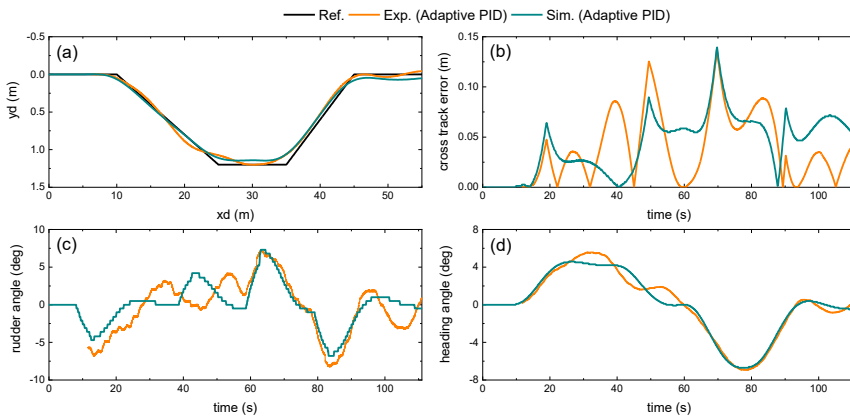


Figure 7.13 Comparison of numerical and experimental performance of adaptive PID controller for fold line path: (a) trajectories; (b) cross track error; (c) rudder angle; (d) heading angle.

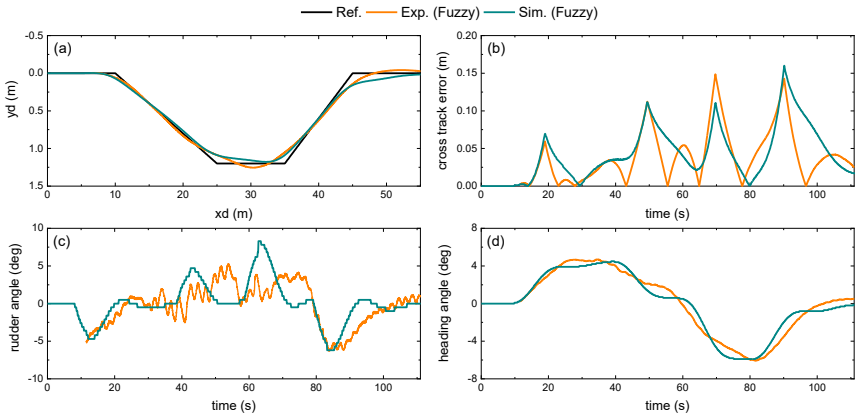


Figure 7.14 Comparison of numerical and experimental performance of fuzzy controller for fold line path: (a) trajectories; (b) cross track error; (c) rudder angle; (d) heading angle.

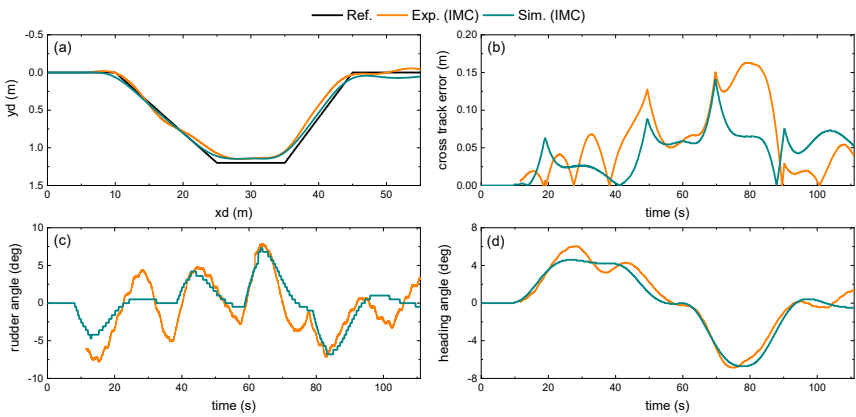


Figure 7.15 Comparison of numerical and experimental performance of IMC controller for fold line path: (a) trajectories; (b) cross track error; (c) rudder angle; (d) heading angle.

To better illustrate the difference between the simulation and experimental results, the evaluation mechanism of controller performance in section 5.10 is adopted. The statistics of evaluation indexes are summarized in Table 7.2 and Figure 7.16, where R.E. is the relative error of numerical results compared with the corresponding experimental results. In general, the numerical results showed good agreement with experimental results, especially for the mean (mTEI) and maximum (MTE) trajectory errors, and heading deviation (mHEI). In terms of the above three evaluation indexes of the adaptive PID, fuzzy and IMC controllers, there were less than 8.81% difference between numerical and experimental results except for the track error of IMC controller (mTEI, MTE). However, discrepancies were observed in the rudder behaviour of three controllers. Compared with

experimental results, the simulation runs used smaller and smoother rudders (mRI, mRTV). This phenomenon might be attributed to environmental disturbance, sensor error, and measurement noise, etc., during experiments. Another probable reason is that the maximum steering torque was set in the fast time simulator. In spite of some disagreement for rudder behaviour, however, these slight discrepancies are acceptable, and the numerical simulations can represent experimental results.

Table 7.2 Statistics of numerical and experimental results for folding line path.

Properties	Adaptive PID		Fuzzy		IMC	
	Exp.	Sim.	Exp.	Sim.	Exp.	Sim.
mTEI (m)	0.0412	0.0433	0.0397	0.0427	0.0613	0.0432
R.E.	--	5.08%	--	7.61%	--	-29.58%
MTE (m)	0.1355	0.1394	0.1486	0.1600	0.1630	0.1407
R.E.	--	2.86%	--	7.67%	--	-13.68%
mHEI (deg)	2.6868	2.4843	2.3170	2.2120	2.7344	2.4935
R.E.	--	-7.54%	--	-4.53%	--	-8.81%
mRI (deg)	2.9261	1.8691	2.1116	1.6336	3.1227	1.8698
R.E.	--	-36.12%	--	-22.64%	--	-40.12%
mRTV (deg)	0.1313	0.0523	0.1617	0.0568	0.1455	0.0523
R.E.	--	-60.14%	--	-64.84%	--	-64.04%

Note: Relative Error (R.E.) = (|Simulation-Experiment| ÷ Experiment)×100%

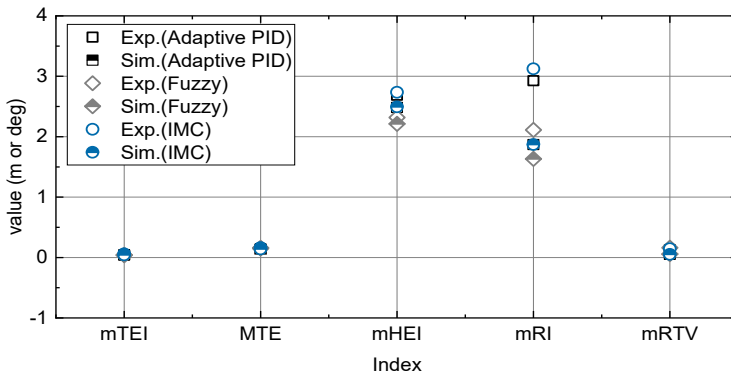


Figure 7.16 Statistics of numerical and experimental results for folding line path.

7.5.2 Curved path and obstacle avoidance

Comparisons were also conducted for the curved path. Figure 7.17 compares the numerical and experimental performance of the adaptive PID controller. The simulated trajectory showed satisfactory agreement with the experimental

trajectory despite small discrepancies near bends (Figure 7.17(a)). The maximum track deviation of experiment was slightly larger than that of simulation (Figure 7.17(b)). Moreover, compared with the experimental results, the ship adopted smaller rudders in the simulation runs (Figure 7.17(c)). Similar results for the fuzzy and IMC controllers are shown in Figure 7.18 and Figure 7.19.

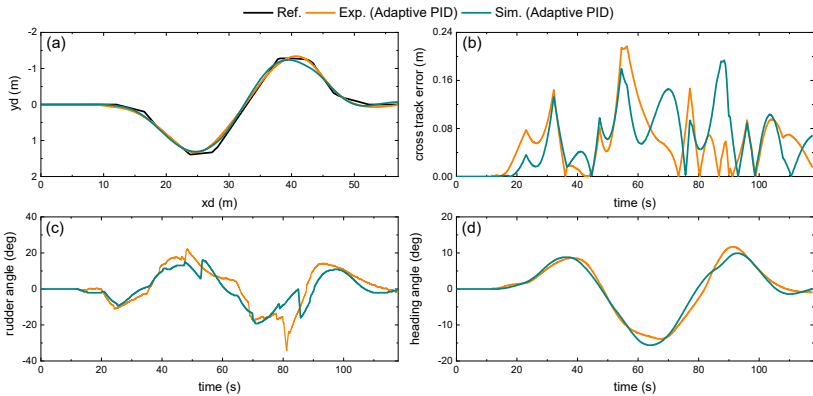


Figure 7.17 Comparison of numerical and experimental performance of adaptive PID controller for curved path: (a) trajectories; (b) cross track error; (c) rudder deflection; (d) heading angle.

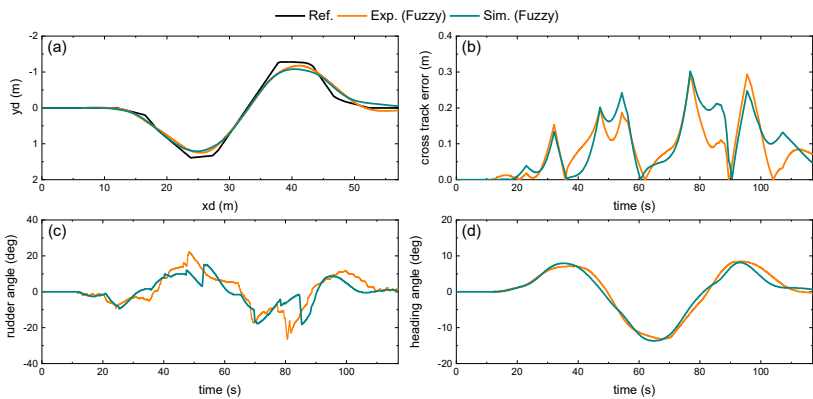


Figure 7.18 Comparison of numerical and experimental performance of fuzzy controller for curved path: (a) trajectories; (b) cross track error; (c) rudder deflection; (d) heading angle.

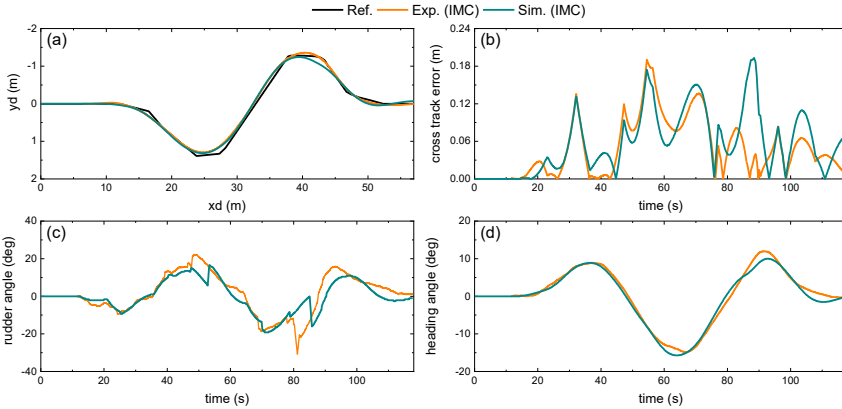


Figure 7.19 Comparison of numerical and experimental performance of IMC controller for curved path: (a) trajectories; (b) cross track error; (c) rudder deflection; (d) heading angle.

Table 7.3 and Figure 7.20 present the statistics of numerical and experimental results for the curved path. Generally, the numerical results matched well with the experimental results from the aspect of the mean (mTEI) and maximum (MTE) trajectory errors, and heading deviation (mHEI), with less than 10.90% difference. Similar to the folding line study, there were discrepancies for rudder deflection (mRI, mRTV) between the simulation and the experiment.

Table 7.3 Statistics of numerical and experimental results for curved path.

Properties	Adaptive PID		Fuzzy		IMC	
	Exp.	Sim.	Exp.	Sim.	Exp.	Sim.
mTEI (m)	0.0592	0.0581	0.0918	0.0909	0.0536	0.0578
R.E.	--	-1.87%	--	-0.99%	--	7.91%
MTE (m)	0.2173	0.1936	0.2938	0.3019	0.1901	0.1933
R.E.	--	-10.90%	--	2.76%	--	1.71%
mHEI (deg)	2.5373	2.5479	2.5604	2.3359	2.4667	2.5568
R.E.	--	0.42%	--	-8.77%	--	3.65%
mRI (deg)	9.0284	6.2074	7.4370	5.0366	9.1404	6.2612
R.E.	--	-31.25%	--	-32.28%	--	-31.50%
mRTV (deg)	0.2221	0.1708	0.2280	0.1722	0.2189	0.1728
R.E.	--	-23.07%	--	-24.47%	--	-21.06%

Note: Relative Error (R.E.) = (|Simulation-Experiment| ÷ Experiment) × 100%

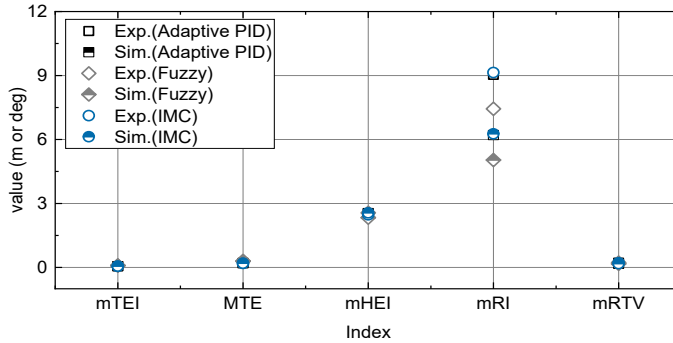


Figure 7.20 Statistics of numerical and experimental simulation results for curved path.

To further illustrate the performance of three controllers in different water depths, Table 7.4 shows the statistics of numerical and experimental results for the curved path at 8 knots and UKCs from 10% to 100%. For illustration purposes, the performance of the adaptive PID controller at different UKCs are plotted in Figure 7.21 and Figure 7.22. The same conclusions can be drawn for different UKCs as previous discussions, in which the numerical results showed satisfactory agreement with the experimental results despite acceptable discrepancies were observed.

Through the numerical simulations and the experimental validation, the results imply that three controllers are capable to follow the desired paths and avoid obstacles. Satisfactory control effects indicate they can be used in the fast time simulator with high tracking capacity.

Table 7.4 Statistics of numerical and experimental results for curved path at different UKCs.

UKC (%)	h/T_M (-)	Adaptive PID									
		mTEI (m)		MTE (m)		mHEI (deg)		mRI (deg)		mRTV (deg)	
		Exp.	Sim.	Exp.	Sim.	Exp.	Sim.	Exp.	Sim.	Exp.	Sim.
100	2.0	0.044	0.048	0.160	0.176	3.280	2.851	7.205	4.362	0.333	0.229
35	1.35	0.063	0.060	0.168	0.211	2.889	2.967	7.388	6.219	0.269	0.193
20	1.2	0.059	0.058	0.217	0.194	2.537	2.548	9.028	6.207	0.222	0.171
10	1.1	0.078	0.068	0.234	0.213	2.685	2.618	9.233	9.527	0.213	0.218
Fuzzy											
100	2.0	0.110	0.101	0.268	0.350	3.501	3.456	8.716	4.867	0.224	0.178
35	1.35	0.060	0.078	0.208	0.248	2.488	2.601	6.676	5.060	0.232	0.179
20	1.2	0.092	0.091	0.294	0.302	2.560	2.336	7.437	5.037	0.228	0.172
10	1.1	0.097	0.081	0.294	0.270	2.564	2.179	8.475	6.893	0.226	0.191

IMC											
100	2.0	0.051	0.045	0.216	0.169	3.265	2.884	7.497	4.351	0.327	0.219
35	1.35	0.065	0.061	0.213	0.206	2.868	2.957	6.452	6.169	0.262	0.198
20	1.2	0.054	0.058	0.190	0.193	2.467	2.557	9.140	6.261	0.219	0.173
10	1.1	0.064	0.070	0.186	0.223	2.369	2.614	10.082	9.918	0.227	0.220

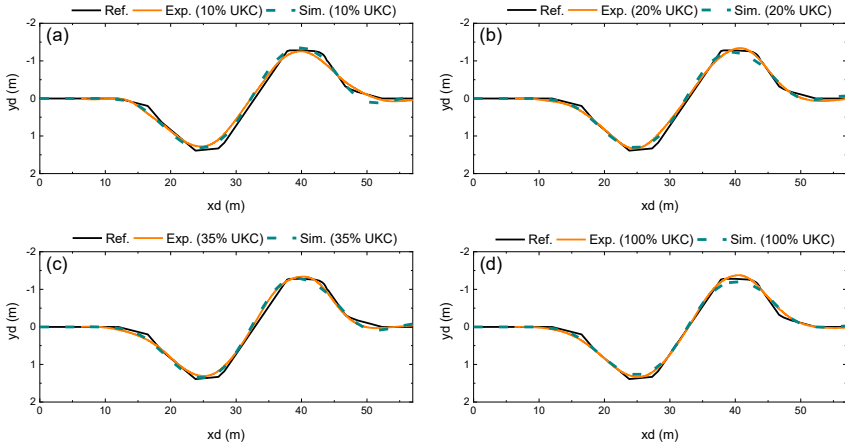


Figure 7.21 Comparison of numerical and experimental performance of the adaptive PID controller for curved path at different UKCs: (a) 10% UKC; (b) 20% UKC; (c) 35% UKC; (d) 100% UKC.

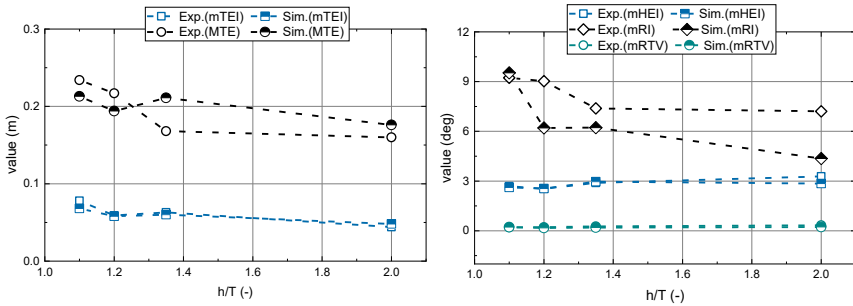


Figure 7.22 Statistics of numerical and experimental results of the adaptive PID controller for curved path at different UKCs.

7.6 Application of the track controller on the Panama Canal

7.6.1 Performance of controllers

To study the applicability of controllers in real scenarios, the controllers were evaluated in the simulation of the ship sailing in the Panama Canal. Figure 7.23 and Figure 7.24 show the information of Panama Canal between the Gatún Lake and the Pacific Locks. The main part of the Canal has a width of 218 m at full depth, which is increased in the bends on the reaches between Chagres River Crossing and the bifurcation. This 17 km (9 nm) long section has on both sides bank slopes of 1:1 (45°) to 3:2 (56°). A Canal environment has been modelled where the cross sections are simplified to a symmetric trapezium with slopes of 3:2 (56°) and a constant water depth of 14.4 m, as shown in Figure 7.25. The simulation runs were conducted at 8 knots and 20% UKC, and the desired trajectory was defined by the waypoint coordinates mentioned in Table 7.5.

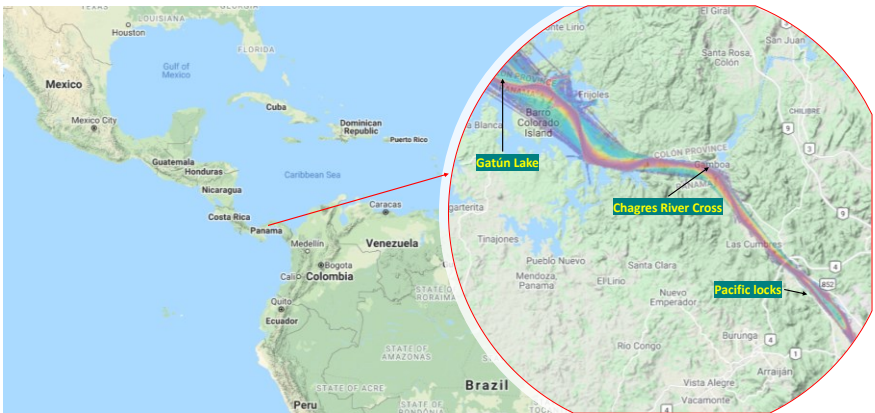


Figure 7.23 Location of the Panama Canal (©Google Maps).

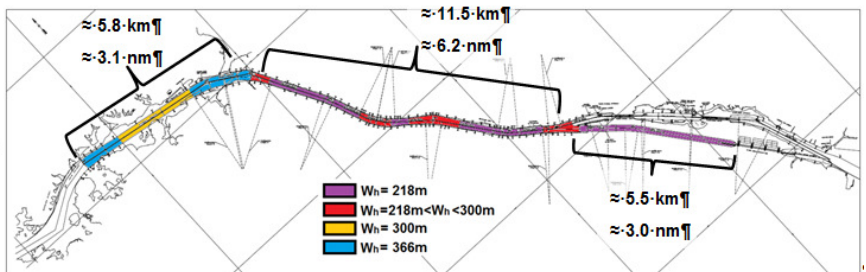


Figure 7.24 Panama Canal from Gatún Lake (left) to the Pacific locks.

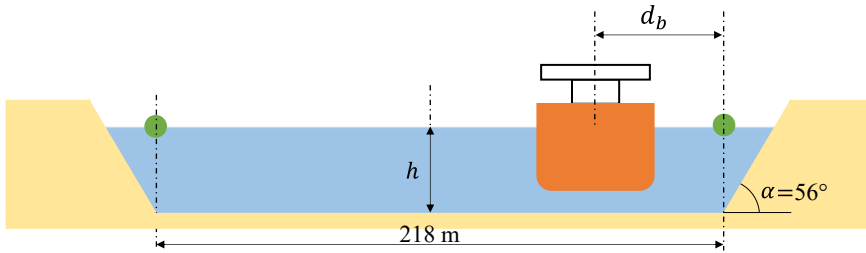


Figure 7.25 Simplified cross section with slopes of 56° on both sides and a width on full depth of 218 m, and a ship with $B \times T_M$ of $50 \times 12.0 \text{ m}^2$.

Table 7.5 List of waypoints of the planned trajectory.

Waypoints (m)		
WP ₁ (20507,6354)	WP ₂ (18743,4092)	WP ₃ (18266,3560)
WP ₄ (16850,2297)	WP ₅ (16396,1874)	WP ₆ (15282,1015)
WP ₇ (15111,864)	WP ₈ (14899,616)	WP ₉ (13678,-986)
WP ₁₀ (13191,-1470)	WP ₁₁ (12410,-2065)	WP ₁₂ (12199,-2262)
WP ₁₃ (11960,-2579)	WP ₁₄ (11752,-2999)	WP ₁₅ (11326,-4085)
WP ₁₆ (10097,-6289)	WP ₁₇ (9893,-6593)	WP ₁₈ (9647,-6812)
WP ₁₉ (9531,-6902)	WP ₂₀ (9451,-6959)	WP ₂₁ (9390,-7000)
WP ₂₂ (9259,-7075)	WP ₂₃ (9122,-7149)	WP ₂₄ (8980,-7222)
WP ₂₅ (8656,-7378)	WP ₂₆ (8399,-7483)	WP ₂₇ (7963,-7606)
WP ₂₈ (7571,-7683)	WP ₂₉ (4019,-8232)	WP ₃₀ (3720,-8251)
WP ₃₁ (3107,-8233)	WP ₃₂ (2600,-8105)	WP ₃₃ (2210,-7921)
WP ₃₄ (1886,-7753)	WP ₃₅ (1575,-7597)	WP ₃₆ (1280,-7502)
WP ₃₇ (1051,-7476)	WP ₃₈ (899,-7470)	WP ₃₉ (654,-7470)
WP ₄₀ (340,-7496)	WP ₄₁ (-22,-7538)	

Figure 7.26 and Figure 7.28 exhibit the tracking capability of the controllers in the canal, see the enlarged image in Figure 7.27 for better understanding. One can observe in Figure 7.26 that three controllers could control the ship following the desired path in the canal. Furthermore, the maximum cross track error of the adaptive PID, fuzzy and IMC controllers were around 15.1 m (30% breadth), 12.2 m (24% breadth), and 15.2 m (30% breadth), respectively (Figure 7.28(a)). According to the safety criteria of ship sailing in the canal (PIANC, 1992), the maximum track deviation from the desired trajectory should not be greater than 50% of the own ship's breadth. Therefore, the fast time simulation runs met the corresponding criteria and achieved satisfactory control effects.

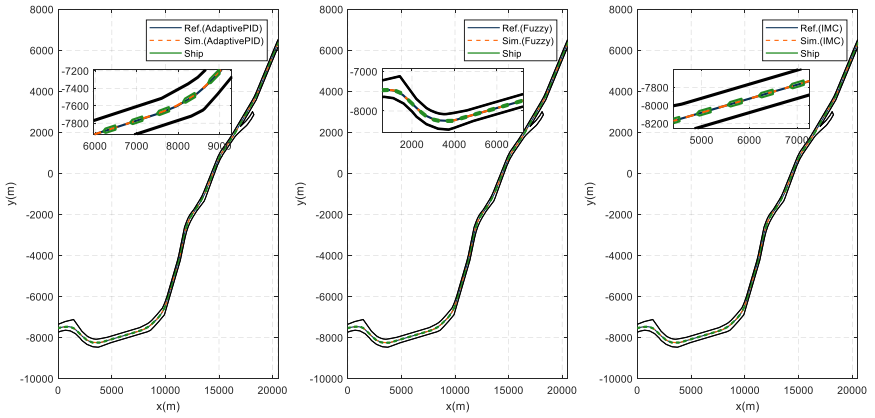


Figure 7.26 Tracking capability of adaptive PID, fuzzy and IMC controllers for simulation in the Panama Canal.

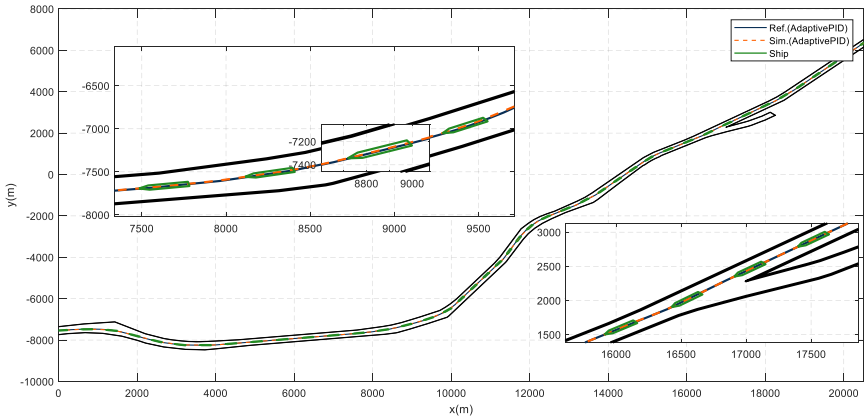


Figure 7.27 Tracking capability of adaptive PID controller for simulation in the Panama Canal.

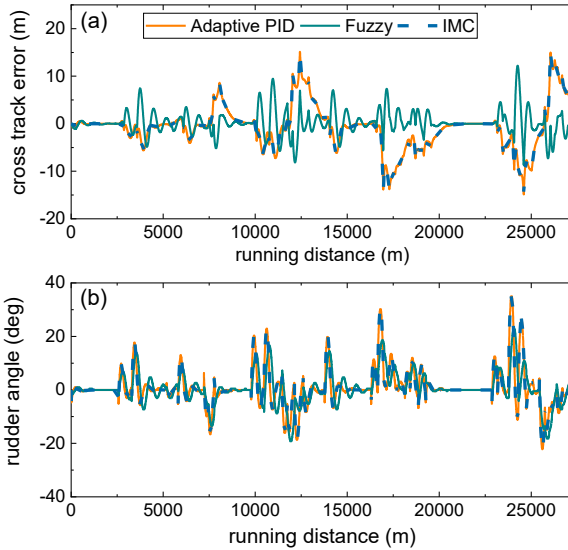


Figure 7.28 Motion response of the adaptive PID, fuzzy and IMC controllers in a real canal: (a) cross track error; (b) rudder angle.

7.6.2 Bank effect on controllers' performance

The asymmetric flow around a ship induced by the vicinity of banks causes pressure differences between port and starboard sides. As a result, a lateral force will act on the ship, mostly directed towards the closest bank, as well as a yawing moment pushing her bow towards the centre of the waterway. This phenomenon, known as the bank effect, depends on many parameters, such as bank shape, ship-bank distance, water depth, ship speed and propeller action, etc. A reliable estimation of bank effects is important for determining the limiting conditions in which a ship can safely navigate a waterway. To investigate the bank effects on controllers' performance on the Panama Canal, four case studies have been selected, where the ship was set at a different distance to the bank (d_b) and the corresponding positions of the ship are shown in Figure 7.29.

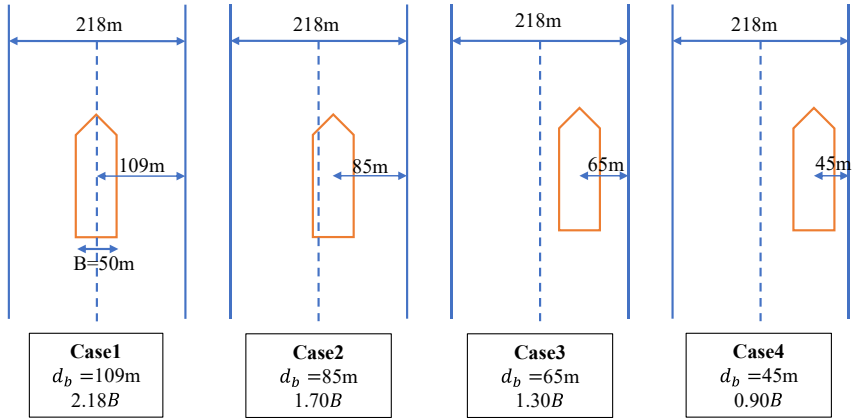
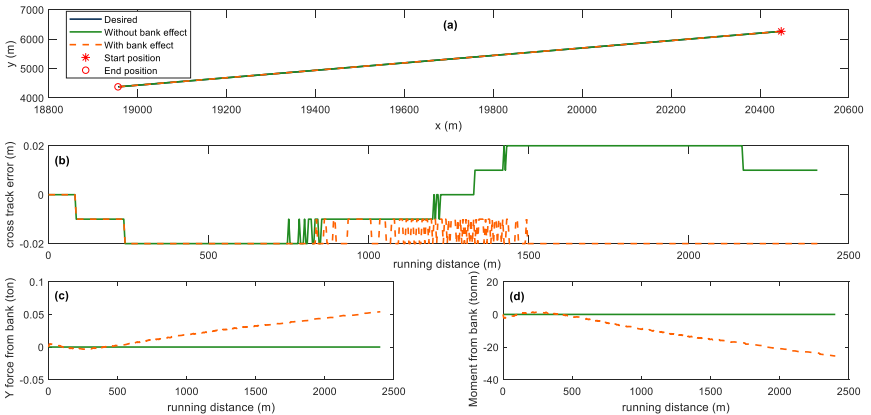


Figure 7.29 Positions of ship at different distances to bank (or buoy line).

To demonstrate the bank effects, for each aforementioned case study the simulations were carried out in two scenarios: with bank effects and without bank effects. For illustration purposes, the results of the adaptive PID controller at 8 knots and 20% UKC are presented as case studies (case 1, 3, 4 are considered as examples, and all results (case 1-4) are summarized in Table 7.6).

When the ship was located in the middle of the canal (case 1), the performance of the adaptive PID controller is shown in Figure 7.30. It can be seen that there was little difference for the trajectories obtained from simulations with and without bank effects, and their average track errors between the desired path and simulated ones were 0.02 m and 0.01 m, respectively. Figure 7.30(e) plots the trajectories obtained by the adaptive PID controller with and without considering bank effects. The trajectories overlapped together and there was no visible difference. This might be because the ship sailed in the middle of the channel, thus the bank effects from each side compensated each other, and the bank effects were not obvious.



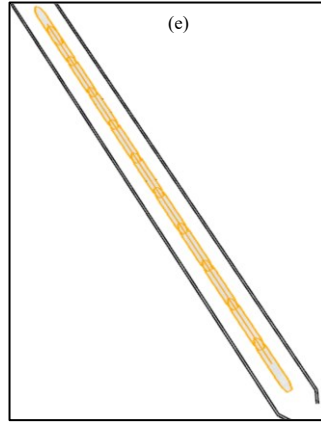
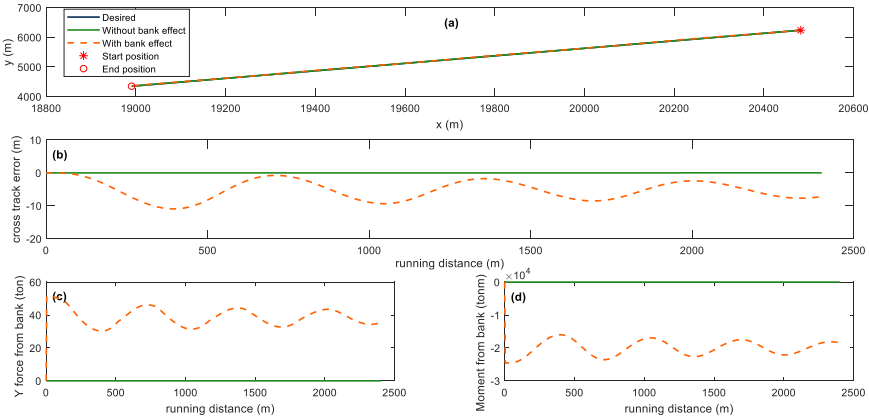


Figure 7.30 Performance of the adaptive PID controller with and without considering bank effects when the ship sailed in the middle of canal (case 1): (a) trajectories; (b) cross track error; (c) Y force from bank; (d) yaw moment from bank; (e) trajectories in the canal (overlap in this case).

Case 3 was selected to show the performance of track controller when the ship was located at 65 m to the bank. Slight difference between the simulated trajectories with and without bank effects could be seen from Figure 7.31. When the bank effects were considered, the maximum and mean track errors were 10.95 m and 5.29 m, which were obviously larger than the sense without considering bank effects (Table 7.6). This could be attributed to the forces on the ship due to bank effects to instantaneously change from zero to quite large values, causing the vessel to deviate (Figure 7.31). But the deviations were in a reasonable range, and the results were acceptable.



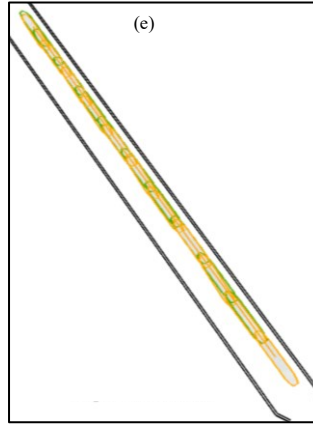
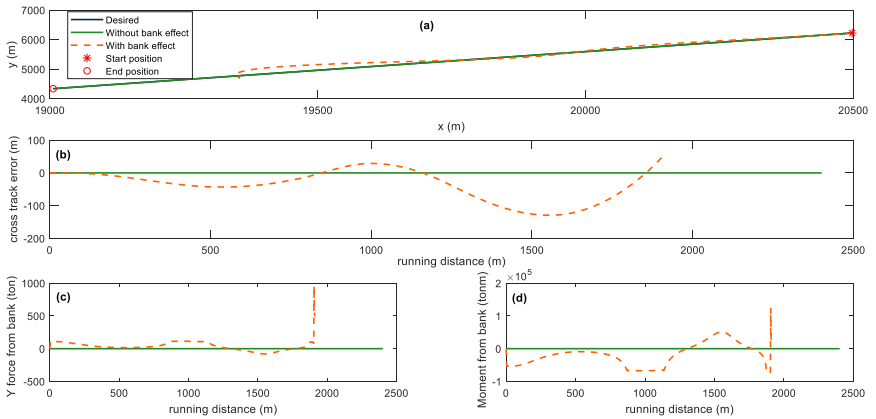


Figure 7.31 Performance of the adaptive PID controller with and without considering bank effects when the ship sailed case 3 position in the canal: (a) trajectories; (b) cross track error; (c) Y force from bank; (d) yaw moment from bank; (e) trajectories in the canal.

The forces and moment on the ship due to bank effects do not always lead to the expected results, as shown in Figure 7.32. When the distance between the ship and the bank was too small (case 4), the bank effects became very obvious. Because the size of the ship was large ($L_{pp} \times B$, 309 m \times 50 m), there was not enough manoeuvring space for the ship to get back on track. In such scenarios, these forces and moments caused by bank effects were too large, which resulted in a too large deviation of the ship and crashing into the bank.



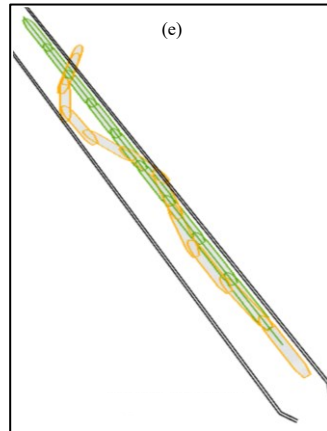


Figure 7.32 Performance of the adaptive PID controller with and without considering bank effects when the ship sailed in the middle of canal (case 4): (a) trajectories; (b) cross track error; (c) Y force from bank; (d) yaw moment from bank; (e) trajectories in the canal.

Table 7.6 and Figure 7.33 present the influence of bank effects on the cross track error, sway force, and yaw moment. One can observe that there was almost no influence due to bank elements at a distance far away from the vessel (case 1). The adaptive PID controller could give acceptable results when a reasonable ship-bank distance was considered (Case 2 and Case 3). However, when this ship-bank distance was too small, it was difficult to control the ship due to bank effects (case 4). One also can find that the tracking error, sway force and yaw moment show increasing trends with smaller ship-bank distance (d_b). As the thesis will become too large if all analyses are shown and similar results can be found for the fuzzy and IMC controllers. Thus, the results of fuzzy and IMC controller are not presented in this research.

Table 7.6 Comparisons of the adaptive PID controller’s performance at 8 knots and 20% UKC with and without considering bank effects.

Cases	Bank effect	MTE (m)	mTEI (m)	MY _B (ton)	mY _B (ton)	MYM _B (tonm)	mYM _B (tonm)	Bank Influence
Case1	With	0.02	0.02	0.05	0.02	25.46	11.39	Negligible
	Without	0.02	0.01	0	0	0	0	
Case2	With	3.64	2.20	23.25	20.55	1.10e+04	9.86e+03	Acceptable
	Without	0.02	0.01	0	0	0	0	
Case3	With	10.95	5.29	51.67	38.67	2.46e+04	2.00e+04	Acceptable
	Without	0.02	0.01	0	0	0	0	
Case4	With	129.25	45.21	958.90	55.54	1.24e+05	3.11e+04	Obvious
	Without	0.02	0.01	0	0	0	0	

Note: MTE: Maximum Track Error; mTEI: mean Track Error Integral; MY_B: Maximum sway force; mY_B: mean sway force; MYM_B: Maximum yaw moment; mYM_B: mean yaw moment.

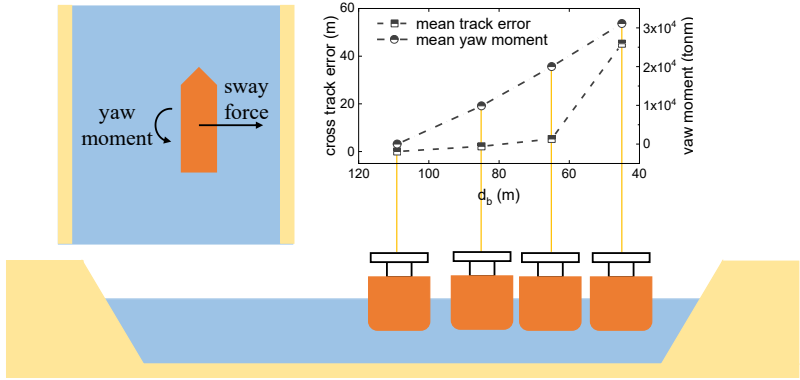


Figure 7.33 Influence of bank effects on the adaptive PID controller’s performance at 8 knots and 20% UKC.

In order to further study the influence of bank effects on the track controller performance when the ship sailed in the entire canal, simulations were conducted with and without considering bank effects. Figure 7.34 and Figure 7.35 present the performance of the adaptive PID controller at speed of 8 knots and 20% UKC. In both scenarios, one can observe that the ship could follow the desired path with satisfactory track deviations (Figure 7.34 and Figure 7.35(a)). The maximum lateral deviations were within ± 20 m (~ 0.4 breadth). From Figure 7.34, it can be also found that under the influence of the bank effects, the position of the ship lagged behind, and there was a certain phase difference (along track error). On one hand, it is attributed to the constant propeller rates that were used during simulations and the speeds could not be adjusted during manoeuvring; on the other hand, it is due to the ship-bank interaction induced forces and moments changing the heading of the ship and increasing the resistance hence reducing the forward speeds (Figure 7.35(d)). In addition, it can be seen from Figure 7.35(a) that bank effects had a slight influence on the amplitude of lateral deviations.

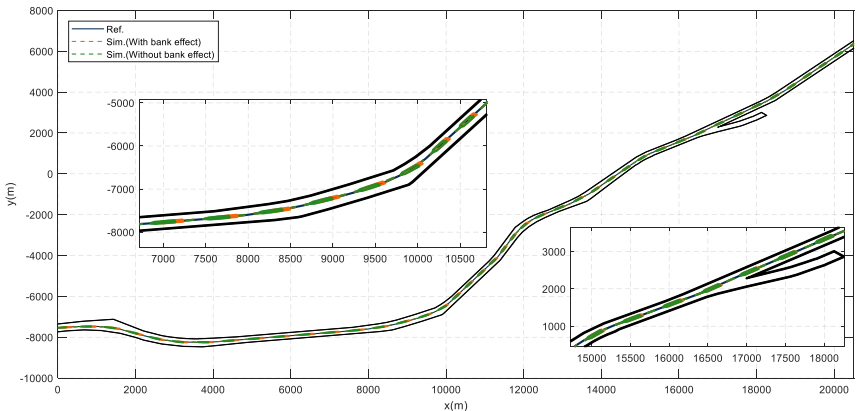


Figure 7.34 Trajectories obtained by the adaptive PID controller with and without considering bank effects when the ship sailed in the entire canal.

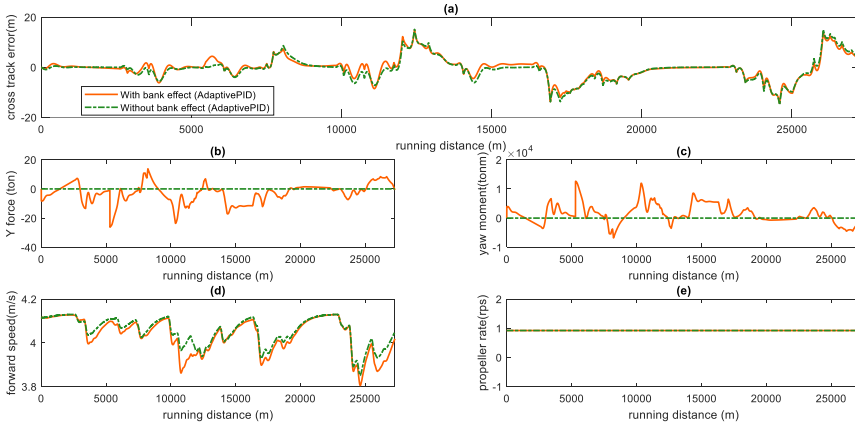


Figure 7.35 Performance of the adaptive PID controller with and without considering bank effects when the ship sailed in the entire canal.

Figure 7.36 to Figure 7.39 present the performance of fuzzy and IMC controllers. Similar conclusions can be obtained. It is worth mentioning that the bank effects had a larger influence on the fuzzy controller than that of adaptive PID and IMC controllers. One can observe from Figure 7.36 that for the fuzzy controller the along track error is more obvious, and the difference of cross track errors are larger (Figure 7.37(a)), but the lateral deviations are still in an acceptable range. Therefore, the presented controllers can control the ship following the desired path in the canal despite the existence of bank effects.

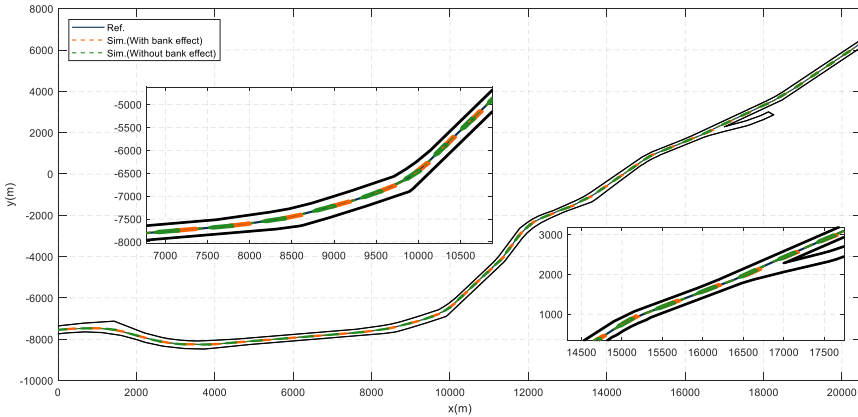


Figure 7.36 Trajectories obtained by the fuzzy controller with and without considering bank effects when the ship sailed in the entire canal.

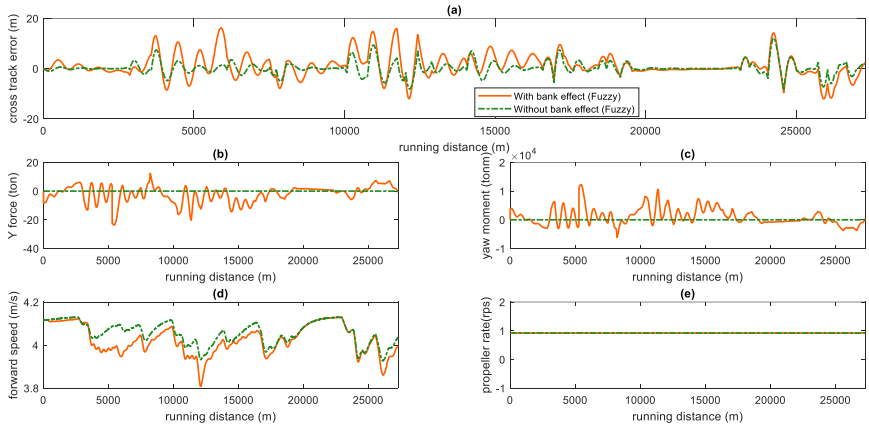


Figure 7.37 Performance of the fuzzy controller with and without considering bank effects when the ship sailed in the entire canal.

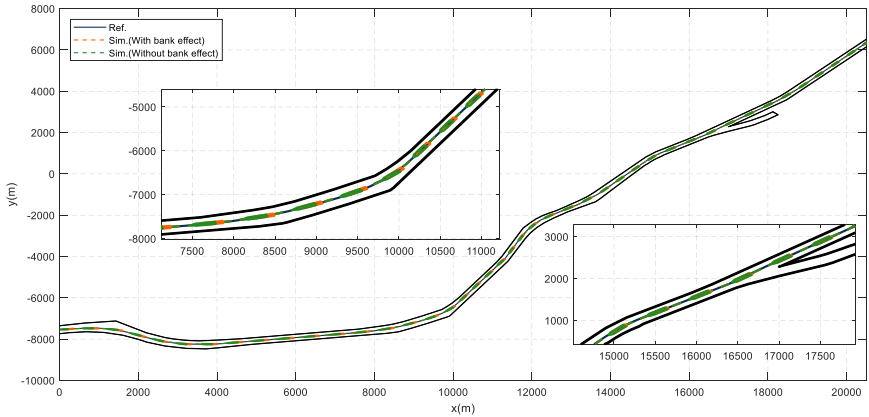


Figure 7.38 Trajectories obtained by the IMC controller with and without considering bank effects when the ship sailed in the entire canal.

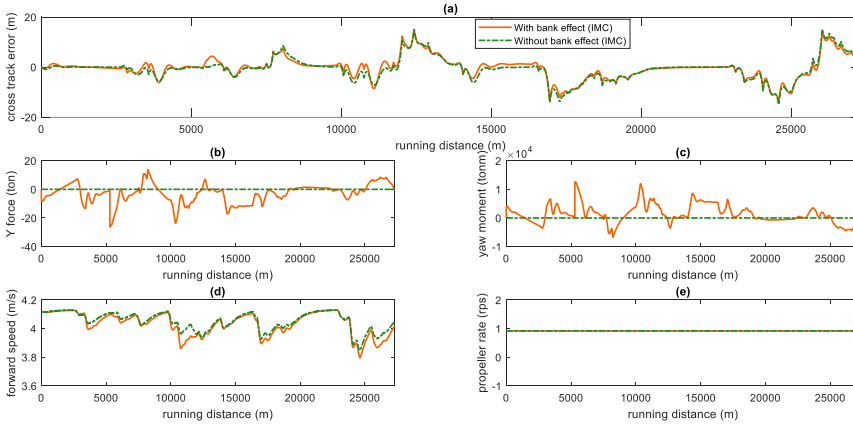


Figure 7.39 Performance of the IMC controller with and without considering bank effects when the ship sailed in the entire canal.

7.6.3 Influence of speed controller

In order to investigate the influence of speed controller, the adaptive PID controller was used in the simulation of the ship sailing in the aforementioned canal, and the performance of adaptive PID at speed of 8 knots and 20% UKC with and without speed controller is presented as a case study.

Figure 7.40 shows the tracking capability of adaptive PID control. It can be observed that after adding the speed controller, the along track error was obviously reduced but there were still very small deviations. As mentioned before, there are two reasons resulting in these deviations, one is without using the speed controller, and the other is bank effects. After using the speed controller, it can be confirmed that the bank effects still have an impact on the track controller’s performance.

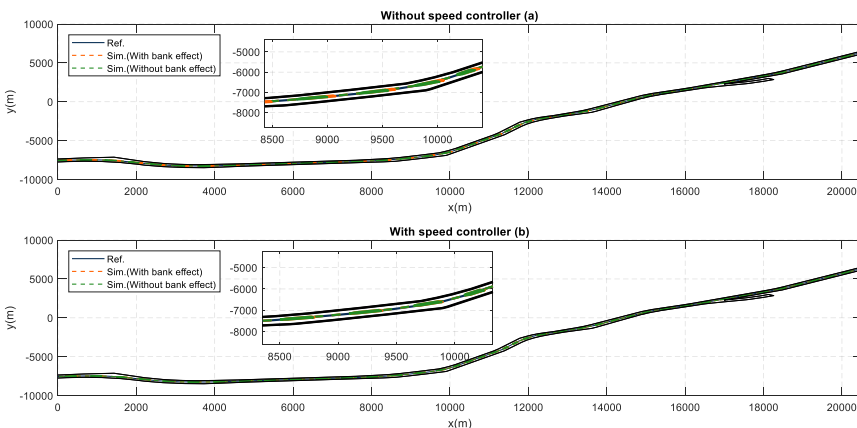


Figure 7.40 Trajectories obtained by the adaptive PID controller with (a) and without (b) speed controller when the ship sailed in the entire canal.

The greater influence of the speed controller was on the forward speed and propeller rate (Figure 7.41). It can be seen from Figure 7.41(b) that the speed controller was able to maintain a constant speed despite a slight speed change near the bends. The speed controller achieved thus a satisfactory effect. In addition, one can observe from Figure 7.41(a) and Figure 7.41(c) that if no speed controller was used, there were significant changes in forward speed, because the propeller did not take any action and only maintained a constant propeller rate. Mind that the influence of the speed controller on the other two controllers are similar to the results obtained by the adaptive PID controller, which can be found in Figure 7.42 to Figure 7.45. Thus, the speed controller plays a very important role in reducing the along track error and maintaining a constant speed.

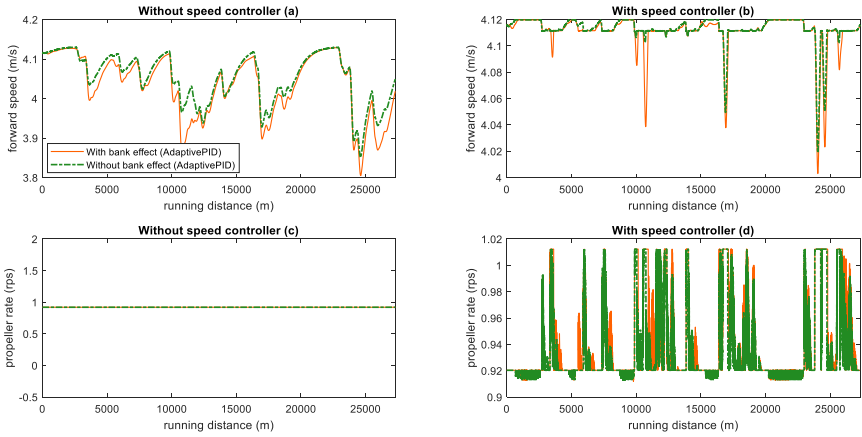


Figure 7.41 Performance of the adaptive PID controller with and without speed controller when the ship sailed in the entire canal.

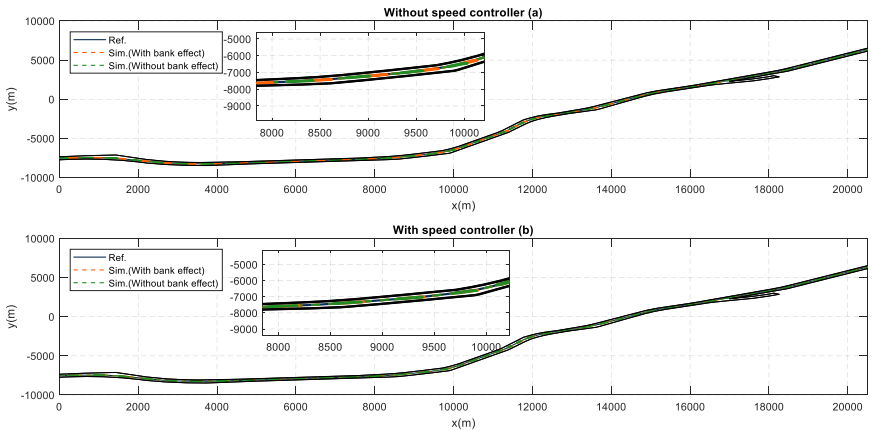


Figure 7.42 Trajectories obtained by the fuzzy controller with (a) and without (b) speed controller when the ship sailed in the entire canal.

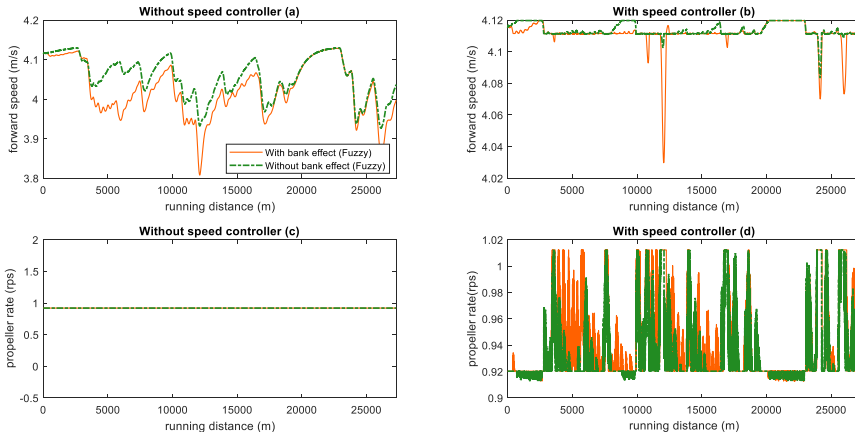


Figure 7.43 Performance of the fuzzy controller with and without speed controller when the ship sailed in the entire canal.

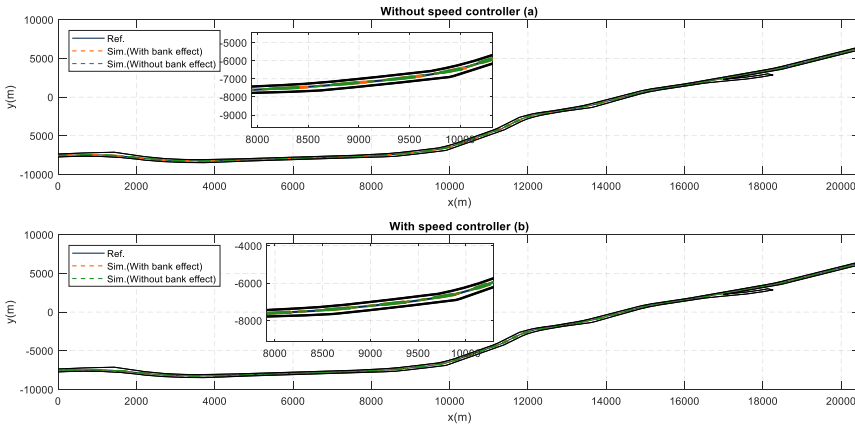


Figure 7.44 Trajectories obtained by the IMC controller with (a) and without (b) speed controller when the ship sailed in the entire canal.

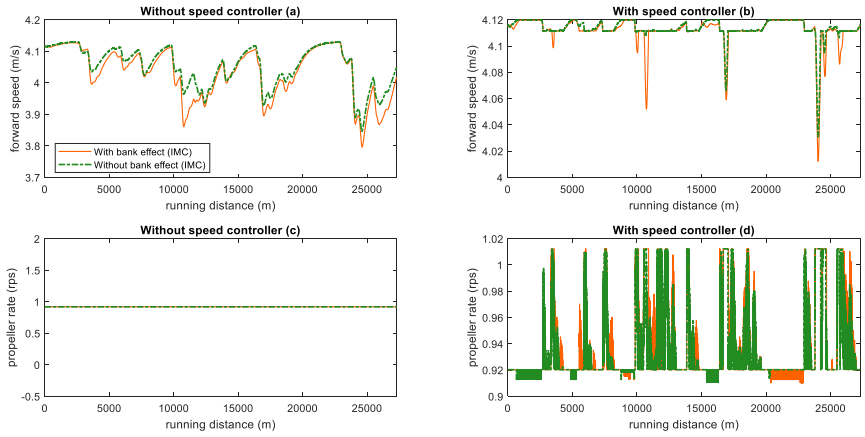


Figure 7.45 Performance of the IMC controller with and without speed controller when the ship sailed in the entire canal.

7.7 Application of the track controller on the Western Scheldt

7.7.1 Overview

To compare the performance between the present track controller (PMTTC, section 7.2.1) used in the fast-time simulator and the proposed controllers. For illustration purposes, the fuzzy based track controller (FuzzyTC, section 7.2.2) is considered in this section. The performance of PMTTC and FuzzyTC were investigated in navigation simulations on the Western Scheldt, flowing through the Netherlands and Belgium (Figure 7.46). The bathymetry, the water levels and the current were defined on a triangular mesh of the channel presented in Figure 7.47. The meshes provided high accuracy (20 m) in the navigation fairway and increased cell sizes at larger distances from the fairway.

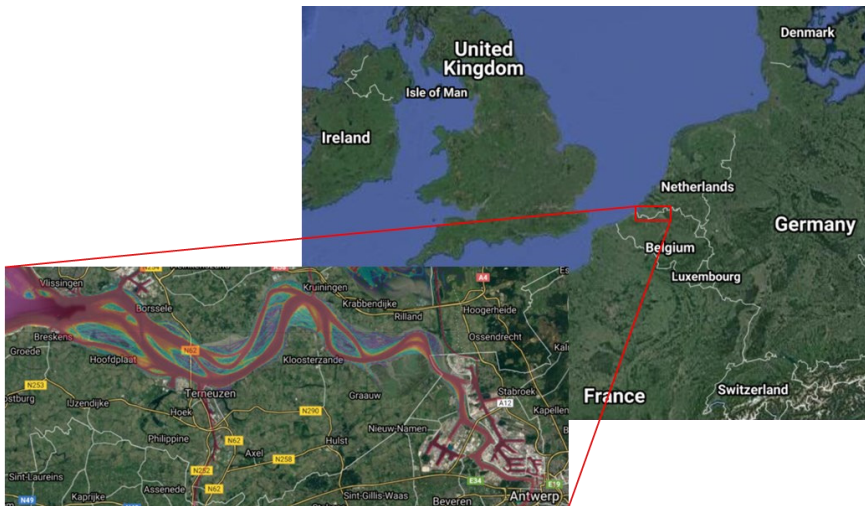


Figure 7.46 Location of the Western Scheldt.

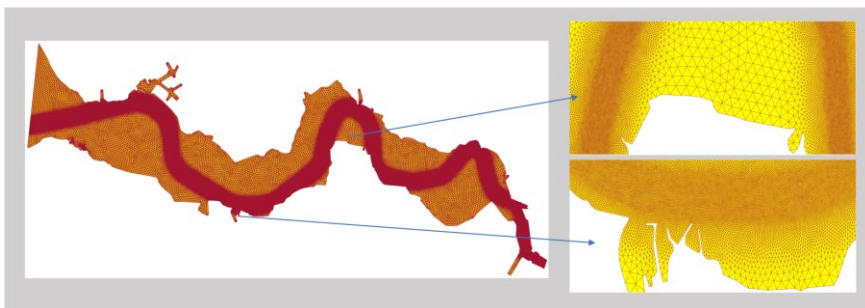


Figure 7.47 Triangular mesh of the Western Scheldt.

Simulations were conducted with a container ship, her main particulars are presented in Table 7.7, and 3D views of the container ship (taken from the FHR simulator database) are shown in Figure 7.48. The ship was equipped with a single

propeller and a single rudder, and the maximum rudder angle and rudder rate allowed were set as 35 deg and 2.8 deg/s, respectively. The hydrodynamic derivatives of the ship model were obtained from towing tank tests performed in the Towing Tank for Manoeuvres in Confined Water in Antwerp (collaboration between FHR and UGent). Tests were performed at UKC's 10%, 35% and 100% and with different bank configurations allowing to develop mathematical models for both the shallow water hydrodynamics (Delefortrie et al., 2016) and the ship bank interaction (Lataire et al., 2007). The accuracy of the ship's manoeuvring model has been validated during real-time simulations performed by experienced river pilots.

Table 7.7 Main particulars of the container ship.

Item	Value	Units
L_{OA}	399	(m)
L_{PP}	385	(m)
B	54.0	(m)
T_M	13.5	(m)
m	1.94E+5	(ton)
I_{xx}	5.55E+10	(kg m ²)
I_{yy}	1.86E+12	(kg m ²)
I_{zz}	1.79E+12	(kg m ²)
x_G	-6.0	(m)
y_G	0.0	(m)
z_G	0.0	(m)

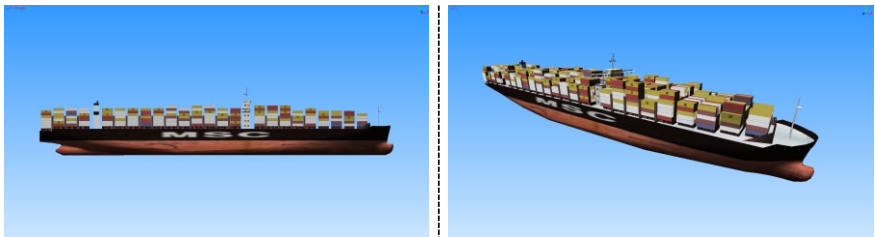


Figure 7.48 3D views of the container ship.

7.7.2 Track Controller Input

7.7.2.1 Reference trajectory and speeds

Both track controllers were applied with the same input for the reference trajectory and speeds. In this paper only inbound simulations were considered. The reference trajectory was based on the starboard side (1/3) of the dredged navigation width of the river (see Figure 7.49). The running distance (km) defined with respect to this reference trajectory on Figure 7.49 was used for geographical positioning of the data. At the beginning of the simulations (at a running distance 3.5 km), an initialisation phase was considered until the vessel reached a distance 10 km corresponding to the entrance of the Western Scheldt at Flushing (*Vlissingen*). The

simulations ended at distance 80 km when the vessel reached the shallow patch of *Frederik*. The evaluation of both track controllers was limited to the trajectory between running distance 10 km and 80 km. Other important passages concerned the bend of *Hansweert* (distance 50 km) and the bend of *Bath* (distance 70 km).



Figure 7.49 Reference trajectory (blue) for inbound vessel defined at 1/3rd of the dredged fairway width.

The ship speeds applied in the track controllers were based on the AIS-data covering the full area from 1st October 2018 to 1st January 2020. AIS-data were provided by the Scheldt Radar Chain (SRK). In order to obtain relevant speed information for the track controller, the AIS-data were filtered to inbound container vessels, longer than 350 m, with destination *Deurganckdok* (this is the most upstream destination of Ultra Large Container Ship (ULCS)). Figure 7.50 shows the track plots of the resulting 325 AIS-voyages.

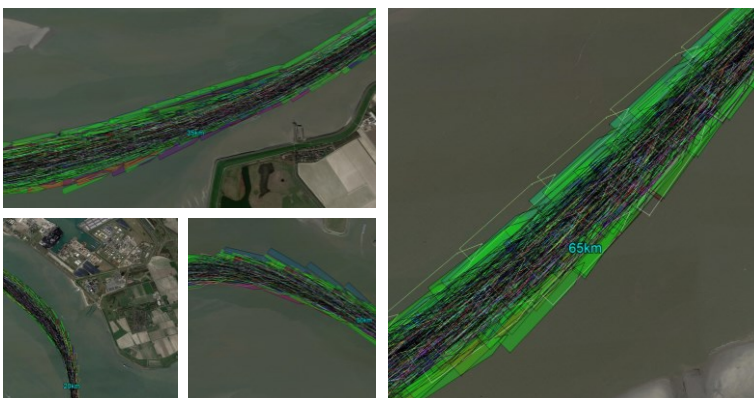


Figure 7.50 Track plots of a selection of AIS-voyages in the Western Scheldt from 1st October 2018 to 1st January 2020: 325 inbound container ships with a length larger than 350 m.

The speed over ground (SOG) applied during the AIS-voyages was related to the reference trajectory of the track controller for which statistical parameters are presented in Figure 7.51. From Figure 7.51, one can observe that the median speeds (black line) varied from 6 knots to 14 knots for 325 container ships during the entire track. When the ship sailed between positions 15 km and 70 km, the median speed was maintained at around 13 knots. At the end of the trajectory a minimum speed through water of 8 knots was maintained because the lower speeds at the running distance larger than 75 km were combined with tugboat assistance which was not taken into account in the simulations.

Based on the percentile-values a relatively large variety in ship speeds can be observed at one location. This variety is related to the tidal condition the vessel was operating in and more specifically to the current situation (ebb or flood). In this research, the reference speeds for the track controller were defined as speeds through water equal to the median AIS-speeds (percentile 50%). During the simulations, the track controller converted the reference speed through water to a reference speed over ground based on the actual (longitudinal) current condition. The SOG was used as an input to the speed controller.

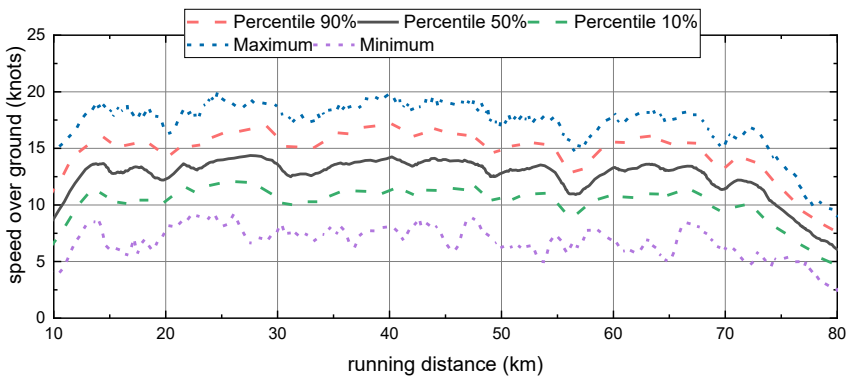


Figure 7.51 Reference forward speeds obtained from the AIS data of 325 container ships ($L_{OA} > 350$ m) in the Western Scheldt from 1st October 2018 to 1st January 2020.

7.7.2.2 Parameter settings

The parameters of both track controllers are shown in Table 7.8 and were resulting from an iterative optimisation process. For the PMTC no unique set of weight coefficients could be found that provided an acceptable trajectory in all tidal conditions. As a result, evaluations with PMTC were based on three simulations with different settings. The simulation with the smallest maximum cross track error was then selected.

Table 7.8 Parameters of the prescience model based track controller (PMTC) and fuzzy based track controller (FuzzyTC).

PMTC			FuzzyTC		
Item	Value		Item	Value	
c_F	1.0	1.0	0.0	ψ_e^{max} (deg)	9
c_M	0.5	1.0	1.0	$d\psi_e^{max}/dt$ (deg s ⁻¹)	4
c_A	0.0	0.5	0.0	c	1.05
Δt (s)	90	90	90	ω_{los}	0.5
$\Delta\delta$ (deg)	2	2	2	K_{pu} (m ⁻¹)	0.1429
Δt_δ (s)	2	2	2	K_{iu} (s ⁻²)	0.0143
Δt_n (s)	60	60	60		
RunFreq (Hz)	5	5	5	RunFreq (Hz)	40

7.7.3 Results and discussions

7.7.3.1 Overview

Simulation experiments were carried out using two different motion control systems: prescience model-based track controller (section 7.2.1) and fuzzy based track controller (section 7.2.2). A first evaluation, presented in section 7.7.3.2, was performed in deep water and without assuming any currents. Secondly both track controllers were applied in a real bathymetry and during a full tidal range. In section 7.7.3.3 the applicability of the track controllers in shallow and confined water and with a wide variation of current conditions was evaluated.

7.7.3.2 Comparisons in calm and deep water

Simulations in calm and deep water were performed in a virtual environment that was obtained by defining the bathymetry at a constant depth of -100 m and setting all current vectors to zero. The reference trajectory, reference speeds and controller settings were defined according to the definitions in section 7.7.2.

7.7.3.2.1 Tracking performance and CPU consumption

In this section, the PMTC and FuzzyTC are compared via analysing the performance of the ship passing through the river (Figure 7.52, 10 km to 80 km). For illustration purposes, Figure 7.52 shows the trajectories between 60 km and 70 km obtained by the PMTC and the FuzzyTC. One can observe from Figure 7.52 that both control systems could manoeuvre the ship following the reference path with satisfactory control performance. Figure 7.53 and Table 7.9 present the cross track errors and CPU performance of two control systems for the entire trajectory (10 km to 80 km). Compared with the PMTC in Figure 7.53 and Table 7.9, the mean cross track error of the FuzzyTC was reduced by 7.50% from 14.79 m (0.27 breadth) to 13.68 m (0.25 breadth), despite a 3.67% increase for maximum track error. The FuzzyTC had a narrower interquartile range of cross track error than the PMTC (Figure 7.53(b)).

An important advantage of the FuzzyTC concerned the numerical performance. Running a simulation using the FuzzyTC at 40 Hz took about 7 minutes, while the PMTC at 5 Hz took around 70 minutes. The computing speed increased 80 times with the FuzzyTC compared to the PMTC, and the CPU time was significantly reduced.

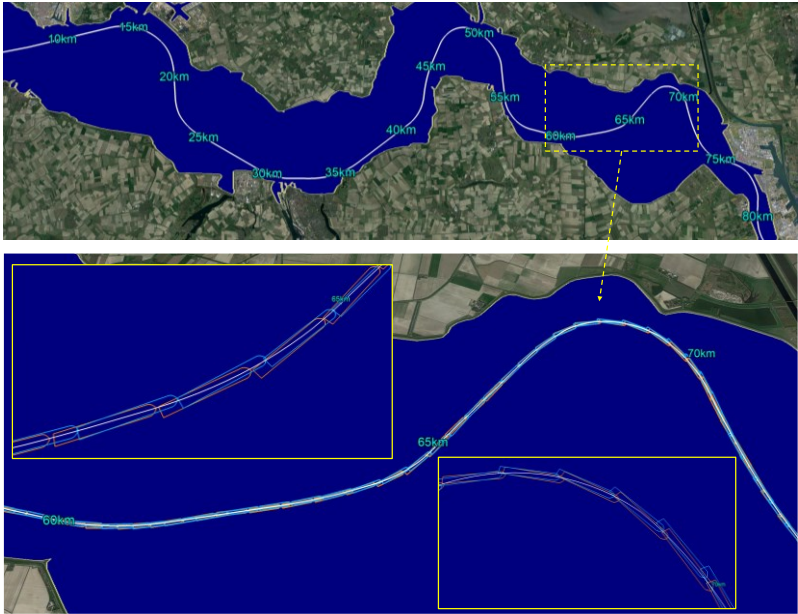


Figure 7.52 Reference trajectory (white) and trajectories obtained by PMTC (blue) and FuzzyTC (orange) under calm and deep water (60-70 km).

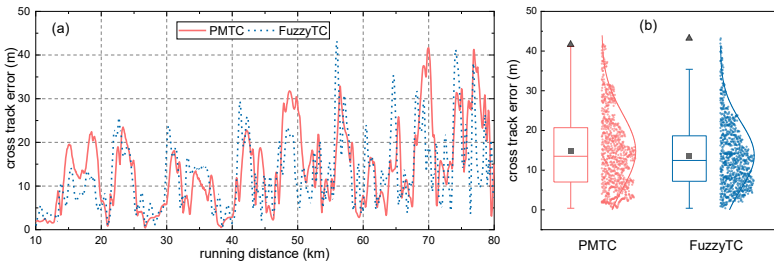


Figure 7.53 Cross track error of the midship position for PMTC and FuzzyTC (a); Box plots of cross track error for PMTC and FuzzyTC (b). The bottom and top of the box represent the 25th and 75th percentile; the band near the middle is the median value; the lower and upper whiskers represent the value of 25th percentile $- 1.5$ IQR (in this case it is the minimum value because there are no data lower than zero) and the value of 75th percentile $+ 1.5$ IQR respectively; IQR, interquartile range (between 25th and 75th percentile); black triangle and rectangle represent the maximum and mean values respectively; red and blue dots are the cross track errors of PMTC and FuzzyTC respectively.

Table 7.9 Cross track errors and CPU performance obtained by PMTC and FuzzyTC under calm and deep water.

Controllers	Cross track error		CPU performance	
	Mean (m)	Maximum (m)	RunFreq (Hz)	CPU time (minutes)
PMTC	14.79 (0.27 B)	41.66 (0.77 B)	5	70
FuzzyTC	13.68 (0.25 B)	43.19 (0.80 B)	40	7
Variation	-7.50%	+3.67%	×8	1/10

7.7.3.2.2 Rudder and propeller application

The control actions (rudder and propeller) of PMTC and FuzzyTC are displayed in Figure 7.54. As shown in Figure 7.54(a), the rudder angle and propeller rate of the PMTC control system presented sawtooth fluctuations. It can be attributed to the fact that the rudder deflection and propeller revolution of the PMTC system took discrete values and were updated periodically. As such the PMTC controller tried to reproduce the human interaction between a pilot and a helmsman and the discrete adaption of propeller rates corresponding to the telegraph settings.

For the FuzzyTC, the control actions showed relatively smooth evolutions. The rudder angle was determined according to the desired course angle, and the propeller rate was adjusted via the speed controller based on the changes of speed. It is worth mentioning that the FuzzyTC used rudder more frequently. The mean and maximum absolute rudder angle of PMTC (4.1 deg and 28.0 deg) and FuzzyTC (4.7 deg and 25.0 deg) were similar.

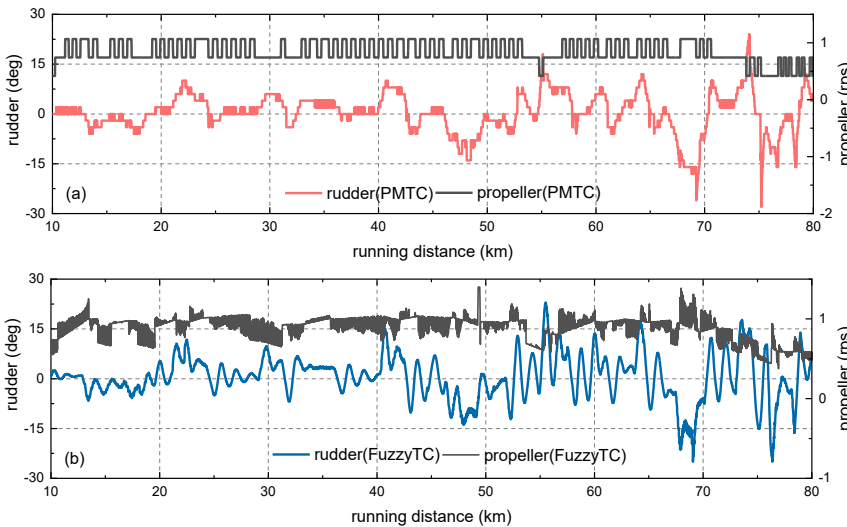


Figure 7.54 Control actions (rudder and propeller) of PMTC (a); Control actions of FuzzyTC (b).

7.7.3.2.3 Forward speed

Figure 7.55 shows the forward speeds and the errors between reference and actual speeds for the PMTC and the FuzzyTC. In Figure 7.55(a,b), one can find that both control systems could manoeuvre the ship following the reference speed. But for the PMTC system, the deviation between the reference and actual speeds was larger than that of the FuzzyTC (Figure 7.55(c)). Moreover, significant fluctuations of speed for the PMTC system can be observed due to the use of discrete propeller rates (Figure 7.55(a)), whereas the FuzzyTC can follow the reference speed smoother and more accurately owing to the use of the speed controller (Figure 7.55(b)).

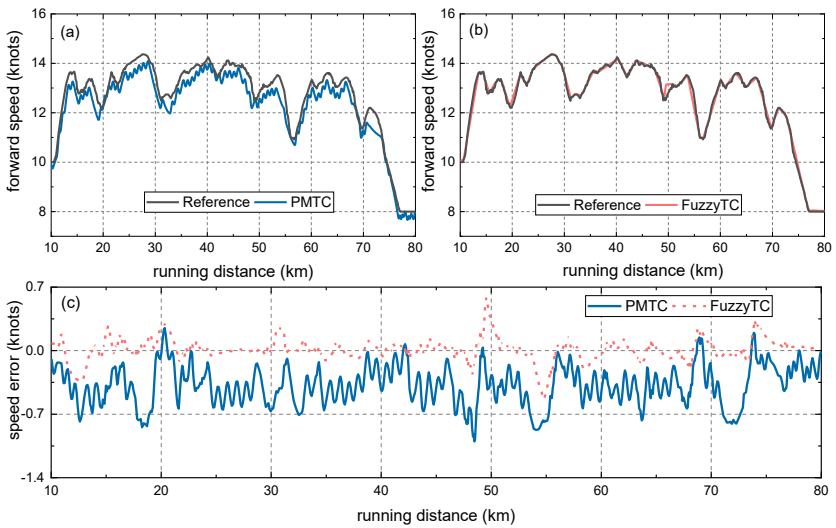


Figure 7.55 Reference and actual forward speeds and speed errors. (a) reference and actual forward speed of PMTC; (b) reference and actual forward speed of FuzzyTC; (c) errors between reference and actual speeds of PMTC and FuzzyTC.

7.7.3.3 Comparisons in shallow water in tidal conditions

7.7.3.3.1 Overview

In this section, simulations were performed in a realistic environment. The bathymetry was defined according to actual conditions in the year 2019 and the tidal conditions corresponded to a mean spring tide cycle. For this, the results of hydrological calculations of tide and current were used as an input. In order to run simulations in different tidal conditions, a simulation was initiated every 10 minutes over a full tidal cycle covering 13 hours. As such 78 fast-time simulations were performed. Figure 7.56 presents the tidal variation at the observation points: *Vlissingen*, *Hansweert* and *Prosperpolder*.

Furthermore, the gross Under Keel Clearance (UKC) of the ship varied with both the tide and the bathymetry, which can be calculated by:

$$UKC = (\text{bottom depth} + \text{tidal water level}) - (\text{ship's draft}) \quad (7.2)$$

Then, UKC data were obtained based on the 78 simulation runs, and the statistical results are summarised in Figure 7.57. From the statistics, the minimum UKC was 10.8% of the ship's draft. The minimum UKC stipulated for the Western Scheldt is 12.5%. If the shallowest part of the Western Scheldt is passed at low tide, then a vessel with draft 13.5 m violates this criterion. As a result, this simulation corresponds to a condition that would not be allowed in reality.

Figure 7.58 presents the statistical results of longitudinal and lateral currents obtained from the 78 tidal condition simulation runs. One can observe in Figure 7.58 that the maximum values both in longitudinal current (4 knots) and lateral current (1.3 knots) correspond to flood conditions shortly before high tide.

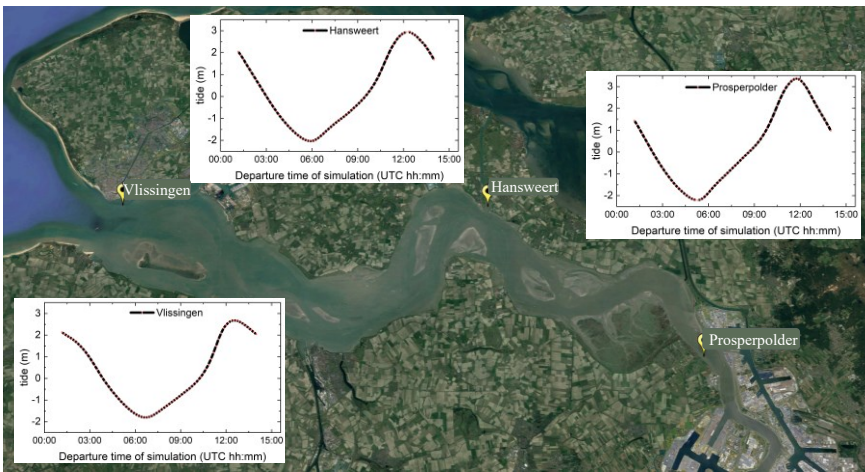


Figure 7.56 Tidal variation in *Vlissingen*, *Hansweert* and *Prosperpolder* for inbound simulations initiated from 01h10 to 14h00 on 9th March 2020.

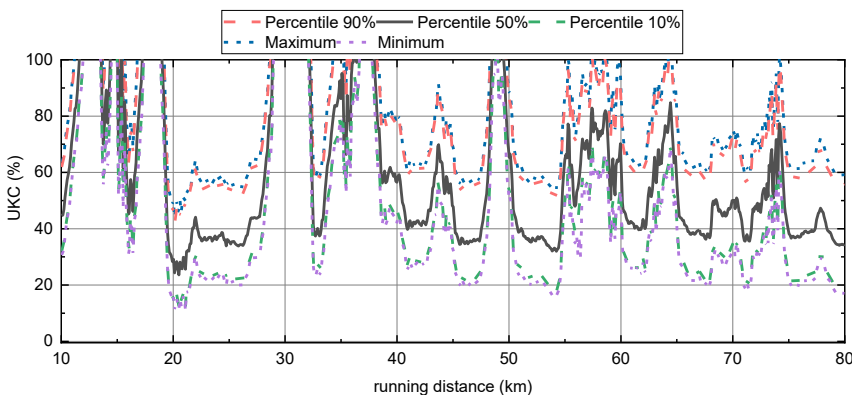


Figure 7.57 Statistical results of Under Keel clearance (UKC) obtained based on the 78 tidal condition simulation runs.

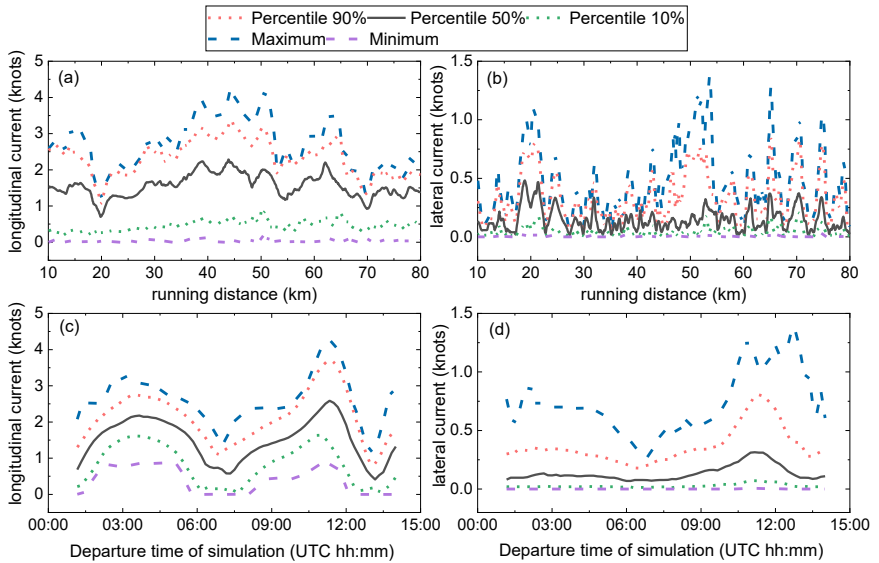


Figure 7.58 Statistical results of (absolute) longitudinal and lateral currents obtained based on the 78 tidal condition simulation runs: (a) running distance versus longitudinal current; (b) running distance versus lateral current; (c) departure time of simulation versus longitudinal current (tidal evolution longitudinal current); (d) departure time of simulation versus lateral current (tidal evolution lateral current).

7.7.3.2 Tracking performance

In order to illustrate the performance of PMTC and FuzzyTC under external disturbances, Figure 7.59 depicts the trajectories obtained by the above two controllers (around 50 km and 65-70 km, departure time of simulation UTC 11:30). One can observe that PMTC (blue) and FuzzyTC (orange) could control the ship on the reference straight-line and curve paths (white), even under the effect of external disturbances. The ship was able to predict the orientation change of the desired path segments to follow the path with small overshoots.

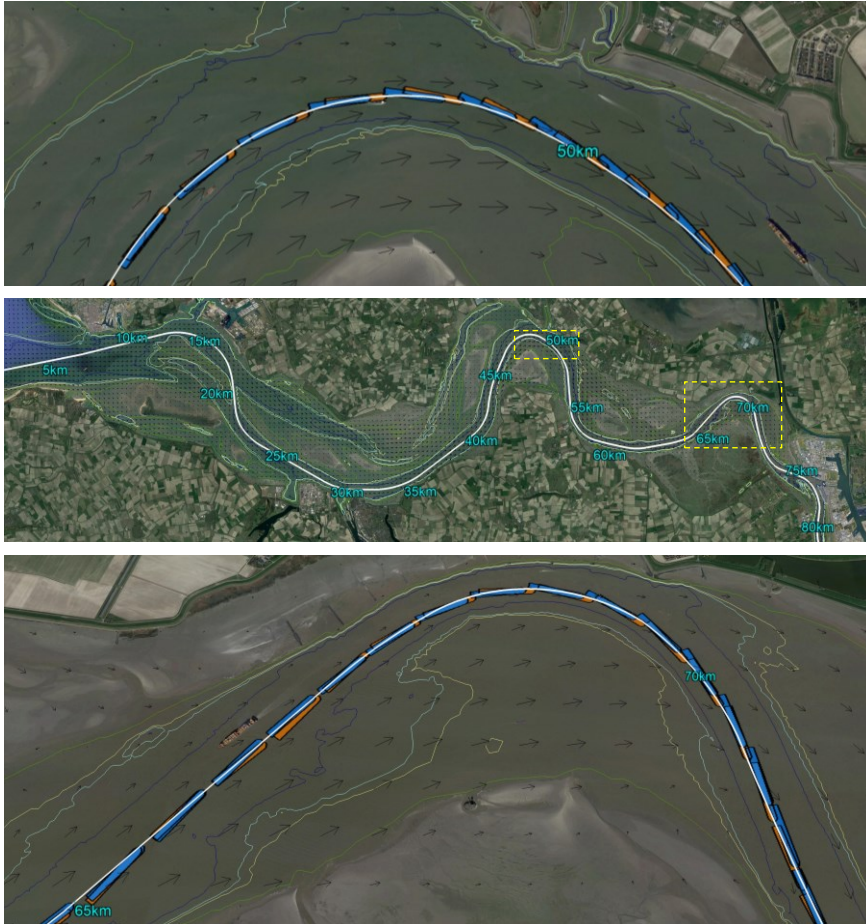


Figure 7.59 Reference trajectory (white) and trajectories obtained by PMTC (blue) and FuzzyTC (orange) under full tidal cycle (50 km and 65-70 km, departure time of simulation UTC 11:30).

The statistical results of cross track errors and tidal evolution track errors are presented in Figure 7.60 and Figure 7.61, which were obtained from 78 fast-time simulation runs for the entire trajectory (10 km to 80 km) and full tidal cycle (01h10 to 14h00). According to the statistics, the mean and maximum track errors of PMTC were 12.95 m ($0.24 B$) and 85.86 m ($1.59 B$) respectively, the errors of FuzzyTC were slightly increased to 15.39 m ($0.28 B$) and 89.12 m ($1.65 B$). The track errors might be caused by the effect of environmental disturbances or controllers' parameters. For instance, when the ship sailed near 50 km at flood current (Figure 7.59), an important lateral current occurred that made the ship deviate from the reference path (see Figure 7.58(b)). Although there were individual positions with large deviations, the average deviation was acceptable for the two control systems. The deviations can be reduced by optimizing the parameters of controllers.

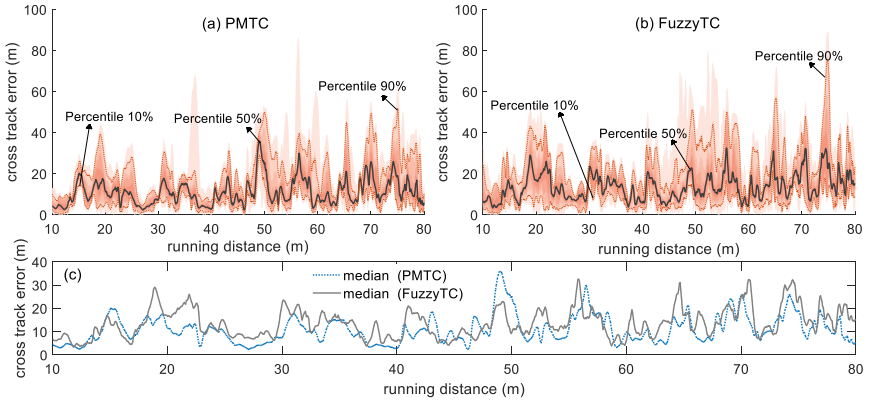


Figure 7.60 Statistical results of cross track errors as function of running distance from 78 fast-time simulation runs for the whole trajectory (10 km to 80 km) and full tidal cycle (01h10 to 14h00).

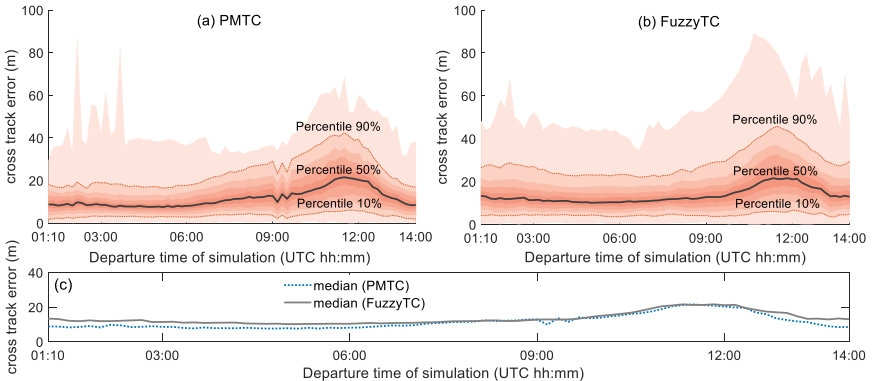


Figure 7.61 Statistical results of cross track errors as function of time or tidal evolution from 78 fast-time simulation runs for the whole trajectory (10 km to 80 km) and full tidal cycle (01h10 to 14h00).

7.7.3.3 Rudder application

Figure 7.62 compares the rudder application of the PMTC and FuzzyTC. The mean absolute rudder angle of PMTC was 5.89 deg, which was increased by 13.7% to 6.70 deg for FuzzyTC. Note that the FuzzyTC used rudder more frequently than the PMTC (Figure 7.62(a,b)).

The rudder application of PMTC and FuzzyTC for the entire trajectory and the full tidal cycle are plotted in Figure 7.63, where the value of rudder was the absolute percentage of the maximum rudder (35 deg). This illustration allows to identify those locations and conditions that require most rudder application. As such the rudder angle (in combination with the cross track error) can be considered a measure for the navigability of the ship in this environment.

One can observe in Figure 7.63 that the rudder deflection varied with the running distance (bathymetry). For both control systems the largest rudder angles were applied in the Bend of Bath (67 km to 70 km). The Bend of *Bath* is a sharp bend with a shallow zone's up- and downstream the bend. Furthermore at flood tide important cross currents occur (see Figure 7.59). When the evolution in time is considered, Figure 7.63 reveals that the most important rudder angles are required at low water (corresponding to departure time 05:20), resulting in the shallowest conditions. This observation illustrates the shallow water effects (including bank effects) on the manoeuvrability of the vessel requiring larger rudder angles to perform the same bend radius. Compared with the PMTC in Figure 7.63, the rudder for FuzzyTC provided a smoother variation and a clearer relation between tidal conditions and manoeuvrability.

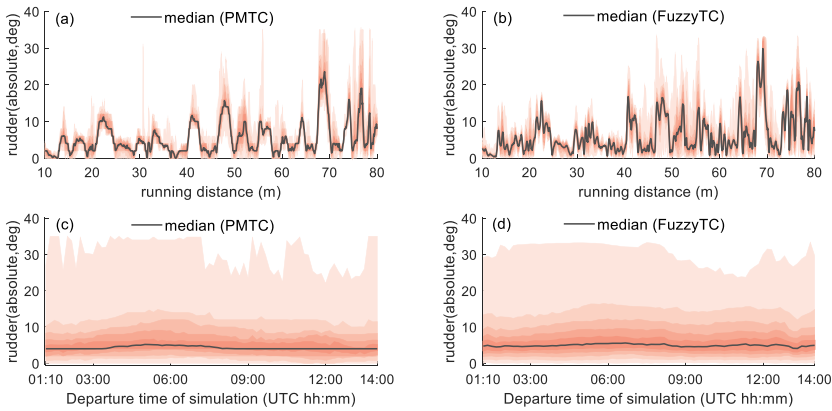


Figure 7.62 Statistical results of (absolute) rudder angle for PMTC and FuzzyTC obtained from the 78 tidal condition simulation runs: (a) running distance versus rudder (PMTC); (b) running distance versus rudder (FuzzyTC); (c) time versus tidal evolution rudder (PMTC); (d) time versus tidal evolution rudder (FuzzyTC).

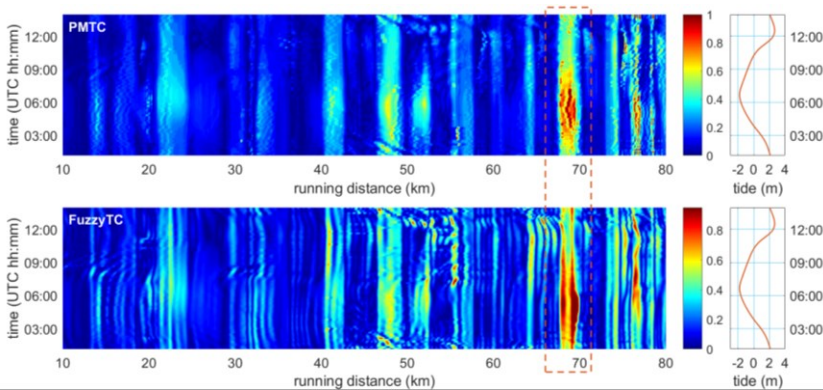


Figure 7.63 Rudder application based on normalised absolute rudder angle for PMTC and FuzzyTC obtained from 78 fast-time simulation runs for the entire trajectory (10 km to 80 km) and full tidal cycle (01h10 to 14h00).

7.8 Reference

- Delefortrie, G., Eloot, K., Lataire, E., Van Hoydonck, W., et al., 2016.** *Captive model tests based on 6 DOF shallow water manoeuvring model.* In *International conference on ship manoeuvring in shallow and confined water with special focus on ship bottom interaction (4th MASHCON)*. Hamburg, Germany.
- Lataire, E., Vantorre, M., Candries, M., Eloot, K., et al., 2018.** *Systematic techniques for fairway evaluation based on ship manoeuvring simulations.* In *The 34th PIANC World Congress*. Panama City, Panama.
- Lataire, E., Vantorre, M., Laforce, E., Eloot, K., et al., 2007.** *Navigation in confined waters influence of bank characteristics on ship-bank interaction.* In *2nd International Conference on Marine Research and Transportation (ICMRT'07)*. Ischia, Italy.
- PIANC., 1992.** *Capability of ship manoeuvring simulation models for approach channels and fairway in harbours (report).*
- Vantorre, M., Laforce, E., and Claeysens, P., 1997.** *Development of an autopilot for fast-time simulation in confined waterways.* In *11th Ship control systems symposium*. Southampton, UK.

Ship motion control systems

8	Conclusions and recommendations	273
8.1	Conclusions	273
8.1.1	General discussion.....	273
8.1.2	System identification for obtaining ship mathematical models.....	274
8.1.3	New path following control system.....	274
8.1.4	Build experiment and simulation platforms.....	275
8.1.5	Experimental studies	276
8.1.6	Numerical simulation studies	277
8.2	Recommendations	279
8.2.1	Theoretical studies.....	279
8.2.2	Experimental studies	280
8.2.3	Simulation studies	280

The science of today is the technology of tomorrow.

--Edward Teller

8

Conclusions and recommendations

8.1 Conclusions

8.1.1 General discussion

The main goal of this research was to design, implement, test and apply concise and robust ship motion control systems to improve the control performance in shallow water and to meet actual engineering needs. The research work was mainly carried out from the perspective of practical application. The main research content and results are shown in Figure 8.1, which will be further elaborated in the following sections.

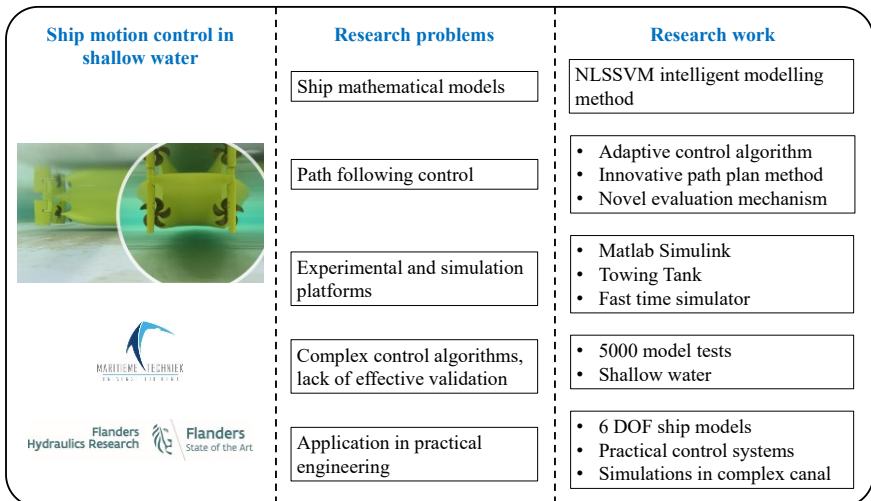


Figure 8.1 Main research content and results.

8.1.2 System identification for obtaining ship mathematical models

In order to accurately determine the parameters of ship motion models in shallow water and to solve the complexities involved with the estimation of nonlinear terms by traditional approaches, a novel Nonlinear Least Squares Support Vector Machine (NLSSVM) has been proposed and two case studies using the proposed method have been presented in Chapter 3. To illustrate the validity and applicability of the proposed method, numerical simulation and model test data were combined and utilized to estimate unknown parameters and to predict ship's motions. Firstly, simulation data were applied in the NLSSVM model to obtain the estimated parameters. These were compared with known parameters to validate and verify the proposed approach. Then the conventional identification methods NLS and FLS were compared with the proposed approach. The result demonstrated that the NLSSVM could overperform the other two methods with higher accuracy and overcome the drawbacks of conventional methods to identify nonlinear terms. Furthermore, based on the model test data at various speeds and water depths, the model parameters were determined by the NLSSVM method. The good agreement between experimental and predicted results demonstrated the applicability of the proposed algorithm in shallow water. To summarize, the NLSSVM approach could accurately identify the linear and nonlinear parameters of ship motion models in shallow water.

8.1.3 New path following control system

8.1.3.1 Adaptive control algorithm

A new adaptive PID controller was proposed to solve the speed and water depth dependency problem of the PID controller coefficients (sections 6.7.2 and 6.7.4). The optimal PID-values were first determined by means of the IMC algorithm, the speed and water depth dependency of the PID-values was then investigated. Based on the PID-values found for different forward speeds and UKCs, a relationship between these PID-values and the corresponding sailing speeds and experimental water depths was found. The validity of this relationship was tested by means of model tests and fast-time simulations at various sailing speeds and water depths. According to the results from both the experiments and simulations, the proposed adaptive controller can provide satisfactory control performance with high tracking accuracy.

By realizing this, the optimal PID-values only need to be determined by six parameters, the PID-values at other speeds and water depths can be derived automatically according to the corresponding relationship. The time that is saved could be used to conduct additional manoeuvring tests. Moreover, the speed and water depth dependency guarantee proper track keeping behaviour in case the changes of speed and water depth are induced during manoeuvring.

8.1.3.2 Novel path planning algorithm

A novel path planning algorithm, named angle-guidance tuned-distance fast marching square method (ATFMS), was proposed to automatically generate a

smooth and optimal path in a complex environment (Chapter 4). The ATFMS was developed according to the basic fast marching method (FMM) by introducing new functions and characteristics to meet actual engineering needs. Besides the path planning, the implementation of obstacle avoidance and waypoint-selection were also studied.

The results show that using the traditional FMM-based method the shortest paths are generated, but it also leads to paths with the highest collision risks with the geographical boundaries. In contrast, the proposed ATFMS algorithm is able to determine safe paths which keep a safe distance to the boundaries and go through the deeper water areas. In the ATFMS algorithm, the distances between the planned paths and obstacles can be adjusted with different saturation values, which can improve the flexibility of path planning and solve the trade-off between safety and sailing distance.

According to the principle of the ATFMS algorithm, a desired path with virtual obstacles has been planned in the towing tank environment. The generated waypoints were then used in the path following control. The results reveal that the proposed path planning algorithm can provide effective and satisfactory waypoints used for path following control.

8.1.3.3 Innovative evaluation mechanism

An innovative method, combining the model evaluation mechanism and the grey relational decision-making theory, was proposed to comprehensively evaluate the performance of autopilots (Chapter 5). In this mechanism, five evaluation indexes were selected to describe the ship's motion, the grey theory was then used to determine the optimum controller based on these evaluation indexes. Compared with qualitative analysis, the proposed evaluation mechanism can quantitatively and scientifically evaluate the performance of controllers, which is beneficial to improve the accuracy of evaluation.

8.1.4 Build experiment and simulation platforms

Based on the literature study, new ship motion control systems have been developed and studied. The control systems were firstly tested in a Matlab Simulink environment to ensure the effectiveness of the relevant algorithms; Then, the developed control systems were programmed in the towing tank to validate their control performance in real scenarios. Finally, they were implemented in the ship manoeuvring simulator to conduct fast-time simulation studies. Figure 8.2 shows the relevant experimental and simulation platforms. The establishment of the test platform makes it possible to test, validate and apply the controllers, which can investigate their performance more scientifically and effectively.



Figure 8.2 Experiment and simulation platforms.

8.1.5 Experimental studies

In the towing tank of FHR around 5,000 model tests have been conducted with focus on testing the controllers' performance in shallow water. The experimental studies were performed with a scale model of an LNG carrier, and the model tests were executed at different forward speeds and water depths. Different control missions including course control and path following control were investigated in shallow water conditions. During tests, the ship's position, velocity, propeller revolution, rudder deflection and other relevant information were measured, which were further used to evaluate the performance of controllers. In addition, the effects of speed and water depth on the performance of acceleration tests, zigzag tests, course keeping and course changing tests, as well as path following tests have been analysed.

From the experimental results in Chapter 6, all studied controllers (PID, IMC, fuzzy and adaptive PID) were successfully implemented in the towing tank autopilot system, and the ship model was able to follow a predefined course or path with satisfactory control effects in shallow water.

According to the statistical results obtained from analyzing all model tests, the adaptive PID controller was selected as the best performing controller in most experiments, implying it could obtain a better performance compared to the PID, IMC and fuzzy controllers. The IMC and fuzzy controllers performed similarly. Moreover, the frequencies for each controller obtaining the best performance varied in different scenarios, which might be attributed to the influence of the number of waypoints and the look ahead distance, etc. The results indicate that the tested controllers can be applied in the towing tank, but for the optimum selection of an autopilot algorithm, multiple factors including controller parameters, trajectory, and test condition, etc. should be taken into consideration.

The PID controller did not achieve a satisfactory control effect, which does not mean the method is not good but this is probably due to the fact that a constant bandwidth frequency was used in the PID controller during experiments. It implies that the parameters of the PID controller need to vary with changing test conditions. To improve the performance of the PID controller, the adaptive control methods such as fuzzy PID should be considered to tune the controller parameters online.

The performance of model-based controllers (PID, IMC, and adaptive PID) relies not only on the controller coefficients such as K_p , K_i and K_d , but also on the accuracy of the identified ship model parameters (the time constant T and the gain K of the Notomo model). Thus, it is relatively complex to obtain optimal performance. On the contrary, the model-free control strategies, such as the fuzzy controller, are relatively simple because only the controller coefficients need to be tuned. From a practical point of view, first one can consider the use of model free controllers (fuzzy controllers), followed by adaptive controllers (adaptive PID), then IMC and PID, etc.

In shallow water, the studied autopilots can control the ship following the desired paths. But water-depth restrictions result in a decrease of the ship's manoeuvrability, which means that the ship becomes harder to manoeuvre in shallower water. Moreover, the speeds and water depths have a significant influence on the outcome of standard manoeuvring tests, the controllers' parameters and the performance. When designing the controller, these effects should be taken into consideration.

8.1.6 Numerical simulation studies

The numerical simulation studies were carried out using fast time simulations. Firstly, the control algorithms were implemented in the ship manoeuvring simulator, and their performance were analysed by controlling a 6 DOF ship model following the prescribed courses or paths at different speeds and water depths. Then, the numerical simulation results were validated through comparison with the experimental results. Finally, the applicability of the controllers was studied through simulation of a ship transiting the Panama Canal and the Western Scheldt river. In addition, a speed controller was adopted during the simulation studies in order to counteract speed loss during manoeuvring. The speed controller was implemented as a PI controller algorithm.

Before conducting simulation studies, the accuracy of the 6 DOF mathematical model used in the ship manoeuvring simulator was investigated by comparisons between the numerical and the experimental zigzag trials at various speeds and water depths (Chapter 7). From the comparison, the performance of the 6 DOF mathematical model matched well with the corresponding physical model. Hence the accuracy of 6 DOF model was proved satisfactory for further simulations.

According to the numerical results in Chapter 7, it can be concluded that all present controllers (adaptive PID, fuzzy and IMC) were able to control the ship successfully in shallow water. Satisfactory control effects were achieved by the studied controllers with acceptable track deviations.

This will fill the gap in the current research, where most research only considers controllers in a simulation environment and limited information on their performance in real cases (no validation) is available, especially in shallow water.

Compared with the present prescience model based track controller (PMTC) used in the fast-time simulator, the computational cost (CPU time) of the proposed

fuzzy based track controller (FuzzyTC) was much better, and the computing speed was increased by 80 times. The FuzzyTC had also a better speed controller.

8.2 Recommendations

8.2.1 Theoretical studies

The adaptive PID controller proposed in this work can solve the speed and water depth dependent problem. As mentioned before, the time constant T and gain K of Nomoto model are very crucial for the determination of controllers' coefficients (e.g. PID controller). These parameters change with speed, loading condition, and water depths, etc. In addition to solving the speed and water depth dependency problem, the controller should be able to adapt to various environmental changes. To deal with this issue, an online model parameter identification method should be developed to update the model parameters in real time as a response to the changes in the external environment.

Moreover, with the development of modern control theory and artificial intelligence, more efforts are recommended to be put in the development of intelligent control methods, such as neural networks to further improve the performance of controllers. New developments can also be expected in the frame of unmanned shipping, for which feasibility studies are in progress. The rapid development of accurate position detection systems makes such tendencies more feasible and will increase the demand for advanced automated controls.

Ship formation control has become one of the most interesting topics in unmanned surface ships research due to the wide range of applications (search and rescue, surveillance, cooperative mapping, etc.). Although a single ship is currently able to perform very complex tasks on its own, some of these tasks can be performed in a more efficient way using a group of ships. To achieve this objective, a control approach (formation control) with the goal to achieve certain formations with a group of ships is required. The formation control problem needs further investigation to perform the task better.

From the point of view of path planning, in this work, the path planning algorithm was developed with the consideration of static obstacles and without dynamic obstacles. To avoid moving ships or obstacles, the online path planning algorithms considering the collision avoidance rules (COLREGs) should be further implemented. Except for static and dynamic obstacles, the developed path planning approach should take into account the influence of the marine environment. For instance, ships sail in shallow and confined waters, where the manoeuvrability of ships becomes limited, and a limited manoeuvrability implies a reduced safety. Therefore, the bathymetry or water depth is an important environmental factor which needs to be considered for the computation of a safe path.

The impact of the look-ahead distance and waypoints selection of LOS guidance law are to be checked. Moreover, adaptive LOS guidance laws should be studied more closely. It can be expected that the advanced guidance method can set look-ahead distance, select waypoints, and compensate the unknown sideslip angle automatically according to the changing navigation environment.

8.2.2 Experimental studies

During model tests, only one type of ship model (LNG) was used to investigate the performance of controllers in shallow water. Additional studies can be further extended to other ship types and dimensions which will need more insight in their analysis.

The evaluation of the developed control system has been investigated in the towing tank. Although disturbances were always possible due to waves generated at acceleration (or disturbance from the previous test), the model tests were regarded as conducted in calm water. To have a clearer understanding of the control system working under the influence of waves, wind, and bank effects, etc., further investigations are required.

Experimental studies will be of great use to be extended into full-scale testing on vessels. Compared with the model tests, full scale results can reflect the actual behaviour of controllers free of scale effects and any model assumptions.

During model tests, four virtual obstacles were considered in path following control. The influence of physical obstacles instead of virtual ones can be further investigated. The control system can be tested to include static and dynamic obstacles during experimental studies to increase the autonomy of the ship.

8.2.3 Simulation studies

The mathematical manoeuvring models used in the ship manoeuvring simulator are 6 DOF mathematical models with a large number of regression coefficients determined from extensive captive model tests. For many applications, such as path following or trajectory tracking control, it is required to have a more simplified manoeuvring model that predicts the horizontal ship motions for a vessel with positive ship speed with acceptable accuracy. A simplified model based on a limited number of coefficients also opens the possibility to derive coefficients by system identification or from artificial intelligence algorithms based on towing tank tests or full scale measurements.

For an established control system multiple tests should be simulated in realistic channel conditions. In addition, the development of such a control system should meet the needs for multiple ships, starting with the planning of two encounterings and two overtaking ships on the same (or inverse) trajectory, followed by more complex shipping configurations.

A more powerful tool for manoeuvring simulations is required to allow the simulation of a total channel transit from pilot station to berth and vice versa, which can be applied in waterway design, assessment of safety of shipping traffic, voyage planning. Moreover, the developed tools and algorithms will also be applicable for control of unmanned vessels, development of automatic berthing procedures, etc.

Ship motion control systems

9	<i>Publications and Grants</i>	283
9.1	List of publications	283
9.2	List of Grants	284

He who knows others is wise, he who knows himself is enlightened.

--Lao Tzu

9

Publications and Grants

9.1 List of publications

Published

1. **Chen, C.Y.**, Delefortrie, G., Lataire, E., Effects of water depth and speed on ship motion control from medium deep to very shallow water. *Ocean Engineering*, 2021 (231), 109102. (Q1(A1) Journal)
2. **Chen, C.Y.**, Delefortrie, G., Lataire, E., Experimental investigation of practical autopilots for unmanned surface vehicles in shallow water. *Ocean Engineering*, 2020 (218), 108246. (Q1(A1) Journal)
3. **Chen, C.Y.**, Tello Ruiz, M., Delefortrie, G., Mei, T.L., Vantorre, M., Lataire, E., Parameter estimation for a ship's roll response model in shallow water using an intelligent machine learning method. *Ocean engineering*, 2019 (191), 106479. (Q1(A1) Journal)
4. **Chen, C.Y.**, Tello Ruiz, M., Lataire, E., Delefortrie, G., Mansuy, M., Mei, T.L., Vantorre, M., Ship manoeuvring model parameter identification using intelligent machine learning method and the beetle antennae search algorithm. 2019 OMAE-International Conference on Ocean, Offshore and Arctic Engineering. Glasgow, UK, 2019. (Conference)
5. **Chen, C.Y.**, Tello Ruiz, M., Delefortrie, G., Lataire, E., An energy-efficient adaptive course control system for surface ships. IWSH 2019-11th international workshop on ship and marine hydrodynamics. Hamburg, Germany, 2019. (Conference)
6. **Chen, C.Y.**, Vantorre, M., Lataire, E., Candries, M., Eloot, K., Verwilligen, J., Intelligent control strategies used in fast time ship manoeuvring simulations. MARSIM 2018 Conference. Halifax, Canada, 2018. (Conference)
7. Mei, T.L., Lu, Y., Tello Ruiz, M., Vantorre, M., Lataire, E., **Chen, C.Y.**, Zou Z.J., Hybrid Method for Predicting Ship Manoeuvrability in Regular Waves.

Journal of Offshore Mechanics and Arctic Engineering, 2021, 143(2): 021203. (Q3(A1) Journal)

8. Mei, T.L., Delefortrie, G., Tello Ruiz, M., Lataire, E., Vantorre, M., **Chen, C.Y.**, Zou Z.J., Numerical and experimental study on the wave-body interaction problem with the effect of forward speed and finite water depth in regular waves. Ocean engineering, 2019(192), 1-11. (Q1(A1) Journal)
9. Lataire, E., Vantorre, M., Candries, M., Eloit, K., Verwilligen, J., Delefortrie, G., **Chen, C.Y.**, Mansuy, M., Systematic techniques for fairway evaluation based on ship manoeuvring simulations. PIANC-World Congress. Panama, 2018, 474-486. (Conference)

Peer reviewing

10. **Chen, C.Y.**, Delefortrie, G., Mansuy, M., Lataire, E., Path following controllers for maritime autonomous surface ships: simulation, experiment, and application in shallow water. (Ocean Engineering, Q1(A1) Journal)
11. **Chen, C.Y.**, Verwilligen, J., Mansuy, M., Eloit, K., Lataire, E., Delefortrie, G., Design and application of track controllers for fast-time manoeuvring simulations in shallow and confined water. (Applied Ocean Research, Q2(A1) Journal)

In submission

12. **Chen, C.Y.**, Lataire, E., Delefortrie, G., Adaptive course controllers with nonlinear control strategies for ships in shallow water. (IEEE Transactions on Control Systems Technology, Q1(A1) Journal)

9.2 List of Grants

1. China Scholarship Council (CSC), 201706570007.
2. Special Research Fund (BOF), 01SC8418.
3. Mobility Fund (CWO) of Ghent University.

Ship motion control systems

10 Appendices.....	287
10.1 General discussion.....	287
10.2 Configuration of the simulator.....	287
10.2.1 Input and output to the simulator.....	287
10.2.2 Configuration of autopilot file.....	288
10.2.3 Controller parameters.....	291
10.2.4 Configuration of speed controller.....	297
10.3 Reference.....	300

Success is to be measured not so much by the position that one has reached in life as by the obstacles which he has overcome.

--Booker T. Washington

10

Appendices

10.1 General discussion

Chapter 10 is the appendices and elucidates how to configure the fast time simulator. It is like a user manual for fast time simulations, which provides the information and examples to set the simulator. It is necessary to mention that in the fast time simulator, some codes and comments are marked in Dutch.

10.2 Configuration of the simulator

10.2.1 Input and output to the simulator

The input to the fast time simulator is organised by a number of files, including ship database, autopilot, channel information and environment, etc.

- **Ship database** in which the ship is represented by mass, dimensions, windage area, etc. and the manoeuvring characteristics of the ship is expressed in hydrodynamic derivatives.
- **Autopilot** setting includes controller types, values for the rudder angle, propeller rate, tug operation, etc. which, depending on the type of manoeuvre, will be taken into account in order to execute the given manoeuvre. In addition to a number of predefined standard manoeuvres such as zigzag, turning circles, and stop tests, etc., it is also possible to define a track or a course for the ship to be followed (path following or course control).
- **Channel information** contains bathymetry, water depths, obstacles, etc.
- **Environment files** are used to describe several external conditions. For instance: wind field, wave field, current pattern, and water level, etc.
- **Initial configuration** is concerning choice for seagoing or inland, axis system, starting position, and desired track, etc.

Table 10.1 shows an example of the input to the fast time simulator, which contains the references to all input files.

Table 10.1 Example of the inputs to the fast time simulator.

Ship files
EQP,C:/export/SimRoot/SimFast/project/full_scale_test/shipdatabase\AlShamal/eqp_AlShamal.xml
LDC,C:/export/SimRoot/SimFast/project/full_scale_test/shipdatabase\AlShamal/load_AlShamal.xml
BEW,C:/export/SimRoot/SimFast/project/full_scale_test/shipdatabase\AlShamal/bew_AlShamal_model.xml
RMP,C:/export/SimRoot/SimFast/project/full_scale_test/shipdatabase\AlShamal/qflex.rmp
CNT,C:/export/SimRoot/SimFast/project/full_scale_test/shipdatabase\AlShamal/qflex.cnt

Autopilot
/export/SimRoot/SimFast/project/full_scale_test/invoer/alg/autopilot.xml

Channel information
BOD,/export/SimRoot/SimFast/project/full_scale_test/invoer/bod/channel.inv

Environment
SNE,/export/SimRoot/SimFast/project/full_scale_test/invoer/sne/sne_98.inv
INI,/export/SimRoot/SimFast/project/full_scale_test/invoer/ini/14_143_ini.inv
KAN,/export/SimRoot/SimFast/project/full_scale_test/invoer/kan/schipkan.in
v
OEV,/export/SimRoot/SimFast/project/full_scale_test/invoer/oev/d2b.inv
...

Initial configuration
ALG,/export/SimRoot/SimFast/project/full_scale_test/invoer/alg/track.inv

The main output consists of:

- Position, velocities, heading of the ship;
- Distance and heading deviations;
- Propeller revolution and rudder angle;
- Water depth at the midship position;
- Wind, wave, current forces acting on the ship;
- Forces from bank effects;
- Tug forces.

10.2.2 Configuration of autopilot file

10.2.2.1 Selection of autopilot types

The control algorithms presented in Chapter 5 have been implemented in the fast time simulator. Two new types of autopilot manoeuvres are considered:

- COURSECONTROL corresponds to a course keeping or changing test.
- TRACKCONTROL corresponds to a path following test.

In the autopilot file, the following type should be chosen:

For the course test, the control type “COURSECONTROL” and the desired heading angle should be given in the autopilot file.

```
<coeff name="type_auto" unit="-" type="string" value="COURSECONTROL"
comment="Kies het type autopilot"></coeff>
```

```
<coeff name="Heading" unit="deg" type="real" value="-10.0"
comment="gewenste koershoek"></coeff>
```

For the track control, both the type of control and the sailing distance (“vaarlengte” in Dutch) are required.

```
<coeff name="type_auto" unit="-" type="string" value="TRACKCONTROL"
comment="Kies het type autopilot"></coeff>
```

```
<coeff name="vaarlengte" unit="-" type="real" value="27300"
comment="Lengte van de vaart in tijdstappen van 0.1s of baanafstand
(VOLG_BAAN/TRACKCONTROL)"></coeff>
```

10.2.2.2 Thruster setting

The number of thrusters (“AANTAL_THRUSTERS”) should be provided:

```
<coeff name="AANTAL_THRUSTERS" unit="-" type="integer" value="2"
comment="aantal THRUSTERS"></coeff>
```

The type of thruster should be selected:

- Port thruster;
- Starboard thruster;
- Bow thruster;
- Stern thruster;

The propeller rate (rps) or telegraph position when CPP-propellers should be given:

```
<col name="toeren" type="real" unit="omw/s" comment="schroeftoerental in
omw/s of telegraafpositie bij CPP-propellers" />
```

For instance, the LNG ship model used in this work is equipped with two thrusters, their propeller rates are 1.0373 rps. The setting is given as follows:

```
<row>1; 1.0373 ; 0</row>
```

```
<row>2; 1.0373 ; 0</row>
```

10.2.2.3 Rudder setting

The number of rudders, initial rudder angles and speed of rudder should be provided in the following fields:

```
coeff name="AANTAL_ROEREN" unit="-" type="integer" value="2"
comment="aantal ROEREN"></coeff>
```

```
<col name="nr_roer" type="integer" unit="-" lookup="exact" />
```

```
<col name="roerstand" type="real" unit="graden" comment="roerhoek,
positief naar BB" />
```

```
<col name="status" type="integer" unit="-" comment="Snelheid van
roeraanpassen 0: stuurmachine defect, 1: halve werking, 2: normale werking" />
```

```
<row>1; 0 ; 2</row>
```

```
<row>2; 0 ; 2</row>
```

10.2.2.4 Track and look ahead distance

The track with waypoints should be given in the “alg” file, in the same fashion as a track is presently defined (Delefortrie et al., 2020). Mind that in the new algorithm, the curvature of the bends is not important, only the coordinates of the sections are used, however, for consistency with the existing track definitions, curvatures need to be given.

As stated in section 4.3.2, the LOS guidance position P_{los} is determined by a look ahead distance L_A formulated as:

$$L_A = \sqrt{(\Delta y + cL_{pp})^2 + (\Delta y)^2} \quad (10.1)$$

where L_A is the look ahead distance, L_{pp} is the length between perpendiculars, Δy is the cross track error, which is defined as the distance between the ship current position P and its orthogonal projection position on the desired track, c is the parameter that needs to be tuned. The look ahead distance plays a very important role in obtaining satisfactory control performance, which is related to the ship length, waypoints, and the size of ship, etc. An appropriate parameter c should be given in the following field:

```
<coeff name="cLookAhead" type="real" value="1.7" />
```

The default of “*cLookAhead*” is 1.5, and the recommended value is 0.5-2.0.

While the parameter ω_{los} introduced in section 4.3.3 should be given in:

```
<coeff name="WaypointSelect" type="real" value="0.5" />
```

The parameter ω_{los} is used to determine the radius ($R_k = \omega_{los}L_{pp}$) of acceptance circle for the current waypoint (section 4.3.3). Normally the default 0.5 is used.

10.2.2.5 Selection of controller type and filtering strategy

In the autopilot file, the field

```
<coeff name="ControllerType" type="integer" value="0" />
```

represents the choice of the controller, the following codes should be used when selecting a controller:

- “0” for the PID controller with constant values of K_p , K_i and K_d (see section 5.2 or 5.3);
- “10” for the PID controller with values of K_p , K_i and K_d which are a function of the propeller rate (see section 5.4);
- “20” for the fuzzy PID controller (see section 5.6);
- “30” for the fuzzy controller (see section 5.5).

Nonlinear feedback or decoration filtering strategy is governed by the field:

```
<coeff name="Strategy" type="integer" value="0" />
```

with following codes:

- “0” in case no filter is used (see section 5.8);
- “10” for the sine feedback of the input (see section 5.8);
- “11” for the atan feedback of the input (see section 5.8);
- “12” for the tanh feedback of the input (see section 5.8);
- “20” for the sine feedback of the output (see section 5.8);
- “21” for the atan feedback of the output (see section 5.8);
- “22” for the tanh feedback of the output (see section 5.8);

The value of the tuning parameter ω should be provided in the following field:

```
<coeff name="TuningParameter" type="real" value="0.6" />
```

Note that the nonlinear feedback and decoration filtering strategies are normally used for the course control to reduce the rudder fluctuations.

10.2.3 Controller parameters

10.2.3.1 PID controller

If the PID controller is selected, then the field of controller type should be written as “0”.

```
<coeff name="ControllerType" type="integer" value="0" />
```

The constant values of the PID gains should be given in the following fields:

```
<coeff name="COURSECONTROL_P" unit="-" type="real" value="3.6171"
comment="proportionele roeractie t.g.v. een afwijking t.o.v. de gewenste
koers"></coeff>
```

<coeff name="COURSECONTROL_I" unit="1/s" type="real" value="0.0303" comment="roeractie t.g.v. een cumulatieve afwijking t.o.v. de gewenste koers - 0.0079"></coeff>

<coeff name="COURSECONTROL_D" unit="s" type="real" value="30.0918" comment="roeractie t.g.v. een afwijkende giersnelheid"></coeff>

The PID controller gains K_p , K_i , and K_d can be calculated according to the method proposed by Fossen (2011) (see section 5.2.3), retrievable at section 12.2.3 in the Handbook of marine craft hydrodynamics and motion control (Fossen, 2011).

The above described control method express their PID parameters of a function of the gain K and the time constant T , as stated before the determination of K and T is crucial. They can be determined based on the step test (see section 5.2.2.1) or the zigzag test (see section 5.2.2.2). Mind that a step test is possibly executed in the towing tank and the simulator, however, it is dangerous to conduct the step test in FHR towing tank due to the limited width of tank. Hence, the zigzag test is a better choice.

For towing tank tests at FHR, a $10^\circ/2.5^\circ$ or $20^\circ/5^\circ$ zigzag manoeuvre can be executed due to the limitation of size and vicinity of the tank walls in the test facility. In comparison, the $20^\circ/5^\circ$ zigzag test is recommended because it can provide more accurate information to obtain K and T . For simulation studies, the standard $20^\circ/20^\circ$ zigzag manoeuvre can be used. From zigzag tests, one can obtain the time, yaw rate and rudder deflection data, etc. A regression method is then used to determine K and T based on the following equation:

$$T\dot{r} + r = K\delta \tag{10.2}$$

The regression method can be a simple least squares algorithm (see section 3.3.2) or intelligent identification method (see section 3.3.4), etc. Finally, the PID controller parameters can be determined by Eqs. (5.10)-(5.12). Table 10.2 shows the procedure for the determination of PID parameters based on the Fossen (2011) method.

Table 10.2 Procedure for the determination of PID parameters based on Fossen (2011) method.

1. Determine the gain K and the time constant T of Nomoto model;
2. Specify the bandwidth $w_b > 0$ and the relative damping ratio $\zeta > 0$;
3. Compute the natural frequency: $w_n = \frac{1}{\sqrt{1-2\zeta^2 + \sqrt{4\zeta^4 - 4\zeta^2 + 2}}} w_b$;
4. Compute the P gain: $K_p = \frac{\omega_n^2 T}{K} > 0$;
5. Compute the I gain: $K_i = \frac{\omega_n^3 T}{10K} > 0$;
6. Compute the D gain: $K_d = \frac{2\zeta\omega_n T - 1}{K} > 0$.

The PID parameters can be also determined based on the IMC algorithm (section 5.3, Eqs. (5.20)-(5.22)). Except for the time constant T and the gain K , one more parameter β_c need to be tuned. For towing tank tests, the parameter β_c was determined by testing different options, and the value of β_c that led to satisfactory results was directly used in experiments to further examine its applicability. According to experimental results, a tuning parameter on model scale $1 \leq \beta_c \leq 10$ was used. For simulation studies, the β_c should be transferred to a value on full scale:

$$\beta_{cF} = \sqrt{\lambda} \beta_{cM} \quad (10.3)$$

where β_{cF} and β_{cM} represent the designed parameter β_c on full scale and model scale, respectively; λ refers to the scale ratio. Table 10.3 presents the procedure for the determination of PID parameters based on the IMC algorithm.

Table 10.3 Procedure for the determination of PID parameters based on the IMC algorithm.

-
1. Determine the gain K and the time constant T of Nomoto model;
 2. Specify the designed parameter β_c ;
 3. Compute the P gain: $K_p = \frac{(8/3)\beta_c + T}{3\beta_c^2 K}$;
 4. Compute the I gain: $K_i = \frac{1}{3\beta_c^2 K}$;
 5. Compute the D gain: $K_d = \frac{(8/3)\beta_c T - (8/9)\beta_c^2}{3\beta_c^2 K}$.
-

10.2.3.2 Propeller adaptive PID controller

If the adaptive PID controller is selected, then the field of controller type should be written as "10".

```
<coeff name="ControllerType" type="integer" value="10" />
```

The adaptive coefficients for the PID controller should be provided in the following fields:

```
<coeff name="COURSECONTROL_P" unit="-" type="real" value="3.6375"
comment="proportionele roeractie t.g.v. een afwijking t.o.v. de gewenste
koers"></coeff>
```

```
<coeff name="COURSECONTROL_I" unit="1/s" type="real" value="0.0295"
comment="roeractie t.g.v. een cumulatieve afwijking t.o.v. de gewenste koers -
0.0079"></coeff>
```

```
<coeff name="COURSECONTROL_D" unit="s" type="real" value="25.7020"
comment="roeractie t.g.v. een afwijkende giersnelheid"></coeff>
```

In this case the fields represent the following:

- *COURSECONTROL_P*: the appropriate coefficient K_{pn} so that $K_p = K_{pn}n^0$;
- *COURSECONTROL_I*: the appropriate coefficient K_{in} so that $K_i = K_{in}n^1$;
- *COURSECONTROL_D*: the appropriate coefficient K_{dn} so that $K_d = K_{dn}n^{-1}$;

where K_{pn} , K_{in} and K_{dn} are propeller adaptive PID coefficients, n is the propeller rate.

Table 10.4 Procedure for the determination of propeller adaptive PID parameters based on the IMC algorithm.

1. Determine the gain K and the time constant T of Nomoto model;
2. Specify the designed parameter β_c ;
3. Compute the P gain at a certain propeller rate: $K_p = \frac{(8/3)\beta_c T}{3\beta_c^2 K}$;
4. Compute the I gain at a certain propeller rate: $K_i = \frac{1}{3\beta_c^2 K}$;
5. Compute the D gain at a certain propeller rate: $K_d = \frac{(8/3)\beta_c T - (8/9)\beta_c^2}{3\beta_c^2 K}$;
6. Compute the propeller adaptive P gain: K_{pn} ;
7. Compute the propeller adaptive I gain: K_{in} ;
8. Compute the propeller adaptive D gain: K_{dn} .

For illustration purposes, an example to determine the adaptive PID controller parameters in the simulation studies is presented as follows:

1. Conduct the acceleration test to determine the relationship between propeller rates and forward speeds. Table 10.5 and Figure 10.1 show the relationship between propeller rates and forward speeds in 20% UKC.

Table 10.5 Relationship between propeller rates and forward speeds in 20% UKC.

Propeller rate (rps)	0.4602	0.6903	0.9203	1.1504
Speed (knots)	4	6	8	10

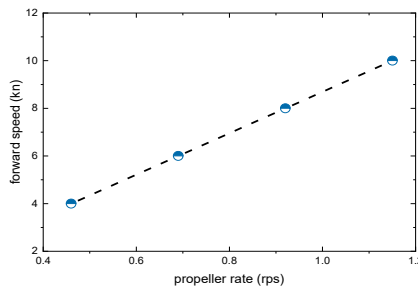


Figure 10.1 Relationship between propeller rate and speed in 20% UKC.

2. Perform zigzag (e.g. 20°/20°) manoeuvre simulations and use system identification method to obtain the gain K and the time constant T . Table 10.6 gives the results of K and T at different forward speeds (propeller rates).

Table 10.6 The values of K and T of Nomoto model at different forward speeds.

Propeller rate (rps)	0.4602	0.6903	0.9203	1.1504
Speed (knots)	4	6	8	10
K (s^{-1})	0.0051	0.0075	0.0100	0.0124
T (s)	69.3895	45.5552	33.8012	26.8249

3. Compute the PID gains at a certain speed: tune the parameter β_c , and calculate K_p , K_i and K_d at the defined speed according to the following equations:

$$K_p = \frac{(8/3)\beta_c T}{3\beta_c^2 K} \quad (10.4)$$

$$K_i = \frac{1}{3\beta_c^2 K} \quad (10.5)$$

$$K_d = \frac{(8/3)\beta_c T - (8/9)\beta_c^2}{3\beta_c^2 K} \quad (10.6)$$

Taken the results at speed of 8 knots (0.9203 rps) as an example, $\beta_c=1.54$, $K=0.01s^{-1}$, $T=33.8012$ s, then $K_p=12.9994$, $K_i=0.1874 s^{-1}$, $K_d=195.6533$ s.

4. Compute the propeller adaptive PID gains K_{pn} , K_{in} and K_{dn} :

$$K_{pn} = K_p = 12.9994 \quad (10.7)$$

$$K_{in} = K_i/n = 0.1874/0.9203 = 0.2036 \quad (10.8)$$

$$K_{dn} = K_d n = 195.6533 * 0.9203 = 180.0597 \quad (10.9)$$

Based on the relationship $K_p = K_{pn}$, $K_i = K_{in} n^1$, $K_d = K_{dn} n^{-1}$, the PID gains at other speeds (propeller rates) can be derived according to the relationship between the propeller rate and the controller parameters.

In autopilot file, one can directly fill in the propeller adaptive PID gains K_{pn} , K_{in} and K_{dn} in following fields:

```
<coeff name="COURSECONTROL_P" unit="-" type="real" value="12.9994"
comment="proportionele roeractie t.g.v. een afwijking t.o.v. de gewenste
koers"></coeff>
```

```
<coeff name="COURSECONTROL_I" unit="1/s" type="real" value="0.2036"
comment="roeractie t.g.v. een cumulatieve afwijking t.o.v. de gewenste koers -
0.0079"></coeff>
```

```
<coeff name="COURSECONTROL_D" unit="s" type="real"
value="180.0597" comment="roeractie t.g.v. een afwijkende
giersnelheid"></coeff>
```

10.2.3.3 Fuzzy controller

For direct fuzzy controller (section 5.5) the following information should be given:

- If the fuzzy controller is selected, then the field of controller type should be written as “30”.

```
<coeff name="ControllerType" type="integer" value="30" />
```
- The type of membership function should be also provided in the following field:

```
<coeff name="FuzzyMembership" type="integer" value="1" />
```

 - “1” for the triangular membership function;
 - “2” for the trapezoidal membership function;
 - “3” for the gaussian membership function.
- The field

```
<coeff name="MaxMainError" type="real" value="0.157" />
```

 represents the maximum heading angle deviation in radians which can be expected. The present example corresponds to an input scaling factor:

$$K_e = \frac{PB=3}{0.157} \approx 19.1 \quad (10.10)$$

The range of maximum heading deviation is around 8-10 deg or 0.140-0.174 rad.

- The field

```
<coeff name="MaxDerivedError" type="real" value="0.07" />
```

 represents the maximum change in time of heading angle deviation in radians/s which can be expected. The present example corresponds to an input scaling factor:

$$K_c = \frac{PB=3}{0.07} \approx 42.8 \quad (10.11)$$

The range of maximum deviation in heading velocity is around 4-5 deg/s or 0.07-0.087 rad/s.

10.2.3.4 Fuzzy PID controller

If the fuzzy PID controller is selected, then the field of controller type should be written as “20”.

```
<coeff name="ControllerType" type="integer" value="20" />
```

For fuzzy PID controller, the same information as fuzzy controller needs to be provided. On top of that the following information should be given:

- The maximum change for K_p per step needs to be provided in

```
<coeff name="MaxPvariation" type="real" value="0.1" />
```

. In the present example “0.1” is used, which corresponds to an output scaling factor:

$$K_{u_p} = \frac{0.1}{PB=3} \approx 0.03 \quad (10.12)$$

- The maximum change for K_i per step needs to be provided in `<coeff name="MaxIvariation" type="real" value="0.001" />`. In the present example “0.001” is used, which corresponds to an output scaling factor:

$$K_{u_i} = \frac{0.001}{PB=3} \approx 3.33e^{-4} \quad (10.13)$$

- The maximum change for K_d per step needs to be provided in `<coeff name="MaxDvariation" type="real" value="1" />`. In the present example “1” is used, which corresponds to an output scaling factor:

$$K_{u_d} = \frac{1}{PB=3} \approx 0.33 \quad (10.14)$$

10.2.4 Configuration of speed controller

A Proportional Integral (PI) speed controller has already implemented in the simulator, its parameters can be set in the autopilot file. Before using the speed controller, the position (m) and the desired speed (m/s) at the position should be given in the following fields:

```
<col name="auto_positie" type="real" unit="m" comment="positie op m waarop
snelheid gewenst is" />
```

```
<col name="auto_snelheid" type="real" unit="m/s" comment="gewenste
snelheid in m/s op positie" />
```

```
<row>1; 2000 ; 4.2860</row>
```

```
<row>2; 4000 ; 4.2860</row>
```

For the speed controller, the following information is required:

- One can select whether (or not) use the speed controller in the field `<coeff name="SpeedControl" Type="integer" value="0" comment="0: nee; 1: ja" />` with:
 - “0” represents that the speed controller will not be used during simulation runs, only the constant propeller rate will be used.
 - “1” represents that the speed controller will be used during simulation runs.
- In the simulator, the PI speed controller is used and formulated as:

$$\Delta n = K_{pu} \Delta u + K_{iu} \int \Delta u \quad (10.15)$$

where Δn represents the induced propeller rate increase needed to counteract the surge velocity error Δu , K_{pu} and K_{iu} are the P and I gains of the PI speed controller.

- In the autopilot file, the field `<coeff name="Psnelheid" Type="real" value="4.4719" />` represents K_{pu} gain of the PI speed controller.
- The field `<coeff name="Isnelheid" Type="real" value="0.5" />` represents K_{iu} gain of the PI speed controller.
- The relationship between the propeller rate (rps) and the forward speed (m/s) needs to be given in `<coeff name="Zelfpropulsie" Type="real" value="4.4719" comment="waarde x rps = V in m/s" />`
- Trigger value of speed controller needs to be given in `<coeff name="Vtrigger" Type="real" value="0.05" />`. In present example, 0.05 (m/s) is used, which means that the speed controller will react when the speed difference is 0.05 m/s.
- The range of propeller rate limiter is specified as $[0.9n_{\text{expect}}, 1.1n_{\text{expect}}]$, see section 5.9 for better understanding. The values for setting the propeller rate limits need to be provided in:
`<coeff name="Nlimiter" Type="real" value="1.1" />`
`<coeff name="Nlimiterlow" Type="real" value="0.9" />`

To better illustrate how to set the speed controller, an example will be presented.

The first step is to conduct the acceleration tests (self-propulsion tests) in order to determine the relationship between the propeller rates and the forward speeds. The results for the studied LNG ship in 20%UKC is presented in Table 10.7 and Figure 10.2. It can be seen from Figure 10.2 the relationship between propeller rate and speed can be expressed as:

$$u = 4.4719n \quad (10.16)$$

where u is the forward speed (m/s), and n is the propeller rate (rps).

Table 10.7 Relationship between the propeller rate and forward speed for the studied LNG ship at 20%UKC.

20%UKC, Acceleration test			
min propeller rate (rps)	0.380		
max propeller rate (rps)	1.517		
	Propeller rate(rps)	Speed(m/s)	Speed(knots)
Dead slow	0.380	1.66	3.23
Slow ahead	0.759	3.38	6.57
Half ahead	1.138	5.09	9.89
Full ahead	1.517	6.8	13.22

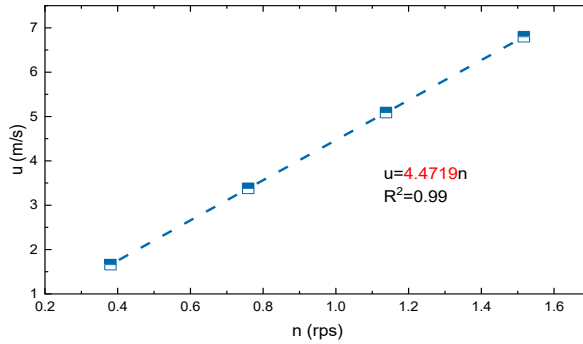


Figure 10.2 Relationship between the propeller rate and forward speed at 20%UKC for the studied LNG ship.

Define regression coefficient between propeller rate (rps) and speed (m/s) as α , in present example, $\alpha = 4.4719$. Then the parameters of speed controller can be set as:

- $P_{\text{snelheid}} = \frac{1}{\alpha}$;
- $I_{\text{snelheid}} = \frac{1}{10\alpha^2}$;
- $Z_{\text{elfpropulsie}} = \alpha$;
- $V_{\text{trigger}} = 0.001$;
- $N_{\text{limiter}} = 1.1$;
- $N_{\text{limiterlow}} = 0.9$;

Mind that the biggest impact on the performance of the speed controller was the parameter ‘Vtrigger’. After comparison analysis, the best selection of Vtrigger is 0.001m/s (1mm/s). If this value is too small, which cannot be detectable on full scale. Then, suboptimal selection is 0.01 m/s (1 cm/s).

10.3 Reference

Delefortrie, G., Eloot, K., and Mostaert, F. , 2020. *Ship manoeuvring behaviour subreport 13: execution of free running tests with the Q-flex (report)*.

Fossen, T. I. , 2011. *Handbook of marine craft hydrodynamics and motion control*. John Wiley & Sons Ltd. United Kingdom.

List of Figures

Figure 1.1 Real time simulator and fast time simulator.....	3
Figure 1.2 Example of the track controller performance on the Canal Ghent-Terneuzen in fast time simulator.	4
Figure 1.3 Application scenarios of maritime autonomous surface ships (MASS) (Tran et al., 2014).	5
Figure 1.4 Unmanned surface vessels (USVs): (a) Mariner USV (photo retrieved from https://www.maritimerobotics.com/mariner); (b) Oceanalpha M40 USV (photo retrieved from https://www.oceanalpha.com/product-item/m40/).	6
Figure 1.5 Rolls-Royce unmanned cargo ships (photo retrieved from https://www.rolls-royce.com/marine).	6
Figure 1.6 LNG terminal in port of Antwerp Bruges (photo retrieved from https://www.fluxys.com/en/products-services/activities/lng).	8
Figure 1.7 Signal and data transmission between the guidance, navigation, and control systems.	9
Figure 1.8 Outline of thesis.	13
Figure 2.1 Methods for determining the hydrodynamic coefficients of the ship manoeuvring mathematical models.	20
Figure 2.2 Historical development from the early autopilot to modern ship control systems.	23
Figure 2.3 Classification of ship motion controllers.	25
Figure 2.4 Illustration of 1-DOF manoeuvring: course keeping and changing.	26
Figure 2.5 Illustration of path following and trajectory tracking control.	26
Figure 2.6 Structure of the ship path following control system.	29
Figure 2.7 Global path planning from a port of Norway to a port of Belgium.	30
Figure 2.8 Local path planning from a port of Norway to a port of Belgium.	31
Figure 2.9 Illustration of line-of-sight (LOS) guidance system.	32
Figure 2.10 Illustration of the vector field guidance for straight-line and circular path following (Nelson et al., 2007).	33
Figure 2.11 General framework of dynamic virtual ship (DVS) guidance principle (Zhang and Zhang, 2015).	34
Figure 3.1 Notation and sign conventions for ship motion description.	60
Figure 3.2 Coordinate systems: earth-centered inertial (ECI) coordinate system $O_{exeyeze}$; earth-bound coordinate system $O_0x_0y_0z_0$; body-bound coordinate system $Oxyz$	60
Figure 3.3 Ship bound and earth bound coordinate systems in 6 DOF: projections on the x_0y_0 -plane, y_0z_0 -plane and x_0z_0 -plane.	61
Figure 3.4 Nonlinear least squares (NLS) system identification method.	73
Figure 3.5 Fitting least squares (FLS) system identification method.	73
Figure 3.6 Beetle Antennae Search (BAS) optimization trajectory: d_i represents the distance between two antennae; l_i is the iterative step length.	77

Figure 3.7 The flow chart of the NLSSVM-BAS model.	79
Figure 3.8 Cross-sectional view of the Ultra Large Container Vessel (ULCV).	81
Figure 3.9 Model test setup and mechanism of free decay tests.	82
Figure 3.10 The initial roll angles at different speeds for 10%UKC (blue line), 20%UKC (red line), 35%UKC (black line), 190%UKC (orange line).	82
Figure 3.11 Identification process of NLSSVM for the roll model.	83
Figure 3.12 Train and test roll angles with known damping coefficients using NLSSVM method at 190% UKC.	84
Figure 3.13 Predicted roll angles and errors with known damping coefficients using NLSSVM method at 190% UKC.	85
Figure 3.14 Nonlinear Least Squares (NLS) identification method for the roll model.	85
Figure 3.15 Fitting Least Squares (FLS) identification method for the roll model.	85
Figure 3.16 Predicted roll angles using NLS, FLS, NLSSVM approaches.	87
Figure 3.17 Predicted roll angle errors using NLS, FLS, NLSSVM approaches.	87
Figure 3.18 Predicted roll angles and errors for 10% UKC.	88
Figure 3.19 Predicted roll angles and errors for 20% UKC.	89
Figure 3.20 Predicted roll angles and errors for 35% UKC.	89
Figure 3.21 Predicted roll angles and errors for 190% UKC.	90
Figure 3.22 Predicted roll angles and errors at 0 knots.	91
Figure 3.23 Predicted roll angles and errors at 6 knots.	91
Figure 3.24 Predicted roll angles and errors at 12 knots.	92
Figure 3.25 Optimisation trajectories of the beetle searching in 2D space.	94
Figure 3.26 Optimisation trajectories of the beetle searching in 3D space.	94
Figure 3.27 Convergence curve of parametric optimisation.	94
Figure 3.28 Predicted yaw rates and errors with pre-defined parameters using simulation data.	95
Figure 3.29 Predicted yaw rates of the NLSSVM model optimised by the BAS, CV and PSO.	97
Figure 3.30 Yaw rate errors of the NLSSVM model optimised by the BAS, CV and PSO.	97
Figure 3.31 Identification results for the time constant T and its relative errors in different noise levels.	98
Figure 3.32 Identification results for the gain K and its relative errors in different noise levels.	99
Figure 3.33 Identification results for the nonlinear constant a and its relative errors in different noise levels.	99
Figure 4.1 Schematic of path planning, guidance, navigation, and control system.	104
Figure 4.2 Plan a desired path by the manual approach.	105
Figure 4.3 Grid point (x, y) and its neighbors.	106
Figure 4.4 Updating process of fast marching method (FMM).	109
Figure 4.5 Arrival time (T) calculated by fast marching method (FMM) in two grid maps: (a) arrival time in a 20×20 grid map (2D); (b) arrival time in a 20×20 grid map (3D); (c) arrival time in a 60×60 grid map (2D); (d) arrival time in a 60×60 grid map (3D).	110

Figure 4.6 Fast marching method (FMM) for path planning: (a) grid map; (b) output of the FMM, arrival time matrix (T); (c) arrival time potential field and planned path; (d) 3D plot for arrival time matrix (T).	111
Figure 4.7 Fast marching square (FMS) method for path planning: (a) grid map and planned path; (b) velocity map and planned path; (c) arrival time matrix (T) and planned path; (d) 3D plot for arrival time matrix (T).	112
Figure 4.8 Comparison between the FMM method and the FMS method for path planning.	113
Figure 4.9 Tuned Fast marching square (TFMS) method for path planning with different saturations. (1) <i>Safety potential map</i> : (a) saturation 0.2; (b) saturation 0.4; (c) saturation 0.6; (d) saturation 0.8; (2) <i>Arrival time matrix</i> : (e) saturation 0.2; (f) saturation 0.4; (g) saturation 0.6; (h) saturation 0.8.	114
Figure 4.10 Illustration of guidance range.	115
Figure 4.11 Comparison of TFMS and ATFMS methods for path planning. ...	115
Figure 4.12 Application of ATFMS method to plan a desired path in towing tank environment (a) grid map, (b) velocity map, (c) time map, (d) planned path. ...	116
Figure 4.13 The principle of the Line-Of-Sight (LOS) guidance method.	117
Figure 4.14 A ship converging to a collinear straight-line using the LOS guidance approach ($AP_k > R_k$).	119
Figure 4.15 A ship converging to a collinear straight-line using LOS guidance approach ($AP_k \leq R_k$).	119
Figure 4.16 Navigation system of experimental ship model.	121
Figure 4.17 Navigation system of experimental ship model (sketch).	122
Figure 5.1 Structure of PID controller.	127
Figure 5.2 Matlab Simulink design for PID controller.	128
Figure 5.3 Determination of K and T based on a step test ($\delta s=10$ deg) at 8 knots and 100% UKC.	129
Figure 5.4 $20^\circ/5^\circ$ zigzag manoeuvre experiment at speed of 8 knots and 100% UKC.	130
Figure 5.5 Internal model controller structure.	131
Figure 5.6 Simplified internal model controller structure: (a) classical feedback form; (b) transfer function form.	131
Figure 5.7 Propeller rate versus PID controller coefficients at 100% UKC. ...	134
Figure 5.8 Overview of the fuzzy controller.	136
Figure 5.9 Matlab Simulink design for fuzzy controller.	136
Figure 5.10 Triangle membership function of the fuzzy controller.	137
Figure 5.11 Trapezoidal membership function of the fuzzy controller.	137
Figure 5.12 Gaussian membership function of the fuzzy controller.	138
Figure 5.13 Fuzzy inference system.	139
Figure 5.14 Structure of Fuzzy-PID controller.	140
Figure 5.15 Matlab Simulink design for fuzzy PID controller.	140
Figure 5.16 Fuzzy inference for ΔKP	142
Figure 5.17 Fuzzy inference for ΔKI	142
Figure 5.18 Fuzzy inference for ΔKD	142
Figure 5.19 Structure of backstepping controller.	144
Figure 5.20 Standard feedback control (a); Nonlinear feedback control (b). ...	148
Figure 5.21 Standard PID controller and nonlinear feedback PID controller. .	149

Figure 5.22 Structure of nonlinear decoration design: (a) standard controller; (b) controller with nonlinear decorator.	150
Figure 5.23 Standard PID controller (a) and nonlinear decoration PID controller (b).	150
Figure 5.24 Controller performance evaluation procedure.	153
Figure 6.1 Bird's eye view of towing tank for Manoeuvres in Confined Water.	160
Figure 6.2 Motion mechanism of towing tank carriage.	161
Figure 6.3 The Q-Flex LNG carrier scale model.	162
Figure 6.4 Twin propeller and twin rudder installed on the scale model.	163
Figure 6.5 Scale model setup during captive model tests: beam frame and instrumentation arrangement.	164
Figure 6.6 Ship model setup during free running tests: (a) beam frame and instrumentation arrangement. (b) clamping mechanism.	166
Figure 6.7 Towing tank main dimensions and its coordinate systems.	167
Figure 6.8 Body-fixed coordinate system of ship model.	167
Figure 6.9 Under keel clearances (UKCs) versus water depths of tests: (a) model scale; (b) full scale.	168
Figure 6.10 Sample photos for different experimental water depths (back view).	169
Figure 6.11 Sample photos for different experimental water depths (side view).	169
Figure 6.12 Number of model tests for each water depth to draft ratio (hTM).	170
Figure 6.13 Test speeds (model scale) at different water depths.	171
Figure 6.14 Zeeman post processing software.	174
Figure 6.15 Regstatx software for free running test analysis.	174
Figure 6.16 Visualize the postprocessing results in the Regstatx software.	175
Figure 6.17 Relationship between the propeller rates and the forward speeds at different water depths (UKCs).	177
Figure 6.18 The effects of water depths on the propeller rates at same speed.	178
Figure 6.19 $\pm 10^\circ/2.5^\circ$ zigzag manoeuvres at 8 knots and 35% UKC.	179
Figure 6.20 $\pm 20^\circ/5^\circ$ zigzag manoeuvres at 8 knots and 35% UKC.	179
Figure 6.21 Trajectories of $20^\circ/5^\circ$ zigzag tests at 10%, 20%, 35% and 100% UKCs for the speed of 8 knots.	180
Figure 6.22 Time histories of heading angle (Ψ), yaw rate (r), drift angle (β), rudder angle (δ), forward speed (u), sinkage (z) of $20^\circ/5^\circ$ zigzag manoeuvres in different water depths for the speed of 8 knots.	181
Figure 6.23 Phase diagram yaw rate (r) over rudder angle (δ) and heading angle (Ψ) of $20^\circ/5^\circ$ zigzag manoeuvres in different water depths for the speed of 8 knots.	182
Figure 6.24 Initial conditions for course keeping (a) and course changing (b).	183
Figure 6.25 Course keeping test with constant speed at 8 knots (0.4752 m/s) and 35% UKC.	184
Figure 6.26 Course keeping test with acceleration from 0 to 11 knots (0.6534 m/s) at 35% UKC.	184
Figure 6.27 Course keeping test with deceleration from 11 knots (0.6534 m/s) to 8 knots (0.4752 m/s) at 35% UKC.	185

Figure 6.28 Course changing test at 8 knots and 35% UKC..... 186

Figure 6.29 Pre-planned paths and their waypoints: straight line (orange); path with obstacles (blue); step line (green); folding line (red)..... 187

Figure 6.30 Planned curved path with four virtual obstacles..... 187

Figure 6.31 PID controller performance at 11 knots and 20% UKC: (a) desired and measured trajectories; (b) cross track error; (c) heading angle error; (d) longitudinal position error; (e) rudder angle; (f) lateral position error. 189

Figure 6.32 IMC controller performance at 11 knots and 20% UKC: (a) desired and measured trajectories; (b) cross track error; (c) heading angle error; (d) longitudinal position error; (e) rudder angle; (f) lateral position error. 189

Figure 6.33 Fuzzy controller performance at 11 knots and 20% UKC: (a) desired and measured trajectories; (b) cross track error; (c) heading angle error; (d) longitudinal position error; (e) rudder angle; (f) lateral position error. 190

Figure 6.34 Adaptive PID controller performance at 11 knots and 20% UKC: (a) desired and measured trajectories; (b) cross track error; (c) heading angle error; (d) longitudinal position error; (e) rudder angle; (f) lateral position error..... 190

Figure 6.35 Comparison results for the trajectory error at 11 knots and 20% UKC: (a) reference and measured trajectories; (b) cross track error; (c) position error histogram of PID controller; (d) position error histogram of IMC controller; (e) position error histogram of fuzzy controller; (f) position error histogram of adaptive PID controller..... 191

Figure 6.36 Comparison results for the heading angle error at 11 knots and 20% UKC. 192

Figure 6.37 Comparison results for the rudder angle at 11 knots and 20% UKC. 192

Figure 6.38 PID controller performance at 8 knots and 20% UKC: (a) desired and measured trajectories; (b) cross track error; (c) heading angle error; (d) longitudinal position error; (e) rudder angle; (f) lateral position error. 195

Figure 6.39 IMC controller performance at 8 knots and 20% UKC: (a) desired and measured trajectories; (b) cross track error; (c) heading angle error; (d) longitudinal position error; (e) rudder angle; (f) lateral position error. 195

Figure 6.40 Fuzzy controller performance at 8 knots and 20% UKC: (a) desired and measured trajectories; (b) cross track error; (c) heading angle error; (d) longitudinal position error; (e) rudder angle; (f) lateral position error. 195

Figure 6.41 Adaptive PID controller performance at 8 knots and 20% UKC: (a) desired and measured trajectories; (b) cross track error; (c) heading angle error; (d) longitudinal position error; (e) rudder angle; (f) lateral position error..... 196

Figure 6.42 Comparison results for the cross track error at 8 knots and 20% UKC. 196

Figure 6.43 Comparison results for the heading angle error at 8 knots and 20% UKC. 197

Figure 6.44 Comparison results for the rudder angle at 8 knots and 20% UKC. 197

Figure 6.45 PID controller performance for following a path with four obstacles at 8 knots and 20% UKC..... 198

Figure 6.46 IMC controller performance for following a path with four obstacles at 8 knots and 20% UKC..... 198

Figure 6.47 Fuzzy controller performance for following a path with four obstacles at 8 knots and 20% UKC.....	198
Figure 6.48 Adaptive PID controller performance for following a path with four obstacles at 8 knots and 20% UKC.	199
Figure 6.49 Controller performance at 11 knots and 20% UKC: (a) PID controller; (b) IMC controller; (c) Fuzzy controller; (d) Adaptive PID controller.	199
Figure 6.50 Comparison results at 11 knots and 20% UKC: (a) cross track error; (b) heading angle error; (c) rudder angle.....	200
Figure 6.51 Frequencies for each controller obtaining the best performance at all test conditions.....	201
Figure 6.52 The tendency of the Nomoto model parameters T and K with different water depth at 4 knots forward speed.	203
Figure 6.53 The tendency of the Nomoto model parameters T and K with different water depth at 6 knots forward speed.	204
Figure 6.54 The tendency of the Nomoto model parameters T and K with different water depth at 8 knots forward speed.	204
Figure 6.55 The tendency of the Nomoto model parameters T and K with different forward speed at 100% UKC.	205
Figure 6.56 The tendency of the Nomoto model parameters T and K with different forward speed at 35% UKC.	206
Figure 6.57 The tendency of the Nomoto model parameters T and K with different forward speed at 20% UKC.....	206
Figure 6.58 The tendency of the Nomoto model parameters T and K with different forward speed at 10% UKC.....	207
Figure 6.59 Relationship between the PID coefficients and water depths (hTM) for the speed of 4, 6 and 8 knots.....	208
Figure 6.60 Relationship between the proportional coefficient Kp and propeller rate n at 10%, 20%, 35%, and 100% UKCs.....	210
Figure 6.61 Relationship between the integral coefficient Ki and propeller rate n at 10%, 20%, 35%, and 100% UKCs.	210
Figure 6.62 Relationship between the derivative coefficient Kd and propeller rate n at 10%, 20%, 35%, and 100% UKCs.....	211
Figure 6.63 Trajectories obtained by the adaptive PID controller in different water depths at 8 knots.....	212
Figure 6.64 Adaptive PID controller performance in different water depths at 8 knots: (a) desired and measured trajectories; (b) cross track error; (c) rudder angle.	213
Figure 6.65 Trajectories obtained by the IMC controller in different water depths at 8 knots.	213
Figure 6.66 IMC controller performance in different water depths at 8 knots: (a) desired and measured trajectories; (b) cross track error; (c) rudder angle.....	214
Figure 6.67 Evaluation indexes of adaptive PID and IMC controllers in different water depths at 8 knots.	215
Figure 6.68 Adaptive PID controller performance in different water depths at 11 knots: (a) desired and measured trajectories; (b) cross track error; (c) heading angle error; (d) rudder angle.	215

Figure 6.69 IMC controller performance in different water depths at 11 knots: (a) desired and measured trajectories; (b) cross track error; (c) heading angle error; (d) rudder angle.	216
Figure 6.70 Evaluation indexes of adaptive PID and IMC controllers in different water depths at 11 knots.	216
Figure 6.71 Adaptive PID controller's performance using the constant and optimized parameters in different water depths at 8 knots.	218
Figure 6.72 Adaptive PID controller's performance using the constant and optimized parameters in different water depths at 11 knots.	218
Figure 6.73 IMC controller's performance using the constant and optimized parameters in different water depths at 8 knots.	219
Figure 6.74 IMC controller's performance using the constant and optimized parameters in different water depths at 11 knots.	220
Figure 6.75 Trajectories obtained by simulations using the experimental and adaptive parameters at 6 knots and 35% UKC.	221
Figure 6.76 Control effects using the experimental and adaptive parameters at 6 knots and 35% UKC.	222
Figure 6.77 Trajectory obtained by simulation using the adaptive parameters at 6 knots and 50% UKC.	222
Figure 7.1 Full-mission bridge simulator (real-time simulator) at Flanders Hydraulics Research (FHR) and its typical application scenarios.	225
Figure 7.2 Numerical simulation study platforms: real-time simulator and fast-time simulator.	227
Figure 7.3 Principle of prescience model based track controller in the fast-time simulator (Vantorre et al., 1997).	229
Figure 7.4 Cost function of mathematical pilot model (Vantorre et al., 1997).	229
Figure 7.5 Signal flow of the proposed motion control system.	230
Figure 7.6 3D view of the LNG ship: (a) ship's particulars; (b) side view; (c) bow view; (d) top view.	231
Figure 7.7 Comparison of the simulated (Sim.) and experimental (Exp.) 20°/5° zigzag manoeuvre at 11 knots and 20%UKC.	231
Figure 7.8 Statistics of the simulated and experimental 20°/5° zigzag in medium and shallow water.	232
Figure 7.9 Reference and simulated trajectories by the adaptive PID, fuzzy and IMC controllers at 8 knots and 20% UKC.	234
Figure 7.10 Motion responses of ship: (a) cross track error; (b) rudder angle; (c) heading deviation at 8 knots and 20% UKC.	234
Figure 7.11 Reference and simulated trajectories by the adaptive PID, fuzzy and IMC controllers at 8 knots and 20% UKC.	235
Figure 7.12 Motion responses of ship at 8 knots and 20% UKC: (a) cross track error; (b) rudder angle; (c) heading deviation.	235
Figure 7.13 Comparison of numerical and experimental performance of adaptive PID controller for fold line path: (a) trajectories; (b) cross track error; (c) rudder angle; (d) heading angle.	236
Figure 7.14 Comparison of numerical and experimental performance of fuzzy controller for fold line path: (a) trajectories; (b) cross track error; (c) rudder angle; (d) heading angle.	237

Figure 7.15 Comparison of numerical and experimental performance of IMC controller for fold line path: (a) trajectories; (b) cross track error; (c) rudder angle; (d) heading angle.	237
Figure 7.16 Statistics of numerical and experimental results for folding line path.	238
Figure 7.17 Comparison of numerical and experimental performance of adaptive PID controller for curved path: (a) trajectories; (b) cross track error; (c) rudder deflection; (d) heading angle.	239
Figure 7.18 Comparison of numerical and experimental performance of fuzzy controller for curved path: (a) trajectories; (b) cross track error; (c) rudder deflection; (d) heading angle.	239
Figure 7.19 Comparison of numerical and experimental performance of IMC controller for curved path: (a) trajectories; (b) cross track error; (c) rudder deflection; (d) heading angle.	240
Figure 7.20 Statistics of numerical and experimental simulation results for curved path.	241
Figure 7.21 Comparison of numerical and experimental performance of the adaptive PID controller for curved path at different UKCs: (a) 10% UKC; (b) 20% UKC; (c) 35% UKC; (d) 100% UKC.	242
Figure 7.22 Statistics of numerical and experimental results of the adaptive PID controller for curved path at different UKCs.	242
Figure 7.23 Location of the Panama Canal (©Google Maps).	243
Figure 7.24 Panama Canal from Gatún Lake (left) to the Pacific locks.	243
Figure 7.25 Simplified cross section with slopes of 56° on both sides and a width on full depth of 218 m, and a ship with $B \times TM$ of 50 x 12.0 m ²	244
Figure 7.26 Tracking capability of adaptive PID, fuzzy and IMC controllers for simulation in the Panama Canal.	245
Figure 7.27 Tracking capability of adaptive PID controller for simulation in the Panama Canal.	245
Figure 7.28 Motion response of the adaptive PID, fuzzy and IMC controllers in a real canal: (a) cross track error; (b) rudder angle.	246
Figure 7.29 Positions of ship at different distances to bank (or buoy line).	247
Figure 7.30 Performance of the adaptive PID controller with and without considering bank effects when the ship sailed in the middle of canal (case 1): (a) trajectories; (b) cross track error; (c) Y force from bank; (d) yaw moment from bank; (e) trajectories in the canal (overlap in this case).	248
Figure 7.31 Performance of the adaptive PID controller with and without considering bank effects when the ship sailed case 3 position in the canal: (a) trajectories; (b) cross track error; (c) Y force from bank; (d) yaw moment from bank; (e) trajectories in the canal.	249
Figure 7.32 Performance of the adaptive PID controller with and without considering bank effects when the ship sailed in the middle of canal (case 4): (a) trajectories; (b) cross track error; (c) Y force from bank; (d) yaw moment from bank; (e) trajectories in the canal.	250
Figure 7.33 Influence of bank effects on the adaptive PID controller's performance at 8 knots and 20% UKC.	251
Figure 7.34 Trajectories obtained by the adaptive PID controller with and without considering bank effects when the ship sailed in the entire canal.	251

Figure 7.35 Performance of the adaptive PID controller with and without considering bank effects when the ship sailed in the entire canal.	252
Figure 7.36 Trajectories obtained by the fuzzy controller with and without considering bank effects when the ship sailed in the entire canal.	252
Figure 7.37 Performance of the fuzzy controller with and without considering bank effects when the ship sailed in the entire canal.	253
Figure 7.38 Trajectories obtained by the IMC controller with and without considering bank effects when the ship sailed in the entire canal.	253
Figure 7.39 Performance of the IMC controller with and without considering bank effects when the ship sailed in the entire canal.	254
Figure 7.40 Trajectories obtained by the adaptive PID controller with (a) and without (b) speed controller when the ship sailed in the entire canal.	254
Figure 7.41 Performance of the adaptive PID controller with and without speed controller when the ship sailed in the entire canal.	255
Figure 7.42 Trajectories obtained by the fuzzy controller with (a) and without (b) speed controller when the ship sailed in the entire canal.	255
Figure 7.43 Performance of the fuzzy controller with and without speed controller when the ship sailed in the entire canal.	256
Figure 7.44 Trajectories obtained by the IMC controller with (a) and without (b) speed controller when the ship sailed in the entire canal.	256
Figure 7.45 Performance of the IMC controller with and without speed controller when the ship sailed in the entire canal.	257
Figure 7.46 Location of the Western Scheldt.	258
Figure 7.47 Triangular mesh of the Western Scheldt.	258
Figure 7.48 3D views of the container ship.	259
Figure 7.49 Reference trajectory (blue) for inbound vessel defined at 1/3 rd of the dredged fairway width.	260
Figure 7.50 Track plots of a selection of AIS-voyages in the Western Scheldt from 1 st October 2018 to 1 st January 2020: 325 inbound container ships with a length larger than 350 m.	260
Figure 7.51 Reference forward speeds obtained from the AIS data of 325 container ships (<i>LOA</i> > 350 m) in the Western Scheldt from 1st October 2018 to 1st January 2020.	261
Figure 7.52 Reference trajectory (white) and trajectories obtained by PMTC (blue) and FuzzyTC (orange) under calm and deep water (60-70 km).	263
Figure 7.53 Cross track error of the midship position for PMTC and FuzzyTC (a); Box plots of cross track error for PMTC and FuzzyTC (b). The bottom and top of the box represent the 25th and 75th percentile; the band near the middle is the median value; the lower and upper whiskers represent the value of 25th percentile – 1.5 IQR (in this case it is the minimum value because there are no data lower than zero) and the value of 75th percentile + 1.5 IQR respectively; IQR, interquartile range (between 25th and 75th percentile); black triangle and rectangle represent the maximum and mean values respectively; red and blue dots are the cross track errors of PMTC and FuzzyTC respectively.	263
Figure 7.54 Control actions (rudder and propeller) of PMTC (a); Control actions of FuzzyTC (b).	264
Figure 7.55 Reference and actual forward speeds and speed errors. (a) reference and actual forward speed of PMTC; (b) reference and actual forward speed of	

FuzzyTC; (c) errors between reference and actual speeds of PMTC and FuzzyTC.	265
Figure 7.56 Tidal variation in <i>Vlissingen</i> , <i>Hansweert</i> and <i>Prosperpolder</i> for inbound simulations initiated from 01h10 to 14h00 on 9th March 2020.	266
Figure 7.57 Statistical results of Under Keel clearance (UKC) obtained based on the 78 tidal condition simulation runs.	266
Figure 7.58 Statistical results of (absolute) longitudinal and lateral currents obtained based on the 78 tidal condition simulation runs: (a) running distance versus longitudinal current; (b) running distance versus lateral current; (c) departure time of simulation versus longitudinal current (tidal evolution longitudinal current); (d) departure time of simulation versus lateral current (tidal evolution lateral current).	267
Figure 7.59 Reference trajectory (white) and trajectories obtained by PMTC (blue) and FuzzyTC (orange) under full tidal cycle (50 km and 65-70 km, departure time of simulation UTC 11:30).	268
Figure 7.60 Statistical results of cross track errors as function of running distance from 78 fast-time simulation runs for the whole trajectory (10 km to 80 km) and full tidal cycle (01h10 to 14h00).	269
Figure 7.61 Statistical results of cross track errors as function of time or tidal evolution from 78 fast-time simulation runs for the whole trajectory (10 km to 80 km) and full tidal cycle (01h10 to 14h00).	269
Figure 7.62 Statistical results of (absolute) rudder angle for PMTC and FuzzyTC obtained from the 78 tidal condition simulation runs: (a) running distance versus rudder (PMTC); (b) running distance versus rudder (FuzzyTC); (c) time versus tidal evolution rudder (PMTC); (d) time versus tidal evolution rudder (FuzzyTC).	270
Figure 7.63 Rudder application based on normalised absolute rudder angle for PMTC and FuzzyTC obtained from 78 fast-time simulation runs for the entire trajectory (10 km to 80 km) and full tidal cycle (01h10 to 14h00).	270
Figure 8.1 Main research content and results.	273
Figure 8.2 Experiment and simulation platforms.	276
Figure 10.1 Relationship between propeller rate and speed in 20% UKC.	294
Figure 10.2 Relationship between the propeller rate and forward speed at 20%UKC for the studied LNG ship.	299

List of Tables

Table 2.1 Classification of ship mathematical models based upon model formulation.	17
Table 2.2 Examples about the applications of different DOFs mathematical models for the development of ship motion controllers.	19
Table 2.3 Classification of controllers according to the control missions.	26
Table 2.4 Summary of the control approaches with experimental investigation.	35
Table 3.1 Notation and sign conventions for ship motion.	59
Table 3.2 Main particulars of model scale and full scale for the Ultra Large Container Vessel (ULCV).	81
Table 3.3 Initial roll angles at different speeds and UKCs.	82
Table 3.4 Identification processes of the NLSSVM algorithm for the roll model.	83
Table 3.5 Known parameters and identified parameters using the NLSSVM approach.	84
Table 3.6 Comparisons of identification results among NLS, FLS and NLSSVM identification methods.	86
Table 3.7 Comparisons identification results for different UKCs at a speed of 6 knots.	88
Table 3.8 Comparisons identification results for different speeds (20% UKC).	90
Table 3.9 Pre-defined parameters and identified parameters using the NLSSVM-BAS model.	95
Table 3.10 Comparison results among different optimisation methods.	96
Table 3.11 Comparison of the identified time constant T , gain K and nonlinear constant a by the BAS method after adding different Gaussian white noises. ...	98
Table 4.1 FMM algorithm for planning a desired path.	110
Table 4.2 FMS algorithm for planning a desired path.	111
Table 4.3 TFMS algorithm for planning a desired path.	113
Table 4.4 ATFMS algorithm for planning a desired path.	114
Table 5.1 Propeller rate versus PID controller coefficients at 100% UKC.	134
Table 5.2 Fuzzy rule matrix.	138
Table 5.3 Fuzzy rules for ΔKP	141
Table 5.4 Fuzzy rules for ΔKI	141
Table 5.5 Fuzzy rules for ΔKD	141
Table 6.1 Main dimensions of towing tank for Manoeuvres in Confined Water.	160
Table 6.2 Range of positions, velocities, and accelerations of towing tank motion mechanism at FHR.	161
Table 6.3 Main particulars on model and full scale of the Q-Flex LNG carrier (1/75).	162

Table 6.4 Propeller and rudder characteristics (model scale).	163
Table 6.5 Water depths of tests on model scale (<i>hM</i>) and full scale (<i>hF</i>).	168
Table 6.6 Test speeds at different UKCs.	171
Table 6.7 Propeller rates at corresponding telegraph positions for the tested LNG ship.	176
Table 6.8 Relationship between the propeller rates and the forward speeds at different water depths (UKCs).	176
Table 6.9 The effects of water depths on the propeller rates at same speed.	177
Table 6.10 Statistics of 20°/5° zigzag model tests at the speed of 8 knots in different water depths.	182
Table 6.11 Control performance of four controllers for following straight line.	192
Table 6.12 Grey relational degree and rank of four controllers.	194
Table 6.13 Control performance of four controllers for following a path with obstacles.	198
Table 6.14 Experimental conditions of the repeated tests.	201
Table 6.15 Frequencies for each controller obtaining the best performance at all test conditions.	201
Table 6.16 The Nomoto model parameters <i>T</i> and <i>K</i> with different water depth at 4, 6, 8 knots forward speed.	203
Table 6.17 PID controller coefficients at different water depths (UKCs) for the speed of 4, 6 and 8 knots.	207
Table 6.18 Propeller rate versus PID controller coefficients at different speeds for 10%, 20%, 35%, and 100% UKCs.	209
Table 6.19 Relationship between the proportional, integral, derivative coefficients (coef.) and propeller rate at 10%, 20%, 35%, and 100% UKCs.	211
Table 6.20 Parameters of adaptive PID and IMC controllers at 100% UKC for 8 and 11 knots.	212
Table 6.21 Evaluation indexes of adaptive PID and IMC controllers in different water depths at 8 knots.	214
Table 6.22 Evaluation indexes of the adaptive PID and IMC controllers in different water depths at 11 knots.	216
Table 6.23 Adaptive PID controller's performance using the constant and optimized parameters in different water depths at 8 knots and 11 knots.	217
Table 6.24 IMC controller's performance using the constant and optimized parameters in different water depths at 8 knots and 11 knots.	219
Table 6.25 Comparisons between the experimental parameters and the adaptive parameters.	221
Table 6.26 Tracking errors obtained from simulations using experimental and adaptive parameters at 6 knots and 35% UKC.	221
Table 7.1 Statistics of the simulated and experimental 20°/5° zigzag in medium and shallow water.	232
Table 7.2 Statistics of numerical and experimental results for folding line path.	238
Table 7.3 Statistics of numerical and experimental results for curved path.	240
Table 7.4 Statistics of numerical and experimental results for curved path at different UKCs.	241
Table 7.5 List of waypoints of the planned trajectory.	244

Table 7.6 Comparisons of the adaptive PID controller’ performance at 8 knots and 20% UKC with and without considering bank effects. 250

Table 7.7 Main particulars of the container ship. 259

Table 7.8 Parameters of the prescience model based track controller (PMTC) and fuzzy based track controller (FuzzyTC). 262

Table 7.9 Cross track errors and CPU performance obtained by PMTC and FuzzyTC under calm and deep water. 264

Table 10.1 Example of the inputs to the fast time simulator..... 288

Table 10.2 Procedure for the determination of PID parameters based on Fossen (2011) method. 292

Table 10.3 Procedure for the determination of PID parameters based on the IMC algorithm. 293

Table 10.4 Procedure for the determination of propeller adaptive PID parameters based on the IMC algorithm. 294

Table 10.5 Relationship between propeller rates and forward speeds in 20% UKC. 294

Table 10.6 The values of K and T of Nomoto model at different forward speeds. 295

Table 10.7 Relationship between the propeller rate and forward speed for the studied LNG ship at 20%UKC. 298



Model tests on ship motion control systems using a scale model of an LNG carrier in the Towing Tank for Manoeuvres in Confined Water.